INFORMATION TO USERS

This manuscript has been reproduced from the microfilm master. UMI films the text directly from the original or copy submitted. Thus, some thesis and dissertation copies are in typewriter face, while others may be from any type of computer printer.

The quality of this reproduction is dependent upon the quality of the copy submitted. Broken or indistinct print, colored or poor quality illustrations and photographs, print bleedthrough, substandard margins, and improper alignment can adversely affect reproduction.

In the unlikely event that the author did not send UMI a complete manuscript and there are missing pages, these will be noted. Also, if unauthorized copyright material had to be removed, a note will indicate the deletion.

Oversize materials (e.g., maps, drawings, charts) are reproduced by sectioning the original, beginning at the upper left-hand corner and continuing from left to right in equal sections with small overlaps.

Photographs included in the original manuscript have been reproduced xerographically in this copy. Higher quality 6" x 9" black and white photographic prints are available for any photographs or illustrations appearing in this copy for an additional charge. Contact UMI directly to order.

ProQuest Information and Learning
300 North Zeeb Road, Ann Arbor, MI 48106-1346 USA
800-521-0600

ELECTROSTATIC INTERACTIONS AND EXCITON COUPLING IN PHOTOSYNTHETIC LIGHT-HARVESTING COMPLEXES AND REACTION CENTERS

by

Ethan Thoreau Johnson

A dissertation submitted in partial fulfillment of
the requirements for the degree of

Doctor of Philosophy

University of Washington

2002

Program Authorized to Offer Degree: Biochemistry

ProQuest Information and Learning Company
300 North Zeeb Road
P.O. Box 1346
Ann Arbor, MI 48106-1346

Doctoral Dissertation

In presenting this dissertation in partial fulfillment of the requirements for the Doctoral degree at the University of Washington, I agree that the Library shall make its copies freely available for inspection. I further agree that extensive copying of this dissertation is allowable only for scholarly purposes, consistent with "fair use" as prescribed in the U.S. Copyright Law. Requests for copying or reproduction of this dissertation may be referred to Bell and Howell Information and Learning, 300 North Zeeb Road, Ann Arbor, MI 48106-1346, to whom the author has granted "the right to reproduce and sell (a) copies of the manuscript in microform and/or (b) printed copies of the manuscript made from microform."

Signature 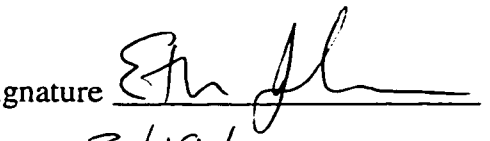

Date 3/19/02

University of Washington
Graduate School

This is to certify that I have examined this copy of a doctoral dissertation by

Ethan Thoreau Johnson

and have found that it is complete and satisfactory in all respects,
and that any and all revisions required by the final
examining committee have been made.

Chair of Supervisory Committee:

William W. Parson

Reading Committee:

William W. Parson

David A. Baker

Rachel E. Klevit

Philip J. Reid

Date 3/20/02

University of Washington

Abstract

ELECTROSTATIC INTERACTIONS AND EXCITON COUPLING IN PHOTOSYNTHETIC LIGHT-HARVESTING COMPLEXES AND REACTION CENTERS

by Ethan Thoreau Johnson

Chairperson of the Supervisory Committee:
Professor William W. Parson
Department of Biochemistry

Protein-pigment complexes are integral to many biochemical reactions. The properties of the pigments in these complexes depend in large part on the protein which serves as both scaffold and solvent. The relative positions of the pigments determine the electronic coupling of the system while local protein charges and vibrational motions alter the energies of the molecules. Photosynthetic light-harvesting complexes and the photosynthetic reaction center serve as excellent models for understanding protein-pigment interactions. The electronic coupling between the pigments of the Light-Harvesting Complex II from *Rhodopseudomonas acidophila* is explored by exciton calculations that treat the excitation of the complex as a combination of monomer and charge-transfer transitions. Comparisons of the calculated absorption and circular dichroism spectra to experimental spectra provide a measure of the delocalization of the excitation and the inhomogeneity of the protein environment. The time-dependent relaxation dynamics of the initial, coherently excited superposition state is also described. In the photosynthetic reaction center from *Rhodobacter sphaeroides*, the effects of ionizable amino acids on the solvation energy of the oxidized primary electron donor are explored by site-directed mutagenesis. Changes in the reduction potential caused by the mutations are measured and compared to theoretical models that

treat the solvation by the protein and surrounding water. Changes in the electrostatic environment also affect the electronic coupling of the two bacteriochlorophylls within the primary electron donor. The mutations alter the relative energies of the basis states in which the charge is localized on one bacteriochlorophyll or the other, and shift the spin distribution and the absorption of the oxidized state. A vibronic model that includes both symmetric and antisymmetric vibrational modes is introduced to explain consistently the changes in the spin distribution, reduction potential and absorption spectrum of the oxidized state. The results reveal the importance of the protein's vibrational modes to the electronic coupling between the pigments.

TABLE OF CONTENTS

LIST OF FIGURES

LIST OF TABLES

INTRODUCTION

The solvation energy of a chemical group is determined by electrostatic interactions with the surroundings. The generation of a charge-separated state such as $NaCl \bullet Na^{+} + Cl^{-}$ is typically more favorable in water than in nonpolar solvents because the Coulombic energy required to separate the charges is balanced by water dipoles that orient around the charges to decrease the energy of the system. By contrast, nonpolar solvents do not provide favorable interactions to the charge-separated species.

Similar processes occur in proteins (*1*) (*2*) (*3*). Protein and solvent atoms provide both charge-charge and dipolar interactions to stabilize ionized groups important for structural stability or catalysis. These interactions are mediated through ionizable groups, permanent protein dipoles, and induced dipoles from polarizable groups in the protein (*2*). Redox proteins are able to stabilize both neutral and charged forms of bound cofactors through structural changes that shift the protein dipoles, changes in ionization states of nearby residues, and interactions with counterions in the solvent. The ability of an enzyme to increase the rate of a reaction relative to the rate in water probably arises mainly through greater stabilization of the transition state by protein dipoles that have been oriented through the folding process (*4*). In water, the transition state may interact similarly with ordered water molecules, but ordering the water molecules requires an energy estimated to be about half that of the interaction between the water and the transition state (*5*). This effectively increases the energy of the transition state in water relative to protein and slows the reaction. In proteins, the dipoles that stabilize the transition state are already established and no additional energy is required.

The reactions of bacterial photosynthesis provide an excellent system for studying these interactions. The redox properties and energies of the photosynthetic

proteins that catalyze energy and electron transfer can be studied thermodynamically and the kinetics of the reactions can be measured by optical spectroscopy (*6*) (*7*). Additionally, a genetic system has been developed to construct site-directed mutations in the photosynthetic reaction center and specific alterations in the protein environment provide insights into the reaction mechanism (*8*). The structures for two types of bacterial photosynthetic proteins are known from protein crystallography and provide direct information on the location and orientation of the pigments and surrounding protein (*9*). This knowledge forms the basis for a theoretical understanding of the absorption spectra for these proteins, the energy and electron-transfer reactions, and into general problems of dielectric screening and solvation. Because the detailed atomic coordinates are available, the photosynthetic proteins are excellent models for studying how protein structure determines protein function.

Photosynthesis is the biological process that converts light energy to chemical energy and drives the metabolism of terrestrial plants, algae and bacteria. The series of biochemical steps of phostosynthesis involves two main processes that are mediated by pigment-protein complexes located in specialized membranes of these organisms. The reactions of photosynthesis occur in the thylakoid membrane of chloroplasts in plants, while in bacteria these reactions are located in the cytoplasmic membrane (*10*). The first process is the absorption of a photon by light-harvesting antenna complexes, which then excite the photosynthetic reaction centers through energy transfer steps. The second is the electron-transfer sequence that leads to charge-separation in the reaction center and a longer-lived, stable form of chemical energy. In these reactions the pigments must absorb light efficiently and the energy-transfer and electron-transfer reactions must be thermodynamically favorable. These conditions depend in part on both the specific orientation of the pigments and the ability of the protein to stabilize the charge-separated states.

The work presented in this thesis involves both the light-harvesting complex II and the photosynthetic reaction center. In the light-harvesting complex, the pigments are

arranged in a symmetric ring structure (*11*). The spectroscopic characteristics of the complex have been calculated using a simple orbital model that describes the excitations as a linear combination of the excitations of the individual pigments. Calculations on the ground-state properties provide information about the electronic interaction between adjacent pigments and the wavefunctions for the excited state for the system. Dynamical processes are also modeled and the time-dependent decay of electronic coherence is used to further understand the electronic properties of the ring after coherent excitation.

The effects of the protein environment in the reaction center have been studied by site-directed mutagenesis of specific ionizable side chains near the primary electron donor. In the reactions catalyzed by the photosynthetic reaction center, an electron is transferred from a donor molecule to an acceptor molecule, leaving a positive charge on the donor (*6*). Following the initial charge separation, additional electron-transfer reactions increase the separation between the electron and the primary donor and slow the recombination kinetics. The final acceptor reacts with two electrons and two protons to form a stable, neutral molecule, which dissociates from the reaction center and is used to generate an electrochemical proton gradient that drives ATP synthesis. In this thesis, the ability of individual amino acids to solvate the charged states of the photosynthetic reaction center has been explored both experimentally and theoretically. Specific ionizable amino acids have been replaced by neutral groups and the reduction potential, the charge distribution in the oxidized dimer and electron-transfer rates have been measured. The charge-charge interactions between the ionizable sidechains and the oxidized dimer are screened by the polar atoms and residues in the protein, and the strength and distance dependence of the dielectric screening have been compared to theory. The calculations demonstrate that protein dipoles and movement of the backbone and side chains are not sufficient to account for the measured screening of these interactions, and we propose that counterions from either nearby ionizable groups or the solvent make major contributions to the screening.

The organization of the thesis is as follows: the first chapter is an introduction to photosynthetic systems and a brief description of the experiments that reveal important aspects of these systems. The second and third chapters discuss the results of molecular orbital calculations for the ground-state absorption and the excited-state dynamics of the light-harvesting complex II. Finally, the last three chapters relate the story of the mutations of ionizable groups near the primary donor in the reaction center. Chapter 4 focuses on the solvation energies of the reaction centers, chapter 5 discusses the effects of the mutations on the oxidized dimer and chapter 6 describes the changes in the absorption spectrum and the primary electron-transfer kinetics.

CHAPTER 1: INTRODUCTION TO PHOTOSYNTHESIS

The purple nonsulfur bacteria have been used as model photosynthetic organisms because the purified photosynthetic proteins are stable and procedures for genetic manipulation of these proteins have been developed (*8*). Although it does not evolve O_2, their single photosystem is analogous to photosystem II in green plants (*12*). Purple nonsulfur bacteria live in ponds, lakes and some soils, thriving in regions below aerobic growth (*13*). In stagnant bodies of water, oxygen is depleted as the depth of the water increases and decomposition of plant and animal residues occurs through anaerobic fermentation. The purple nonsulfur bacteria live in the anaerobic environment and require light to photoassimilate a wide variety of low molecular weight organic molecules. These organisms do not directly compete with green plants for light because their respective absorption spectra are shifted relative to each other (*14*).

In electron micrographs, the inner membrane of purple bacteria shows a structure that is highly folded upon itself to increase the surface area available for the absorption of light (*10*). The main proteins involved in the absorption of light and photochemistry are multi-subunit integral membrane proteins called the light-harvesting complexes I (LH1) and II (LH2) and the photosynthetic reaction center (RC). The primary electron donors and acceptors are bacteriochlorophylls (Bchls) and bacteriopheophytins (Bphes), which are similar to Bchls but lack the central Mg atom, and the final electron acceptors are quinones. Additionally, these proteins contain carotenoid molecules that are used primarily to protect the proteins from intense radiation.

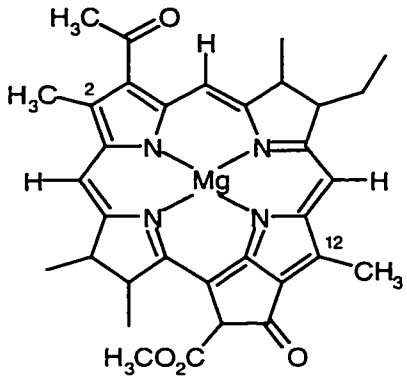

bacteriochlorophyll-a

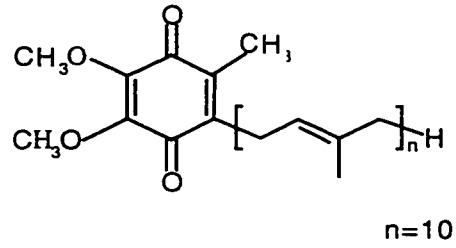

ubiquinone-10

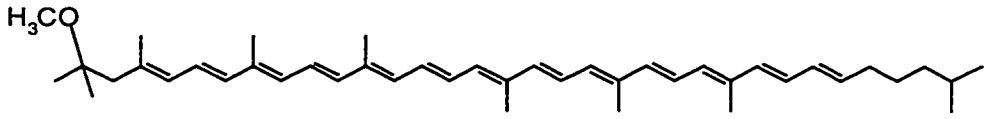

spheroidene

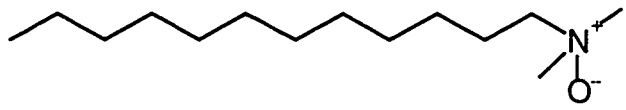

Lauryldimethylamine oxide

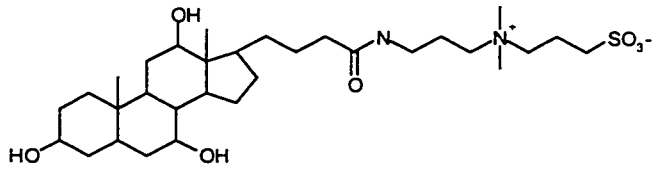

CHAPS

Figure 1. Chemical structures of several cofactors of the photosynthetic proteins and detergent molecules used to solubilize the Light-harvesting complex II and photosynthetic reaction center.

The exact arrangement of the proteins in the photosynthetic membrane is not known and the path of energy transfer from the antenna protein that absorbs the photon to the reaction center is not fully characterized. In general, however, photosynthesis begins by the excitation of a LH2 complex by absorption of a photon. The energy of the photon is stored in the electronic excited state of the LH2 complex and through Förster energy transfer the excitation migrates through many LH2 complexes until it encounters a LH1 complex. It is not known if the LH2 molecules are ordered into an array in the membrane or are more randomly distributed (*15*). There is evidence from electron microscopy for a complex formed between the LH1 complex and the RC and these proteins are found to have a 1:1 stoichiometry. The energy is funneled from the LH1 complex to the RC to excite the primary electorn donor, which is a pair (P) of Bchls.

X-ray structures

An understanding of the functional characteristics of photosynthesis has been advanced by the solution of the crystal structures for both the RC and the LH2 complex by protein crystallography. Many theoretical studies and mutagenesis experiments on energy and electron transfer have been motivated by the specific information about the relative orientation of the cofactors and their relationship to the protein. The structures of the bacteriochlorphylls, quinones, and carotenoids, which are the main cofactors in these reactions, are shown in Figure 1. Because these proteins are membrane bound and have a large amount of hydrophobic surface, they often are studied in intact membranes called chromatophores, which are membrane invaginations that have been pinched off to form small vesicles during cell lysis. Purification and characterization requires that a detergent to dissolve the protein into detergent-micelles. The structures for several of the common detergents used in this study are also shown.

Figure 2 shows the structure for the LH2 complex isolated from *Rhodopseudomonas acidophila* (*11*) and reveals a beautifully symmetric ring structure of nine polypeptide dimers that coordinate two sets of Bchls. The outer set of 9 pigments are oriented so that the planes of the Bchl molecules are parallel to the

membrane. These pigments do not interact strongly. The planes of the 18 Bchls are oriented perpendicular to the plane of the membrane and are stacked in domino fashion around a central point. This stacking causes the molecular orbitals to overlap and excitonically couples the ring. One feature of the symmetric structure is that energy transfer between adjacent LH2 complexes is efficient regardless of their orientation.

The photosynthetic RC is also a pigment-protein complex that coordinates several cofactors (*16-19*). The RC is constructed from three polypeptide chains named L, M, and H for light, medium, and heavy, in reference to their apparent molecular weights measured by gel electrophoresis. L and M are nearly homologous subunits of five transmembrane helices that form a heterodimer with two-fold rotational pseudosymmetry. Together, these subunits coordinate 4 Bchls and 2 Bphes, 2 quinones, a non-heme iron and a carotenoid arranged in the nearly symmetric structure shown in Figure 3. The L and M subunits each coordinates a Bchl (P_L or P_M), and these two Bchls dimerize to form the primary electron donor (P), also called the "special pair". In addition to these pigments there are two accessory Bchls (B_L and B_M) and two Bphes (H_L and H_M).

The axial ligands to the Bchls are histidine residues on the L and M subunits. The ligands to P_L and P_M are, respectively, histidines L173 and M202 and the accessory Bchls B_L and B_M are bound to histidines L153 and M182. In previous studies, one or the other of these histidines have been replaced by leucine, which is not able to coordinate a Bchl, and a Bphe is inserted in place of the Bchl. These substitutions dramatically change the symmetry of the pigments and have been used to study both the electronic properties of P and the primary electron transfer event (*20*) (*21*) (*22*).

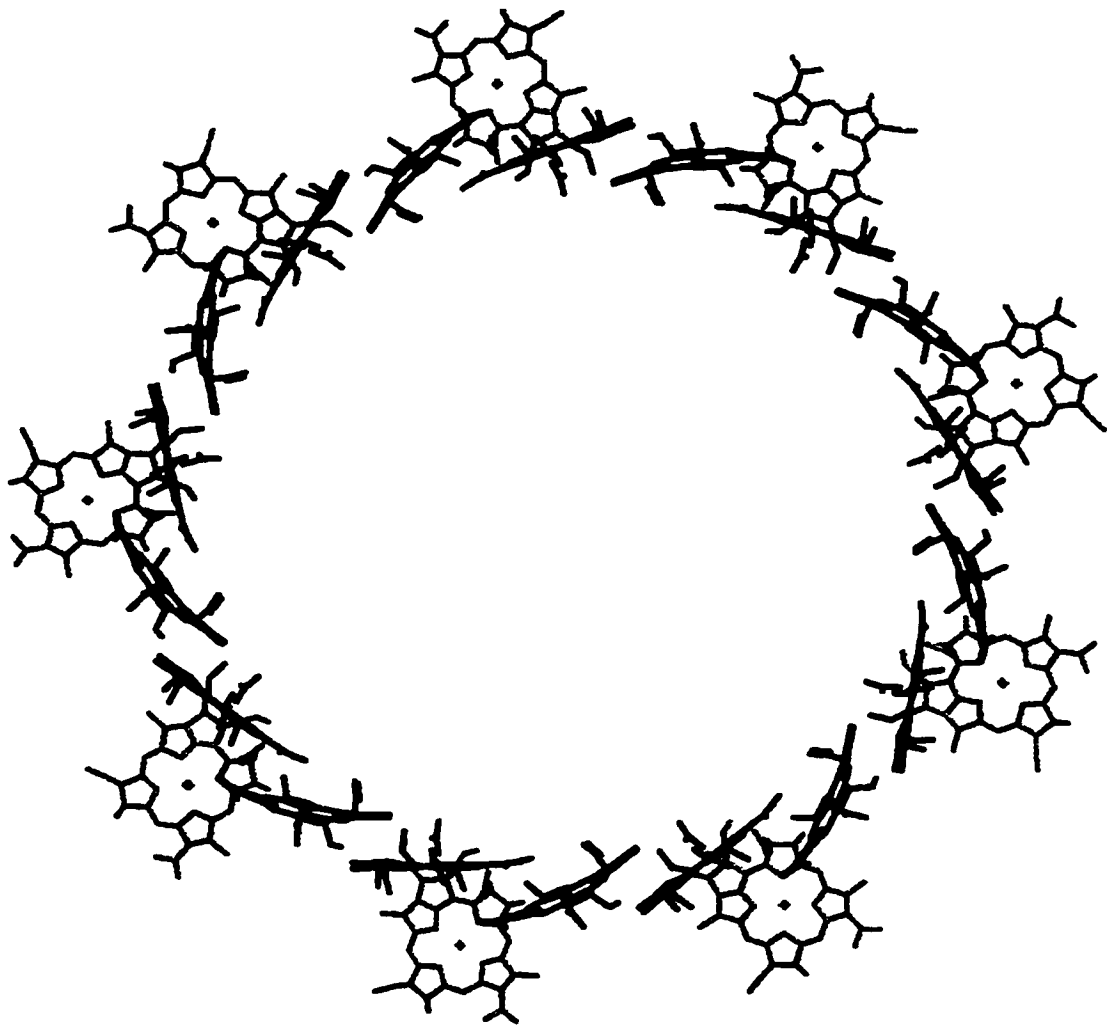

Figure 2. Crystal structure of the Light-harvesting complex II from *Rp. acidophila*. The ring of B850 molecules (black) and the B800 molecules (gray) are oriented so that the view is along the membrane normal. The polypeptide subunits have been removed for clarity.

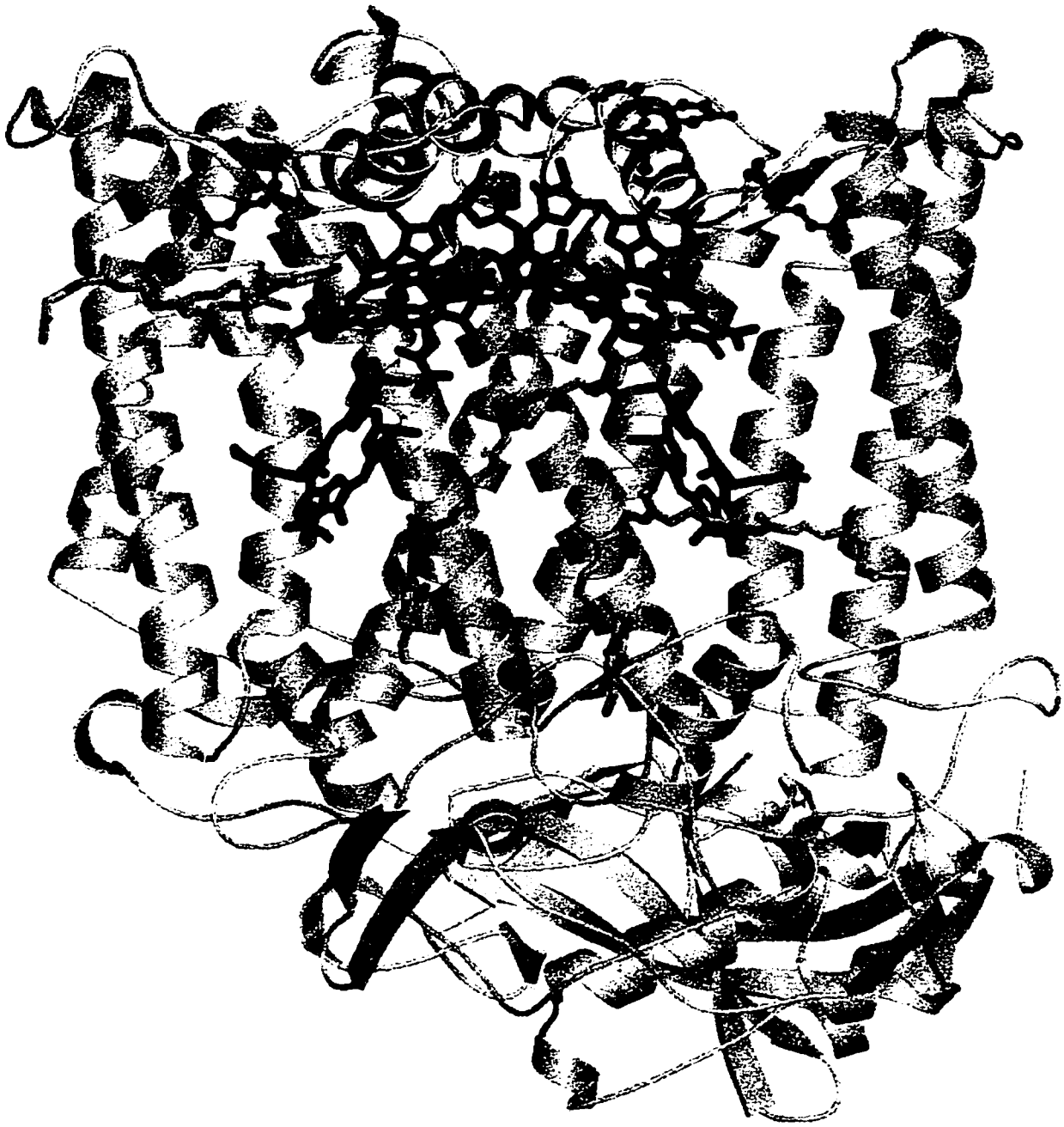

Figure 3. Crystal structure of the photosynthetic reaction center from *Rb. sphaeroides*. The "special pair" bacteriochlorophylls (green), "accessory" Bchls (blue), bacteriopheophytins (red), the quinones (gray) and the non-heme Fe (red) are shown. The side chains for R(L135), D(L155), Y(L164), C(L247) and R(M164) are shown in a ball-and-stick representation.

In addition to the axial ligands, several other residues have been mutated to study the effects of the protein environment on P. P_L and P_M have two carbonyl groups that are conjugated to the π system and can act as hydrogen bond acceptors. These groups are the 2^1 acetyls that are located in the overlap region of the two Bchls and the 12^1 ketos that are positioned on the outermost edges of P_L and P_M. In the wild-type structure, there is only one hydrogen bond and this is between the acetyl group of P_L and H(L168). This is removed in the H(L168)F mutation. Potential hydrogen bonds to the acetyl of P_M and the keto groups of P_L and P_M are introduced by the mutations F(M197)H, L(L131)H and L(M160)H (*23*).

The effects of ionizable groups on the thermodynamics and kinetics of the RC have not been well studied. This is in part due to the absence of ionizable groups near the pigments. P, B and H are buried in the interior of a protein within the region of the membrane and this nonpolar environment excludes the charged and polar amino acids. Arginines L135 and M164 are, respectively, the closest ionizable residues to P_L and P_M, and are at a distance of approximately 7 Å edge-to-edge. Asp L155 is also close to both P and B_L and is solvent accessible. The H subunit has a single transmembrane helix that anchors it to the L and M subunits. Most of H is solvent accessible and has many ionizable groups on its surface. This subunit has residues that are important in the photochemistry of the quinones (*24*).

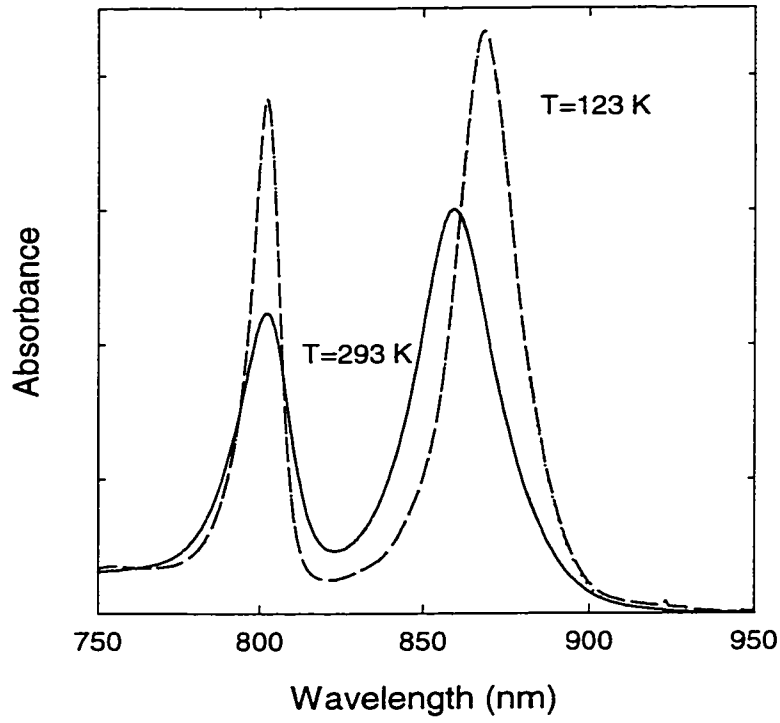

Figure 4. Absorption spectrum of the Light-harvesting complex II from Rp. acidophila at T = 293 K (solid line) and T = 123 K (dashed line).

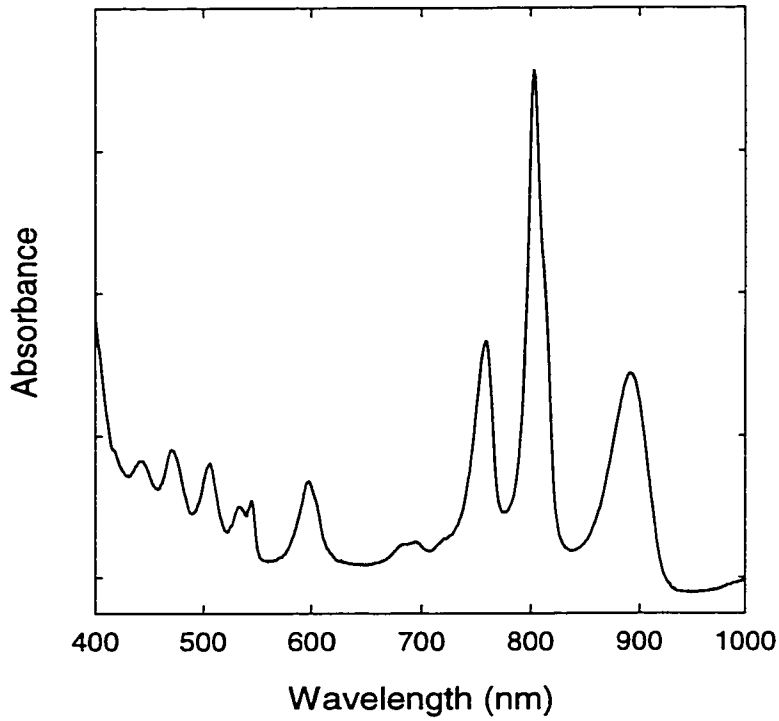

Figure 5. Absorption spectrum of photosynthetic reaction center from Rb. sphaeroides at 78 K.

Optical Absorption

As described above several types of pigments are bound to the LH2 and RC proteins. The ground-state absorption of the complexes reveal clues about the structure of the pigments and the strengths of the pigment-pigment interactions, which depend on their relative separations and orientations. With the crystal structure in hand, the absorption spectra can be calculated directly and the pigments' interactions can be understood in the context of the atomic coordinates. The near-IR absorption spectra is dominated by the Bchl molecules. The absorption of monomeric Bchl has been well described by a 4 orbital model that includes the two highest filled (HOMO) and two lowest unfilled molecular orbitals (LUMO) (*25*). Combinations of transitions between these orbitals lead to the prominent absorption bands Q_y, Q_x, and Soret bands at, respectiveley, 772 nm, 605-608 nm and 365 nm in methanol (*26*). The ground-state absorption spectra for the LH2 complex at 123 K and 293 K are shown in Figure 4. As will be discussed in detail in Chapter 2, the two absorption bands at 800 and 850 nm arise independently from the rings of 9 and 18 Bchls. Briefly, the 9 pigments are very weakly coupled and essentially behave as monomeric Bchls. The ring of 18 pigments is more strongly coupled and mixing of the monomer transitions and charge-transfer (CT) transitions leads to a red-shift of the absorption maximum to 850 nm. Features near 500 are the Q_x bands on the Bchls and further to the blue near 400 are the absorption bands for the bound carotenoid molecules.

The absorption spectrum of the RC (Figure 5) has three major bands in the near-IR that correspond to three pairs of pigments. The 760 nm absorption band of the Bphes H_L and H_M is at higher energies than the bands of the accessory Bchls B_L and B_M, which absorb at 800 nm. Both pairs of molecules are only weakly interacting although they are all part of an excitonically connected system with the "special pair" (*27*). The Bchls of P are excitonically coupled and the monomer transitions have been shown to mix with charge-transfer (CT) transitions to shift the peak of the absorption to 865 nm at room

temperature and to 890 nm at 80 K (*28*). This absorption band is dramatically altered by the subsitution of Bphe for either P_L or P_M, highlighting the coupled nature of this absorption band (*20*). The Q_x transitions for the Bchls overlap to form the 600 nm band, while the Q_x absorption bands of H_L and H_M are resolved near 540 nm. After excitation and electron transfer the Q_x band of H_L is bleached, demonstrating that electron transfer selectively reduces H_L in apparent conflict with the near symmetry of the protein. The carotenoid has a broad absorption band in the region of 400 nm.

Electron transfer

After excitation, either from energy transfer from LH1 or by direct absorption of light, an electron is transferred from the excited state P^* to a bacteriopheophytin (H) through the accessory bacteriochlorophyll (B) to form the state P^+BH^-. In wild-type RCs from *Rb. sphaeroides* at room temperature, this reaction occurs in approximately 3 picoseconds (3×10^{-12} s) (*6*) (*7*). In 200 ps the electron is transferred to a quinone (Q_A) and then in 100 μs to a second quinone (Q_B). In a few microseconds P^+ is reduced by a cytochrome to restore P to its original state. After a second electron is transferred to Q_B, the quinol dissociates from the RC and is subsequently oxidized by the cytochrome bc_1 complex (ubiquinol cytochrome c oxidoreductase) to generate a proton gradient, which drives the production of ATP by ATP synthetase (*29*). These reactions are summarized in Figure 6.

What drives this electron transfer process? What is the role of the protein in this reaction? Is it simply the scaffold that holds the pigments in place, or does the protein provide favorable interactions with the pigments to stabilize the charge-separated states? As a puzzle that still needs to be worked out, only one side of the pigments is used in the electron transfer reactions. While the symmetry of the structure suggests that the electron could transfer down both sides, it happens that only one branch of pigments is active in the wild-type structure. This is a consequence of both the protein environment and the coupling between the pigments. In some mutants that have an

apsartic acid near this pigment, there is 15 percent electron transfer down the pigments on the M subunit (*30*).

Influence of electrostatics on the RC

Several theoretical studies have discussed the role of electrostatics in the electron transfer steps of the RC (*31*) (*32*). The influence of protein dipoles on the stabilization of the charge-separated states have been studied in detail both theoretically and experimentally. The solvation energy change of $PBH{\bullet}P^{+}BH^{-}$ have been examined in detail and the effects of Tyr M210, a residue located between B_L and H_L and oriented so that its dipole can stabilize B_L^{-} or H_L^{-}, has been studied both theoretically and experimentally. Based upon the microscopic orientation of the protein dipoles the effect of changing the Tyr to Phe destabilizes $PBH{\bullet}P^{+}BH^{-}$ by approximately 4 kcal/mol (*33*). This should result in a slowing of the primary electron transfer kinetics, and this is indeed what is measured experimentally. Changing Tyr (M210) to Phe or Trp slows dramatically the initial electron transfer steps (*34*). Therefore, the orientation of both permanent and induced protein dipoles can change the energetics of the reaction and change the photochemistry.

The effects of the ionizable groups on the electron transfer energetics have been calculated and there is disagreement about the contribution of the static field to the energies of the charge-separated states. Alden *et. al.* (*31*) use a self-consistent calculation that microscopically treats the protein and solvent dipoles to calculate the contribution of ionizable groups to the energy difference between $P^{+}B^{-}H$ and $P^{+}BH^{-}$. They conclude that most of the ionizable groups are screened strongly and probably do not have much effect on the relative energies of the charge-separated states. There are a few exceptions, however, and several ionizable groups are expected to influence the relative energies of $P^{+}B^{-}H$ and $P^{+}BH^{-}$. A prominent residue is Asp (L155), which is located near B and expected to destabilize $P^{+}B^{-}H$ relative to $P^{+}H^{-}$. Arg (L103) is located

near H and should stabilize P^+BH^-, and Arg (L135) should affect the energies of P^+B^-H and P^+BH^- through interactions with both P and B.

These conclusions are in contrast with the studies of Gunner *et al.* (*32*), who used Delphi calculations with an interior dielectric of 2 to calculate the effects of ionizable groups in the RC of *R. viridis*. They concluded that the difficulty of forming a charge-separated state in a low dielctric medium is overcome by large static fields arising from the surrounding ionizable groups. Significant electric fields place the cofactors on the L and M subunits in significantly different potentials, which could determine the rates and asymmetry of electron transfer. In agreement with Alden *et al.*, the residues mentioned above are also expected to have conspicuous roles in the energies of these states. Arg (L103) would favor charge separation by stabilizing H-, Asp (L155) would stabilize P^+ to favor separation, while Arg (L135) would oppose charge separation by destabilization of P^+.

In general, although the effects of short range electrostatics arising either from monopole or dipole interactions can be important, long-range monopole interactions may be screened effectively and may not contribute significantly to the energies of the charge-separated states. The residues closest to the cofactors probably are the most important, with long-range interactions providing only small perturbations. The direct relationship between the separation of the charged residue and the cofactor and the influence of the residue on the chemistry can be obtained by an investigation of site-directed mutations that alter the energies of redox states and the rates of electron transfer.

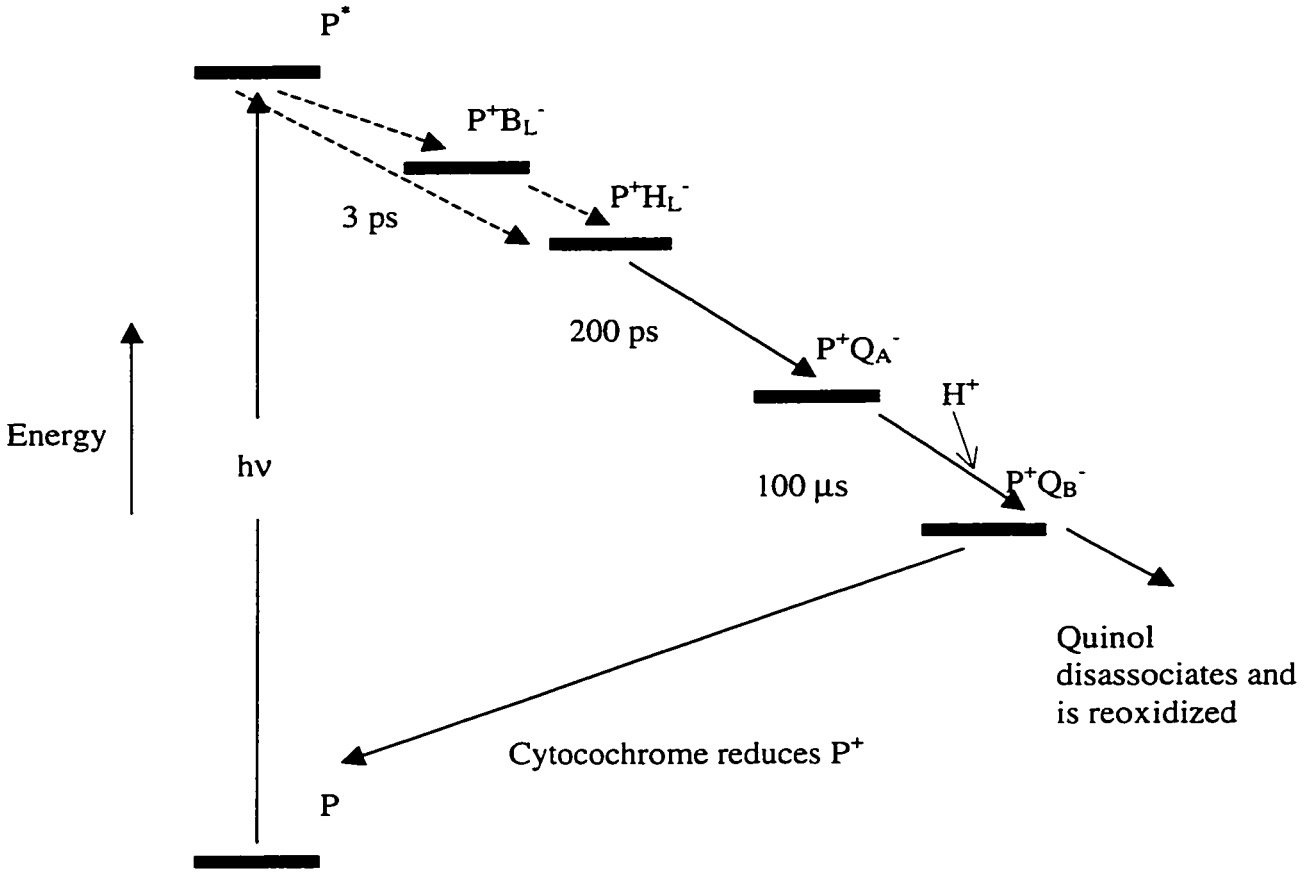

Figure 6. Free-energy diagram showing the charge-separated states involved in the electron-transfer reactions in the photosynthetic reaction center. Light excites the "special pair" of bacteriochlorophylls (P) to the excited state P^*. P^* is oxidized and an electron is transferred to H_L, Q_A and finally to Q_B.

CHAPTER 2: CALCULATIONS OF SPECTROSCOPIC PROPERTIES OF THE LH2 BACTERIOCHLOROPHYLL-PROTEIN ANTENNA COMPLEX FROM *RHODOPSEUDOMONAS ACIDOPHILA*[1]

The light-harvesting (LH) antenna systems of photosynthetic bacteria and plants transfer excitation energy rapidly to the photosynthetic reaction centers, where the energy is trapped in an electron-transfer reaction (*15, 35, 36*). Photosynthetic bacteria contain two major types of antenna complexes. One of these (LH1 or B875) is believed to surround the reaction centers, while the other (LH2 or B800-850) forms a peripheral network of pigment-protein complexes, each of which holds between 20 and 30 molecules of bacteriochlorophyll (BChl). The recent solution of crystal structures of LH2 complexes from *Rhodopseudomonas acidophila* (*11*) and *Rhodospirillum molischianum* (*37*) has opened the door to an increasingly detailed understanding of the unusual spectroscopic and dynamic properties of the bacterial antenna complexes.

The LH2 complex from *Rp. acidophila* strain 10050 consists of nine copies of each of two proteins (α and β), 27 BChl-*a* molecules and 18 carotenoids, arranged in a cylindrical structure with C_9 crystallographic symmetry (*11*). The pigments form an inner ring of 18 BChls with a center-to-center distance of about 9 Å and an outer ring of 9 BChls with center-to-center distances of about 21 Å. The two rings are offset by 16.5 Å along the cylinder axis. The normals to the molecular planes of the BChls in the inner ring are aligned approximately perpendicular to the symmetry axis, whereas those of BChls in the outer ring are approximately parallel to this axis. Figure 7 shows the structure of the repeating unit of two BChls in the inner ring and one in the outer. One of the BChls in the inner ring is noticeably distorted from planarity (*36*).

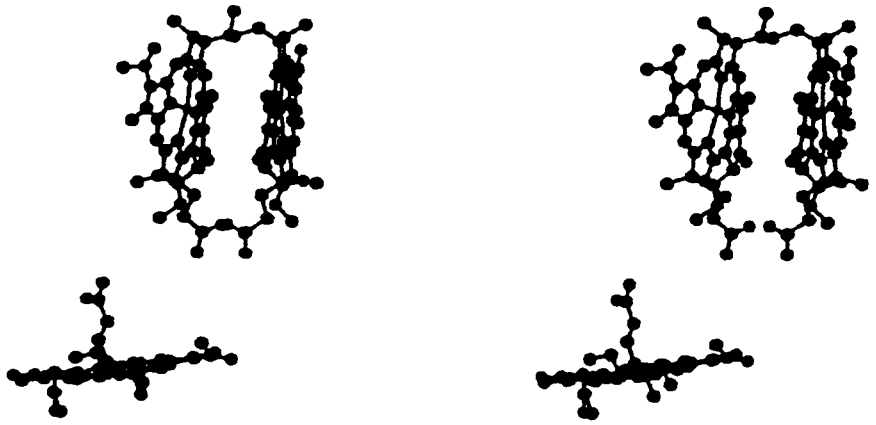

Figure 7. Stereo view of the three BChl-*a* molecules in the asymmetric unit of the LH2 complex of *Rp. acidophila*, from a perspective approximately perpendicular to the C_9 symmetry axis. A B850 BChl bound to an α polypeptide is at the top right, a B850 BChl bound to a β polypeptide at the top left, and a B800 BChl at the bottom.

The absorption spectra of LH2 complexes from *Rp. acidophila* and other related bacterial species differ substantially from the spectrum of monomeric BChl in solution. The long-wavelength (Q_y) absorption band of monomeric BChl-*a in vitro* occurs at 770 to 780 nm and has negligible rotational strength. LH2 complexes have two strong absorption bands in the near IR, one in the region of 850 to 860 nm and the other near 800 nm (Fig. 8A). The long-wavelength absorption band of the LH2 complex of *Rp. acidophila* occurs at 859 nm at room temperature and at 870 nm at 4 K (*38*). The CD spectrum (Fig. 8B) displays a negative lobe on the red side of the long-wavelength absorption band, a positive lobe on the blue side of this band, and a somewhat weaker pair of lobes with reversed signs on either side of the 800-nm band.

The crystal structure of the LH2 complex suggests that the 18 closely spaced and, presumably, strongly coupled BChls give rise to the absorption band in the 850-nm region, while the outer, more weakly coupled BChls are responsible for the absorption band at 800 nm (*36, 39*). This supposition is in accord with the larger dipole strength of the 860-nm band and with measurements of linear dichroism (*40*). The BChls in the inner and outer rings have therefore been termed the "B850" and "B800" BChls, respectively. Fluorescence emission occurs mainly to the red of the B850 band, but the fluorescence excitation spectrum exhibits a strong component at 800 nm as well as at 850 nm, indicative of efficient energy transfer from B800 to B850 (*41*). Time-resolved measurements have shown that, in the similar complex from *Rhodobacter sphaeroides*, the transfer occurs with a time constant of about 0.7 ps at 295 K (*42-44*).

A knowledge of the electronic states that give rise to the absorption and emission spectra of the LH2 complex is critical to a detailed understanding the mechanism of energy transfer. The most practical way to approach a system of this size probably is to use a semiempirical quantum mechanical method such as the quantum-mechanical-consistent-force-field/π-electron (QCFF/PI) method (*45, 46*) to treat the individual BChl

molecules, and to introduce intermolecular interactions at the level of configuration interactions (CI). Warshel and Parson (*27, 28*) used this strategy to explore the spectroscopic properties of the reaction center of *Rp. viridis*. Their treatment included charge-transfer (CT) states explicitly and used transition monopoles rather than point dipoles to evaluate exciton interactions. The same approach later was used to treat oxidized reaction centers (*47*) and crystalline methylbacteriopheophorbide-*a* (*48*). Sauer et al. (*39*) recently described similar calculations that reproduced some of the spectroscopic properties of the *Rp. acidophila* LH2 complex. To account for the energy of the long-wavelength absorption band, it appeared necessary to lower the monomer transition energies assigned to the B850 BChls by about 240 cm^{-1} relative to the energies of the B800 BChls. Although the calculated CD spectrum did not match the measured spectrum well, bands with positive and negative rotational strengths were obtained in the correct regions. In these calculations, the same molecular orbitals were used for all the BChls. Mixing of the Q_y transitions with CT, Q_x and Soret transitions was not included explicitly, and absorption line shapes were introduced by dressing the calculated stick spectra with Gaussians.

In the present work, the QCFF/PI-CI approach is used to calculate the absorption and CD spectra of the LH2 complex of *Rp. acidophila*. We have refined the treatment of the distance dependences of intermolecular exciton and CT interactions, used different molecular orbitals and transition energies for BChls with the three geometries seen in the crystal structure, included inhomogeneous distributions of monomer transition energies, and used a realistic treatment of the absorption line shapes based on experimentally measured vibronic parameters and homogeneous linewidths. We focus particularly on the question of whether the main excited states of the LH2 complex are extensively delocalized over the chromophore rings, or are localized on smaller groups of pigments.

Methods

Monomer wavefunctions and spectroscopic properties. The wave functions for isolated BChl molecules were obtained by the QCFF/PI method using the heteroatom parameters from Table IV of Warshel and Lapicirella (*46*). Molecular π-orbitals for the individual molecules are written as linear combinations of atomic orbitals

$$\phi_n^s = \sum_t v_{n,t}^s \chi_t^s \qquad (1)$$

where χ_t^s is an atomic 2pπ orbital on atom t of molecule s, and the expansion coefficients ($v_{n,t}^s$) are obtained by solving the self-consistent field equation (*45*). The major optical absorption bands of BChl are due to transitions involving the top two filled molecular orbitals and the two lowest unfilled orbitals (*25, 49*). We will denote this set of orbitals for molecule s by ϕ_1^s to ϕ_4^s in order of increasing energy. Separate sets of orbitals were generated for BChl molecules in each of the three different geometries found in the LH2 crystal structure (see Figure 7). The coefficients obtained for the three structures are given in the Supplementary Material. In the present study, we did not consider perturbations of the orbitals by hydrogen bonding or electrostatic interactions with the protein.

Wave functions for the excited states of an individual BChl can be written as

$$\Psi_N^s = \sum_N c_{i,N}^s \, {}^1\Psi_N^s \quad (2)$$

where ${}^1\Psi_N^s$ is the Slater determinant corresponding to a singlet excitation from orbital ϕ_{n1}^s to ϕ_{n2}^s (${}^1\Psi_N^s \equiv {}^1\Psi_{n1\rightarrow n2}^s$) and the $c_{i,N}^s$ are intramolecular CI coefficients. In the four-orbital model this treatment yields four excited states termed Q_y, Q_x, B_y and B_x (*27*). The Q_y and B_y transitions are due primarily to excitations from ϕ_2 to ϕ_3 and from ϕ_1 to ϕ_4; the Q_x and B_x transitions, to excitations from ϕ_2 to ϕ_4 and from ϕ_1 to ϕ_3. The

calculated Q_y excitation energies varied significantly for molecules with the three different geometries in the crystal structure. Relative to B800, the energy for B850-α was lower by 216 cm^{-1} and that for B850-β (which has the largest departure from planarity) was lower by 307 cm^{-1}. Jentzen et al. (*50*) and Barkigia et al.(*51*) have described similar variations in calculated Q_y excitation energies with structural distortions in BChl and other related molecules.

Transition dipoles for the intramolecular excitations ($\vec{\mu}_i^s$) were calculated using the "transition gradient" or "dipole velocity" representation:

$$\vec{\mu}_i^s \approx \left(e\hbar\sqrt{2}/2\pi mc\bar{\nu}_i^s\right)\sum_N c_{i,N}^s \sum_{t1}\sum_{t2} \nu_{n1,t1}^s \nu_{n2,t2}^s \left\langle \chi_{t2}^s \left| \tilde{\nabla} \right| \chi_{t1}^s \right\rangle$$

$$= \left(e\hbar\sqrt{2}/2\pi mc\bar{\nu}_i^s\right)\sum_N c_{i,N}^s \sum_{t1}\sum_{t2>t1} \left(\nu_{n1,t1}^s \nu_{n2,t2}^s - \nu_{n1,t2}^s \nu_{n2,t1}^s\right) \left\langle \chi_{t2}^s \left| \tilde{\nabla} \right| \chi_{t1}^s \right\rangle \quad (3)$$

where $\bar{\nu}_i^s$ is the energy of transition i of molecule s, $\tilde{\nabla} = (\partial/\partial x, \partial/\partial y, \partial/\partial z)$, e and m are the electron charge and mass, and c is the speed of light. Here, and for all the subsequent calculations, we set $\bar{\nu}_i^s$ at 12,500 cm^{-1} for the Q_y transition of BChl with the B800 geometry, corresponding to a wavelength of 800 nm. We reduced the energies for B850-α and B850-β to 12,284 and 12,193 cm^{-1}, respectively, in accord with the calculated energy differences between the three structures. The Q_x, B_x and B_y transitions were assigned energies of 16,667, 24,390 and 27027 cm^{-1}, respectively, for all three structures.

The terms in eq. 3 were evaluated for all intramolecular atom pairs ($t1$, $t2$) with interatomic distances less than 20 Å, although decreasing the cutoff distance to 5 Å had little effect on the results. To take into account the distortions of the BChl molecules from planarity, the individual interatomic matrix elements were calculated from the expression

$$\left\langle \chi^s_{t2} \mid \tilde{\nabla} \mid \chi^s_{t1} \right\rangle = (\eta_{x,t1}\eta_{y,t2} + \eta_{y,t1}\eta_{x,t2})\nabla_{xy}\hat{i}$$

$$+ (\eta_{y,t1}\eta_{y,t2}\nabla_\sigma + (\eta_{x,t1}\eta_{x,t2} + \eta_{z,t1}\eta_{z,t2})\nabla_\pi)\,\hat{j}$$

$$+ (\eta_{z,t1}\eta_{y,t2} + \eta_{y,t1}\eta_{z,t2})\nabla_{xy}\hat{k} \quad (4)$$

Here $\eta_{x,t}$, $\eta_{y,t}$ and $\eta_{z,t}$ are direction cosines of the 2pπ orbital on atom t (χ^s_t) with respect to a Cartesian coordinate system (x,y,z) defined so that the y axis is along the line from atom $t1$ to $t2$; $\hat{i}$, $\hat{j}$ and $\hat{k}$ are unit vectors in this system; and ∇_σ, ∇_π and ∇_{xy} are the matrix elements of $\tilde{\nabla}$ for pairs of Slater-type 2p orbitals in canonical orientations and at the appropriate interatomic distance. ∇_π is for two p_x or p_z orbitals; ∇_σ, for two p_y orbitals; and ∇_{xy}, for p_x and p_y orbitals. ($\nabla_{zy} = \nabla_{xy}$ and $\nabla_{xz} = 0$.) The dependences of ∇_σ, ∇_π and ∇_{xy} on the interatomic distance and the Slater orbital parameter ζ for C, N and O atoms were evaluated as described in Appendix A.

The CI coefficients ($c^s_{i,N}$) for the intramolecular transitions were adjusted to optimize the agreement between the dipole strengths ($|\vec{\mu}^s_i|^2$) calculated with equation 3 and those measured experimentally for monomeric BChl-*a* in solution. A dipole strength of 50 D^2 (D = 1 debye) was used for the Q_y transitions, and 19 D^2 for Q_x (see Appendix B). Because the B_y and B_x transitions are not well resolved in the absorption spectra, we did not attempt to refine the $c^s_{i,N}$ for these transitions independently, but rather used the values obtained by a symmetry transformation of the Q_y and Q_x coefficients (*27*). Separate sets of CI coefficients were obtained for BChl molecules with the three different geometries in the crystal structure (Fig. 7), on the assumption that the dipole strengths are the same for all three geometries. The optimized coefficients are given in the Supplementary Material. Although the actual dipole strengths undoubtedly vary somewhat, the differences between the CI coefficients obtained for the three structures are small and have little effect on the results presented

below. Note that our adjustment of the CI coefficients is part of the initial parameterization of the wavefunctions of monomeric BChl, and does not represent an empirical fitting of spectroscopic data on the LH2 complex.

Molecular magnetic transition dipoles also were calculated with the gradient representation:

$$m_i^s \approx \left(-e\hbar i\sqrt{2}/2\pi mc\right)\sum_N c_{i,N}^s \sum_{t1}\sum_{t2} v_{n1,t1}^s v_{n2,t2}^s \left\langle \chi_{t2}^s \left| r \times \tilde{\nabla} \right| \chi_{t1}^s \right\rangle$$

$$\approx \left(-e\hbar i\sqrt{2}/2\pi mc\right)\sum_N c_{i,N}^s \sum_{t1}\sum_{t2>t1} \left(v_{n1,t1}^s v_{n2,t2}^s - v_{n1,t2}^s v_{n2,t1}^s\right) r_{t1,t2}^o \times \left\langle \chi_{t2}^s \left| \tilde{\nabla} \right| \chi_{t1}^s \right\rangle \quad (5)$$

where $r_{t1,t2}^o$ is the vector from the origin of the coordinate system to the point midway between atoms $t1$ and $t2$.

Oligomer Wavefunctions. Interactions between the BChls in an oligomeric structure can be introduced by writing a CI matrix for the excited states of the system:

$$\mathbf{U} = \begin{bmatrix} [\,\mathbf{U}^{loc}\,] & [\mathbf{U}^{loc,CT}] \\ [\mathbf{U}^{CT,loc}] & [\,\mathbf{U}^{CT}\,] \end{bmatrix} \quad (6)$$

The excitation energies of the intramolecular or "local" transitions (Q_y, Q_x, B_y and B_x) of the individual BChls appear as diagonal terms in the upper left-hand block of **U** ($\mathbf{U}^{loc}$). The off-diagonal terms in this block represent exciton interactions between the transitions of separate molecules. In the lower right-hand block ($\mathbf{U}^{CT}$), the diagonal terms are the energies of intermolecular charge-transfer transitions, and the off-diagonal terms represent mixing of different CT transitions. The $\mathbf{U}^{CT,loc}$ and $\mathbf{U}^{loc,CT}$ blocks describe the mixing of local and CT transitions. In the B800-B850 complex of *Rp. acidophila* each of the 27 BChl monomers has four possible singlet excitations, giving a total of 108 local excited states. Although we will be concerned mainly with absorption bands in the near IR, which depend primarily on the Q_y transitions, it is

important in principle to retain the higher-energy transitions as well because of their possible contributions to hyperchromism or hypochromism of the long-wavelength bands (*52*). In addition to the local transitions, each pair of BChls has 8 possible CT transitions (an electron originating in either ϕ_1^{s1} or ϕ_2^{s1} of BChl *s*1 can move to either ϕ_3^{s2} or ϕ_4^{s2} of BChl *s*2, and an electron originating in ϕ_1^{s2} or ϕ_2^{s2} can move to ϕ_3^{s1} or ϕ_4^{s1}). Again, although only the $\phi_2 \rightarrow \phi_3$ CT transitions are expected to make significant contributions to the near-IR absorption bands, we retained the higher-energy CT transitions for consistency. The CT transitions have no intrinsic dipole strength, but contribute to the absorption and CD spectra to the extent that they mix with the intramolecular transitions. Because the matrix elements that control this mixing ($\mathbf{U}^{\mathbf{CT,loc}}$ and $\mathbf{U}^{\mathbf{loc,CT}}$) drop off very rapidly with distance (see below), it is sufficient to consider CT interactions only between neighboring molecules in the ring of B850 BChls. This restriction reduces the number of CT transitions to 144 (8 x 18). The total size of **U** is, therefore, 252 x 252.

The exciton-interaction matrix element that mixes local transition *i* of one BChl with transition *k* of another can be expanded with the transition-monopole expression

$$U^{loc}_{i(s1),k(s1)} = 2\Omega_{i(s1),k(s2)} \sum_N c^{s1}_{i,N} \sum_{t1} v^{s1}_{n1,t1} v^{s1}_{n2,t1} \sum_M c^{s2}_{k,M} \sum_{t2} v^{s2}_{m1,t2} v^{s2}_{m2,t2} \gamma_{t1,t2} / d_{t1,t2} \quad (7)$$

where $\gamma_{t1,t2}$ is the electron-electron repulsion integral between 2pπ electrons on atom *t*1 of BChl *s*1 and atom *t*2 of BChl *s*2, $d_{t1,t2}$ is a dielectric screening factor, and $\Omega_{i(1),k(2)}$ is a factor that corrects for imperfections in the molecular orbitals (see below).

To evaluate the repulsion integrals, we used the two-center integrals originally derived by Roothaan (*53*). The Roothaan integrals for pairs of 2p orbitals in canonical orientations and at the appropriate interatomic distances (R_σ, R_π, R_{xz}, and R_{xy}) were weighted by products of direction cosines in a manner analogous to that described above for the intramolecular gradient integrals:

$$\gamma_{t1,t2} = (\eta_{y,t1}\eta_{y,t2})^2 R_\sigma + ((\eta_{x,t1}\eta_{x,t2} + \eta_{z,t1}\eta_{z,t2})^2) R_\pi + ((\eta_{x,t1}\eta_{z,t2})^2 + (\eta_{z,t1}\eta_{x,t2})^2) R_{xz}$$

$$+ ((\eta_{x,t1}\eta_{y,t2})^2 + (\eta_{y,t1}\eta_{x,t2})^2 + (\eta_{z,t2}\eta_{y,t1})^2 + (\eta_{y,t2}\eta_{z,t1})^2) R_{xy} \qquad (8)$$

At interatomic distances beyond about 6 Å, values for the repulsion integrals calculated in this way are essentially identical to those obtained with the simpler expression used in previous calculations on reaction centers (*27*). At shorter distances, the Roothaan integrals probably capture more accurately the dependence on the relative orientations of the two orbitals. However, this has only minor effects on the calculated spectroscopic properties of the LH2 complex.

The dielectric screening factor in eq. 7 represents the effects of high-frequency induced dipoles in the protein and solvent. At large interatomic distances, $d_{t1,t2}$ should be approximately n^2, where n is the refractive index of the protein; at short distances, $d_{t1,t2}$ should approach 1. We therefore used a distance-dependent screening factor:

$$d_{t1,t2} = n^2 + (1 - n^2) e^{-(r_{t1,t2}/r_0)^3} \qquad (9)$$

where $r_{t1,t2}$ is the distance between atoms $t1$ and $t2$, $n^2 = 2$, and r_o is an adjustable parameter on the order of 4 Å (*54*). The dependence of the results on the choice of r_o is discussed below.

The correction factor $\Omega_{i(s1),k(s2)}$ is given by

$$\Omega_{i(s1),k(s2)} = \left[\left(D^{\nabla}_{i(s1)} / D^{R}_{i(s1)} \right) \left(D^{\nabla}_{k(s2)} / D^{R}_{k(s2)} \right) \right]^{1/2} \qquad (10)$$

Here $D^{\nabla}_{i(s1)}$ and $D^{\nabla}_{k(s2)}$ are the dipole strengths calculated by eq. 3 for transition i and k of monomeric BChls $s1$ and $s2$, respectively, and $D^{R}_{i(s1)}$ and $D^{R}_{k(s2)}$ are the dipole strengths calculated using the dipole operator (*i.e.*, with $\vec{r}$ replacing $\tilde{\nabla}$ and $\sqrt{2}e$ replacing the factor $e\hbar\sqrt{2}/2\pi mc\,\bar{\nu}^{s}_{i}$). This correction has been used in calculations of excimer

fluorescence of polycyclic aromatic molecules, (*55, 56*) and in previous calculations on reaction centers (*27, 47, 57*). The magnitude of $\Omega_{i(s1),k(s2)}$ for BChl Q_y transitions is typically about 0.5.

We now turn to the portions of **U** that involve CT transitions. For a transition from orbital $n1$ of BChl $s1$ to $n2$ of BChl $s2$ ($\phi_{n1}^{s1} \rightarrow \phi_{n2}^{s2}$), the CT energy that constitutes one of the diagonal elements of $\mathbf{U}^{CT}$ can be written:

$$U^{CT}_{n1(s1)\rightarrow n2(s2),n1(s1)\rightarrow n2(s2)} = \Delta E^{gas} + \Delta V^{QQ} + \Delta V^{sol} \qquad (11)$$

where ΔE^{gas} is the gas-phase energy difference between orbitals $n1$ and $n2$ ($E_{n2}^{s2} - E_{n1}^{s1}$), ΔV^{QQ} is the change in charge-charge interactions between the two BChls (without dielectric screening) and ΔV^{sol} represents the change in electrostatic interactions with the partial charges and induced dipoles of the protein and solvent atoms. Because the model used in the present study did not include the protein and solvent explicitly, ΔV^{sol} could not be evaluated microscopically. We therefore used eq. 11 only to estimate the relative energies of the 8 CT transitions in which an electron moves from one to the other of a given pair of BChls and of corresponding transitions involving BChls in different positions. ΔV^{sol} was assumed to be the same for all the CT states, and the relative CT energies were calculated simply from the sum of ΔE^{gas} and ΔV^{QQ} with

$$\Delta V^{QQ} = \sum_{t1} \left(v_{n1,t1}^{s1}\right)^2 \sum_{t2} \left(v_{n2,t2}^{s2}\right)^2 \gamma_{t1,t2} \qquad (12)$$

Table 1 lists the relative energies of the various transitions. The lowest CT transition is transfer of an electron from ϕ_2 of a B850α BChl to ϕ_3 of the B850β BChl in the neighboring dimer. The energy for transferring an electron within an $\alpha\beta$ dimer is calculated to be higher by about 950 cm^{-1}. To examine how CT transitions affect the calculated spectroscopic properties, all of the CT transitions were moved up or down in

energy together by adding an adjustable constant to the relative energies given in the third and fourth columns of the table.

Table 1: Relative B850 Charge-Transfer Energies.[a]

Transition[b]	ΔE^{gas}	$\Delta E^{gas} + \Delta VQQ$	
		1-1[c]	1-2[d]
$\alpha\phi_2 \rightarrow \beta\phi_3$	(0)	950	(0)
$\alpha\phi_1 \rightarrow \beta\phi_3$	4,050	4,300	4,250
$\alpha\phi_2 \rightarrow \beta\phi_4$	14,250	14,250	14,500
$\alpha\phi_1 \rightarrow \beta\phi_4$	18,300	18,300	18,750
$\beta\phi_2 \rightarrow \alpha\phi_3$	1000	1,750	1,150
$\beta\phi_1 \rightarrow \alpha\phi_3$	4,900	5,150	5,100
$\beta\phi_2 \rightarrow \alpha\phi_4$	14,150	14,800	14,300
$\beta\phi_1 \rightarrow \alpha\phi_4$	18,000	18,150	18,500

[a]Energies are given in cm^{-1} relative to the energy of the $\alpha\phi_2 \rightarrow \beta\phi_3$ transition between adjacent αβ B850 dimers.

[b]B850 BChl types and orbitals.

[c]Transitions within an individual αβ B850 dimer.

[d]Transitions between adjacent αβ B850 dimers. ΔE^{gas} is the same for intra- and inter-dimer transitions.

The off-diagonal terms that mix two CT transitions in the same direction are given by

$$U^{CT}_{n1(s1)\rightarrow n2(s2),m1(s1)\rightarrow m2(s2)} = -\sum_{t1} v^{s1}_{n1,t1} v^{s1}_{m1,t1} \sum_{t2} v^{s2}_{n2,t2} v^{s2}_{m2,t2} \gamma_{t1,t2} / d_{t1,t2} \quad (13)$$

The corresponding terms for CT transitions in opposite directions are zero (*27*).

The terms of the $\mathbf{U^{loc,CT}}$ submatrix, which describe interactions between local and CT transitions, are

$$U^{loc,CT}_{i(s1),m1(s1)\rightarrow m2(s2)} = \sum_{N} c^{s1}_{i,N} \delta_{n1,m1} \sum_{t1} v^{s1}_{n2,t1} \sum_{t2} v^{s2}_{m2,t2} \beta_{t1,t2}$$

$$U^{loc,CT}_{i(s2),m1(s1)\rightarrow m2(s2)} = -\sum_{N} c^{s2}_{i,N} \delta_{n2,m2} \sum_{t1} v^{s1}_{m1,t1} \sum_{t2} v^{s2}_{n2,t2} \beta_{t1,t2} \quad (14)$$

where $\beta_{t1,t2}$ is the atomic resonance integral for electrons on atoms $t1$ and $t2$. $\beta_{t1,t2}$ can be evaluated by resolving it into σ and π components:

$$\beta_{t1,t2} \approx \eta_{y,t1}\eta_{y,t2}\beta_{\sigma} + (\eta_{x,t1}\eta_{x,t2} + \eta_{z,t1}\eta_{z,t2})\beta_{\pi} \quad (15)$$

Semiempirical expressions for the σ and π resonance integrals β_{σ} and β_{π} as functions of interatomic distance $r_{t1,t2}$ have been given previously: (*27, 45*)

$$\beta_{\sigma} = \exp(-2.7\rho/2)(8.51\times10^4 + 4.26\times10^4\rho + 4.26\times10^3\rho^2 - 1.42\times10^3\rho^3 - 3.55\times10^2\rho^4) \quad (16a)$$

and $\beta_{\pi} = 3.11\times10^5\exp(-1.95r_{t1,t2})$ (16b)

where $r_{t1,t2}$ is in Å, β_{σ} and β_{π} are in cm^{-1}, and $\rho = 5.385r_{t1,t2}$. However, these expressions are parameterized reliably only for short distances, and probably

underestimate the resonance integrals for longer distances in condensed media (*58-61*). We therefore used the expressions

$$\beta_\sigma = -2.73\times10^6\exp(-1.95r_{t1,t2}) - 1.81\times10^4\exp(-0.7r_{t1,t2}) \qquad (17a)$$

and $$\beta_\pi = 2.80\times10^5\exp(-1.95r_{t1,t2}) + 3.89\times10^2\exp(-0.7r_{t1,t2}) \qquad (17b)$$

The second term on the right in eq. 17a was chosen to fit experimental data on the kinetics of long-range electron transfer reactions in proteins (*62*). The exponent and coefficient of the first term on the right in 17a were optimized by holding the second term constant and fitting the biexponential expression to equation 16a in the range $3.0 \leq r_{t1,t2} \leq 4.0$. Equation 17b was obtained by adding a term with an exponent of $-0.7r_{t1,t2}$ to equation 16b. The coefficients of the two exponentials here were adjusted so that the ratio of the values of β_π given by 17b and 16b at 4.0 Å was the same as the ratio of the values of β_σ given by 17a and 16a. Equations 17a and b are not intended to be used for $r_{t1,t2} < 3.0$.

The excited states of the LH2 complex now can be written

$$\vartheta_j = \sum_i C_i^j \varphi_i \quad (18)$$

where the φ_i are the 252 basis transitions. The coefficients C_i^j and the excitation energies are obtained by diagonalizing **U**.

The zero-order wave function for the ground state is

$$\vartheta_o = \prod_s \Psi_o^s \quad (19)$$

where Ψ_o^s is the ground state of molecule *s*. ϑ_0 can mix with doubly-excited states in which two different BChls are both in excited singlet states. Considering 4 singly-

excited states of each molecule, a complex of S BChls has $8S\text{x}(S\text{-}1)$ doubly-excited states, or 5,616 in the present case. Their individual contributions to the ground state are small and can be obtained from the terms of $\mathbf{U}^{\mathbf{loc}}$ (*63*). The coefficient for the state in which molecules $s1$ and $s2$ are in excited states i and k is

$$G_{i(s1),k(s2)} \approx -\left[U^{loc}_{i(s1),k(s2)}/\left(\bar{\nu}_i^{s1} + \bar{\nu}_k^{s2}\right)\right]G_o \quad (20)$$

where

$$G_o = \left\{1 + \sum_{s1}\sum_{i}\sum_{s2}\sum_{k}\left[U^{loc}_{i(s1),k(s2)}/\left(\bar{\nu}_i^{s1} + \bar{\nu}_k^{s2}\right)\right]^2\right\}^{-1/2} \quad (s1 \neq s2) \quad (21)$$

The small lowering of the ground-state energy was neglected.

Absorption and CD Spectra of the Complex. Transition dipoles for excitation of the LH2 complex to state are obtained by summing the transition dipoles of the individual molecules, weighting the contribution of each local transition by coefficient C_i^j and including the contributions from downward transitions of the doubly excited states that are part of the ground state. The electric and magnetic transition dipoles are:

$$\bar{\mu}_j^T = \sum_{s1}\sum_{i}\left\{G_o C^j_{i(s1)} + \sum_{s2} G_{i(s1),k(s2)} C^j_{k(s2)}\right\}\bar{\mu}_i \quad (22)$$

$$m_j^T = \sum_{s1}\sum_{i}\left\{G_o C^j_{i(s1)} + \sum_{s2} G_{i(s1),k(s2)} C^j_{k(s2)}\right\} m_i \quad (23)$$

The rotational strengths are given by $\Re_j^T = -\,\mathrm{Im}\left\{\bar{\mu}_j^T \cdot m_j^T\right\}$.

To calculate the overall absorption and CD spectra, the homogeneous contributions from excitation to state ϑ_j were expressed as

$$\varepsilon_j(\bar{\nu}) = [f^2/n][4\pi^2\mathcal{N}/3000\ln 10\hbar c]\left|\mu_j^T\right|^2\bar{\nu}_j\xi_j(\bar{\nu}) \quad (24)$$

and $$\varepsilon_j^{left}(\bar{\nu}) - \varepsilon_j^{right}(\bar{\nu}) = [f^2/n][16\pi^2\mathcal{N}/3000\ln 10\hbar c]\Re_j^T\xi_j(\bar{\nu}) \quad (25)$$

Here $\bar{\nu}$ is the energy of the measuring light (cm^{-1}); $\bar{\nu}_j$ is the zero-point energy difference between ϑ_j and the ground state; N is Avogadro's number; n is the refractive index of water (1.33); f is the cavity-field correction factor $3n^2/(2n^2+1)$ (see Appendix B); and $\xi_j(\bar{\nu})$ is the line-shape factor (*64*):

$$\xi_j(\bar{\nu}) = \sum_{p_1} \cdots \sum_{p_M} B_{\omega,P,T} \sum_{q_1} \sum_{q_M} \left[\prod_{m=1}^{M} \Lambda^{(m)}_{p_m,q_m}\right]\left[\frac{l_{1/2}\Gamma_j}{2\pi}\right] \Bigg/ \left\{\left[\frac{l_{1/2}\Gamma_j}{2\pi}\right]^2 + \left[\bar{\nu} - \bar{\nu}_j - \hbar\sum_{m=1}^{M}(q_m - p_m)\omega_m\right]^2\right\} \quad (26)$$

In eq. 26, ω_m is the energy of the mth vibrational mode that couples the ground state to excited state j (m = 1, 2, ... M); p_m and q_m (= 0, 1, 2, ..., ∞) are vibrational levels of this mode in the ground and excited states, respectively; $\Lambda^m_{p_m,q_m}$ is the Franck-Condon factor for a vibronic transition between these levels; l (=1,2,...∞) is the position of (q_1,q_2,...,q_m) in the ladder of vibrational levels; Γ_j is the homogeneous linewidth (FWHM) of the l=1 transition; and $B_{\omega,P,T}$ is the Boltzmann weighting factor:

$$B_{\omega,P,T} = \left\{\exp\left[-\hbar\left(\sum_{m=1}^{M} p_m\omega_m\right)\Big/k_BT\right]\right\} \Bigg/ \left\{\sum_{p_1}\cdots\sum_{p_M} \exp\left[-\hbar\left(\sum_{m=1}^{M} p_m\omega_m\right)\Big/k_BT\right]\right\} \quad (27)$$

We included three of the dominant vibrational modes that have been characterized in hole-burning studies on the *Rb. sphaeroides* LH2 complex (*38, 65, 66*). The energies (ω_m) and Huang-Rhys factors (S_m) assigned to these modes are listed in Table 2. Vibrational levels 0 through 20 were included for each mode up to a cutoff of 3,000 cm^{-1}, which provided excellent convergence for the S_m and ω_m values used here. The Franck-Condon factors ($\Lambda^m_{p_m,q_m}$) were evaluated using expressions given by Manneback

(*67*). A homogeneous linewidth (Γ_j) of 2.0 cm^{-1} was used for the l=1 transitions of the B800 BChls, (*66*) 3.75 cm^{-1} for the lowest-energy transition of the B850 BChls, (*38, 65, 66*) and (in most of the calculations) 150 cm^{-1} for other l=1 transitions of the B850 BChls including both intramolecular and CT transitions. The assignment of a given transition predominantly to either the B800 or the B850 BChls was made on the basis of the squares of the coefficients ($C^j_{i(s)}$) for the different types of BChl.

Table 2: Vibrational parameters

Mode	ω [a]	S_{exci} [b]	S_{CT} [c]
1	20	0.30	4.0
2	200	0.05	4.0
3	750	0.04	1.0

[a]Energy (cm^{-1}).

[b]Huang-Rhys factor (dimensionless displacement) for exciton transitions composed primarily of combinations of local (intramolecular) transitions; from refs.[6,35,36]

[c]Assumed Huang-Rhys factor for transitions composed primarily of CT transitions. This parameter has not been measured experimentally but is expected to be considerably greater than the S_{exci}.

Inhomogenous broadening was treated by using a Monte Carlo routine similar to that described by Jimenez et al.(*44*) to add a Gaussian distribution of uncorrelated perturbations to the diagonal terms of **U**. The zero-point transition energies, dipole strengths and rotational strengths were stored for 1000 iterations of the calculations and were averaged over spectral intervals of 10 cm^{-1}. The localization factor $L(\bar{\nu})$ (see below) also was stored for transition energies up to 12,700 cm^{-1} on each iteration, and then averaged with the same resolution.

Experimental. LH2 complexes were prepared from *Rb. acidophila* strain 10050 with lauryldimethylamine oxide as described (*68*). Bacteriochlorophyll was assayed spectrophotometrically after extraction into acetone-methanol 7:2 (v:v), using an extinction coefficient of 76 $mM^{-1}cm^{-1}$ at 772 nm (*69*). Circular dichroism spectra were measured with the help of Drs. N. Price and S. Kelly at the BBSRC Scottish Circular Dichroism Facility, Stirling, U.K. The low-temperature absorption spectrum was measured with the help of Drs. S. Lin and R. Blankenship at Arizona State University, Tempe, AZ. Molar extinction coefficients were calculated on the assumption that each LH2 complex in the preparation contains 27 molecules of BChl.

Results and Discussion.

Measured Absorption and CD Spectra. Figure 8 shows absorption and CD spectra of the *Rp. acidophila* LH2 complex at 293 and 123 K. The spectra measured at 293 K are similar to spectra described previously,(*70, 71*) but give absolute values for the molar extinction coefficients. These values were obtained by measuring the BChl contents of samples with known absorbance (see Methods). For samples suspended in 20 mM Tris HCl, pH 8.0, 0.1% lauryldimethylamine oxide at 293 K, the extinction coefficient at 860 nm was found to be 3.01 ± 0.21 $\mu M^{-1}cm^{-1}$ (mean and standard error of the mean of

8 measurements). Assuming that the 858-nm band is due exclusively to the 18 B850 BChls, the extinction coefficient is equivalent to 0.167 ± 0.012 $(\mu M\ BChl)^{-1}cm^{-1}$, which agrees well with the value of 0.170 ± 0.005 that Sturgis et al.(*72*) have measured for B850 in *Rb. sphaeroides*. In 60% glycerol 40% (20 mM Tris HCl, pH 8.0, 0.1% lauryldimethylamine oxide), the solvent used for Fig. 8, the B800 and B850 bands both shifted to the red by 0.5 to 1 nm but the widths and peak extinction coefficients were, within experimental uncertainty, the same as in solutions without glycerol. However, the ratio of the two peak extinction coefficients varied over a range of about 10% in samples that were frozen and rethawed. The extinction coefficient quoted by Sturgis et al. (*72*) for B800 in *Rb. sphaeroides* is about 25% lower than our value in *Rp. acidophila*. As previous workers have described, (*38, 71*) the B850 absorption band shifts to longer wavelengths with decreasing temperature. A notable feature of the CD spectra, which also has been pointed out previously, (*39*) is that the CD crosses zero significantly to the red of the absorption maxima in both the B800 and the B850 regions. The CD spectrum at low temperatures has not been measured previously to our knowledge.

Calculated Exciton Interaction Energies. Table 3 gives the dominant Q_y exciton interaction energies in the *Rp. acidophila* LH2 complex, as calculated with several treatments of the dielectric screening factor $d_{t1,t2}$ in eq. 9. Although the largest interaction energies involve pairs of B850 BChls within αβ dimers, the interactions of neighboring B850-α and B850-β BChls in adjacent dimers have comparable magnitudes. The interactions involving B800 BChls are weaker by a factor of more than 10. As Sauer et al.(*39*) have noted, the coupling of each B800 BChl to the second nearest B850 BChl ($B850^2_\alpha$ in Table 3) is about twice as strong as the coupling to the closest B850 ($B850^1_\alpha$).

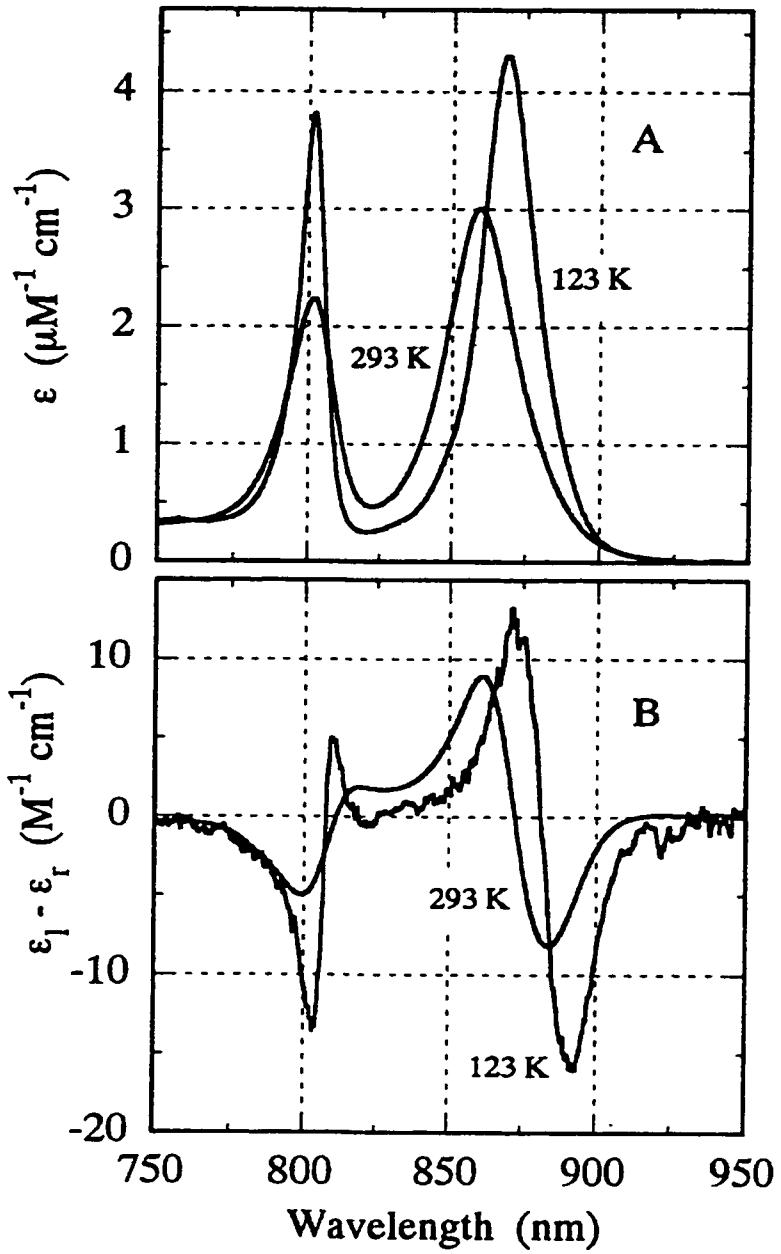

Figure 8. Measured absorption (*A*) and CD (*B*) spectra of purified *Rp. acidophila* LH2 complexes suspended in 40% (20 mM Tris HCl, pH 8.0, 0.1% lauryldimethylamine oxide) 60% glycerol at 293 K and 123 K. A linear baseline was subtracted to set the CD to zero at 700 and 950 nm. Note that the units of the absorbance and CD scales differ by a factor of 10^6. The experimental uncertainties in ε and $\varepsilon_l - \varepsilon_r$ are approximately ±10%.

Table 3: Dominant Q_y Exciton Interaction Energies Calculated with Various Treatments of Dielectric Screening

i, j [a]	$U(i,j)$ (cm^{-1})					
	$r_o = 2$ [b]	$r_o = 4$	$r_o = 6$	$r_o = 8$	$r_o = 15$	$r_o = \infty$
$B850^1_\alpha, B850^1_\beta$	197	254	436	545	440	394
$B850^1_\alpha, B850^2_\beta$	158	209	378	461	345	317
$B800^1, B800^2$	-15	-15	-15	15	-15	-30
$B800^1, B850^1_\alpha$	-8	-8	-8	-8	-8	17
$B800^1, B850^1_\beta$	-2	-2	-2	-2	-2	-4
$B800^1, B850^2_\alpha$	16	16	16	16	16	36
$B800^1, B850^2_\beta$	4	4	4	4	4	8

[a]BChls. Superscript 1 denotes a BChl in a given αβ dimer; 2 denotes a BChl in an adjacent dimer.

[b]r_o in eq. 9 (Å); $n^2 = 2.0$. When $r_o = \infty$, $d_{t1,t2} = 1$, independent of distance; when $r_o = 2$, $d_{t1,t2}$ is effectively fixed at 2.0 because the interatomic distances are all greater than 2 Å.

Dielectric effects are difficult to treat accurately in proteins because of the heterogeneity and anisotropy inherent in protein structures. In principle, a realistic treatment would include the microscopic structure of the protein explicitly in the

evaluation of both the diagonal and off-diagonal matrix elements. In the present work we used a simpler and necessarily cruder method of incorporating electrostatic screening in the off-diagonal terms. Because the QCFF/PI orbitals and the CI coefficients are parameterized on the basis of measured optical properties of molecules in solution rather than *in vacuo*, they take into account dielectric screening of the intramolecular electron-electron repulsion integrals. Setting the screening factor $d_{t1,t2}$ in eq. 7 equal to 1.0 therefore seems appropriate for short interatomic distances. At large distances $d_{t1,t2}$ should approach the high-frequency dielectric constant (n^2) measured in liquids, which is on the order of 1.8 to 2.0. For most of the calculations described below, $d_{t1,t2}$ was given the distance dependence specified by eq. 9, with n^2 = 2.0 and r_o = 4.0 Å. Paradoxically, for some values of r_o, the calculated exciton interactions of neighboring B850 BChls are stronger than they would be if $d_{t1,t2}$ were 1.0, independent of distance (see Table 3). This occurs in the particular geometry of the LH2 complex because eq. 9 favors contributions from pairs of atoms with shorter interatomic distances; it would not necessarily be true for BChl dimers in other orientations. The effects of varying the choice of r_o on the calculated absorption and CD spectra are discussed in more detail below.

Absorption and Circular Dichroism of a Homogeneous Model. It is instructive to begin calculations of the spectroscopic properties of LH2 with a model in which the monomer transition energies are the same for all BChls of a given structural type, *i.e.* with an interaction matrix **U** that has no diagonal disorder. Absorption and CD spectra calculated for such a model are shown in Fig. 9. As in the inhomogeneous models considered below, each LH2 complex has 18 exciton states that result mainly from Q_y excitations of the B850 BChls and 9 states that result mainly from Q_y excitations of the B800 BChls. In the first 9 of the B850 exciton states, the coefficients (C_i^j) for the Q_y excitations of a given B850-α-B850-β dimer generally have opposite signs (Fig. 10).

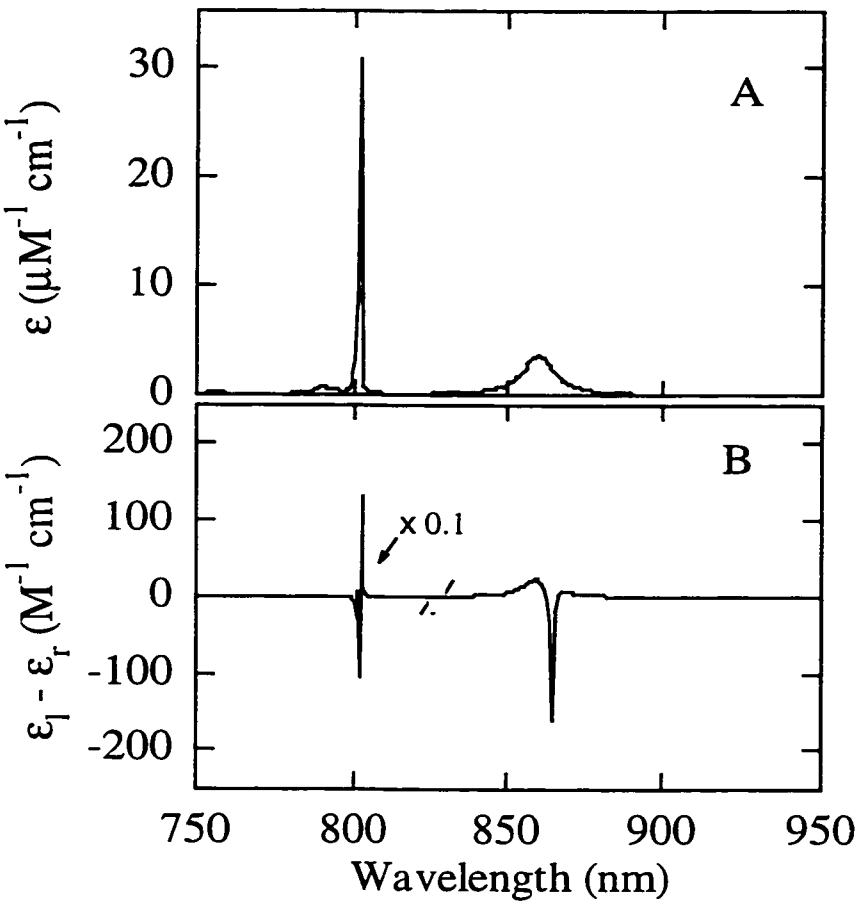

Figure 9. Absorption and (*A*) and CD (*B*) spectra calculated for a homogeneous model of the LH2 complex. The monomer transition energies are given in the text and the vibrational parameters in Table II. Other parameters were: $\Gamma_{j>1}^{B850} = 150\ cm^{-1}$, $\Gamma_1^{B850} = 3.75\ cm^{-1}$, $\Gamma_j^{B800} = 2.0\ cm^{-1}$, $n^2 = 2.0$, $r_O = 4$ Å, lowest CT energy = 12,100 cm^{-1} and $T = 0$ K.

The 0-0 excitation energies of these 9 states are calculated to fall in the range of 11,600 to 12,200 cm^{-1} (820 to 862 nm). In states 10-18, the corresponding coefficients generally have the same sign, and the excitation energies are in the region of 12,400 to 12,650 cm^{-1} (790 to 806 nm). The lowest 9 B850 states thus are constructed, to a first approximation, of antisymmetric exciton states of B850 αβ dimers, and the upper 9 of symmetric dimer states. However, several factors make this description only approximate even within the confines of the homogeneous model. First, the magnitudes of C_i^j for the two Q_y excitations in an αβ B850 dimer are different because the β BChls have lower intramolecular Q_y transition energies. Second, the intramolecular Q_y transitions are mixed to various extents with CT transitions. And third, as noted above, excitonic coupling of B850 BChls in adjacent dimers is almost as strong as the coupling within a dimer (Table 3).

In the B850 state with the lowest energy, the squares of the coefficients for the local Q_y excitations ($|C_{i(s)}^j|^2$) are 0.050 for all the B850 α BChls and 0.056 for the β BChls (see Fig. 10A). The probability of finding a Q_y excitation on a particular molecule in this state thus is nearly constant around the B850 ring. The $|C_{i(s)}^j|^2$ for the 18 B850 Q_y excitations sum to 0.954, indicating that about 5% of the excitations represent higher-energy local transitions, CT transitions, and transitions of the B800 BChls. Because the vector sum of the Q_y transition dipoles of the individual B850 molecules is close to zero, the dipole strength associated with the lowest-energy state is extremely small and makes no significant contribution to the absorption spectrum. This result can be derived easily from a group theoretical representation. In the homogeneous model, the circular array of BChls in the *Rp. acidophila* LH2 complex has C_9 symmetry. The lowest- and highest-energy exciton levels of the ring are described by the *A* irreducible representation of the C_9 point group, in which only transitions normal to the ring plane are allowed. Because the individual transition

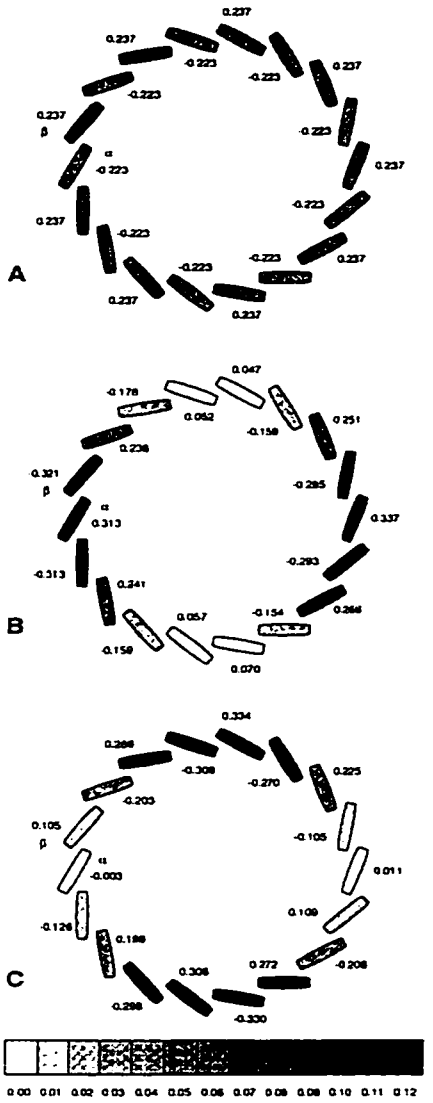

Figure 10. Coefficients of the B850 Q_y transitions in lowest three eigenstates of a homogeneous model of the LH2 complex. Panel *A* is the lowest excited state; *B* and *C* are the two degenerate states just above the lowest. Coefficients for α BChls are indicated inside the rings; coefficients for β BChls, outside. The gray scale (bottom) indicates the squares of the coefficients.

dipoles of the B850 BChls lie nearly in this plane, the dipole strength for excitations into either of the *A* states is very small. The B850 absorption band arises almost exclusively from excitations into a degenerate pair of exciton states with E_1 character, which lie approximately 60 cm^{-1} above the forbidden *A* state and have orthogonal transition dipoles in the plane of the ring (Figs. 10B and C). The other excited states of the B850 array can be described by E_2, E_3, and E_4 irreducible representations and all are formally dipole-forbidden. These general features of circular antenna systems have been pointed out previously by several investigators (*38, 39, 44, 73-76*).

If we consider either one of the two allowed exciton states alone, the Q_y $|C^i_{i(s)}|^2$ vary from molecule to molecule (see Figs. 10B and C). However, the sums of the $|C^i_{i(s)}|^2$ for the two E_1 states are the same for all molecules of a given type (0.098 for α BChls and 0.114 for β). Because there is no way to prepare a pure system in one of these degenerate states, the measurable excitation density would be nearly constant around the ring.

Although the antisymmetric *A* excitation carries little dipole strength, it has a large magnetic transition dipole normal to the plane, and a negative rotational strength on the order of -10 $D \cdot \mu_B$ (debye·Bohr magneton). The two dipole-allowed E_1 states both have in-plane magnetic transition dipoles and positive rotational strengths on the order of 8 $D \cdot \mu_B$. The homogeneous model thus accounts qualitatively for the positive and negative CD bands seen in the 860-nm region (Fig. 8B).

The 9 exciton states that arise predominantly from Q_y transitions of the B800 BChls are clustered near 12,500 cm^{-1} (800 nm). This puts the B800 exciton states close to resonance with some of the upper exciton components of the B850 ring. Because the monomeric B800 transitions are degenerate in the homogeneous model, the exciton states obtained by diagonalizing **U** are inherently delocalized over the entire complex. They can be described by the same *A*, E_1, E_2, E_3 and E_4 irreducible representations used

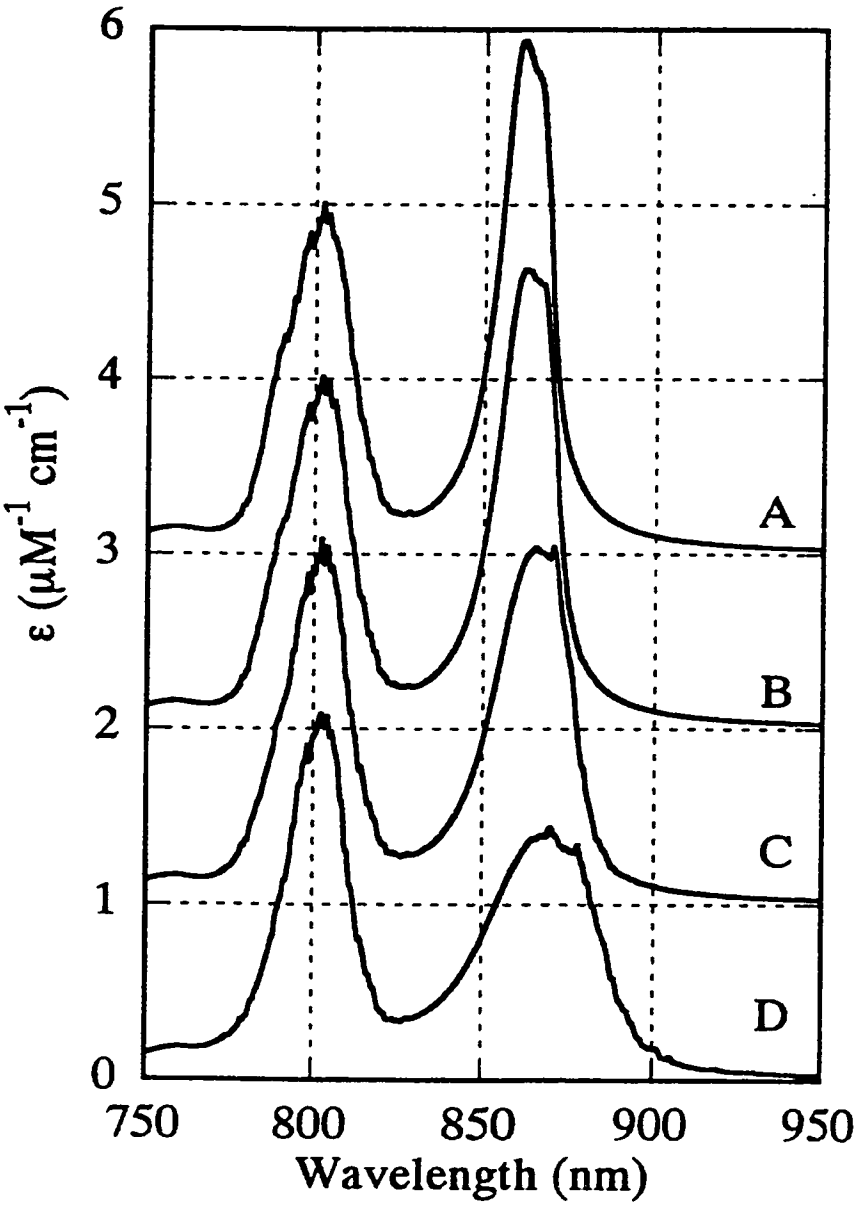

Figure 11. Absorption spectra calculated using uncorrelated Gaussian distributions of the basis transition energies, with σ_{B800} = 130 cm^{-1} and σ_{B850} = 100 (*A*), 130 (*B*), 200 (*C*), or 300 (*D*) cm^{-1}. Other parameters were as in Fig. 3. The ordinate scale is for *D*; the other spectra are displaced vertically in increments of 1 $\mu M^{-1}cm^{-1}$.

for the B850 states, and again only the two degenerate E_1 excitations are allowed. However, this treatment is not physically realistic because variations in the local environments of the BChls give the monomer transitions a distribution of energies. If

the difference between the Q_y energies of neighboring molecules is larger than the interaction matrix elements, the B800 transitions will tend to localize on individual molecules or small sets of molecules. We turn now to a model that incorporates this effect for both the B800 and the B850 BChls.

Effects of Inhomogeneity. The forbidden transitions of the B800 and B850 BChls can gain dipole strength as a result of inhomogeneities that perturb the symmetry of the chromophore rings. Such inhomogeneity must exist at some level in any biological system, given the glass-like nature of proteins (*77*). To explore how inhomogeneity disrupts the exciton structure of the LH2 complex, we used a Monte Carlo routine to give the $\pi \rightarrow \pi^*$ and CT basis transitions uncorrelated Gaussian distributions of transition energies. Absorption and CD spectra were averaged over 10^3 iterations of the calculations. Figure 11 shows absorption spectra obtained with four values of the standard deviation of the energy distribution for the basis transitions involving the B850 BChls (σ_{B850} = 100, 130, 200, and 300 cm^{-1}). The transitions of the B800 BChls were given a standard deviation (σ_{B800}) of 130 cm^{-1} in all four cases, in accord with the results of hole-burning studies on B800 in *Rb. sphaeroides* and *Rp. acidophila* (*65, 66, 78*). As in the homogeneous model, the calculations give strong absorption bands in the regions of 800 and 860 nm. However, transitions into the lowest-energy exciton state now appear as a shoulder on the red side of the B850 band, which becomes increasingly prominent as σ for the B850 BChls is increased. Such a shoulder has been seen in spectra measured experimentally at 4 K, (*38*) although it is not resolved in the spectra shown in Fig. 8. Wu et al.(*38*) place the peak of the low-energy band 200 cm^{-1} below the main absorption peak and estimate the area under the band to be approximately 3% of the total area of the B850 absorption band.

Hole-burning action spectra have shown that the low-energy feature of the B850 band has a width (FWHM) in the range of 60 cm^{-1} to 120 cm^{-1} in *Rp. acidophila* (depending on the sample) and approximately 100 cm^{-1} in *Rb. sphaeroides* (*38, 65, 66*). The zero-phonon hole for this transition has a width of about 3.2 cm^{-1}, which corresponds to a homogeneous lifetime (T_2) of ~7 ps. The total width of 60 to 120 cm^{-1} presumably reflects site inhomogeneity in the monomer transition energies, the interaction matrix elements, or both. Figure 11 shows that as the inhomogeneity of the monomer energies is increased the low-energy band broadens and moves to longer wavelengths relative to the absorption maximum. The calculated intensities, widths, and positions of the low-energy band are given in Table 4. The spectral properties calculated with $\sigma_{B850} \approx$ 100-130 cm^{-1} are in reasonably good accord with the properties measured experimentally, (*38*) although the relative strength of the low-energy shoulder is somewhat too large and the energy separation from the main absorption maximum is smaller than observed. Setting σ_{B800} and σ_{B850} in the range of 130 cm^{-1} also gives good agreement with the overall absorption spectrum. The 800-nm band is broader than observed, but this could reflect the simplifications in our treatment of the homogeneous linewidths of the upper B850 transitions (see below).

Table 4: Calculated Properties of the Low-Energy Band [a]

σ_{B850} (cm^{-1})	peak [b,c] (cm^{-1})	relative area [d] (%)	width [c,e] (cm^{-1})
100	-67	6	70
130	-79	8	90
200	-79	12	130
300	-110	12	210

[a]Each line represents the mean of 1000 iterations of the calculations with the indicated value of σ_{B850} and other parameters as in Fig. 11.

[b]Peak position (Franck-Condon maximum) relative to the main absorption maximum.

[c]calculated for $T = 0$ K with the vibrational parameters of Table 2, $\Gamma_{j>1}^{B850} = 150\ cm^{-1}$ and $\Gamma_1^{B850} = 3.75\ cm^{-1}$.

[d]Area relative to the main absorption band.

[e]FWHM.

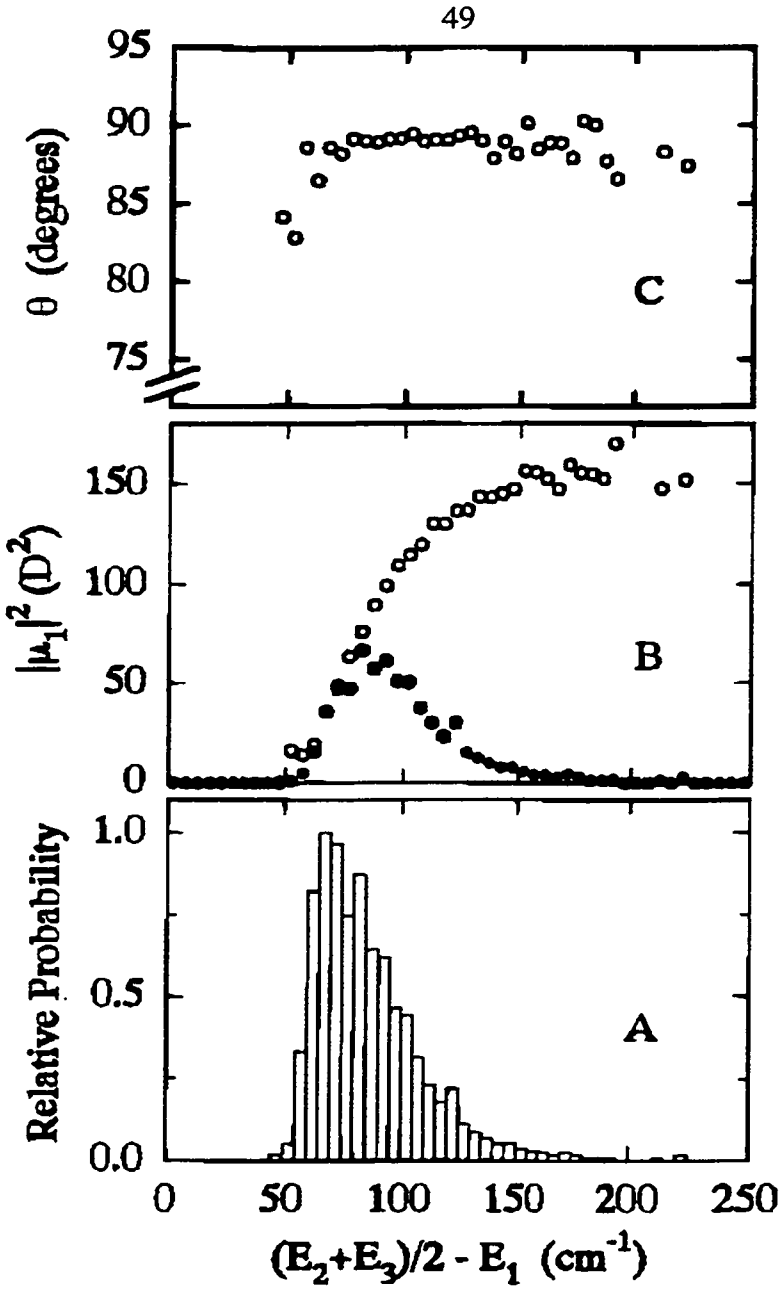

Figure 12. Properties of the lowest exciton transition, calculated by 1000 Monte Carlo variations of the basis transition energies with $\sigma_{B850} = 130\ cm^{-1}$ and other parameters as in Fig. 3. The abscissa $[(E_2 + E_3)/2 - E_1]$ is the difference between the energy of the lowest transition and the mean energy of the next two transitions. Calculated properties were averaged over energy intervals of 5 cm^{-1}. (*A*) Normalized distribution of $(E_2 + E_3)/2 - E_1$. (*B*) Dipole strength of the lowest transition (O) and the product of the dipole strength and the relative probability of having the indicated energy difference (⊗). (*C*) Angle (θ) between the C_9 symmetry axis and the transition dipole of the lowest exciton transition.

For the model with $\sigma_{B850} = 130$ cm^{-1}, the calculated energy separation between the absorption maxima of the low-energy band and the main B850 band is 79 cm^{-1} (Table 4). This separation is larger than the mean energy gap between the lowest state and the higher, allowed states because the absorption in the low-energy band is weighted strongly in favor of trials that yield larger values of the energy gap. Figure 12 illustrates the relationship between the dipole strength of the lowest excitation and the energy gap separating the lowest state from the next two states above it. Whereas the distribution of the energy gap ($(E_2 + E_3)/2 - E_1$) peaks in the range of 65 to 70 cm^{-1} (Fig. 12A), configurations of diagonal energies that give larger energy differences transfer more dipole strength to the lowest excitation and thus contribute disproportionately to the shoulder of the absorption spectrum (Fig. 12B). This point could have significant consequences for the interpretation of time-resolved spectral data at low temperatures because energy transfer among an inhomogeneous ensemble of LH2 complexes would result in a red shift of the fluorescence.

Figure 12C shows how the calculated angle (θ) between the C_9 symmetry axis and the transition dipole of the low-energy transition depends on $(E_2 + E_3)/2 - E_1$. As was mentioned above, θ would be zero for a homogeneous system with C_9 symmetry. However, because the transition dipoles of the individual B850 BChls are nearly perpendicular to the symmetry axis, relatively small amounts of inhomogeneity are sufficient to tip θ to values in the region of 90°. The dominant transition dipoles in the low-energy band thus would be nearly coplanar with the transition dipoles associated with the main B850 absorption band, but on average would have no preferred orientation in this plane. This agrees with the experimental observation that the fluorescence of oriented LH2 complexes is polarized in the plane of the ring, (*79*) and with the fluorescence anisotropy of approximately +0.1 measured when the LH2 complex is excited in the B850 band (*40, 80*). By contrast, a fluorescence anisotropy of -0.2 would be expected for the weak emission from the *A* state of a homogeneous system.

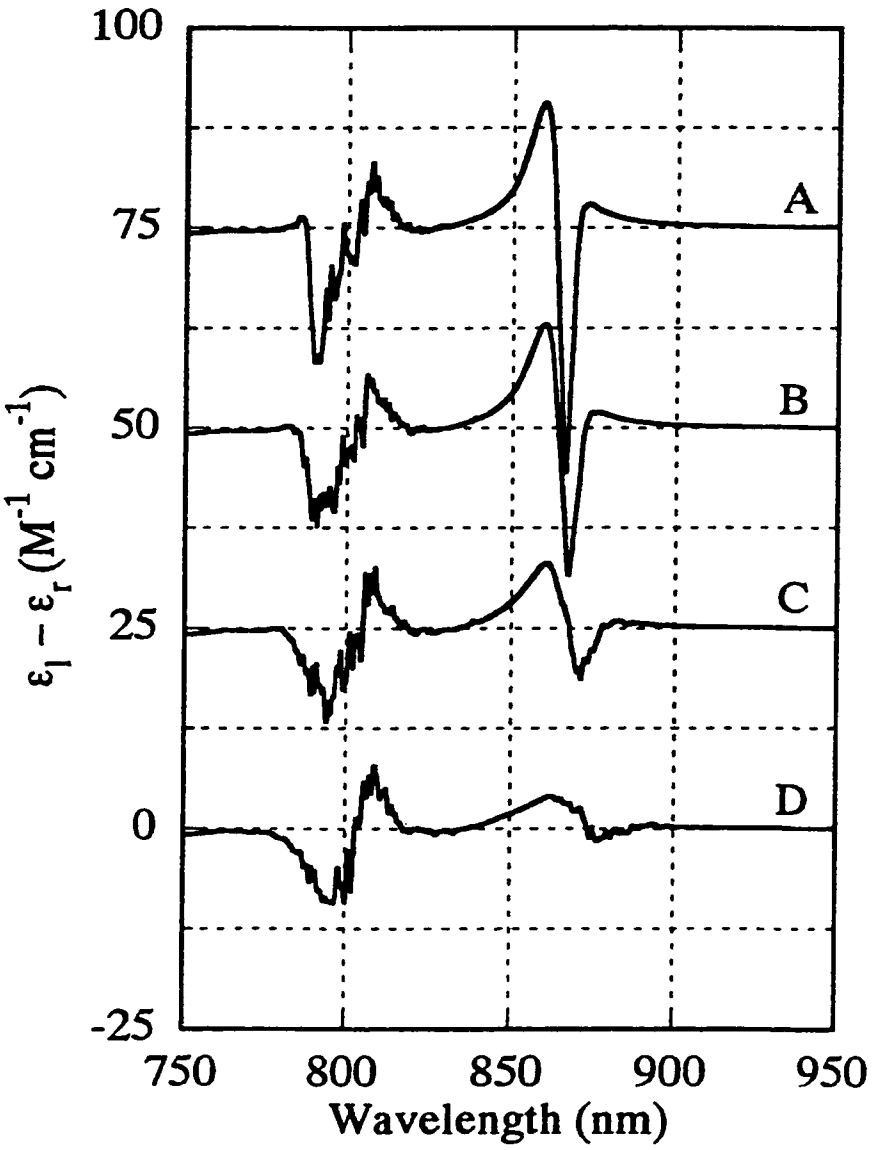

Figure 13. CD spectra calculated as in Fig. 5 with σ_{B800} = 130 cm^{-1} and σ_{B850} = 100 (*A*), 130 (*B*), 200 (*C*), or 300 (*D*) cm^{-1}. The ordinate scale is for *D*; the other spectra are displaced vertically in increments of 25 $M^{-1}cm^{-1}$.

Figure 13 shows the calculated CD spectra obtained with σ_{B850} = 100, 130, 200 and 300 cm^{-1}. Again, the results obtained with σ_{B850} in the range of 100 to 130 cm^{-1} agree well with the experimental spectrum (Fig. 8B). As in the homogeneous model, a major band with negative rotational strength is found on the red side of the B850 region and a positive band on the blue side. Because the negative CD band is associated with the shoulder on the absorption band, the calculated CD crosses zero to the red of the absorption maximum, in accord with experiment. Sauer et al.(*39*) have noted that this displacement is difficult to explain on the assumption that excitations are restricted to small groups of pigments but arises naturally in models that include delocalized exciton states. The pair of positive and negative bands in the 800-nm region is due primarily to transitions of the B800 BChls, with higher-energy B850 states contributing a broad negative band near 790 nm and a broad positive band at shorter wavelengths.

Homogeneous linewidths: The detailed shapes of the calculated absorption and CD spectra depend on the homogeneous linewidths (Γ) assigned to the transitions (see eqs. 26 and 27). The spectra presented in Figs. 11 and 13 were generated by using a homogeneous linewidth ($\Gamma_{j>1}^{B850}$) of 150 cm^{-1} for all the B850 Q_y exciton levels other than the lowest. Figure 14 shows the dependence of the calculated spectra on the choice of this width. The homogeneous linewidths for the lowest B850 exciton level (Γ_1^{B850}) and for all the B800 levels (Γ_j^{B800}) were fixed at 3.75 and 2.0 cm^{-1}, respectively, in accord with the widths of zero-phonon holes burned on the red sides of the 850- and 800-nm absorption bands at low temperatures (*38, 65, 66*). Setting $\Gamma_{j>1}^{B850}$ at 150 cm^{-1} gives the 850-nm band approximately the correct overall width and also matches the relative peak heights of the B850 and B800 bands when σ_{B850} and σ_{B800} are 130 cm^{-1}. The negative CD band at long wavelengths is much less sensitive to $\Gamma_{j>1}^{B850}$ than the positive band just above it, again because it is associated mainly with the lowest exciton level.

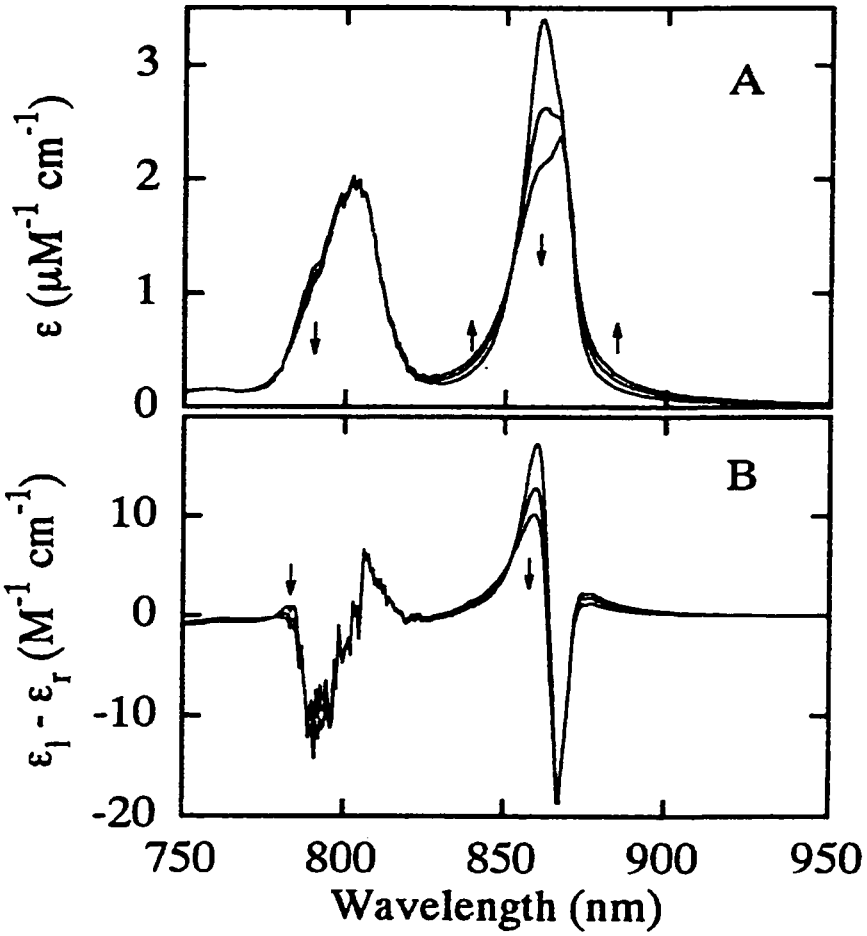

Figure 14. Absorption (*A*) and CD (*B*) spectra calculated as in Figs. 5 and 7, but with σB850 fixed at 130 cm^{-1} and $\Gamma_{j>1}^{B850}$ = 100, 150, or 200 cm^{-1}. Arrows indicate the direction of increasing $\Gamma_{j>1}^{B850}$.

For a discrete excited state, a homogeneous linewidth of 150 cm^{-1} would correspond to a lifetime (T_2) of ~35 fs. In pump-probe studies of *Rb. sphaeroides* chromatophores at room temperature, Nagarajan et al. (*81*) recently measured time constants of approximately 20 and 35 fs for the decay of anisotropy and a relaxation of the stimulated emission and excited-state absorption of B850. These time constants were interpreted as reflecting electronic dephasing and relaxation from strongly-allowed exciton states into a weakly allowed state at lower energies. In hole-burning studies of *Rb. sphaeroides* and *Rp. acidophila* LH2 complexes at 4 K, Small and coworkers (*38, 65, 66*) have measured sample-dependent, aggregate homogeneous linewidths on the order of 200 cm^{-1}. However, these measurements give the envelope (or exciton bandwidth) of the zero-phonon holes of all exciton levels with significant dipole strength in the 850-nm region. The measured hole width is, therefore, necessarily broader than the homogeneous width associated with a single level. A homogeneous linewidth of 150 cm^{-1} for the individual B850 transitions thus seems reasonable, although the use of a single value of Γ for all of these transitions is clearly an approximation. The linewidths of the high-lying exciton states are likely to be broader than those of lower levels due to the existence of multiple decay pathways from the higher states. Zero-phonon holewidths measured on the blue side of the 800-nm absorption band, for example, are larger than those measured on the red side (*78*).

The calculated spectra in Figs. 11 and 13 include a shoulder on the blue side of the 800-nm band, which reflects absorption into the upper exciton states of the B850 chromophores. Reddy et al.(*66*) have observed that hole-burning into the B850 band produces a broad satellite hole at ~785 nm, and have assigned this feature to a vibronic band centered approximately 920 cm^{-1} above the B850 absorption maximum. Their assignment was based largely on a peak seen in high-resolution fluorescence excitation spectra of monomeric BChl-*a* at low temperature (*82*). Our calculations favor assigning the 735-nm feature to upper exciton components of B850, but do not provide a basis for

predicting the homogeneous linewidth of these states. As pointed out above, the B850 exciton transitions in the 780 nm region could have large homogeneous widths due to rapid relaxation into lower exciton levels of B850 and/or B800. Using a larger homogeneous linewidth for the upper B850 transitions would disperse their contributions to the absorption spectrum and sharpen the remaining 800-nm band of the B800 BChls.

Effects of CT transitions. For the calculations described thus far, the energy of the lowest CT transition between adjacent B850 αβ dimers ($\alpha\phi_2 \rightarrow \beta\phi_3$) was fixed at 12,100 cm^{-1}, which is in the range of the CT energies suggested for *Rp. viridis* reaction centers (*57*). The energies of the higher CT transitions were positioned above this by the relative values of $\Delta E^{gas} + \Delta V^{QQ}$ given in Table 1. Similar results (not shown) were obtained if the relative CT energies were set by ΔE^{gas} alone. Because the model did not include the protein explicitly, the CT energies could not be calculated independently. If all of the CT states were raised by 10,000 cm^{-1} to move them far out of resonance with the B850 Q_y transitions, the calculated B850 absorption band maximum shifted to the blue by 121 cm^{-1}, the mean dipole strength of the lowest exciton band increased from 75.5 to 87.4 D^2, and the mean rotational strength of this band decreased in magnitude from -5.7 to -5.1 $D \cdot \mu_B$. However, CT states appear to be much less important in the LH2 complex than they are in reaction centers, (*57*) where the distance between the macrocyclic planes of the special pair of BChls is shorter by about 0.4 Å. As discussed in Methods, mixing of CT transitions with local excitations falls off abruptly with distance.

The conclusion that CT transitions make, at most, only small contributions to the spectroscopic properties is consistent with the observation that electron-phonon coupling is considerably weaker in the LH2 complex than it is in reaction centers (*65, 66*). Strong electron-phonon coupling (a Huang-Rhys factor greater than 1.0) is expected for systems where the excitation causes a significant change in dipole moment

and, consequently, a large change in equilibrium nuclear positions (*83*). The Huang-Rhys factors of considerably less than 1.0 that have been measured for the 800 and 850 nm absorption bands of the LH2 complex (see Table 2) are comparable to those of monomeric BChl-*a* in solution (*82*). The Stokes shift, which provides another measure of nuclear displacements in the excited state, also is smaller in the LH2 complex than in reaction centers; the Stokes shift for the *Rb. sphaeroides* LH2 complex at 295 K is 84 cm^{-1}, (*41*) compared to approximately 535 cm^{-1} for *Rb. sphaeroides* reaction centers (*84*).

Exciton states with little CT character often display narrowed absorption spectra relative to the monomeric species (*85, 86*). The measured widths (FWHM) of the B800 and B850 bands of the LH2 complex at 293 K are approximately 320 and 415 cm^{-1}, respectively (Fig. 8). Widths reported for monomeric BChl in solution range from 515 cm^{-1} in CCl_4 to 930 cm^{-1} in methanol (*87*). The absorption bands thus are narrowed modestly in the LH2 complex, although this could be attributable to the more ordered environment of the pigments in the protein. As discussed above, rapid relaxations among the exciton states probably broaden the B850 band homogeneously relative to B800.

Effects of Dielectric Screening: For the calculations described above, effects of dielectric screening were treated by using eqs. 7 and 9 with r_o = 4 Å. We carried out similar calculations with r_o = 2, 6 and 8 Å, and also with $d_{t1,t2}$ fixed at 1 ($r_o = \infty$). Figure 15 shows representative absorption and CD spectra obtained with r_o = 2 and 6 Å. As r_o is increased over this range, the B850 band shifts to longer wavelengths and grows in strength while the positive and negative CD bands at long wavelengths become weaker. The 800-nm band sharpens as the higher-energy exciton states of the B850 BChls move out of resonance with the B800 states. However, the qualitative features of the absorption and CD spectra are largely preserved. A value of r_o in the

region of 4 Å seems physically realistic because it corresponds roughly to the limit of parameterizations based on intramolecular properties.

Localization of the Exciton States: As was mentioned above, inhomogeneity in the LH2 complex could cause the exciton states to be localized on small groups of BChls. Fidder et al. (*88*) have considered such localization in linear aggregates with diagonal and off-diagonal disorder. They define the degree of localization for states at energy $\bar{\nu}$ as:

$$L(\bar{\nu}) = \left\langle \sum_i \left(C_i^j\right)^4 \right\rangle_{\bar{\nu}} \qquad (28)$$

As above, C_i^j is the coefficient of basis state i in excited state j of the complex; $\langle ... \rangle_{\bar{\nu}}$ represents an average over all states j with energies in a small interval $\bar{\nu} \pm \delta/2$. An excited state due to a single transition of an individual molecule has $L(\bar{\nu}) = 1.0$, while a state representing a uniform distribution of a single type of transition over N molecules would have $L(\bar{\nu}) = 1/N$. A smaller value of $L(\bar{\nu})$ thus implies a more delocalized state. The value of $L(\bar{\nu})$ at the 0-0 transition energy cannot, however, be interpreted simply as the reciprocal of the number of molecules that participate in an excited state. The two allowed exciton states of the homogeneous model are properties of the entire B850 ring and yet give $L(\bar{\nu}) \approx 0.076$ rather than 0.056 (1/18) because the $|C_i^j|$ are not the same for all 18 BChls in each individual state (see Figs. 10B and C). Conversely, mixing with higher-energy local excitations and CT transitions will decrease $L(\bar{\nu})$ even if the coefficients for this mixing are the same for all the molecules. For the forbidden, low-energy state of the homogeneous model, which includes about 5% excitations other than B850 Q_y transitions (see above), $L(\bar{\nu})$ is 0.051.

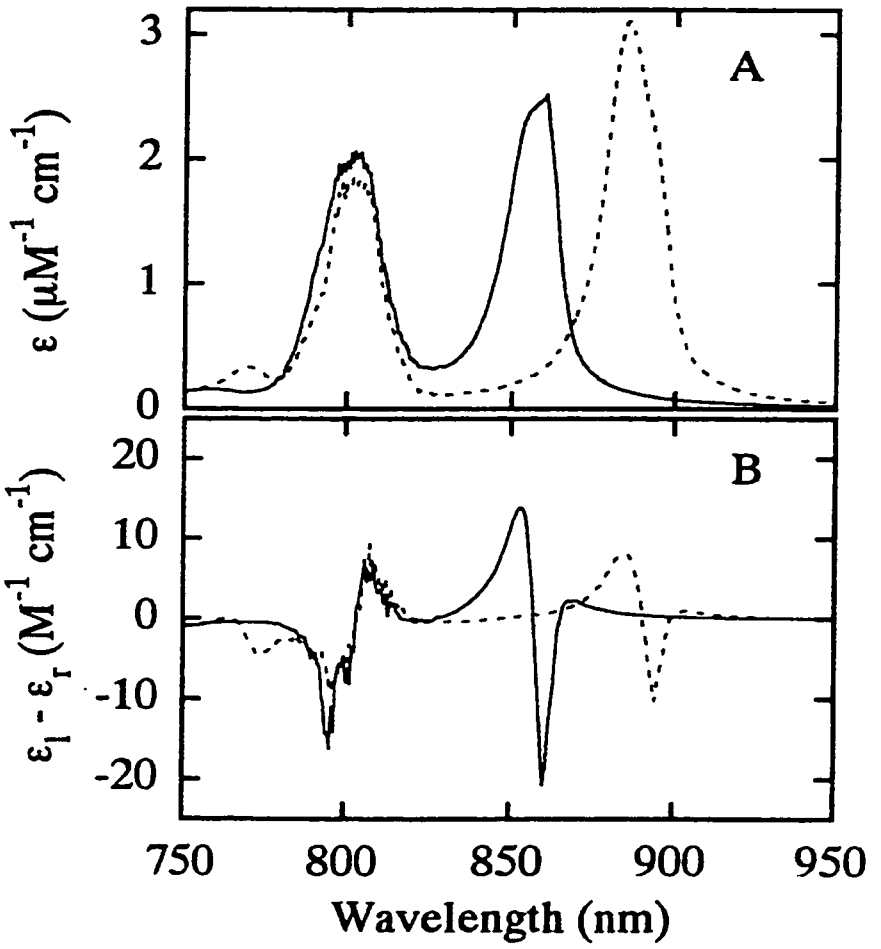

Figure 15. Absorption (*A*) and CD (*B*) spectra calculated as in Figs. 5 and 7, but with σ_{B850} fixed at 130 cm^{-1} and r_O = 2 (—) or 6 (····) Å.

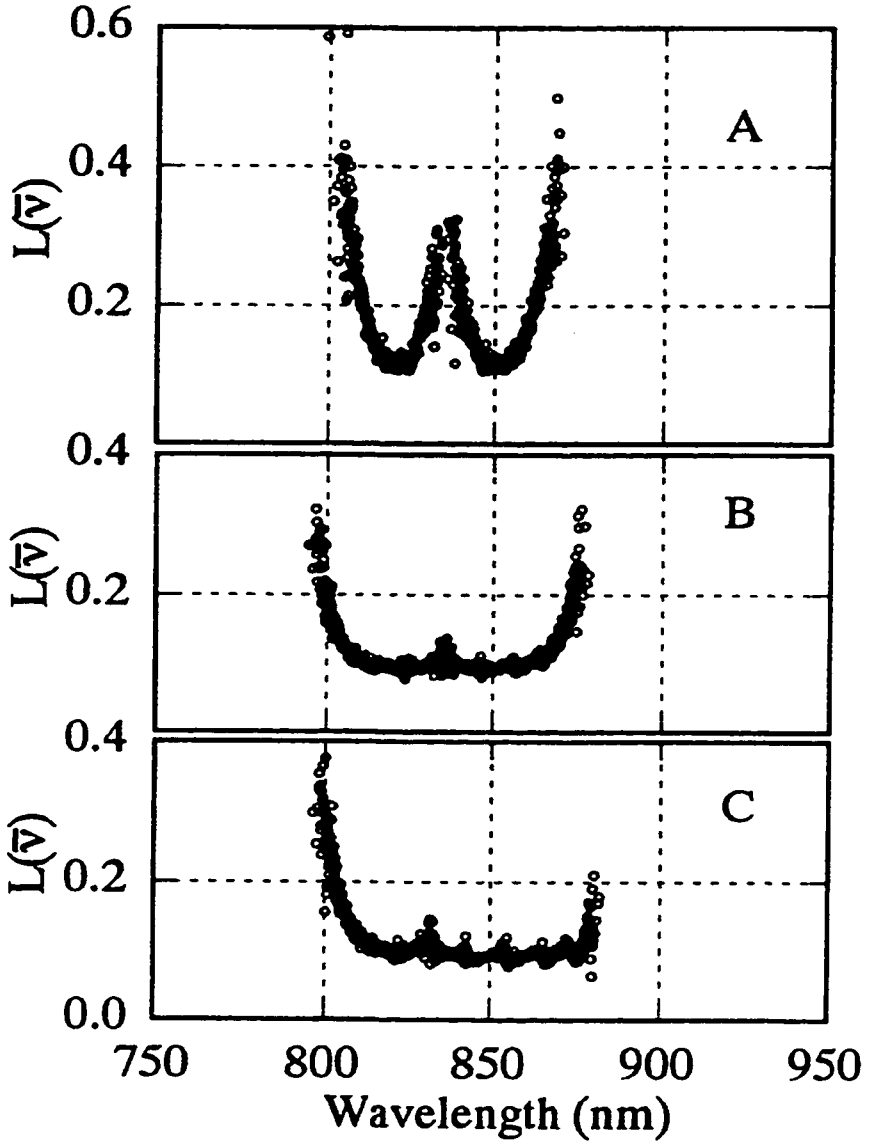

Figure 16. Localization function, averaged over energy intervals of 10 cm^{-1}, for a model that considers only the Q_y transitions of the B850 BChls. The monomer transition energies had a mean of 11,968 cm^{-1} and a standard deviation of 85 cm^{-1}; 10^3 Monte Carlo variations of the energies were made. (*A*) With only nearest-neighbor interactions and the exciton-interaction matrix elements given by Jimenez et al.[12] (*B*) With only nearest-neighbor interactions; matrix elements calculated by eqs. 8-11 with $n^2 = 2.0$ and $r_O = 4$Å. (*C*) Including Q_y exciton interactions of all 18 B850 BChls; matrix elements as in *B*.

Jimenez et al.(*44*) have used a Monte Carlo method to calculate $L(\bar{\nu})$ for a model that considered only the Q_y transitions of the B850 BChls and only nearest-neighbor interaction matrix elements. The B850α and β BChls were assumed to have the same mean 0-0 transition energy (11,968 cm^{-1}). We have reproduced their results by using the same interaction matrix elements and mean 0-0 transition energies. The $L(\bar{\nu})$ values plotted in Figure 16A show the results from 10^3 calculations with $\sigma_{B850} = 85$ cm^{-1} (FWHM = 200 cm^{-1}). As Jimenez et al. found, $L(\bar{\nu})$ is approximately 0.14 at the 858-nm absorption maximum and rises steeply at longer wavelengths. Figure 16B shows similar calculations that again consider only Q_y transitions and only nearest-neighbor interactions, but with the interaction matrix elements calculated in the present paper (254 and 209 cm^{-1} for intra- and inter-dimer interactions, respectively, as compared to the values of 230 and 110 cm^{-1} used by Jimenez et al.). Using the larger matrix elements shifts the absorption maximum to 868 nm and decreases $L(\bar{\nu})$ at this wavelength to 0.12. Figure 16C shows calculations of $L(\bar{\nu})$ that still retain the mean Q_y 0-0 transition energy used by Jimenez et al. but include the off-diagonal matrix elements involving Q_y transitions of non-nearest neighbors in the B850 ring. The inclusion of the additional off-diagonal matrix elements shifts the absorption maximum to 870 nm and reduces $L(\bar{\nu})$ here to 0.09. These results point to the importance of including all the significant interaction terms in the calculations and of using as realistic a model as possible to evaluate the off-diagonal matrix elements.

Figure 11 shows the values of $L(\bar{\nu})$ obtained with the full interaction matrix, including CT states and the Q_y, Q_x, B_x and B_y transitions of all 27 BChls, and with our values for the mean 0-0 monomer transition energies (12,500 cm^{-1} for B800, 12,284 cm^{-1} for B850-β, and 12,193 cm^{-1} for B850-α BChls). The $L(\bar{\nu})$ terms were calculated separately for states of predominantly B800 $\pi\pi^*$ character and B850 $\pi\pi^*$ character. States with more than 50% CT character were not included in the computations of

$L(\bar{\nu})$. (No states with dominant CT character were found below 12,100 cm^{-1}.) As in Fig. 11, calculations were done with four values of σ_{B850} (100, 130, 200 and 300 cm^{-1}); a standard deviation of 130 cm^{-1} was used for the B800 transitions in all cases. With values of σ_{B850} that are consistent with the observed absorption and CD spectra (100-130 cm^{-1}), $L(\bar{\nu})$ remains below 0.1 over most of the B850 absorption band, indicating that excitations are extensively delocalized over the B850 ring. The higher value of $L(\bar{\nu})$ in the B800 absorption band (0.6) indicates that excitations here are considerably more localized, although they still appear to spread over more than one BChl.

Concluding Remarks

Although the details of the spectra depend to some extent on the treatment of dielectric screening, on the energies assigned to the monomeric pigments, and on adjustable parameters such as the CT energies and homogeneous linewidths, the calculated absorption and CD spectra are in good accord with experiment and the qualitative results are reasonably robust to alterations in the theoretical parameterization. Experimental results from hole-burning studies have been incorporated wherever possible in the treatment of the homogeneous and inhomogeneous linewidths and the frequencies and Huang-Rhys factors of the dominant vibrational modes. This experimental information aids particularly in determining the contributions of inhomogeneity to the spectra. More accurate transition energies for the monomers might be obtained by considering hydrogen bonding and other interactions with the protein explicitly and possibly by using INDO calculations (*89, 90*) in place of QCFF/PI. Sturgis et al. (*90*) have suggested that the shift of the monomeric BChl absorption from 780 nm to the region of 800 nm in the LH2 complex results mainly from hydrogen bonding to the 2-acetyl group.

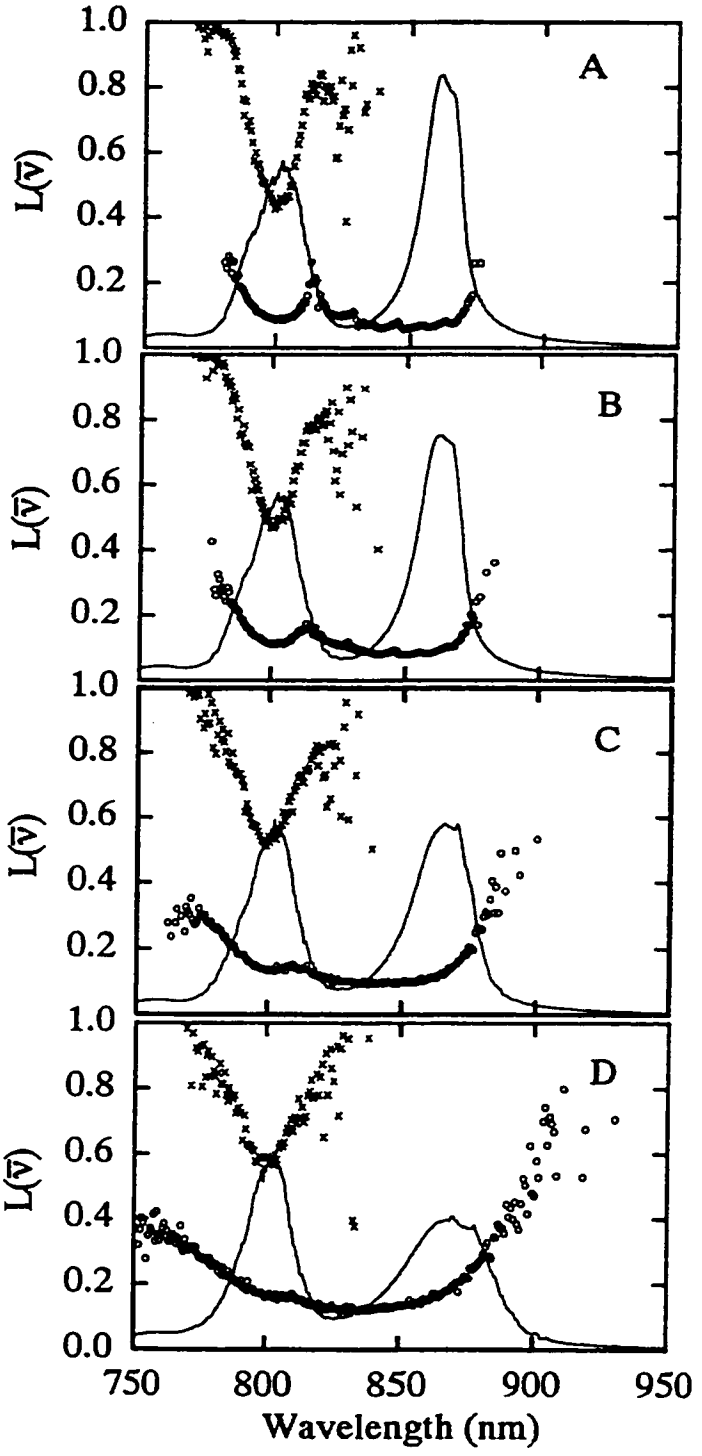

Figure 17. Localization functions for B850 (o) and B800 (x) states, averaged over energy intervals of 10 cm^{-1}, calculated using the full interaction matrix as in Fig. 5 with σ_{B800} = 130 cm^{-1} and σ_{B850} = 100 (*A*), 130 (*B*), 200 (*C*), or 300 (*D*) cm^{-1}. The calculated absorption spectra also are shown.

It is important to note that the crystal structure of the LH2 complex was determined at room temperature and that the calculated interaction matrix elements were based on this structure, whereas the hole-burning studies[6,35,36,48] that provided estimates of the vibronic parameters and the homogeneous linewidths Γ_j^{B800} and Γ_1^{B850} were carried out at 4 K. The value of 150 cm^{-1} used for $\Gamma_{j>1}^{B850}$ was based partly on the hole-burning results, but also on time-resolved measurements at room temperature (*81*). For simplicity, all the spectral line shapes were calculated for 0 K. The spectra are expected to broaden at higher temperatures, but probably not exactly as predicted by eqs. 26 and 27 with fixed values of Γ_j^{B800}, Γ_1^{B850} and $\Gamma_{j>1}^{B850}$. As Wu et al. (*38*) have noted, the shift of the B850 absorption band to the red (Fig. 8) suggests that interactions among the BChls are stronger at low temperatures than at room temperature.

The results presented here indicate that, at early times after the absorption of light, excitations of the B850 BChls in *Rp. acidophila* are delocalized extensively over the ring of 18 pigments. This contrasts with the conclusions of several investigators, (*44, 73, 91-94*) who have suggested that excitations are localized on groups of 2 to 5 BChls. However, recent measurements of the magnitude (*95*) and anisotropy (*81*) of flash-induced absorbance changes appear to support the view that the exciton states of LH2 complexes in *Rb. sphaeroides* and *Chromatium tepidum* are strongly delocalized. Measurements of the magnitudes of flash-induced absorbance changes suggest that the exciton states of LH1 antenna complexes also involve a large fraction of the BChls, (*75, 95-97*) although other workers (*76, 93, 98, 99*) again have favored more localized excitations. In the present calculations, increased localization is seen in the B800 band and on the red edge of the B850 band where the absorption is weighted in favor of complexes with atypically large diagonal disorder (Figs. 12 and 17), but the calculated values of $L(\bar{\nu})$ suggest that even excitations in the B800 band are initially delocalized to a significant extent.

Although the calculated spectral line shapes include homogeneous broadening, we have not explicitly considered relaxations that could cause excitations to become increasingly localized with time (*100*). One observation that may be difficult to reconcile with the persistence of strongly delocalized excitations is that the fluorescence quantum yield from the LH2 complex increases with decreasing temperature (*71, 101, 102*). Unless the fluorescence lifetime also increases substantially, the fluorescence yield should decline as k_BT drops below the E_2 - E_1 energy gap of approximately 60 cm^{-1}. Between 300 and 77 K, the increase in fluorescence yield appears to be explained by a corresponding increase in the fluorescence lifetime,(*100*) which presumably reflects a slowing of nonradiative decay processes. However, the fluorescence lifetime seems not to have been measured at temperatures below 77 K, where the yield continues to increase (*71, 101*).

In work to be presented elsewhere, we have used the model described here to calculate changes in the absorption and emission spectra that would be caused by excitation of the LH2 complex, and also to calculate Stark effects on the absorption spectrum. Comparisons with the measured Stark spectrum (*103*) allow more accurate positioning of the CT energies than is possible by modeling only the absorption and CD spectra.

Appendix A: Matrix elements of $\tilde{\nabla}$.

The Slater $2p_z$ orbital, in polar coordinates centered on the atom, can be written $\chi = (\zeta^5/\pi)^{1/2} r\cos\theta\exp\{-\zeta r\}$ with ζ = 3.685, 4.299 and 3.071 Å^{-1} for N, O and C, respectively. The matrix elements $\langle\chi_2|\tilde{\nabla}|\chi_1\rangle$ are functions of the interatomic distance (R) and the ζ parameters for the two atoms (ζ_1 and ζ_2). Let $p = (\zeta_1 + \zeta_2)R/2$, $q = (\zeta_2 - \zeta_1)R/2$, $A_k \equiv \int_1^\infty w^k \exp(-pw)dw$ and $B_k \equiv \int_{-1}^1 w^k \exp(-qw)dw$. Then, following procedures described by Mulliken et al., (*104*) Král (*105*) and Harada and Nakanishi (*106*), we find

$$\nabla\sigma = (\zeta_1\zeta_2)^{5/2}(R^4/8)\{A_0B_2 - A_2B_0 + A_1B_3 - A_3B_1$$
$$+(\zeta_1R/2)(A_1(B_0 - B_2) + B_1(A_0 - A_2) + B_3(A_4 - A_2) + A_3(B_4 - B_2))\} \quad (A1)$$

$$\nabla\pi = (\zeta_1\zeta_2)^{5/2}(\zeta_1R^5/32)\{(B_1 - B_3)(A_0 - 2A_2 + A_4) + (A_1 - A_3)(B_0 - 2B_2 + B_4)\} \quad (A2)$$

$$\nabla_{xy} = (\zeta_1\zeta_2)^{5/2}(R^4/8)\{A_0B_2 - A_2B_0 + A_1B_3 - A_3B_1$$
$$+(\zeta_1R/4)((A_3 - A_1)(B_0 - B_4) + (B_3 - B_1)(A_0 - A_4))\} \quad (A3)$$

Equations A2 and A3 were given previously by Král (*105*). A_k and B_k can be evaluated with expressions given by Miller et al. (*107*):

$$A_k = (e^{-p} + kA_{k-1})/p \quad \text{(A4)}$$

$$B_k = 2\sum_{i=0}^{3}[q^{2i}/(2i)!(k+2i+1)] \text{ for } k \text{ even} \quad \text{(A5)}$$

$$B_k = -2\sum_{i=0}^{3}[q^{2i+1}/(2i+1)!(k+2i+2)] \quad \text{for } k \text{ odd} \quad \text{(A6)}$$

Appendix B. The dipole strength of BChl-a:

There is some uncertainty in the choice of the experimental dipole strengths because the absorption spectrum of BChl-a depends on the solvent. The dipole strength is related to the molar extinction coefficient (ε) by the expression

$$|\vec{\mu}|^2 = (3000 \ln 10\hbar c/8\pi^3 \mathcal{N})(n/f^2)\int(\varepsilon/\nu)d\nu \quad \text{(B1)}$$

where N is Avogadro's number, n is the refractive index of the solvent, f is the local-field correction factor, and ν is the frequency. Connolly et al.(*87*) have reported on the absorption maximum ($\bar{\nu}_o$), peak molar extinction coefficient (ε_0), and full width at half height (W) of the Q_y absorption band of BChl-*a* in 14 solvents covering a wide range of polarity. If we consider only the 0-0 absorption band and assume a Gaussian bandshape, the dipole strength $|\mu^2|$ is given by $9.778\text{x}10^{-3}\varepsilon_0 W n f^{-2}\bar{\nu}_o^{-1}D^2$ (*106*). Figure

18 shows plots of the dipole strength calculated using two different expressions for *f*. The Lorentz expression $f = (n^2+2)/3$, which has been used by Shipman (*108*) for chlorophyll-*a* and -*b*, models the molecule as a spherical virtual cavity in the solvent, while the cavity-field expression $f = 3n^2/(2n^2+1)$ pertains to an actual spherical cavity (*109*). A model based on a virtual elipsoidal cavity might be more appropriate. However, the values of the dipole strength calculated using the cavity-field expression are essentially independent of *n*, suggesting that this treatment corrects reasonably well for solvent effects in the particular case of BChl-*a* (see Fig. 18). The mean value of $|\mu^2|$ is 39.9 ± 0.3 D^2. By contrast, the values obtained using the Lorentz correction decrease systematically with *n*. This dependence is not removed by excluding H-bonding solvents.

The dipole strengths calculated in this way neglect a broad vibrational shoulder on the blue side of the absorption band. From spectra presented by Becker et al. (*110*), we calculate that including the vibrational structure up to 2,000 cm^{-1} above the peak increases the calculated dipole strength to 51.3 D^2 in methanol (where the 0-0 band is relatively broad) and to 52.8 D^2 in pyridine (where the 0-0 band is relatively sharp).

Scherz and Parson (*52*) measured a dipole strength of 41 D^2 for the Q_y band of BChl-*a* in acetone (including the vibrational shoulder), and 13 D^2 for the Q_x band (including only the 0-0 band). These values were obtained with the Lorentz correction factor. Using the cavity-field factor increases them to 48 and 15 D^2, respectively. Including the vibrational structure would increase the Q_x dipole strength to approximately 19 D^2.

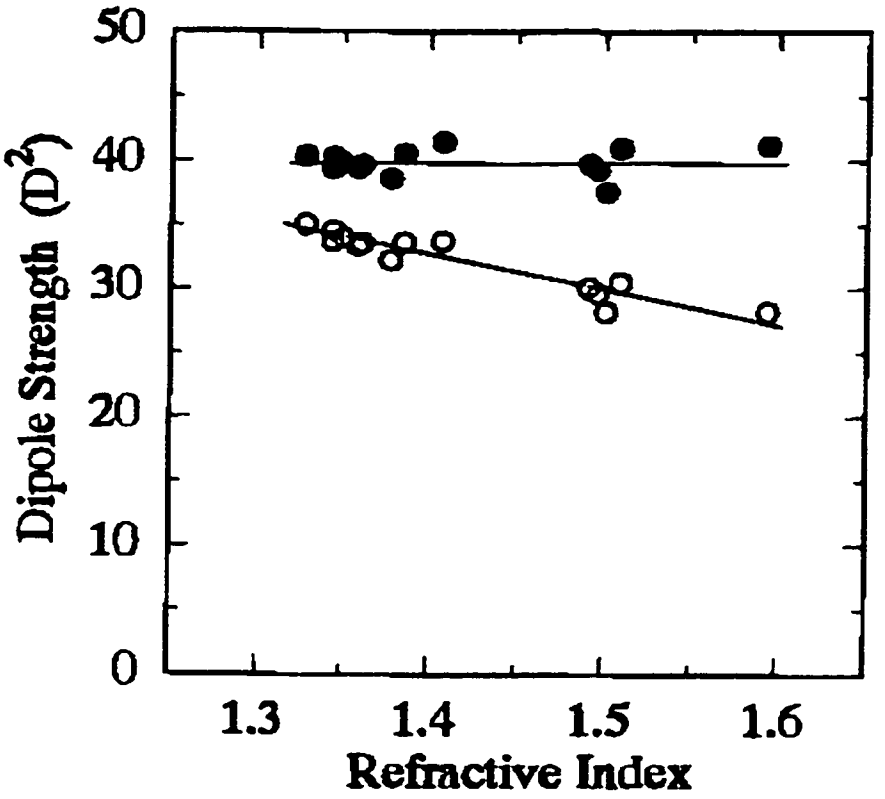

Figure 18. Dipole strength of monomeric BChl-*a* in 14 solvents as a function of the refractive index, calculated from experimental data of Connolly et al.[61] with two different treatments of the local-field correction factor (*f*). O, $f = (n^2+2)/3$; ⊗, $f = 3n^2/(2n^2+1)$

CHAPTER 3: FEMTOSECOND PUMP-PROBE SPECTROSCOPY OF THE B850 ANTENNA COMPLEX OF *RHODOBACTER SPHAEROIDES* AT ROOM TEMPERATURE[2]

Photosynthetic organisms contain pigment-protein "antenna" complexes that absorb light and transfer energy efficiently and rapidly to the photochemical reaction center. The peripheral antenna complex (LH2) from the purple, photosynthetic bacteria *Rhodopseudomonas acidophila* strain 10050 contains nine copies of each of two polypeptides (α and β), 27 bacteriochlorophyll-*a* (BChl-*a*) molecules and 18 carotenoids in a cylindrical structure with C_9 crystallographic symmetry (*11*). Eighteen of the BChls are arranged in a ring with a radius of about 25 Å. These molecules are oriented so that the bacteriochlorin ring normals are approximately perpendicular to the symmetry axis and their long-wavelength (Q_y) transition dipoles lie close to the plane of the ring. The other 9 BChls form an outer ring that is displaced along the symmetry axis. The LH2 complex from the widely-studied species *Rhodobacter sphaeroides* probably contains similar rings of pigments. An LH2 complex with C_8 symmetry is found in *Rhodospirillum molischianum* (*37*).

LH2 complexes typically have absorption bands in the regions of 800 and 850 nm. Semiempirical molecular orbital calculations based on the *Rps. acidophila* crystal structure indicate that the major ring of eighteen BChls accounts for the long-wavelength band while the outer ring of nine BChls is responsible for the 800-nm band.[3,4] The BChls in the inner and outer rings can, therefore, be termed the "B850" and "B800" pigments, respectively.

---

[2] Reproduced with permission from *J. Phys. Chem. B*, *103*, 2297-2309, 1999. Copyright 1999 American Chemical Society.

The absorption, circular dichroism, and hole-burning spectra of the LH2 complex are reproduced reasonably well by theoretical treatments that consider exciton states of the entire complex, but invoke moderate disorder in the excitation energies of the individual BChls (*39, 111-113*). The red shift of the 850-nm absorption band relative to the Q_y transition of BChl *in vitro* (770 nm) appears to reflect a combination of excitonic coupling (*39, 111*), pigment-protein interactions (*114*), distortions of the BChl macrocycles (*51, 111*) and, to a minor extent, mixing with charge-transfer transitions (*111*). In a homogeneous system the wavefunction of the lowest exciton state would be distributed almost uniformly around the B850 ring, and because the Q_y transition dipoles of the B850 BChls all lie approximately in the plane of the ring, the dipole strength for excitation to this state would be very small. Most of the dipole strength of the B850 band would come from a degenerate pair of orthogonally polarized transitions at slightly higher energy (*39, 111*). However, energetic or structural disorder that disrupts the symmetry of the complex will cause excitations to localize on smaller subsets of the pigments, making both the low-energy transition and transitions at higher energies weakly allowed (*65, 99, 100, 115-118*). Evidence for such disorder has come from hole-burning spectroscopy: excitation on the red edge of the absorption band burns a narrow hole that has been assigned to the lowest exciton state (*65*).

Additional evidence for disorder in the LH2 complex comes from the observation that the radiative rate constant is nearly independent of temperature (*119*). In a homogeneous system the emission should drop to zero at low temperatures. The flourescence properties thus suggest that emission occurs from a relatively localized excited state, while the absorption, circular dichroism and hole spectra appear to require more delocalized exciton states. The paradox probably results in part from the different time scales probed by conventional absorption and emission spectroscopies. In hole-burning studies, excitation on the blue side of the B850 absorption band results in a broad hole that covers essentially the entire band, suggesting that the excited complex relaxes within the manifold of exciton levels on a sub-picosecond time scale (*65*).

Because the spontaneous fluorescence has a lifetime of several hundred picoseconds in the absence of the reaction center, measurements of fluorescence would report mainly on times following this relaxation. The nature of the rapid relaxation is of interest because it bears on how photosynthetic antenna complexes absorb and transfer energy, and because it may provide an experimental window to protein dynamics on very short time scales.

To explore how the excited LH2 complex evolves with time, we previously measured the changes in absorbance and stimulated emission caused by excitation with 35-fs pulses centered at 875 nm (*120*). The spectra included an absorbance increase due to excited-state absorption (ESA) and a negative feature at longer wavelengths due to stimulated emission (SE) and bleaching of ground-state absorption (GSB). Both features underwent substantial relaxations on the time scale of 10 to 100 fs. We also observed an anomalously large initial anisotropy (~0.7) in the bleaching and stimulated-emission signal, which decayed to 0.1 on the same time scale as the spectral relaxations. We interpreted these results in the simple model of a homogeneous system in which excitations are delocalized over the whole ring. The high initial anisotropy was ascribed to coherent excitation of a degenerate pair of allowed states, and the relaxations to electronic dephasing and equilibration with a forbidden state at lower energies.

In the present study, we investigate the effects of exciting the LH2 complex with spectrally narrower excitation pulses on either the blue or red side of the B850 absorption maximum. We also describe more extensive measurements of anisotropy with finer time resolution, explore how the measured anisotropy depends on the excitation and detection wavelengths, and consider the effects of perturbed free induction decay and coherent coupling of the pump and probe pulses. Finally, we show that the main features of the results can be reproduced well by a theoretical treatment that considers electronic dephasing and thermal equilibration of exciton levels in an ensemble of systems with moderate disorder.

Methods

Experimental. A Ti-sapphire laser described previously (*120*) provided excitation and probe pulses at a repetition rate of 100 kHz. The pump pulses had a maximum energy of approximately 0.5 nJ. Their center wavelength and spectral width were controlled by a moveable slit. The probe pulses, which had an energy of about 50 pJ, had a full width at half-maximal amplitude (FWHM) of approximately 25 fs at the sample, assuming a $\mathrm{sech}^2(t)$ shape. The FWHM of the cross-correlation of the pump and probe pulses was approximately 60 fs. After passing through the sample, the probe beam was dispersed by a spectrometer with a bandwidth of 5 nm and recorded by a photodiode and lock-in amplifier (*120*).

Although extra-cavity prisms were used for dispersion compensation the pulses still retained some negative chirping. When the center of the pump pulse was tuned from 830 to 870 nm (20 nm on either side of the B850 band), the peak of the pump-probe cross-correlation function shifted by 18 fs. The shift was approximately linear with wavelength. Chirping of the probe pulse causes the actual pump-probe delay to increase with increasing wavelength. Correcting for this effect increases the signals slightly at early times on the blue side of the spectrum, and decreases the signals at early times on the red side, but the correction is relatively small. The data presented below are uncorrected.

For anisotropy measurements, signals with parallel and perpendicular polarization of the pump and probe beams were recorded at each setting of the delay stage by rotating the polarization of the pump beam with a half-wave plate. This method is preferable to collecting the time-dependent parallel and perpendicular signals separately, because errors in the stage position are identical for both signals and thus affect the measured anisotropy only minimally. The anisotropies that we reported previously (*120*) probably were overestimated as a result of an error of ~1 μm in

reproducing the stage position. Such an error also would affect the apparent decay kinetics of the anisotropy.

Because measurements of the transient difference spectra require dispersing the probe beam after the sample, the preferred method of examining the anisotropy is to vary the pump polarization as we have done. However, the polarization is rotated by retarding the optical component parallel to the slow axis of the retarder plate, which introduces a slight delay and temporal broadening of the pump pulse for one polarization relative to the other. Although this problem appears not to have been described previously, we observed the effect clearly in the pump-probe cross-correlation traces. The observed retardation corresponded to ~0.7 fs or ~$\lambda/4$, as expected. We neglected this effect in the analysis of the anisotropy data because attempting to correct for it probably would introduce other errors of a similar magnitude. The retardation was such (excitation occurred slightly earlier with perpendicular polarization than with parallel) that the calculated initial anisotropies are *lower* limits. Partial depolarization of the pump and/or probe beam by the mirrors between the half-wave plate and the sample also can cause an underestimate of the true anisotropy (see below).

We checked the anisotropy signals for a dependence of the amplitudes or decay kinetics on the excitation intensity, and found none. For this, the pulse energies were reduced by adjusting the radio-frequency power applied to the Bragg crystal in the pulse selector (*120*). This method preserves the shapes and spectra of the pulses, but decreases the signal/noise ratio because it reduces both the pump and probe intensities.

Chromatophores from *Rb. sphaeroides* strain ΔQBALM/Q, which contains LH2 but not reaction centers or LH1 complexes, were prepared as described (*120*) and were diluted in 50 mM TRIS-HCl, pH 8.0, to an absorbance of 0.2 ± 0.1 at 850 nm. Cuvettes with a pathlength of 0.1 mm were used for measurements of spectral relaxations and 0.2 mm for anisotropy measurements. The signals were larger with the 0.2-mm cuvettes

because the pump and probe beams overlapped across a distance of about 0.15 mm, but otherwise were not noticeably different. All measurements were made at room temperature. Data were analyzed globally by singular-value-decomposition using methods described previously (*120*).

Theoretical. Exciton states of the LH2 complex were evaluated on the basis of the *Rp. acidophila* crystal structure as described by Alden et al. (*111*) but with the interaction matrices restricted to the Q_y transitions of the 18 B850 BChls; charge-transfer transitions and the Q_x, B_y and B_x transitions were omitted, along with all transitions of the B800 pigments. This simplification reduces the interaction matrix for the singly-excited complex (U) from 252x252 to 18x18 with relatively minor effects on the calculated absorption spectrum in the 850-nm region. The mean values of the monomer excitation energies were set at 12,450 cm^{-1} for BChls bound to α polypeptides and 12,350 cm^{-1} for those bound to β polypeptides. (We have not investigated the importance of retaining the small calculated (*111*) difference between the transition energies of the BChls bound to the α and β polypeptides in the present study, but it probably is minor.) Off-diagonal elements were calculated with the dielectric screening parameters $n^2 = 2$ and $r_o = 4$ Å,[4] and were increased uniformly by 18%. This scaling put the interaction between an αβ pair of BChls (the largest off-diagonal terms of U) at 300 cm^{-1}.

The 171x171 interaction matrix for a doubly-excited system (V) was constructed from U as described by van Amerongen and Struve (*121*) and Pullerits et al.(*73*) V includes states in which an individual BChl molecule is doubly excited, in addition to states in which Q_y excitations reside simultaneously on two different BChls. Excitation of an individual BChl from the first to the second excited state was assigned a transition energy 100 cm^{-1} greater than the Q_y excitation and a transition dipole parallel to the Q_y transition dipole (*121, 122*). The ratio of the magnitudes of the transition dipoles for the first and second excitations was taken to be 0.5. (The results do not depend strongly on

this ratio because most of the excited-state absorption involves the more numerous states in which two different BChls are excited.) Eigenstates of singly- and doubly-excited complexes were obtained by diagonalizing U and V separately.

The ground-state absorption spectrum was calculated as described,(*111*) but with the simplifications that (1) all transitions, including the lowest, were assigned a Lorentzian homogeneous line shape with a FWHM of 250 cm^{-1}, (2) no vibronic structure was included, and (3) mixing of doubly-excited states with the ground state was neglected. Inhomogeneous broadening was introduced by giving the monomer transition energies (the diagonal terms of U) Gaussian disorder with a standard deviation (σ) of 200 or 300 cm^{-1} (FWHM = $\sqrt{8 \ln 2}\,\sigma$ = 471 or 706 cm^{-1}). This gave the diagonal terms of V correlated disorder with a standard deviation $\sqrt{2}\,\sigma$.

To calculate the light-induced changes in absorption and emission, a reduced density matrix $\boldsymbol{\rho}$ was defined for a singly-excited system in the exciton representation, and then averaged over orientations and a distribution of monomer transition energies for an ensemble of such systems. The ground-state system was assumed to be excited by a pulse with a spectral width similar to those of the pulses used experimentally (see Figure 19) and peaking either 184 cm^{-1} to the blue or 222 cm^{-1} to the red of the calculated absorption maximum. To represent a coherent superposition of the allowed "one-exciton" states, the density matrix at time $t = 0$ was taken to be:

$$\rho_{ab}(t=0,\hat{e}_i) = \Gamma^{-1}(\hat{e}_i \cdot \hat{\mu}_a)(\hat{e}_i \cdot \hat{\mu}_b)J_{ab}. \quad (1a)$$

Here $\hat{e}_i$, $\hat{\mu}_a$ and $\hat{\mu}_b$ are unit vectors parallel to the electric field of the pump pulse and to the transition dipoles ($\vec{\mu}_a$ and $\vec{\mu}_b$) for excitation from the ground state to exciton states a and b; J_{ab} is a spectral overlap integral of the pump pulse with the two excitation spectra; and Γ is a normalization factor. The spectral overlap integrals are:

$$J_{ab} = |\bar{\mu}_a||\bar{\mu}_b| \int I(\nu)\{W_a(\nu)W_b(\nu)\}^{1/2} d\nu \,, (1b)$$

where $I(\nu)d\nu$ is the excitation intensity at frequency ν and $W_a(\nu)$ is the normalized Lorentzian lineshape for excitation to state a. The use of the geometric mean $(W_aW_b)^{1/2}$ for the off-diagonal terms of $\boldsymbol{\rho}$ at time 0 follows Rahman et al. (*123*)

The normalization factor Γ is:

$$\Gamma = \left\langle \sum_a (\hat{e}_i \cdot \hat{\mu}_a)^2 J_a \right\rangle_{O,E} = \frac{1}{3} \left\langle \sum_a J_a \right\rangle_E , \quad (1c)$$

where $\langle ... \rangle_O$ indicates averaging over all orientations with respect to $\hat{e}_i$ and $\langle ... \rangle_E$ denotes averaging over the distribution of the monomer transition energies. With this normalization, $\mathrm{Tr}\{ \langle \boldsymbol{\rho} \rangle_{O,E} \} = 1$ for an inhomogeneous ensemble of randomly-oriented systems.

The intensity of SE from an orientationally-averaged exciton state a at time zero is:

$$F_a(\nu, \hat{e}_i, \hat{e}_f) = C \left\{ \sum_{b=1}^{18} \left\langle (\hat{e}_f \cdot \bar{\mu}_a)(\hat{e}_f \cdot \bar{\mu}_b) \rho_{a,b}(0, \hat{e}_i) \right\rangle_O \right\} W_a(\nu)$$

$$= C\Gamma^{-1} \left\{ \sum_{b=1}^{18} \left\langle (\hat{e}_i \cdot \hat{\mu}_a)(\hat{e}_i \cdot \hat{\mu}_b)(\hat{e}_f \cdot \hat{\mu}_a)(\hat{e}_f \cdot \hat{\mu}_b) \right\rangle_O (J_a J_b)^{1/2} |\bar{\mu}_a||\bar{\mu}_b| \right\} W_a(\nu), \quad (2a)$$

where $\hat{e}_f$ is the probe polarization and C is a constant that depends on the pump and probe intensities, the refractive index of the medium, local field corrections, and physical constants. The sum runs over all the one-exciton states. We used the same homogeneous lineshape $W_a(\nu)$ for SE or ESA as for ground-state absorption (FWHM = 250 cm^{-1}).

Excited-state absorption from state a to a doubly-excited ("two-exciton") state η at time zero is given similarly by:

$$A_{a\eta}(\nu,\hat{e}_i,\hat{e}_f) \;=$$

$$C\Gamma^{-1}\left\{\sum_{b=1}^{18}\left\langle(\hat{e}_i\cdot\hat{\mu}_a)(\hat{e}_i\cdot\hat{\mu}_b)(\hat{e}_f\cdot\hat{\mu}_{a\eta})(\hat{e}_f\cdot\hat{\mu}_{b\eta})\right\rangle_O (J_a J_b)^{1/2}\left|\bar{\mu}_{a\eta}\right|\left|\bar{\mu}_{b\eta}\right|\right\}W_{a\eta}(\nu), \quad (2b)$$

where $\bar{\mu}_{a\eta}$ and $W_{a\eta}(\nu)$ are the transition dipole and lineshape for the excitation $a \rightarrow \eta$.

Setting the off-diagonal terms of $\boldsymbol{\rho}$ to zero gives an incoherent mixture of one-exciton states with the same initial populations. The sums in eqs. 2*a* and *b* then reduce to

$$F_a(\nu,\hat{e}_i,\hat{e}_f)= C\Gamma^{-1}\left\langle(\hat{e}_i\cdot\hat{\mu}_a)^2(\hat{e}_f\cdot\hat{\mu}_a)^2\right\rangle_O J_a\left|\bar{\mu}_a\right|^2 W_a(\nu) \quad (3a)$$

and $$A_{a\eta}(\nu,\hat{e}_i,\hat{e}_f)= C\Gamma^{-1}\left\langle(\hat{e}_i\cdot\hat{\mu}_a)^2(\hat{e}_f\cdot\hat{\mu}_{a\eta})^2\right\rangle_O J_a\left|\bar{\mu}_{a\eta}\right|^2 W_{a\eta}(\nu). \quad (3b)$$

Finally, if the diagonal terms of $\boldsymbol{\rho}$ are replaced by the populations for a Boltzmann equilibrium at temperature T (with the off-diagonal terms zero), the SE and ESA from state a become:

$$F_a(\nu,\hat{e}_i,\hat{e}_f)= C\Gamma^{-1}\left\{\sum_{b=1}^{18}\left\langle(\hat{e}_i\cdot\hat{\mu}_b)^2(\hat{e}_f\cdot\hat{\mu}_a)^2\right\rangle_O J_b\right\}\exp(-E_a/k_BT)\,Z^{-1}\left|\bar{\mu}_a\right|^2 W_a(\nu) \quad (4a)$$

$$A_{a\eta}(\nu,\hat{e}_i,\hat{e}_f)= C\Gamma^{-1}\left\{\sum_{b=1}^{18}\left\langle(\hat{e}_i\cdot\hat{\mu}_b)^2(\hat{e}_f\cdot\hat{\mu}_{a\eta})^2\right\rangle_O J_b\right\}\exp(-E_a/k_BT)\,Z^{-1}\left|\bar{\mu}_{a\eta}\right|^2 W_{a\eta}(\nu), \quad (4b)$$

where E_a is the energy of exciton state a, k_B is the Boltzmann constant, and $Z = \sum_{a=1}^{18} \exp(-E_a/k_BT)$. The terms of the sums in eqs. 4 represent preparation of state b by the excitation pulse, followed by internal conversion to state a. Note that the Boltzmann equilibrium described by these equations pertains to an individual LH2 complex with a particular set of transition energies. Thermal equilibration of the entire ensemble would remove all memory of the excitation wavelength and polarization.

The contribution of exciton state a to GSB includes a sum similar to those in eqs. 4:

$$G_a(\nu,\hat{e}_i,\hat{e}_f) = CT^{-1}\left\{\sum_{b=1}^{18} \left\langle (\hat{e}_i \cdot \hat{\mu}_b)^2 (\hat{e}_f \cdot \hat{\mu}_a)^2 \right\rangle_O J_b \right\} |\bar{\mu}_a|^2 W_a(\nu). \quad (5)$$

This is independent of the dephasing and thermalization of $\boldsymbol{\rho}$.

After averaging over the distribution of monomer energies, the total signal for an inhomogeneous ensemble is:

$$S(\nu,\hat{e}_i,\hat{e}_f) = \left\langle \sum_a \left\{ -G_a(\nu,\hat{e}_i,\hat{e}_f) - F_a(\nu,\hat{e}_i,\hat{e}_f) + \sum_\eta A_{a\eta}(\nu,\hat{e}_i,\hat{e}_f) \right\} \right\rangle_E . \quad (6)$$

The orientational averages in F_a, $A_{a\eta}$ and G_a depend on the polarization of the probe beam relative to the pump. Expressions for these averages are given in the Appendix. F_a and $A_{a\eta}$ also depend on whether the excitation is coherent (eqs. 2*a* and 2*b*), incoherent (3*a* and *b*), or thermalized (4*a* and *b*). This distinction is idealized because, in an actual measurement, dephasing and thermalization of $\boldsymbol{\rho}$ are coupled processes and are convoluted with the excitation pulse.

Finally, the isotropic signal $K(\nu)$ and anisotropy $r(\nu)$ are:

$$K(\nu) = S(\nu,\hat{x},\hat{x}) + 2S(\nu,\hat{x},\hat{y}) \quad (7a)$$

and $r(\nu)=\dfrac{S(\nu,\hat{x},\hat{x})-S(\nu,\hat{x},\hat{y})}{S(\nu,\hat{x},\hat{x})+2S(\nu,\hat{x},\hat{y})}$, (7*b*)

where $\hat{x}$ and $\hat{y}$ indicate polarization along orthogonal laboratory axes. Calculations of $K(\nu)$ and $r(\nu)$) were repeated for 1000 iterations of the Monte Carlo procedure used to provide diagonal disorder in U and V, and the calculated spectra were averaged in bins with a resolution of 10 cm^{-1}.

To express the enhancement of the isotropic emission strength of the LH2 complex compared to the emission strength of monomeric BChl-*a*, it is useful to define the dimensionless ratio

$$L_e(t)=\left\langle F_{\parallel}+2F_{\perp}\right\rangle_{O.E}\Big/\left|\bar{\mu}^m\right|^2 , \quad (8a)$$

where $|\bar{\mu}^m|^2$ is the Q_y dipole strength for BChl-*a* in solution (we used 50 debye^2),(*111*) $F_{\parallel}=F(t,\hat{x},\hat{x})$, $F_{\perp}=F(t,\hat{x},\hat{y})$, and

$$F(t,\hat{e}_i,\hat{e}_f)=\sum_a\sum_b\ (\hat{e}_f\cdot\bar{\mu}_a)(\hat{e}_f\cdot\bar{\mu}_b)\,\rho_{a,b}(t,\hat{e}_i)\,. \qquad (8b)$$

The sums in eq. 8*b* again run over the exciton states. Evaluating the orientational averages gives:

$$L_e^{coh}=\left\langle\sum_a\sum_b\ (\hat{\mu}_a\cdot\hat{\mu}_b)^2\,|\bar{\mu}_a||\bar{\mu}_b|(J_aJ_b)^{1/2}\right\rangle_E\Big/\left(3\Gamma\left|\bar{\mu}^m\right|^2\right) \quad (9a)$$

for the coherently excited ensemble at time zero, and

$$L_e^{inc}=\left\langle\sum_a\left|\bar{\mu}_a\right|^2 J_a\right\rangle_E\Big/\left(3\Gamma\left|\bar{\mu}^m\right|^2\right) \quad (9b)$$

$$\text{and } L_e^{therm} = \left\langle \left(\sum_a |\bar{\mu}_a|^2 e^{-E_a/k_B T} Z^{-1} \right) \left(\sum_b J_b \right) \right\rangle_E \Big/ \left(3\Gamma |\bar{\mu}^m|^2 \right) \qquad (9c)$$

for the incoherent and thermalized excitations, respectively. As above, the thermalization in eq. 9*c* is restricted to individual LH2 complexes.

L_e^{coh}, L_e^{inc} and L_e^{therm} depend on the geometry, electronic structure and inhomogeneity of the complex and, in the case of L_e^{therm}, on the temperature. With broadband excitation, pulses, L_e^{inc} and L_e^{therm} both go to 1 if the electronic coupling between the BChls is set to zero so that the exciton transition dipoles are transition dipoles of individual molecules ($|\bar{\mu}_a|^2 = |\bar{\mu}_b|^2 = |\bar{\mu}^m|^2$). L_e^{coh} generally is greater than 1 even for systems with no electronic coupling, as long as the monomer transition dipoles have fixed orientations with respect to each other. For 18 noninteracting BChls in a planar arrangement with C_9 or C_{18} symmetry, L_e^{coh} would be 18x1/2 = 9.

Results

1. Spectral Relaxations. Figure 19 shows the absorption spectrum of chromatophores containing the LH2 complex. Also shown are the spectra of pump pulses centered at 838 and 868 nm, which we will call "blue" and "red" excitation pulses, respectively. The excitation probability (product of the pump and absorption spectra) peaks at 843 nm with the blue pulses and 855 nm with the red. In a system with moderate disorder, both pump pulses would excite predominantly the two or three most strongly allowed transitions in the region of 850 nm. The red pulses also would excite the weakly-allowed, low-energy transition, whereas the blue pulses could also excite some of the higher-energy transitions.

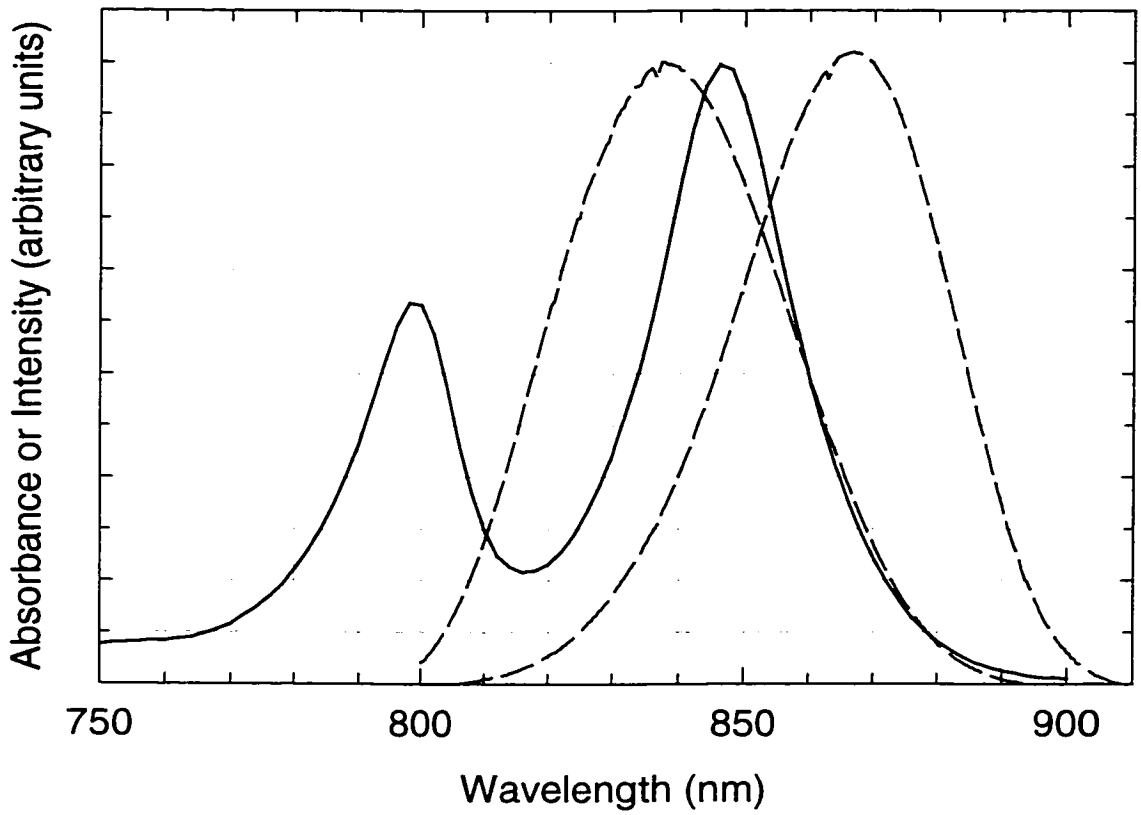

Figure 19. Absorption spectrum of chromatophores from strain ΔQBALM/Q (*solid line*) and intensity spectra of the "blue" and "red" pump pulses (*dashed lines*).

The upper panels of Fig. 20 show the changes in isotropic absorbance and stimulated emission measured at several times after a red or blue excitation pulse. In these measurements, the probe pulses were polarized at the magic angle (54.7°) relative to the pump. Both types of excitation result in ground-state bleaching (GSB) and stimulated emission (SE) in the region of 850 nm and a broad band of excited-state absorption (ESA) near 830 nm. The arrows indicate how the signals change with time. After blue excitation (Fig. 20*A*) the negative feature shifts to longer wavelengths, while SE grows in around 880 nm and the ESA declines. Following red excitation (Fig. 20*B*) the positive and negative signals decrease simultaneously, with little shifting of the spectrum.

Figure 21 compares difference spectra measured at 25, 150 and 350 fs after the two excitation pulses. At 25 fs, the GSB/SE signals generated by blue excitation peak about 5 nm to shorter wavelengths than the signals seen with red excitation. The ESA is weaker relative to the bleaching with the blue excitation and also is blue-shifted by about 5 nm. These differences have largely disappeared by 150 fs, and except for a small difference that decays more slowly (see below), the two spectra are virtually identical at 350 fs. Temporal signals integrated over all detection wavelengths were virtually superimposable for red and blue excitation (not shown).

We typically collected 100 spectra for each excitation, with delay times extending from -150 to +350 fs and wavelengths ranging from 805 to 890 nm. Singular-value decomposition was used to separate the data matrix into a sum of products of the form

$$S(\lambda,t) = \sum_i \xi_i(\lambda)\chi_i(t)\gamma_i, \quad (10)$$

where $\xi_i(\lambda)$ and $\chi_i(t)$ are functions of wavelength and time, respectively, and γ_i is the singular-value amplitude of component i (*81*). Only the first few components were

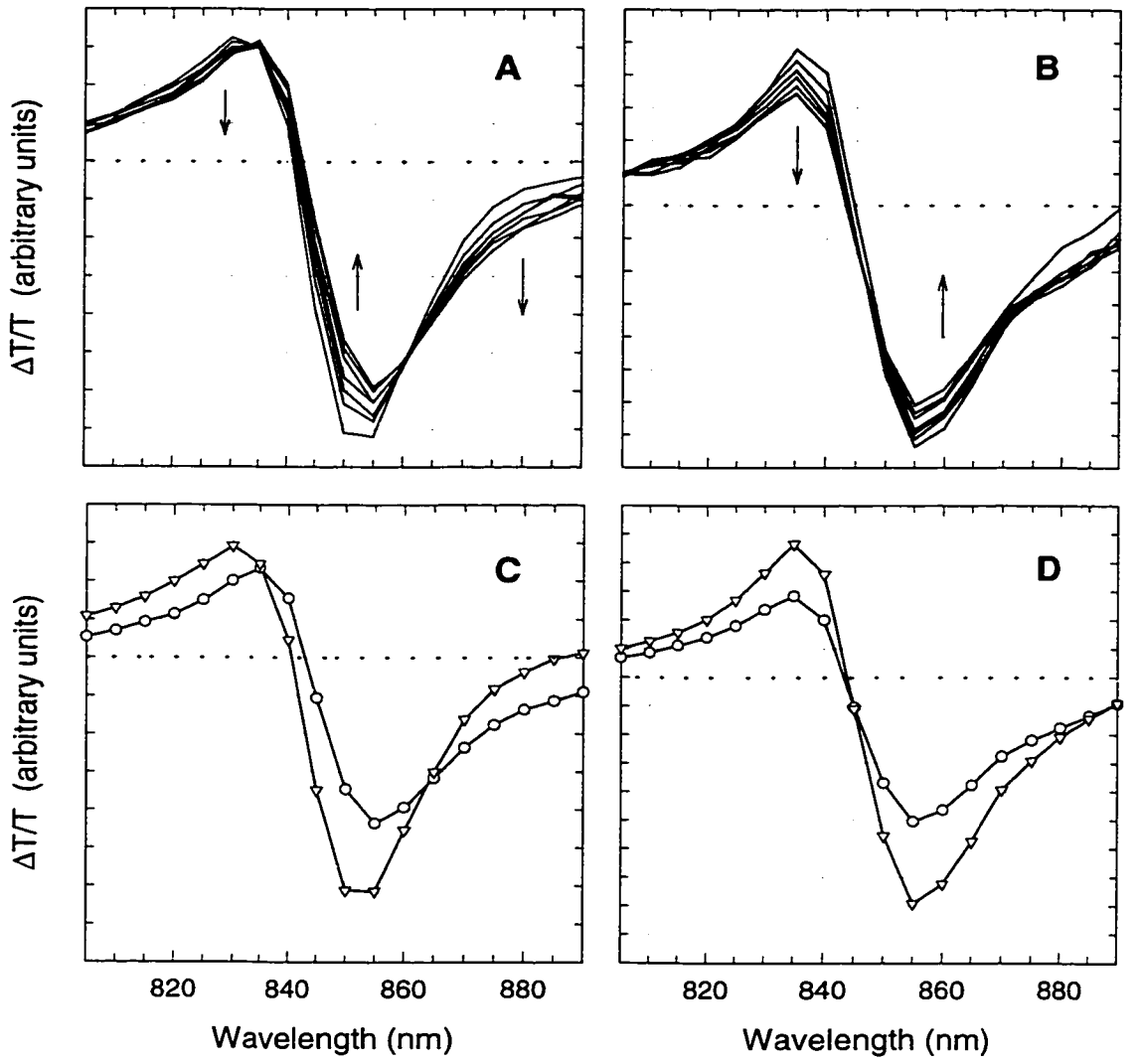

Figure 20. *Upper Panels*: Absorbance difference spectra measured at delay times 25, 50, 75, 100, 150, 200 and 350 fs following excitation with pulses on the blue (*A*) or red (*B*) side of the B850 absorption band. The dotted horizontal lines mark zeros of the ordinate scale. Arrows point in the direction of increasing time delay. The maximum fractional absorbance change was $<10^{-3}$ in all cases. *Lower Panels*: Difference spectra at $t = 0$ (∇) and ∞ ($\circ$) following the blue (*C*) and red (*D*) excitations, reconstructed from the experimental data by singular-value decomposition and global kinetic analysis. The calculated relaxation times were 110 fs and 80 fs for the blue and red excitations, respectively.

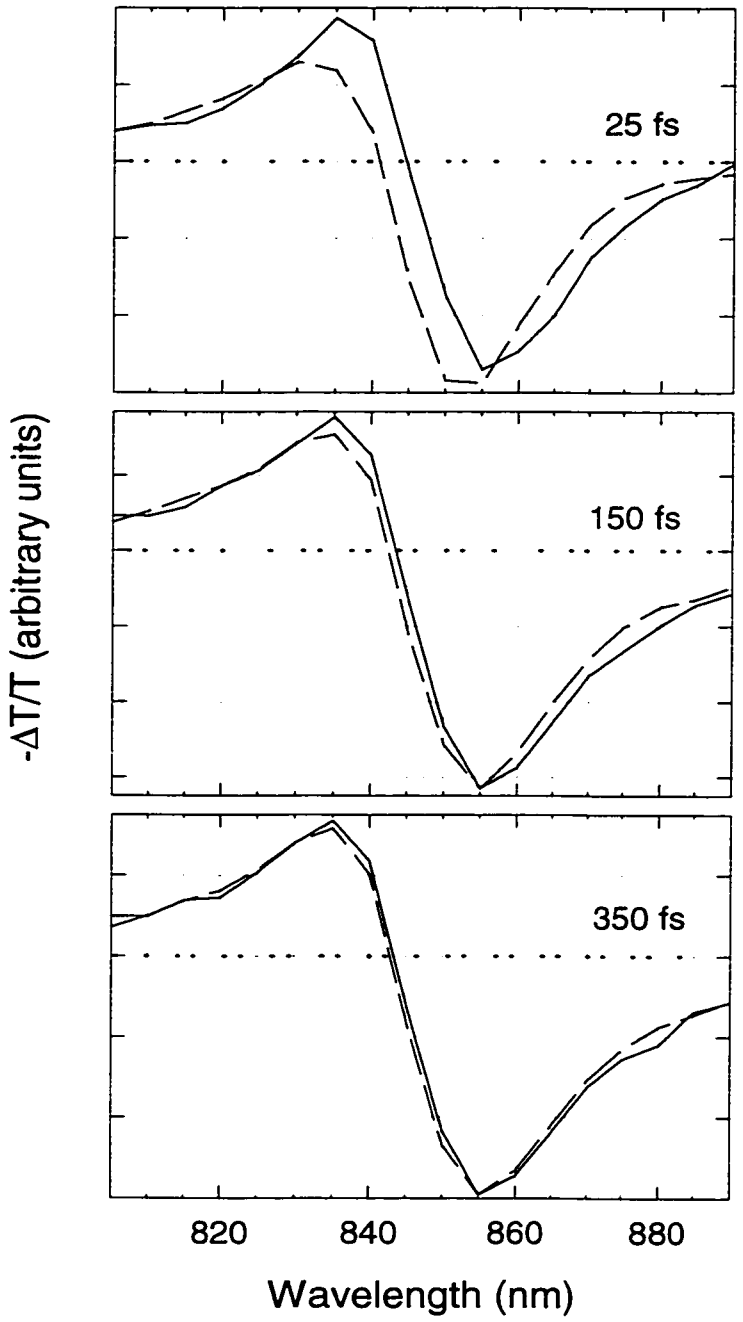

Figure 21. Difference spectra measured at 25, 150 and 350 fs following red (*solid lines*) and blue (*dashed lines*) excitations. Zero time was taken to be the maximum of the pump-probe intensity cross-correlation trace. The spectra were scaled to normalize their amplitudes at 350 fs.

retained (2 for red excitation and 3 for blue). The time courses of the next one or two components had first- or second-derivative shapes and decayed to zero within the period of pump-probe overlap. These were rejected because analyses of simulated data indicated that they probably represent coherent interaction between the pump and probe electric fields in the sample and frequency chirp in the probe pulse. (In our previous study, (*81*) we retained an additional short-lived component. This decreased the dominant time constant returned in the next stage of the analysis.) All the remaining components had very small singular values and waveforms that appeared to reflect only random noise. The significant kinetic waveforms ($\chi_i(t)$) were fit globally to a multiexponential function convoluted with the pump-probe cross-correlation function. An accurate fit usually required three or four exponential terms plus a constant. However, the first few terms probably represented residual effects of pump-probe coherence and/or chirping because they had time constants of less than 20 fs, *i.e.*, less than the pump-probe cross-correlation width. We therefore will discuss only the terms with lifetimes greater than 50 fs.

For data sets that extended to 350 fs, this analysis led to a satisfactory description of the results of either red or blue excitation in terms of a single relaxation. The fits returned a somewhat shorter relaxation time constant for red excitation (83 fs) than for blue (114 fs). Fitting the signals at individual wavelengths separately rather than globally gave shorter time constants, probably because of the greater difficulty of removing contributions from chirping and pump-probe coherence. Adding another decay component did not improve the global fits significantly. However, a similar global analysis of data with time steps of 50 fs and delays extending to 5 ps returned a small additional component with a relaxation time of 1.2±0.4 ps.

Difference spectra for any given delay time can be reconstructed from the significant terms of the sum in eq. 10 (*81*). The spectra for times following the period of pump-probe overlap agreed closely with experimental spectra. Spectra for delay times t = 0 and ∞ are shown in the lower panels of Fig. 20. With either red or blue excitation,

the relaxation reduces the amplitudes of both the positive and negative features by approximately 30% and broadens the negative feature on the long-wavelength side. After blue excitation, the positive and negative features both shift to longer wavelengths by about 3 nm.

2. Anisotropy. The anisotropy of the signals was measured under several different conditions. In one set of experiments we excited samples at 827, 850 or 872 nm and measured the anisotropy at 860 nm. In another, we excited samples with the entire laser bandwidth (here a FWHM of 70 nm) to maximize the time resolution, and measured the anisotropy at various wavelengths between 820 and 875 nm; we also measured the anisotropy with an undispersed probe beam peaking at 832 or 845 nm. In all cases, the "raw" anisotropy of the signals, $(S_{\parallel}-S_{\perp})/(S_{\parallel}+2S_{\perp})$ where $S_{\parallel}$ and $S_{\perp}$ are signals measured with pump and probe polarizations parallel and perpendicular, decayed from an initial value between 0.35 and 0.55 to a value close to 0.1 on a time scale of approximately 30 fs. We checked for saturation effects in the signal by reducing the intensity of the pump and probe beams by a factor of ~3 and obtained an anisotropy decay that was not significantly different. We also eliminated pump-pulse-induced Kerr lensing (*124*) as an artifactual source of the rapid decay of anisotropy by comparing results obtained at 850 nm with the detection wavelength selected by either a monochromator or an interference filter. In principle, the narrow entrance slit of the monochromator might pass different amounts of the probe light depending on the shape of the pump-induced lens, which would vary with the pump polarization. However, the results again were identical to within the noise level of the measurements.

As a test of the procedure for measuring anisotropy, we examined the signals generated by exciting the laser dye IR-132 in dimethyl sulfoxide. Figure 22 shows the results. The raw anisotropy was essentially constant at 0.38 even through most of the

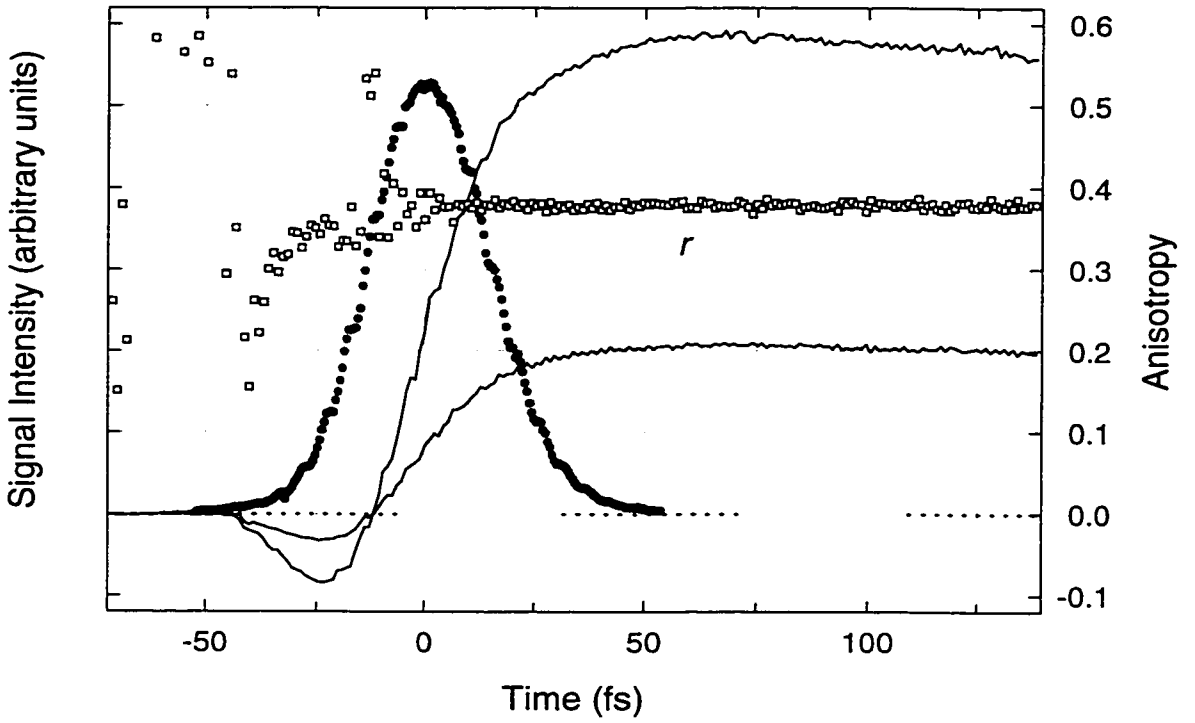

Figure 22. Changes in absorbance and stimulated emission measured with IR-132 in dimethyl sulfoxide with probe beams polarized parallel ($S_{\parallel}$) or perpendicular ($S_{\perp}$) to the pump polarization. Excitation was with broadband pulses centered at 842 nm (FWHM ≈ 90 nm) and detection was at 875 ± 2.5 nm. Also shown are the pump-probe cross-correlation function (●) and the raw anisotropy (r, □) calculated directly from the signals. The apparent decrease in r at $t < 0$ may reflect the different retardation of the pump beam in the two polarizations (see Methods).

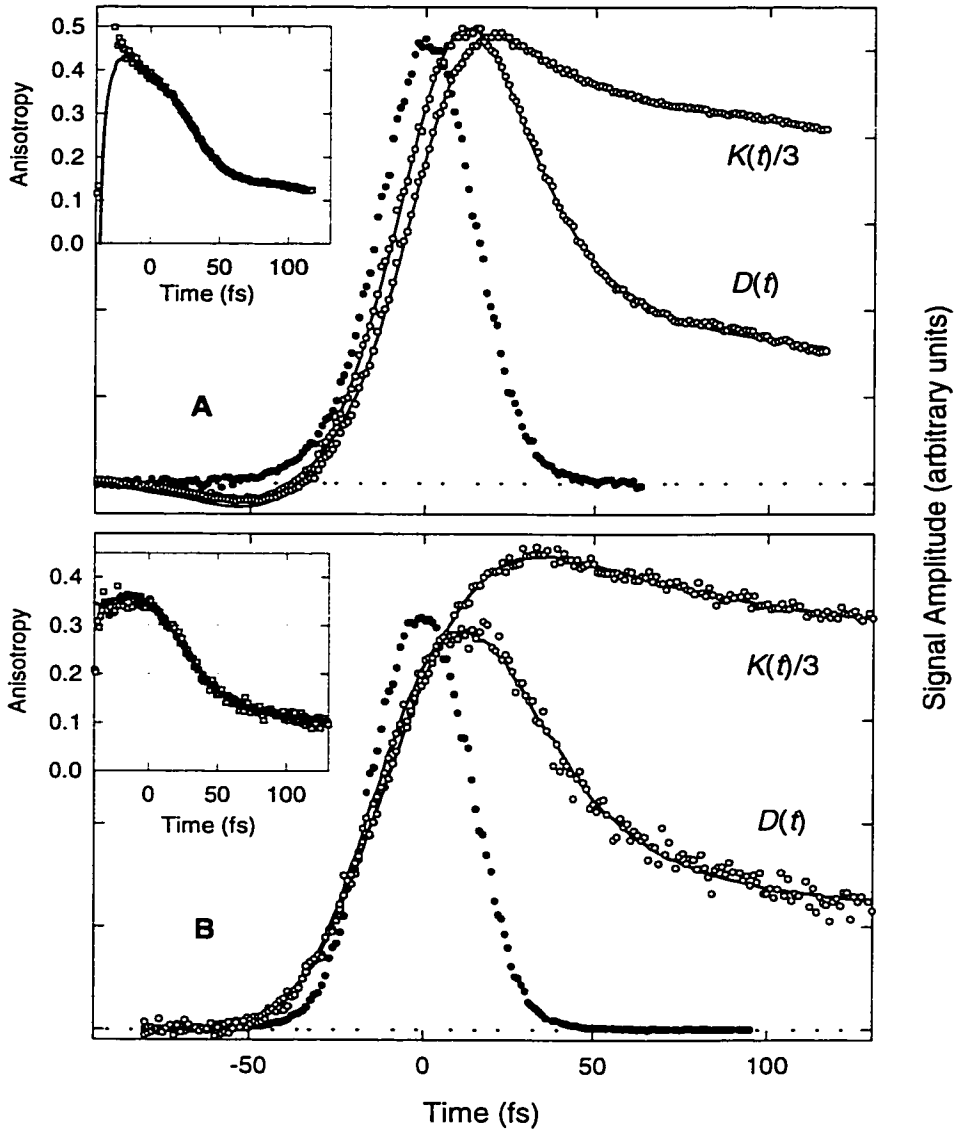

Figure 23. Isotropic [$K(t)/3$] and polarization-difference [$D(t)$] decay signals following excitation by broad-band pulses centered at 843 nm and detection at 830 nm (*top panel*) or over the entire bandwidth of the probe pulses (*bottom panel*). The *open circles* (○) are data points; the curves show the fits obtained as described in the text with the anisotropy decay parameters given in Table 1. The pump-probe cross-correlation functions are shown with *filled circles* (●); these are normalized arbitrarily at their peaks to be similar to the peaks of D. Time zero is the peak of the cross-correlation function. The inserts show the "raw" anisotropies obtained directly from the signals (□) and calculated from the fits to $K(t)$ and $D(t)$ (*solid lines*).

period of pump-probe overlap. The difference between 0.38 and the theoretical value of 0.40 may be due to a slight depolarization of the pump and probe beams by the mirrors between the half-wave plate and the sample. The decrease in the apparent anisotropy at $t < -20$ fs could reflect the delay of ~0.7 fs associated with rotating the pump polarization.

A determination of the true anisotropy of the LH2 signals at early times is problematic because of coherent pump-probe coupling (PPC) and perturbed free-induction decay (PFID). The PFID signal in the probe direction arises because the probe pulse generates ground-excited electronic coherence that radiates at the nominal transition frequency (*125*). If the pump pulse follows the probe during the period of electronic dephasing, it interrupts the free induction decay. This effect is seen as a decay of the coherence signal in the direction of $t < 0$. The coherence signal is heterodyned with the probe pulse, giving rise to oscillations as a function of the frequency detuning (*125*). Assuming that the transition dipoles of the sample do not rotate during the period of electronic dephasing, the PFID and PPC signals will have anisotropies of 0.4. They therefore can interfere with measurements of anisotropies that differ from this value.

To remove the effects of PFID, the data were analyzed by first constructing isotropic and polarization-difference signals as $S_{\parallel}+2S_{\perp}$ and $S_{\parallel}-S_{\perp}$, respectively. The isotropic signal was fit by non-linear least-squares to the function (*126*)

$$K(t) = [K_1(t) + K_2(t)] \otimes P(t + \delta), \quad (11a)$$

where $$K_1(t) = (1-\theta(t))\, a_o \exp\{t/T_2\}\cos(\omega t) \quad (11b)$$

and $$K_2(t) = \theta(t) \sum_{i=1}^{N} a_i \exp\{-t/\zeta_i\}. \quad (11c)$$

In eq. 11*a*, $\otimes$ denotes a convolution integral, $P(t)$ is the measured pump-probe crosscorrelation function, and δ is an adjustable time shift. In eqs. 11*b* and *c*, $\theta(t)$ is the

Heaviside step function (0 for $t < 0$ and 1 for $t \geq 0$), ω is the frequency detuning of the peak of the probe spectrum from the 850-nm absorption peak, the a_i are amplitudes, ζ_i's are time constants, and T_2 is a time constant for decay of electronic coherence. We assume here that the electronic dephasing can be described adequately by a single exponential decay. $K_2(t)$ is the multiexponential function commonly used to fit signals for $t > 0$, while $K_1(t)$ represents PFID. Terms with lifetimes less than the pump-probe cross-correlation width are retained in eq. 11*c* because here the exact form of $K_2(t)$ need not have any particular physical significance.

With $K_1(t)$ and $K_2(t)$ determined by fitting the isotropic signal, the polarization-difference signal ($S_{\parallel}$-$S_{\perp}$) was fit to the function

$$D(t) = [0.4K_1(t) + r(t)K_2(t)] \otimes P(t + \delta). \quad (12)$$

Here the anisotropy of the PFID term is fixed at 0.4 and $r(t)$, the anisotropy decay that we seek, is assumed to be another multiexponential function ($r(t) = r_\infty + \sum_i r_i \exp(-t/\tau_i)$). We assume here that the same $r(t)$ applies to all components of $K_2(t)$, which could be incorrect if $K_2(t)$ contains significant contributions from pump-probe coherence signals (see below).

Examples of the fits are shown in Figure 23 for signals measured at 830 nm (*panel A*) and for signals measured without a monochromator in the probe beam (*B*). In these experiments, the sample was excited with the full spectral width of laser pulses centered around 840 nm; the pump-probe crosscorrelation traces had a typical FWHM of 32 fs. In accord with the results presented in the previous section, the fits of the isotropic signal to $K(t)$ returned a relaxation with a time constant in the range of 80 to 100 fs along with faster components of doubtful physical significance. The fits to both $K(t)$ and $D(t)$ were excellent at 830, 850 and 860 nm, and also with the undispersed probe (see Figure 23). They were less satisfactory at 820 or 875 nm, where the signals were

smaller. The time constants for the anisotropy decay measured at various wavelengths are given in Table 5. Excluding 875 nm, where the fits are poor, the data give a nearly constant value in the vicinity of 0.52 for the initial anisotropy, $r(0)$. The anisotropy decays to approximately 0.1 with an apparent time constant of about 30 fs. The data at most wavelengths could be fit well by using a single exponential expression for $r(t)$, but a biexponential expression improved the fit significantly at 830 nm.

Contributions of PFID to the signals can be seen at negative times in Fig. 23*A*. Here the probe wavelength was on the blue side of the B850 band and the PFID and ESA signals had opposite signs. The apparent dephasing time T_2 obtained from the data for 830, 850 and 860 nm (Table 5) had a mean value of 19 fs with a large uncertainty. PFID is less obvious in the lower panel of Figure 23, where it has the same sign as the dominant signals from GSB and SE and probably is attenuated by the integration over a broader band of wavelengths.

For comparison with the spectral-relaxation data, we also measured anisotropy decays at 860 nm following excitation with pulses centered at 872, 827 or 850 nm. The crosscorrelation FWHM of the pump and probe was approximately 40 fs, and the scan length was 400 fs. As expected, the isotropic signals were different for the three different pump wavelengths. However, the raw anisotropies obtained directly from the experimental signals were essentially indistinguishable. The anisotropy decay functions derived from the fits to $D(t)$ are collected in Table 6. Rows 2-4 in the table are the results of using a single-exponential expression for $r(t)$; rows 5-7 are two-exponential fits. The initial anisotropy had mean values of 0.37 and 0.40 in the one- and two-exponential fits, respectively, and appeared not to vary significantly with the excitation wavelength. In the one-exponential fits, the anisotropy decayed to slightly below 0.1 with a time constant of about 50 fs; with two exponentials, the time constant of the major component was 31 ± 11 fs.

Table 5: Best Fit Parameters to Anisotropy Measured at Various Wavelengths after Broadband Excitation

Detection Wavelength	T_2 (fs)	r_1	τ_1 (fs)	r_2	τ_2 (fs)	r_∞	$r(0)$[d]
820[a,b]	8	0.49	42	-	-	0.07	0.56
830[a]	35	0.38	19	0.14	515	0.01	0.53
850[a]	16	0.43	29	-	-	0.10	0.53
860[a]	6	0.42	34	-	-	0.10	0.52
875[a,b]	12	0.60	43	-	-	0.09	0.69
Broad-band[c]	14	0.37	26	-	-	0.11	0.48
	±6	±0.02	±1			±0.01	±0.02

[a]Detection bandpass was 5 nm.

[b]Fits to the polarization-difference signal were poor at these wavelengths.

[c]The probe pulse was not dispersed after the sample; the values are averages of measurements on two samples.

[d]Initial anisotropy: $r(0) = r_1 + r_2 + r_\infty$.

Table 6: Best Fit Parameters to Anisotropy Measured at 860 nm after Excitation at Various Wavelengths

Excitation Wavelength[a]	r_1	τ_1 (fs)	r_2	τ_2 (fs)	r_∞	$r(0)$[b]
827[c]	0.26	45	-	-	0.08	0.34
850[c]	0.26	51	-	-	0.09	0.35
872[c]	0.32	48	-	-	0.09	0.41
827[d]	0.20	19	0.13	83	0.08	0.41
850[d]	0.25	42	0.10	846[e]	0.01[e]	0.36
872[d]	0.21	31	0.13	82.3	0.09	0.43

[a]Peak (nm).

[b]Initial anisotropy: $r(0) = r_1 (+ r_2) + r_\infty$.

[c]Anisotropy fit to a single exponential function.

[d]Anisotropy fit to a biexponential function.

[e]Not determined reliably (the data extend to 350 fs).

The analysis described above does not consider contributions to $K_2(t)$ from coherent pump-probe coupling (PPC). In a two-level system, PPC signals have an intrinsic anisotropy of 0.4 and would not affect the measurement if the signal from GSB, ESA and SE had a similar anisotropy. The IR-132 measurements (Figure 22) illustrate this point; here all the components of the signal have a constant anisotropy of approximately 0.4. On the other hand, if the signal from GSB, ESA and SE had a constant but lower anisotropy, coherence signals could raise the measured anisotropy close to 0.4 during the period of pump-probe overlap. The anisotropy would decay rapidly to the lower value after this period. Contributions from PPC also could affect the apparent initial value and dynamics of an anisotropy that decays rapidly with time.

We attempted to incorporate PPC in the analysis by including a term with a time constant of zero and a fixed anisotropy of 0.4 in eqs. 11 and 12. However, the fits to the experimental data were poorly determined. The convergence of the parameter values depended strongly on the initial estimates.

To evaluate the expected effects from PPC in a simple two-level system, we simulated the pump-probe spectra by calculating the induced polarization of an optically thin sample to third order in the electric field (*127-129*). The dynamics of the system were modeled by a sum of two overdamped Brownian oscillators with the memory function

$$M(t) = \Delta_1^2 \exp(-t/\tau_1) + \Delta_2^2 \exp(-t/\tau_2). \quad (13)$$

The energy correlation times, τ_1 and τ_2, were taken to be 90 fs and 15 ps, respectively, with the former representing the spectral relaxation time measured for the LH2 complex and the latter representing static inhomogeneity on the experimental time scale. Using shorter correlation times would decrease the effects of coherent pump-probe coupling. At high temperatures, the coupling strengths (Δ_1) are related to the solvent

reorganization energies (λ_i) by $\Delta_i^2 = 2\lambda_i k_B T$.[27] Coupling strengths of Δ_1 = 115 cm^{-1} and Δ_2 = 140 cm^{-1} were chosen to give bandwidths of about 410 cm^{-1} for the calculated absorption and emission spectra and a peak separation of about 130 cm^{-1} in accord with the experimentally measured Stokes shift for the LH2 complex (*103*). Isotropic spectra for PFID, PPC, SE and GSB were calculated separately for various pump-probe delay times, (*128, 129*) using Gaussian pump and probe pulses with widths comparable to those of the pulses used experimentally. Temporal profiles were constructed by integrating the calculated spectra over the experimental detection window of 5 nm around a given detection wavelength.

The sum of the calculated isotropic SE plus GSB was fitted to the convolution of the pump-probe cross-correlation with an isotropic response function, $S(t)$, consisting of a single exponential term plus a constant. To generate the components with parallel or perpendicular polarization, the $S(t)$ returned by this fit was multiplied by $(1+2r(t))$ or $(1-r(t))$, where $r(t)$ is an assumed anisotropy decay function, and the product was reconvoluted with the pump-probe cross-correlation function. The components of the PFID and PPC signals with parallel and perpendicular polarization were obtained directly from the corresponding isotropic signals (without the deconvolution-reconvolution procedure) by assuming a constant anisotropy of 0.4. Finally, all the contributions were combined to give total signals ($S_\parallel$ and $S_\perp$) that were used to calculate the raw anisotropy.

Figure 24 shows the results of this calculation for the assumed anisotropy decay function $r(t) = 0.29\exp(-t/\tau) + 0.11$ with τ = 33 fs. The raw anisotropy obtained experimentally for the LH2 complex under similar conditions is shown for comparison. If the contribution from PPC was omitted, the calculated anisotropy decreased slightly at times near the peak of the excitation pulse (see Fig. 24); however, an anisotropy curve close to that of the complete calculation could be obtained by increasing the amplitude of the time-dependent term in $r(t)$ from 0.29 to 0.31 (not shown). Hence, part

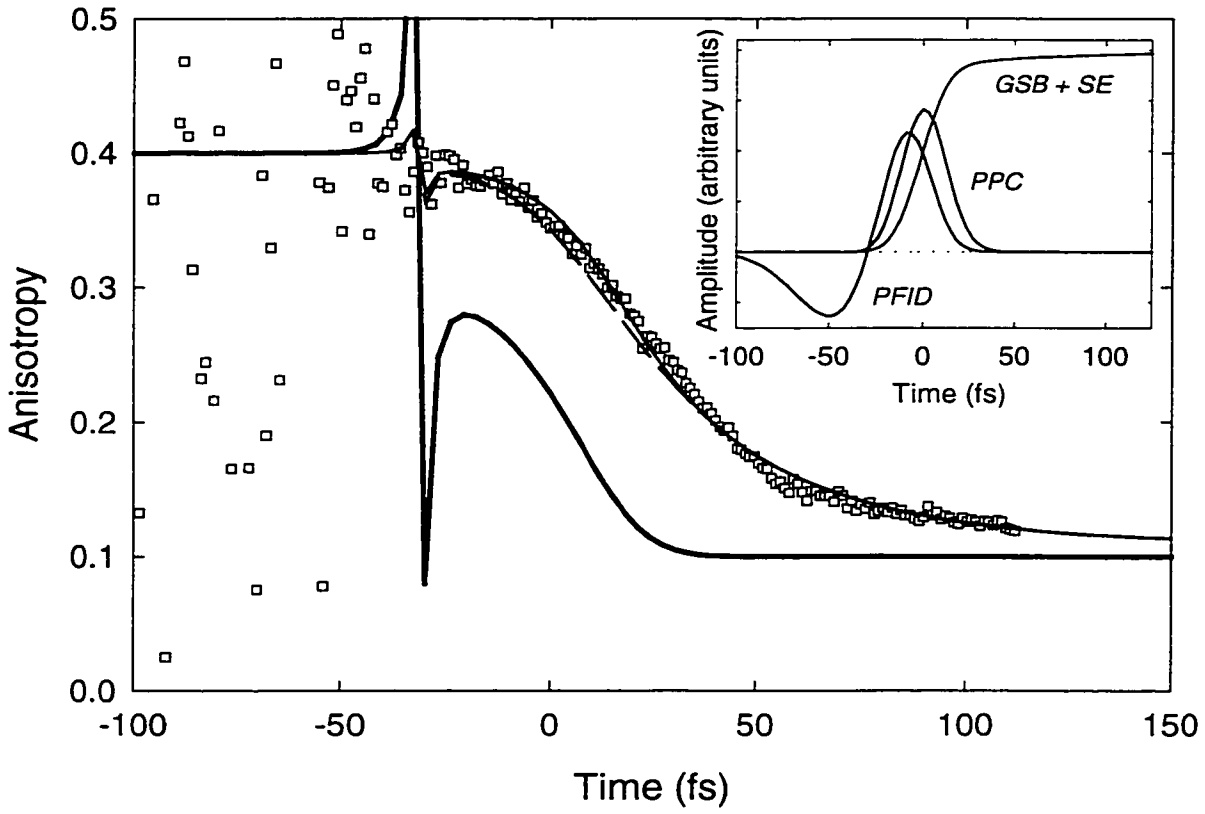

Figure 24. Raw anisotropy of the signals calculated from the third-order polarization of a two-state system with $\Delta_1 = 115\ cm^{-1}$, $\Delta_2 = 140\ cm^{-1}$, $\tau_1 = 90$ fs and $\tau_2 = 15$ ps. The system is excited with a broadband pulse centered at the absorption maximum, and is probed about 10 nm to the red. The curves shown with *solid lines* include PPC, PFID, GSB and SE; PPC is omitted in the calculations shown with a *dashed line*. The GSB+SE signal was assumed to have either a time-dependent anisotropy $r(t) = 0.29\exp(-t/33\ fs) + 0.11$ (*thin lines*), or a constant r of 0.10 (*thick line*). *Squares* (□) show the raw anisotropy measured experimentally at 860 nm after broadband excitation. *Insert*: Calculated contributions from PFID, PPC and GSB plus SE for the two-state system.

of the initial anisotropy estimated above from deconvolutions of the experimental data could reflect the neglectof PPC in the analysis.

Figure 24 also shows a similar calculation for the situation that the anisotropy decay comes entirely from pump-probe coherence coupling and PFID. The anisotropy of the SE plus GSB was taken to be 0.1, independent of time. The simulated anisotropy decayed from 0.4 to 0.1 very rapidly, essentially following the pump-probe crosscorrelation. The decay measured experimentally is significantly slower than this (see Figs. 23 and 24). These simulations indicate that, although PPC probably increases the apparent values of $r(0)$, the measured decay kinetics cannot be explained in this way and most likely are dominated by the actual dynamics of the system.

3. Theory. The spectroscopic relaxations described above can be explained by considering the exciton states of the LH2 complex. To simplify the model, we included only the Q_y transitions of the B850 BChls. GSB, SE and ESA spectra were calculated for ensembles of complexes in which the monomer transition energies were normally distributed with a standard deviation σ of either 200 or 300 cm^{-1}. Previous work[4] has shown that the ground-state absorption and CD spectra can be described reasonably well by using $\sigma \bullet 200$ cm^{-1}. With the present model and a homogeneous FWHM of 250 cm^{-1}, this value of σ gave a ground-state absorption spectrum that peaked at 848 nm and had a FWHM of 320 cm^{-1}. Except where stated, we will describe only the results obtained with these parameters.

The calculations were done for impulsive excitation on either the blue or red side of the absorption band and for three idealized states of the ensemble: (1) a coherent superposition of exciton states created at zero time, (2) an incoherent mixture of exciton states with the same populations, and (3) a Boltzmann equilibrium of exciton states within each LH2 complex at 295 K. Figure 25 shows the calculated isotropic signals for the three states. A comparison of curves 1 and 3 shows that relaxation from a coherent superposition of exciton states to a Boltzmann equilibrium would cause a red

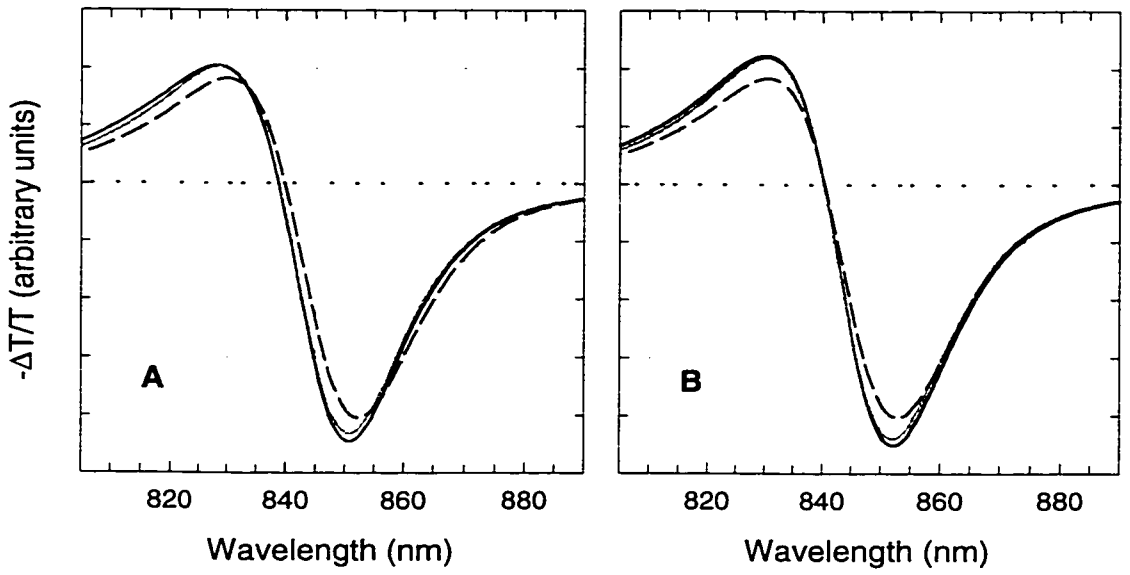

Figure 25. Calculated changes in isotropic absorption and stimulated emission caused by excitation of the B850 pigments with a pulse centered 184 cm^{-1} to the blue (*A*) or 222 cm^{-1} to the red (*B*) of the calculated absorption maximum. Results are shown for three idealized states of an ensemble with Gaussian disorder in the monomer transition energies (σ = 200 cm^{-1}): a coherent superposition of exciton states (*solid black line*), an incoherent mixture of exciton states with the same populations (*gray line*), and a Boltzmann equilibrium of exciton states at 295 K (*dashed black line*).

shift of the signals after blue excitation and mainly a decrease in amplitude after red excitation. The relative magnitudes of the calculated relaxations are similar to the magnitudes seen experimentally (Fig. 20*A*,*B*), though somewhat smaller than those obtained by SVD of the experimental data (Fig. 20*C*,*D*).

The calculated spectra for blue and red excitation remain slightly different following thermalization: the former is shifted to shorter wavelengths by about 1 nm. This is because the inhomogeneous distribution of monomer transition energies is considered to be static, and the model allows thermal equilibration of the exciton levels only within individual LH2 complexes (see Methods). Experimentally, although the excited states generated by blue or red excitation reached a quasi-equilibrium within 350 fs, small differences remained for several ps (Figure 21). The decay of the residual differences could reflect energy transfer from one LH2 complex to another or slow fluctuations of the monomer energies within the complexes.

Figure 26 shows the calculated anisotropies for the three states. Perhaps surprisingly, the anisotropies are relatively insensitive to wavelength, except near the discontinuities where opposing contributions from ESA and GSB cause ($S_{\parallel}$-$S_{\perp}$) and ($S_{\parallel}$+2$S_{\perp}$) to go through zero at slightly different wavelengths. In the regions where the signals are large, the initial anisotropy associated with a coherently excited ensemble is in the range of 0.35, and the final anisotropy after thermal equilibration is about 0.1. These values agree reasonably well with the experimental results obtained by excitation on the blue or red sides of the absorption band (Table 6), although the calculated anisotropies for the coherent excitation are somewhat smaller than the measured values of $r(0)$. Using a broad-band excitation pulse centered on the absorption maximum gave a calculated anisotropy for the coherent excitation that was higher by 0.014 at 860 nm and less sensitive to the probe wavelength. Increasing σ to 300 cm^{-1} decreased the anisotropy for the coherent excitation by 0.010 at 860 nm and increased the variation with wavelength.

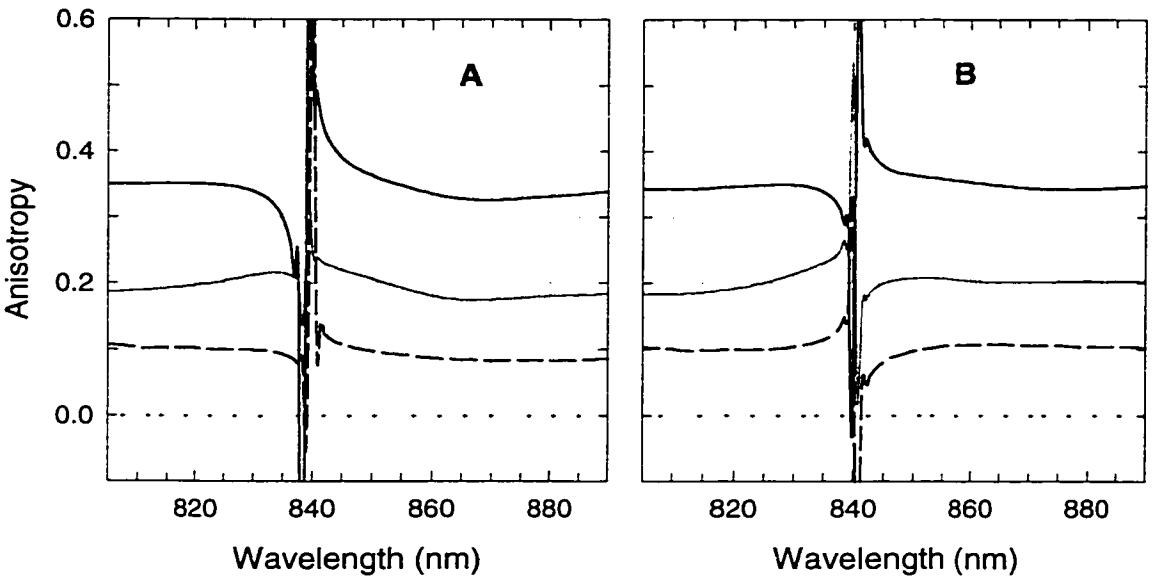

Figure 26. Calculated anisotropies of the changes in absorption and stimulated emission following blue (*A*) or red (*B*) excitation as in Figure 7. The line types correspond to those in Figure 7.

Figure 27*A* shows the individual contributions of GSB, ESA and SE to the calculated signals for blue excitation. Note first that the calculated SE is considerably weaker than the GSB. This is because the ground-state absorption represents the sum of the dipole strengths for 18 upward transitions, while emission represents the decay of a single excited state. SE decreases in amplitude as a result of electronic dephasing and then decreases further and shifts to longer wavelengths as a result of thermal equilibration with the weakly-allowed states at low energies. Excited-state absorption also decreases, while GSB remains constant. Because of the opposing effects of ESA and SE, the loss of coherence causes relatively little change in the total signal (Figure 25); most of the relaxation of the total signal reflects the shift and decrease in SE that accompanies thermalization. This result depends to some extent on the assumed inhomogeneity of the ensemble. If the standard deviation of the monomer energies (σ) is increased to 300 cm^{-1}, electronic dephasing and thermalization contribute more equally to the spectral relaxation (not shown).

The calculated anisotropies of the GSB, ESA and SE are plotted separately in Fig. 27*B*. Stimulated emission from the coherently excited ensemble is calculated to have an anisotropy of approximately 0.71, with little dependence on wavelength. A value of 0.7 is expected for emission from a coherent superposition of two degenerate states with orthogonal transition dipoles,(*121, 130, 131*) and Kumble and Hochstrasser (*132*) have shown that if the excitation pulses were much broader than the B850 band one would always obtain a value of ~0.7 for the initial emission anisotropy regardless of the extent of inhomogeneous broadening. Contributions from out-of-plane transitions can lead to anisotropies exceeding 0.7 (*121*). Stimulated emission from the incoherently excited ensemble has the classical anisotropy of 0.4 expected for a single excited state with a fixed orientation, whereas the thermalized ensemble has the emission anisotropy of 0.1 expected for transition dipoles with random orientations in a plane. The

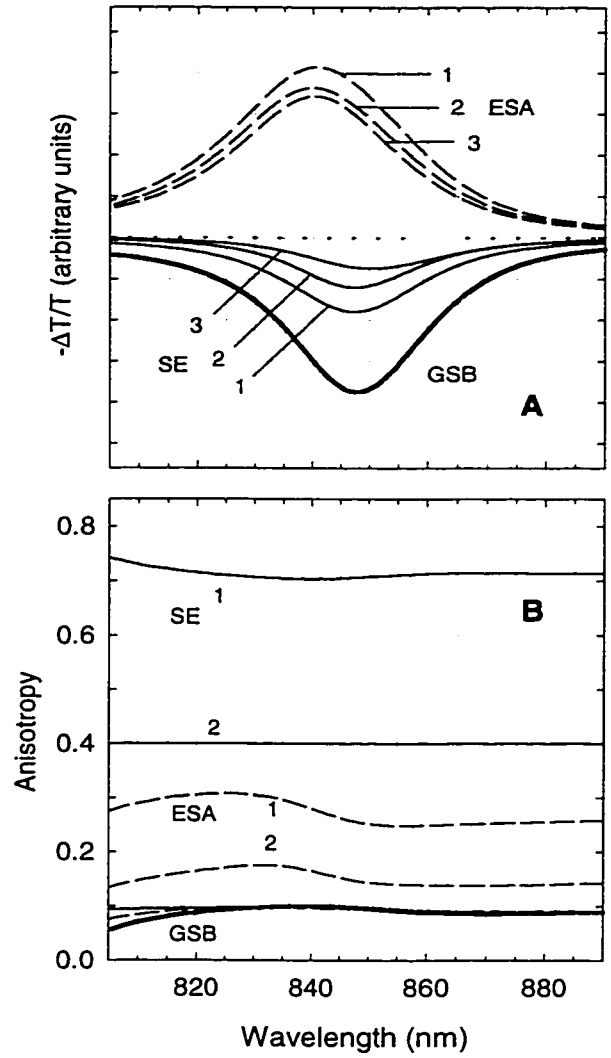

Figure 27. Isotropic amplitudes (*A*) and anisotropies (*B*) of the components of the calculated signals for blue excitation. *Thin solid lines*, stimulated emission; *thick solid line*, ground-state bleaching; *dashed lines*, excited-state absorption; 1, coherently excited ensemble; 2, incoherently excited ensemble; 3, thermalized ensemble. Dephasing and thermalization of the excited ensemble do not change the GSB. The dotted line in *A* is the zero of the ordinate scale.

calculated anisotropies for ESA depend more strongly on the wavelength, but are approximately 0.3, 0.15, and 0.1 for the coherent, incoherent and thermalized excitations, respectively. GSB has an anisotropy of 0.1 over most of the B850 band, but becomes negative in the region of 780 nm where an out-of-plane exciton band contributes to the spectra (*39, 111-113*). Energy transfer among LH2 complexes with random orientations would reduce the anisotropies of SE, ESA and GSB all to zero.

Discussion

The results presented in Figures 20 and 21 show that difference spectra created by excitation of B850 initially depend on the excitation wavelength, but relax to a quasi-equilibrium with a time constant of 100 ± 20 fs. Excitation on the red side of the B850 band gives a somewhat shorter time constant than excitation on the blue side. A final equilibration occurs with a time constant of about 1 ps. Although the relaxation could have components with time constants of less than 50 fs, transients seen on this faster time scale are of questionable significance because they probably include coherences between the pump and probe pulses. Our previous (*81*) estimate of 35 fs for the relaxation time constant reflected a larger contribution from these faster transients.

Excitation-dependent spectral relaxations of the LH2 complex have been described previously by Savikhin and Struve, (*94*) who identified a transient with a time constant of 80 to 100 fs at room temperature. In earlier one-color pump-probe experiments, Chachisvilis et al.(*133*) observed multiphasic relaxations of signals at 855, 864 and 882 nm. The major component had a time constant of about 60 fs at room temperature. The present measurements resolved the relaxation more clearly than was possible in the earlier work, but gave a similar time constant of 100 ± 20 fs.

In previous studies, Pullerits et al.,(*73*) Chachisvilis et al.,(*133*) and Jimenez et al.(*44*) have measured initial anisotropies between 0.3 and 0.4 and anisotropy decay times ranging from 40 to 200 fs. We found the signals to have an initial anisotropy in the range of 0.35 to 0.55, depending on the width of the excitation pulse. The anisotropy decayed to an asymptotic value close to 0.1 with a time constant on the order of 30 fs. When the LH2 complex was excited with a spectrally broad pulse, the anisotropies measured at wavelengths where ESA dominates were similar to the anisotropies at wavelengths where GSB and SE dominate (see Table 5). The initial anisotropy at 860 nm also was relatively insensitive to the excitation wavelength (Table 6), in spite of the fact that the relative contributions of ESA, GSB, and SE to the initial signal at 860 nm depend on the excitation (Fig. 20). Narrowing the excitation pulse spectrum decreased the initial anisotropy at 860 nm to approximately 0.4 (compare Tables 5 and 6), possibly because it restricted the coherent excitation of nondegenerate states.

Several different processes could contribute to the spectral relaxations and the rapid decay of the anisotropy. These include (*a*) decay of electronic coherences within the manifold of exciton states, (*b*) thermal equilibration among excitonic states, (*c*) vibrational cooling and equilibration (Stokes shifts), (*d*) stochastic hopping of excitations localized on BChl dimers or other small clusters, and (*e*) energy transfer among separate LH2 complexes. A complete analysis of the dynamics of these processes is a challenging task because the LH2 complex has a large number of accessible excited states and because the interactions of the pigments with the protein probably fluctuate on many different time scales. However, Figures 25 and 26 show that the main features of the spectral relaxations and the decay of anisotropy are reproduced well by a model that considers only processes *a* and *b*. This conclusion is in accord with recent calculations by Kühn and Sundström(*116*) and Zhang et al,(*117*) who have used similar density-matrix formalisms to analyze the excited LH2 complex. Our calculations also are qualitatively consistent with the finding that the initial and final anisotropies are similar in regions where the signals are dominated by either ESA, GSB

or SE. As suggested above, the small component of the relaxations with a time constant of about 1 ps could reflect thermalization of the monomer transition energies (processes *c* and *d*) or energy transfer from one LH2 complex to another (process *e*).

Kühn and Sundström(*116*) have calculated the dynamics of the relaxations by using multilevel Redfield theory with an explicit spectral density function. The predicted time scale of 0.5 to 1 ps is longer than the observed relaxation time of 0.1 ps, but seems reasonably close considering the complexity of the system. We have not attempted to calculate the dynamics theoretically in the present study. However, the model described above appears capable of rationalizing the observation that the anisotropy decay is faster than the spectral relaxations. With σ = 200 cm^{-1}, electronic dephasing causes a large decrease in the calculated anisotropy (Fig. 26), whereas the relaxations of the overall signal occur mainly during thermalization (Fig. 26). This is because the two most strongly allowed exciton states tend to be close together in energy and to have approximately orthogonal transition dipoles; dephasing and equilibration of these states contributes strongly to the decay of the emission anisotropy, but has relatively little effect on the emission amplitude or wavelength. Dephasing is expected to occur rapidly as a result of both static inhomogeneity and fluctuations of the exciton energies, in addition to population decays.

The calculated differences between the emission strengths of LH2 ensembles with coherent, incoherent, or thermalized excitations can be expressed conveniently by the function L_e as defined in eqs. 8 and 9. L_e gives the isotropic emission strength, integrated over the emission spectrum, relative to the absorption strength of monomeric BChl in solution. It is similar to the "superradiance enhancement factor" (L_s) used by Mukamel and coworkers,(*115, 117*) but is defined in an averaged exciton basis rather than the site (individual BChl) basis and includes an explicit

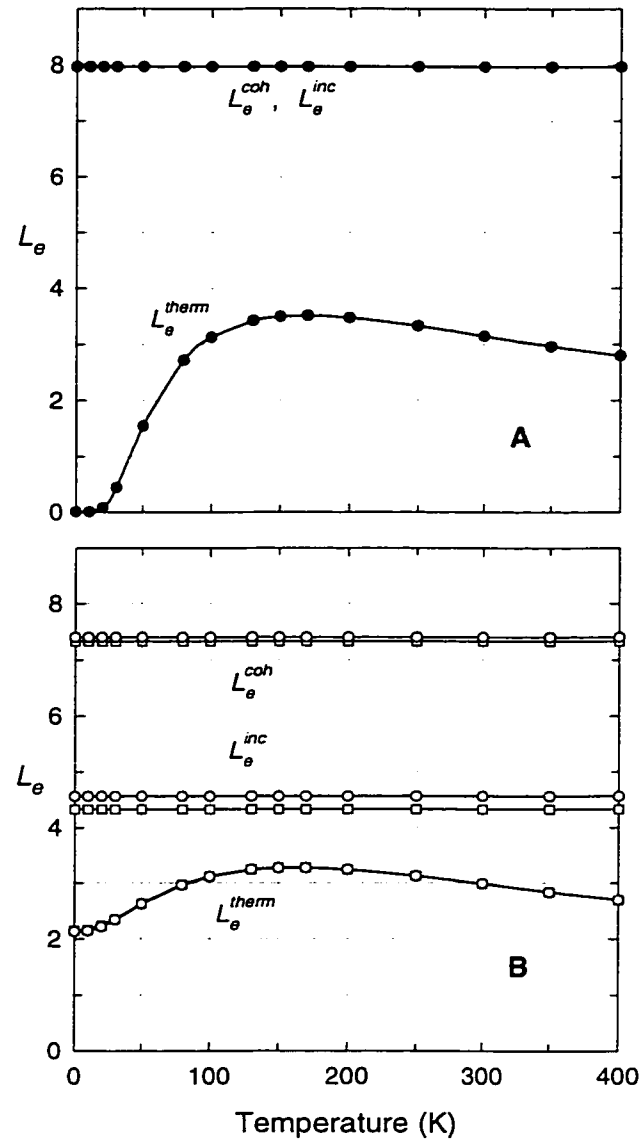

Figure 28. Calculated L_e^{coh}, L_e^{inc} and L_e^{therm} (*A*) for a homogeneous ensemble of LH2 complexes ($\sigma = 0$), and (*B*) for an inhomogeneous ensemble ($\sigma = 200$) with blue (□) or red (○) excitation.

dependence on the excitation pulse. Figure 28 shows the calculated L_e as a function of temperature for coherently excited, incoherently excited, and thermalized ensembles. Values are given for both homogeneous and inhomogeneous ensembles (σ = 0 or 200 cm^{-1}). With excitation pulses on either side of the absorption band, L_e for the coherently-excited inhomogeneous ensemble (L_e^{coh}) is approximately 8. L_e decreases to about 4.5 as the excitation dephases (L_e^{inc}), and to approximately 3 after thermalization at 295 K (L_e^{therm}). L_e^{therm} increases slightly with decreasing temperature down to 150 K, and then decreases to 2.1 at 0 K. The temperature dependence thus is relatively weak, in agreement with previous calculations by Zhang et al.(*117*) and with the fluorescence measurements described by Monshouwer et al.(*119*) The calculated variation of L_e^{therm} with temperature is reduced further if the distribution of monomer transition energies is broadened by using σ = 300 cm^{-1} (not shown). In a homogeneous ensemble of LH2 complexes, L_e^{therm} drops almost to zero at low temperatures (Fig. 22*A*).

The L_e^{therm} of 3 calculated for the inhomogeneous ensemble at 295 K agrees well with experimental measurements of the radiative rate constant (*119, 134*). L_e^{inc} and L_e^{therm} both would reduce to 1 if the electronic coupling between the BChls were removed. However, an L_e^{therm} of 3 does not imply that the excitation is localized on approximately 3 BChls, as has been suggested, (*119, 134*) because the expected value of L_e^{therm} depends on the geometry of the complex. A homogeneous ensemble of LH2 complexes, in which the lowest exciton state is distributed almost uniformly around the ring and the two allowed states have approximately equal lobes of excitation density on opposite sides of the ring,(*39, 111*) gives an L_e^{therm} that is only slightly larger than 3 at 295 K (Fig. 28*A*).

At room temperature, L_e^{coh} provides a clearer distinction between homogeneous and inhomogeneous ensembles. In the homogeneous ensemble L_e^{coh} is essentially the same as L_e^{inc}; in the inhomogeneous ensemble they differ by about a factor of 2 (see Fig. 28). This is because the transition dipoles of the two allowed exciton transitions in a homogeneous ensemble are close to perpendicular, so that the terms $(\vec{\mu}_a \cdot \vec{\mu}_b)^2$ in eq. 9*a* vanish except when $a = b$.

Previous workers have used a variety of other functions to describe the extent of exciton localization in the LH2 complex. Kühn and Sundström(*116*) used the function

$$c_n(t) = \sum_i \left| \left\langle \rho^s_{i,i+n}(t) \right\rangle_E \right|, \quad (14)$$

which expresses the average correlation between the excited-state wavefunctions of BChls i and $i + n$. Here $\boldsymbol{\rho}^{\mathbf{s}}$ is the reduced density matrix in the site representation ($\rho^s_{i,i+n}(t) = \sum_a \sum_b C^a_i C^a_{i+n} \rho_{a,b}(t)$). The coherent and thermalized excitations in our model give values of c_n similar to the values that Kühn and Sundström calculated for short and long times, respectively. Like L_e, c_n is a property of an ensemble. Even after thermalization, each individual complex still can be described well as being in an exciton state that is a property of the entire ring, although the electron distributions in these states vary from complex to complex.

The calculated spectra shown in Figs. 25 and 27 differ from the measured spectra (Figs. 20 and 21) in the breadth of the stimulated emission. The experimental spectra have a more pronounced tail at long wavelengths (see Figures 20 and 21). A comparison of the spectra calculated by Kühn and Sundström(*116*) with spectra measured by Chachisvilis et al.(*133*) shows a similar discrepancy (see Figure 2 in ref. 13). The discrepancy also appears in the calculations by Alden et al.,(*111*) where the energy difference between the main absorption peak and the low-energy shoulder is

about half the difference measured by hole-burning (*65*). The width of the calculated emission spectrum can be increased by broadening the distribution of monomer transition energies (with some degradation of the calculated anisotropies), or by using a larger homogeneous linewidth. Wu et al.(*118*) have shown that agreement between the calculated and observed ground-state spectra can be improved by introducing distortions with E_t symmetry in place of the Gaussian disorder used here and by Alden et al. and Kühn and Sundström.

Discrepancies between the calculated and measured spectra of stimulated emission could arise from the neglect of vibrational relaxations in the calculations (process *c* above). However, hole-burning studies(*65*) indicate that electron-phonon coupling in the LH2 complex is relatively weak, which implies that vibrational contributions to the Stokes shift probably are small compared to electronic relaxations. In addition, observations of vibrational coherences persisting for several picoseconds(*133*) indicate that vibrational relaxations probably are unimportant on the short time scale probed in the present experiments.

Chachisvilis and Sundström(*135*) have shown that coherences between the ground state and doubly-excited states can cause wavelength-dependent transients in the anisotropy signals if the transition dipoles for ground-state absorption and excited-state absorption are not parallel. Although coherences involving two-exciton states will need to be considered if the theoretical model used here is to be made more complete, our experimental results provide no clear evidence for such coherences because the initial anisotropy values are relatively insensitive to wavelength.

It is pertinent to ask whether the spectral relaxations could be explained as well by stochastic energy transfer between BChl dimers or other small clusters of pigments (process *d* above). In principle, absorption of light could generate localized excitations directly if the exciton coupling is less than the dispersion of the site energies or the homogeneous width of the absorption. The homogeneous width of the B850 transitions

can be estimated from the values of T_2 obtained by fitting the PFID signals (Fig. 28 and Table 5). Fits of the isotropic signals at 830, 850 or 860 nm following broadband excitation gave T_2 • 20 fs, corresponding to a Lorentzian distribution with a FWHM of approximately 250 cm^{-1}. This is a maximum estimate of the homogeneous width because it neglects dephasing due to static inhomogeneity. From measurements of stimulated photon echoes, Jimenez et al.(*44*) have suggested that the homogeneous distribution is Gaussian and has a FWHM of 190 cm^{-1}. In the calculations shown in Figures 26-28 we used Lorentzian lineshapes with a FWHM of 250 cm^{-1}. For comparison, the coupling strength between neighboring pigments is calculated to be on the order of 200 to 400 cm^{-1} (*39, 111, 136*). The electronic coupling thus probably is at least as strong as the electron-phonon coupling, which means that the time constant for incoherent excitation transfer would be comparable to the coherence decay time. Energy transfer in B850 cannot, therefore, be truly incoherent. Still, to the extent that inhomogeneity of the monomer transition energies causes the exciton states to localize, fluctuations of these energies would result in stochastic hopping from one site to another, which could cause the spectroscopic properties to change with time.

Stochastic energy transfer would cause the GSB, SE and ESA all to shift in the same direction. Excitation on the blue side of the band would be followed by spectral shifts to the red and *vice versa*. Although the observed signals do shift to longer wavelengths with time following blue excitation, excitation on the red side is followed by a decrease in amplitude throughout the spectrum but little or no shift (Figs. 20 and 21). It is not clear how incoherent hopping of excitations among discrete sites could cause the signals to decrease in amplitude without shifting. In principle, a red shift of the emission associated with vibrational relaxation could mask a blue shift associated with incoherent energy transfer. However, to account for the time-dependent decrease in the amplitudes of SE and ESA, we would have to postulate that the dipole strengths of the BChl dimers vary from site to site in a manner that correlates with the transition energies. This seems inconsistent with the observation that similar decreases in the

signal amplitudes occur when the system is excited on opposite sides of the B850 absorption band.

Conclusions

We have made several experimental observations: The shapes of the light-induced difference spectra measured immediately following excitation of B850 antenna complexes depend on the excitation wavelength. The differences are mostly erased by a kinetic step with a time constant of 100 ± 20 fs. The signals have an initial anisotropy in the range 0.3 to 0.5, depending on the excitation pulse width; the anisotropy decreases to ~ 0.1 with a time constant of about 30 fs. The anisotropy is relatively independent of the detection wavelength. Starting with the B850 pigments in the crystal structure of the LH2 antenna complex, we have calculated the ground-state absorption spectra for ensembles of LH2 complexes with Gaussian distributions of monomer transition energies, and have used a density-matrix treatment to calculate the light-induced changes in absorption and emission. Spectra were calculated for three idealized conditions: a coherent superposition of exciton states created by tunable broadband excitation, an incoherent mixture of exciton states with the same populations, and a Boltzmann distribution of exciton states within each complex. The calculated initial difference spectra depend markedly on the excitation wavelength, and the thermalized spectra less so, both in agreement with experimental results. The calculated anisotropies are comparatively insensitive to the detection wavelength. The anisotropy decay is particularly sensitive to the loss of coherence, suggesting that the different time constants for the decay of anisotropy and spectral relaxation primarily reflect dephasing and thermalization, respectively.

Appendix.

The transition dipoles in eqs. 1-6 are:

$$\bar{\mu}_a = \sum_{i=1}^{N} C_i^a \bar{\mu}_i^m , \quad \text{(A1)}$$

$$\bar{\mu}_{a\eta} = \sum_{j=1}^{N} \sum_{k1=1}^{N} \sum_{k2=k1}^{N} C_j^a C_{k1,k2}^{\eta} \left\{ \delta_{k1,k2}\delta_{j,k1}\phi\bar{\mu}_j^m + \left(1-\delta_{k1,k2}\right)\left(\delta_{j,k1}\bar{\mu}_{k2}^m + \delta_{j,k2}\bar{\mu}_{k1}^m\right)\right\}, \quad \text{(A2)}$$

where $\bar{\mu}_i^m$ is the transition dipole of BChl monomer i, C_i^a is the coefficient for excitation of BChl i in one-exciton eigenstate a, $C_{k1,k2}^{\eta}$ is the coefficient for excitation of BChls $k1$ and $k2$ in two-exciton eigenstate η, ϕ is the ratio of the magnitudes of the transition dipoles for the second and first excitations of an individual BChl, and the sums run over the 18 BChls.

The orientational averages are:

$$\left\langle (\hat{x}\cdot\hat{\mu}_a)^2 (\hat{x}\cdot\hat{\mu}_b)^2 \right\rangle_O = \left(1+2\cos^2\xi_a^b\right)/15 , \quad \text{(A3)}$$

$$\left\langle (\hat{x}\cdot\hat{\mu}_a)^2 (\hat{y}\cdot\hat{\mu}_b)^2 \right\rangle_O = \left(2-\cos^2\xi_a^b\right)/15 , \quad \text{(A4)}$$

$$\left\langle (\hat{x}\cdot\hat{\mu}_a)(\hat{x}\cdot\hat{\mu}_b)(\hat{y}\cdot\hat{\mu}_a)(\hat{y}\cdot\hat{\mu}_b) \right\rangle_O = \left(3\cos^2\xi_a^b - 1\right)/30 , \quad \text{(A5)}$$

$$\left\langle (\hat{x}\cdot\hat{\mu}_a)(\hat{x}\cdot\hat{\mu}_b)(\hat{x}\cdot\hat{\mu}_{a\eta})(\hat{x}\cdot\hat{\mu}_{b\eta}) \right\rangle_O =$$

$$\frac{1}{15}\left\{\cos\xi_a^b\cos\xi_{a\eta}^{b\eta} + \cos\xi_b^{b\eta}\cos\xi_a^{a\eta} + \cos\xi_a^{b\eta}\cos\xi_b^{a\eta}\right\}, \quad \text{(A6)}$$

and $\left\langle (\hat{x}\cdot\hat{\mu}_a)(\hat{x}\cdot\hat{\mu}_b)(\hat{y}\cdot\hat{\mu}_{a\eta})(\hat{y}\cdot\hat{\mu}_{b\eta}) \right\rangle_O =$

$$\frac{2}{15}\left\{\cos\xi_a^b\cos\xi_{a\eta}^{b\eta}\right\} - \frac{1}{30}\left\{\cos\xi_a^{a\eta}\cos\xi_b^{b\eta} + \cos\xi_a^{b\eta}\cos\xi_b^{a\eta}\right\}, \qquad \text{(A7)}$$

where ξ_a^b is the angle between $\hat{\mu}_a$ and $\hat{\mu}_b$.

CHAPTER 4: INVESTIGATION OF ELECTROSTATIC INTERACTIONS IN AN INTEGRAL MEMBRANE PROTEIN

The dielectric screening that determines the strength of interaction between two charged or polar species in a protein is a complicated function of the protein structure and the solvent. Because most globular proteins fold with hydrophobic amino acid residues inside and ionizable residues on the surface, it frequently is suggested that the protein interior has a low dielectric constant on the order of 4 (*137*). However, experimental work even twenty years ago indicated that the dielectric screening of charged groups in proteins often is much stronger than this. Early measurments of the shifts of the midpoint reduction potential (E_m) in a series of cytochrome c derivatives with chemically modified lysine residues demonstrated that the effective dielectric screening factor for surface groups was approximately 50 (*138*). In a more recent study, Zhou and Swenson examined the interactions of a partially buried flavin group with six Glu and Asp residues in a flavodoxin (*139*). All the ionizable groups were on the protein surface, and were within 13 Å of N1 of the flavin. Replacing one of the Glu or Asp residues by a nonionizable amino acid raised the E_m of the $FMNH^-/FMNH^\bullet$ couple by an average of only about 15 mV per unit change in charge. In this case, the effective dielectric screening factor was in the range of 50 to 100, depending on the location of the charged residue.

Lockhart et al. (*140*) have examined the effects of permanent charges and dipoles on the pK_as of ionizable residues in helical model peptides. They found that long-range interactions with permanent charges were strongly screened, and they concluded that the pK_as of ionizable residues were determined mainly by dipolar interactions with the helical backbone. Similarly, Forsyth et al. (*141*) have described the effects of a particular Lys residue on the pK_as of several Asp and Glu residues in turkey ovomucoid

third domain. Previous calculations (*142*) had suggested that the pK_as of these residues were sensitive to interactions with the Lys; however, replacing the Lys by Thr or Glu had little or no measurable effect on the pK_a of any of the acidic acids.

Complementary studies have shown that buried ionizable amino acids can be charged. The arabinose binding protein, for example, has a charged Arg that is not accessible to solvent but is stabilized through hydrogen bonds (*143*). Lysozyme has an ionized Asp that is stabilized similarly (*144, 145*). Hydrogen bonds also appear to stabilize the buried chromophore of the photoactive yellow protein in a charged state (*146*). Localized dipoles near the ends of alpha helices stabilize charged groups in barnase and a sulfate-binding protein (*147*). Mutation of a Val to Asp or Glu adjacent to the heme in myoglobin leads to an ionized amino acid that is stabilized by the positive charge on the heme iron and shifts the E_m of the heme by about -200 mV (*148, 149*). Garcia-Moreno et al. have inserted either a Lys or Glu into the hydrophobic core of a nuclease and determined the pK_a of the buried group from difference potentiometry and measurements of protein stability (*150, 151*). The ionized residues did not unfold the protein and appeared to be stabilized by interactions with protein dipoles and water molecules. Thus, proteins evidently can solvate buried charges effectively through dipolar interactions.

Attempts to calculate the energies of electrostatic interactions in proteins have met with mixed success. There are two main applications for such electrostatics calculations. The first is to calculate the self-energy of a system, defined as the solvation free energy of a group of atoms (e.g., a bound cofactor or the reacting functional groups at one step of an enzymatic reaction) in the absence of interactions with other charged groups. The second application is to evaluate the electrostatic interactions between separate charged groups. Warshel and his coworkers have noted that semi-macroscopic calculations require a larger effective dielectric constant for interactions of charged groups than for self-energies (*152-154*). They argue that the use of a macroscopic dielectric constant (ε) with any value other than 1 simply compensates

for factors that are not treated explicitly. A treatment that does not consider structural relaxations, for example, usually requires a larger dielectric constant than one that allows the structure to fluctuate. However, calculations of the self energies of charged groups in proteins appear to have become reasonably accurate, even though the dielectric constant used for the protein interior (ε_{in}) may have no simple physical interpretation (*154-158*). Using free energy perturbation techniques, Cutler et al. (*159*) were able to account well for the effect of an Arg to Leu mutation on the pK_a of a heme propionate group in cytochrome c. Fersht et al. (*160-162*) have studied surface charge-charge interactions in barnase and subtilisin by constructing a series of basic mutations and measuring the change in the pK_a of a histidine residue. The histidine and the sites of the mutations were on the protein surface and the measured interaction energies were small (0.3 to 0.5 kcal/mol for groups separated by 12 to 17 Å). In this case, the experimental results were reproduced well by continuum electrostatics calculations with a value of 2 for ε_{in} and a dielectric constant of 80 for the solvent (ε_{out}) (*162*). Antosiewicz et al (*163*), however, found that calculations of the pK_as of ionizable residues in a large group of proteins required a much higher value of ε_{in}. The best fit to the data was obtained by setting $\varepsilon_{in} \approx 20$ for both self-energies and charge-charge interactions, suggesting that significant components are missing from the analysis.

Recently, there has been much effort to include protein relaxations into electrostatics calculations. Sham et al. (*152*) have evaluated the effects of relaxations by calculating the interaction energies of pairs of ionizable residues during molecular dynamics trajectories in the charged and uncharged states and comparing the results to those of calculations with the unrelaxed crystallographic structure. Alexov et al. (*155, 164*) used a Monte Carlo procedure that considered many configurations of the polar hydrogens. These workers also considered the variation of heavy-atom positions in families of crystal structures for the same protein. Nielsen et al. (*165*) emphasized the effects of hydrogen-bonding networks and of flipping amino acid side chains.

Most of the studies cited above have involved water-soluble proteins. The photosynthetic reaction center (RC) of *Rhodobacter sphaeroides* provides an excellent model for studying electrostatic interactions in the interior of an integral membrane protein. The RC contains two homologous polypeptides (L and M), each of which has 5 transmembrane α-helices, a third polypeptide (H) with one transmembrane helix, 4 bacteriochlorophylls (P_L, P_M, B_L and B_M), 2 bacteriopheophytins (H_L and H_M) and 2 quinones (Q_A and Q_B) (see (*7*) for a review). Two of the bacteriochlorophylls (P_L and P_M) form a strongly interacting dimer (P) that releases an electron when the RC is excited with light. The electron moves to one of the quinones (Q_A) by way of B_L and H_L. The rapid kinetics and high specificity of the electron-transfer reactions depend in part on the relative energies of the excited state (P*) and charge-separated states such as $P^+B_L^-$ and $P^+B_M^-$. It has been suggested that long-range electrostatic interactions with charged residues poise the energies of these states such that electron transfer to B_L and H_L is more favorable than transfer to B_M and H_M (*32*). Other studies, however, have suggested that the interactions of the electron carriers with ionizable residues are strongly screened and make only minor contributions to the energies (*31*).

Electrostatic interactions with the protein would be expected to play a role in determining the E_m of the P/P^+ couple and the energies of charge-transfer states such as $P_L^+P_M^-$, which influence the spectroscopic properties of the RC. Williams, Allen and coworkers have described an extensive series of mutations that introduce or remove hydrogen bonds to the acetyl and keto groups of P_L and P_M (*23, 166-168*). Each hydrogen bond raises the E_m of P by 50 to 100 mV. The effects are additive, and double and triple mutants are able to alter the redox properties of the dimer significantly. However, the effects of such mutations can not necessarily be attributed purely to electrostatic interactions. Changes in hydrogen bonding could alter the molecular orbitals of P_L and P_M or cause small shifts in the positions of the molecules, either of which could affect the E_m through changes in the resonance interactions of the two bacteriochlorophylls.

In the current work, we have mutated a series of ionizable residues that are close enough to P to affect its electrostatic potential, but sufficiently far away so that the mutations are unlikely to cause major changes in the positions or molecular orbitals of the bacteriochlorophylls. Most of the mutation sites are largely buried in the protein. Changing the charges at these sites stabilizes or destabilizes P^+ relative to P, as measured by shifts in the E_m of P/P^+. The changes in the E_m are compared to the effects predicted by several different computational approaches, and the merits of these methods are discussed.

Methods

Construction and Purification of mutant RCs. Oligonucleotide-mediated site-directed mutagenesis was accomplished with the Chameleon Kit (Stratagene) for the initial mutations of Leu and Glu at both R(L135) and R(M164) and the Quikchange Kit (Stratagene) for the balance of the mutations. The mutagenesis was performed in puc18 or puc19 vectors containing portions of the L or M subunits, following methods developed by Williams et al. (*166, 169, 170*). After transformation into *Escherichia coli* strain DH5α cells and purification of the mutated plasmid DNA, the regions containing the mutations were subcloned into the *puc* operon. The R(M164) mutations were cloned into the pRKSCH vector (*170*). The R(L135), D(L155), Y(L164) and C(L247) mutations were cloned into the pRKSCH/pHis vector, which contains a tail of seven histidine residues at the carboxyl terminal of the M-subunit (*171*). The plasmids were transformed into the *E. coli* strain S-17 and conjugated with ΔLM1.1, a *Rb. sphaeroides* strain that has the RC deleted (*169*). DNA from the mutant RC-complemented ΔLM1.1 strains was purified and sequenced to ensure that the mutations had been introduced correctly.

Wild-type and mutant *Rb. sphaeroides* strains were grown semi-aerobically in rich media for 3-5 days in the dark (*169*). RCs from the R(M164) mutants were isolated by standard procedures (*172, 173*) with minor modifications. The solubilization of the RCs was achieved with 0.65% N,N-dimethyldodecylamine-N-oxide (LDAO, Fluka), a slightly lower concentration than the 1.2% used by Feher and Okamura (*172*), and after ultracentrifugation the supernatant was brought to 1% LDAO and 30% NH_4SO_4 (wt./vol) to precipitate the RCs. The Celite step was omitted and the solubilized floating pellet was dialyzed to remove salts and loaded onto a DEAE column. The RCs were eluted with a gradient of 0.03 M to 0.25 M NaCl. RCs from the R(L135), D(L155), Y(L164) and C(L247) mutations were isolated using a protocol that exploited the histidine tag (*171*), and were purified further by chromatography on DEAE-sepharose (Bio-Rad). The purified RCs were dialyzed against 15 mM Tris HCl pH 8, 0.025% LDAO, and 1 mM EDTA and concentrated to an OD_{800} of 40 in a 1 cm cuvette using an Amicon pressure cell or a Centricon-50 filter device. The purity of the sample was measured by the ratio OD_{800}/OD_{280} and typically was between 1.4 and 1.8.

Redox Potential Measurements. The P/P^+ midpoint redox potential (E_m) was measured with an electrochemical cell essentially as described by Nagarajan et al. (*34*). The gold-mesh working electrode had 333 lines/inch and was modified with 4,4'-dithiodipyridine. The RCs were suspended in 20 mM Tris pH 8, 0.1% LDAO, 1 mM EDTA, 60 mM KCl, with 0.25 mM K^+ ferrocyanide and 0.15 mM K^+ tetracyanomono-(1,10-phenanthroline)-ferrate(II) tetrahydrate as redox mediators. The absorbance of P at the peak of the long-wavelength absorption band (865 nm for wild-type RCs, but shorter wavelengths for some of the mutants) was monitored as a function of the applied potential. The curves were fit to the one-electron Nernst equation:

$$[P]/[P^+] = (A - A_{ox})/(A_{red} - A) = \exp\{0.03894(E_m - E)\}, \quad (1)$$

where A, A_{ox} and A_{red} are, respectively, the absorbance measured at potential E and at potentials well above and well below the E_m. The E_m of wild-type RCs was measured

along with each measurement on a mutant strain, and the shift of the E_m in the mutant was referenced to the wild-type E_m. Oxidative and reductive titrations were fit separately and averaged, and the shifts quoted below for a given mutant are the mean of between 3 and 5 measurements. Potentials are given in mV relative to the hydrogen electrode at pH 7.0.

Models for Electrostatics Calculations. Assuming that the mutation does not affect the gas-phase (molecular orbital) energy difference between P^+ and P, the change in E_m caused by a mutation (ΔE_m) should be proportional to the change in ΔG_{sol}, the difference between the free energies of solvation of P^+ and P by the surrounding protein, water and electrolytes ($\Delta G_{sol} = G_{sol}^{P^+} - G_{sol}^{P}$):

$$\Delta E_m = -\frac{1}{n\mathrm{F}}\Delta\left\{G_{sol}^{P^+} - G_{sol}^{P}\right\} \equiv -\frac{1}{n\mathrm{F}}\Delta\Delta G_{sol}, \quad (2)$$

where F is the Faraday constant (23.06 kcal mol^{-1} V^{-1}) and $n = 1$. We calculated $\Delta\Delta G_{sol}$ by several different approaches, using structural models based on the crystal structure of *Rb. sphaeroides* RCs as described by Ermler et al. (*19*) (Protein Data Bank (*174*) file 1PCR.PDB). Mutations were introduced by replacing the side chain of the wild-type residue starting with C_γ, using a Monte-Carlo procedure to minimize the torsional, electrostatic, and van der Waals energies of the new side chain (*175*). The polar hydrogens of the 108 serine, threonine and tyrosine residues and the 158 crystallographic water molecules (a total of 424 rotatable hydrogens) were oriented initially to optimize the networks of hydrogen bonds, and then were rotated to minimize the total electrostatic, van der Waals and torsional energy of the model. The latter minimization was done by a Metropolis Monte-Carlo, simulated-annealing procedure, in which the temperature was decreased from 1000 to 10 K in 20 steps; 8480 (20x424) random moves were made at each step.

The simulated-annealing procedure was carried out 5 times for each oxidation state of P (P and P^+) in order to generate separate sets of low-energy conformations for the two oxidation states of each structural model. We then evaluated ΔG_{sol} with the linear-response approximation (LRA) (*176*) (*177*):

$$\Delta G_{sol} = \tfrac{1}{2}\left\{\langle \Delta V_{sol} \rangle_P + \langle \Delta V_{sol} \rangle_{P^+}\right\}, \quad (3)$$

where ΔV_{sol} is the difference between the calculated solvation energies of P^+ and P $\left(\Delta V_{sol} = V_{sol}^{P^+} - V_{sol}^{P}\right)$ and $\langle \cdots \rangle_i$ denotes the mean of the values calculated with the structure optimized for electronic state *i*. The LRA incorporates a major component of the dipolar reorganization of the protein in response to a change in the charge on P. ΔV_{sol} was calculated by a variety of approaches as described below.

The atomic charges for the protein are described by Lee et al. (*178*) and the atomic charges of the bacteriochlorophylls and bacteriopheophytins were obtained by the program QCFF/PI (*179*) and were the same as those used in previous calculations of spectroscopic properties of P^+ (*180*). Because the charges are spread over large π-electron systems and all the mutation sites are at least 8 Å from the centers of P_L and P_M, the calculated solvation energies do not depend stongly on the details of the intramolecular charge distribution (*181*). The calculated effects of the mutations did, however, depend to some extent on the division of the net positive charge of P^+ between P_L and P_M. Except where stated otherwise, the net charge was divided equally between the two bacteriochlorophylls.

Equation 2 involves a significant approximation because a complete treatment of the E_m requires considering quantum mechanical electronic and vibronic coupling of P_L and P_M. This can be done by describing P^+ as a linear combination of the basis states $P_L^+P_M$ and $P_LP_M^+$, whose energies are sensitive to mutations of residues near the pigments (*167*) (*168, 182*). The E_m is obtained by diagonalizing the interaction Hamiltonian, in

which the electronic and vibronic coupling factors enter mainly as off-diagonal matrix elements. Calculations of this type, carried out using the formalism described by Gasyna and Schatz (*183*), showed that the changes in the E_m are related predominantly to changes of the basis state energies and are relatively insensitive to the electronic and vibronic coupling factors. The simple treatment expressed by equation 2 thus appears to be an acceptable approximation for our present purposes. The quantum calculations will be presented elsewhere, along with measurements on the ENDOR and FTIR spectra of the mutant RCs (E. T. Johnson, W. W. Parson, F. Müh, W. Lubitz, J. C. Williams, J. P. Allen, J. Breton and E. Nabedryk, unpublished).

PDLD Calculations. The Protein-Dipole Langevin-Dipole (PDLD) method treats dielectric screening by including a self-consistent set of induced dipoles on the non-hydrogen protein atoms and a grid of points representing the surrounding medium (*2, 31, 156*). The total solvation energy for $P \rightarrow P^+$ in structural models relaxed in oxidation state *i* is written

$$\Delta V_{sol} = \Delta V_{Q\mu} + \Delta V_{ind} + \Delta V_{H_2O} + \Delta V_{memb} + \Delta V_{bulk}. \quad (4)$$

Here $\Delta V_{Q\mu}$ ($\Delta V_{Q\mu} \equiv V_{Q\mu}^{P^+} - V_{Q\mu}^{P}$) is the difference between the energies of electrostatic interactions of P and P^+ with the other partial charges of the protein and pigment atoms, calculated with $\varepsilon = 1$, and ΔV_{ind}, ΔV_{H_2O}, ΔV_{memb} and ΔV_{bulk} are, respectively, the corresponding differences in the energy of interactions with induced dipoles in the protein, water, membrane, and the bulk solvent outside the region that is treated microscopically. The protein model for these calculations was trimmed to a 32-Å sphere centered on P, and retained most of the RC (approximately 10,000 atoms).

The induced dipole at any atom or grid point depends on the electric field at that point and on the polarizability of the volume element represented by the point. We set the polarizability of the protein atoms to correspond to the macroscopic polarizability of a homogeneous medium with a dielectric constant of ~2.2 according to the Clausius-

Mosotti equation (*181*). The grid points representing the surrounding medium had a spacing of 2 Å and were divided into water and membrane regions as described by Alden et al. (*31*). In most of the calculations, the membrane region was 25 Å thick and had a polarizability corresponding to a macroscopic dielectric constant of 4, while the water region had a higher polarizability that modeled the low-frequency dielectric behavior of liquid water (*31*). Because the field at any point includes both the static field of the protein atoms and the field from the other induced dipoles, a self-consistent solution was obtained by iteration.

PDLD/S Calculations. The PDLD/S method is a scaled version of PDLD (*178*). Previous work has shown that the induced electronic dipoles of the protein atoms are not sufficient for screening electrostatic interactions, probably in part because they do not reflect dipolar relaxations of the protein (*152*). In PDLD/S, the protein induced dipoles are treated implicitly by introducing an effective dielectric screening factor (ε_{in}) for the interactions with fixed charges of the protein atoms, while the solvent dipoles are evaluated explicitly on a cubic grid as in PDLD. The solvation energy in this model is

$$\Delta V_{sol} = \frac{\Delta V_{Q\mu}}{\varepsilon_{in}} + \left(\Delta V_{H_2O} + \Delta V_{memb} + \Delta V_{bulk}\right)\left(\frac{1}{\varepsilon_{out}} - \frac{1}{\varepsilon_{in}}\right), \quad (5)$$

where ε_{out} is the dielectric constant of the solvent and the other quantities are as in equation 4. For these calculations, we set $\varepsilon_{out} = 80$ and varied ε_{in} between 2 and 20.

Poisson-Boltzmann (DELPHI) Calculations. In the Poisson-Boltzman or discretized-contiuum method, as implemented in the program DELPHI (*184-186*), the protein-solvent system is mapped to a cubic grid with two dielectric regions. The region corresponding to the protein has an adjustable dielectric constant of ε_{in}, and the region corresponding to the solvent usually is given a dielectric constant (ε_{out}) of 80. The reaction field for the protein charges is evaluated by solving linearized Poisson-

Boltzmann equation with the boundary condition that the field from the protein goes to that described by Debye-Huckel theory at large distances. Coulombic interactions between protein atoms ($\Delta V_{Q\mu}$,in our notation, is calculated after the atomic charges have been distributed onto a grid) are screened by ε_{in} as in PDLD/S and the total solvation energy takes the form

$$\Delta V_{sol} = \frac{\Delta V_{Q\mu}}{\varepsilon_{in}} + V_{RF}, \quad (6)$$

where V_{RF} is the energy of interaction of the protein charges with the reaction field. To include a membrane in the discretized-continuum calculations, pseudo-protein atoms with no charges were added to fill a 25-Å region similar to the membrane region described above. This effectively removes solvent from the membrane region and gives this region the same ε_{in} as the protein. The boundary conditions for the potential were treated by using three grids that successively focused down on the protein to a final resolution of 2.4 grid points/Å. The protein filled 20% of the first grid, 85% of the second and 90% of the third. The atomic radii are given by the PARSE dataset (*187*).

Calculations Using Distance-dependent Screening Factors. In these calculations, charge-charge interactions between atoms *i* and *j* are screened by an empirical function of the interatomic distance $\left(f_{ij}(r_{ij})\right)$. The difference in solvation energies between P* and P becomes simply

$$\Delta V_{sol} = \sum_{i}^{atoms\ of\ P} \left(Q_i^{P^*} - Q_i^{P}\right) \sum_{j}^{other\ atoms} \frac{q_j}{f_{ij} r_{ij}}, \quad (7)$$

where Q_i and q_j are the partial charges on atom *i* of P_L or P_M and atom *j* of the protein or a crystallographic water and r_{ij} is the distance between atoms *i* and *j*. The entire protein was included in these calculations.

Several different expressions for f_{ij} were considered. The expression introduced by Warshel et al. (*54*) for modeling shifts of E_m and pK_a values has an exponential dependence on distance:

$$f_{ij} = 1 + 60\left(1 - e^{-\eta r_{ij}}\right), \quad (8)$$

where η is an empirical factor in the range of 0.10 to 0.18. We also tried a simple linear dependence on distance, $f_{ij} = r_{ij}$, and a sigmoidal dependence of the form (*188-190*)

$$f_{ij} = \varepsilon_{out} - \frac{\varepsilon_{out}}{2}\left[(r_{ij}s)^2 + 2r_{ij}s + 2\right] e^{-r_{ij}s}, \quad (9)$$

with $\varepsilon_{out} = 78$ and s (a sigmoidicity parameter) = 0.3.

Molecular Dynamics (MD) Simulations. To examine possible effects of protein backbone reorganization on the E_m of P/P^+, we carried out MD simulations using a slightly modified version of the program ENZYMIX (*178, 191*). The crystal structure was trimmed to a 25 Å radius around the point midway between P and the ionizable group of the mutated residue, and unconstrained motions were allowed within 18 Å of this point. Atoms in the shell between 18 and 25 Å were constrained to their crystallographic coordinates, but were included in the electrostatics calculations. ΔV_{sol} was calculated during the dynamics essentially by equation 4, except that no membrane was included in this model and the Langevin dipoles were replaced by explicit water molecules. Waters were added as needed to fill the region with a radius of 20 Å and were modeled by the surface-constrained-all-atom-solvent (SCAAS) treatment (*192*). The Local Reaction Field method (*193*) with no distance cutoff was used to evaluate all charge-charge interactions.

Separate MD simulations were propagated on the potential surfaces of P and P^+, with the charge of P^+ distributed equally between P_L and P_M. The structural model for each mutant was equilibrated during a 25-ps preliminary trajectory with P in a given

state, and ΔV_{sol} then was recorded every 10 fs during a 100-ps trajectory with time steps of 1 fs. ΔG_{sol} was calculated from $\langle \Delta V_{sol} \rangle_P$ and $\langle \Delta V_{sol} \rangle_{P^*}$ by the LRA expression (equation 3). The MD calculations also provide the reorganization energy by the expression (*176*)

$$\lambda = \tfrac{1}{2}\left\{\left|\langle \Delta V_{sol} \rangle_P - \langle \Delta V_{sol} \rangle_{P^*}\right|\right\}. \quad (10)$$

Effects of counterions in the MD simulations were examined by including a single Na^+ or Cl^- ion in the water near the charged amino acid, so as to make the net charge of the system zero when P was in its reduced state. No additional counterion was added for P^+. One would expect a counterion for P^+ to have similar effects in the wild-type and mutant RCs, and so to make only small contributions to ΔE_m. However, because P is relatively far from the solvent-accessible surface of the protein, it provides little constraint on the location of a counterion in the solvent, and very long MD trajectories would be required in order for the solvation energy of the counterion to converge. For trajectories of the length used here (100 ps), the fluctuations of this solvation energy are large relative to the energy differences of interest. Molecular-dynamics simulations of the L(247) mutations were not stable, again suggesting that the trajectories were too short to reorganize the counterion and surrounding protein around a completely buried charge.

Results

Mutation Sites. Figure 29 shows the locations of the five residues we mutated to explore long-range electrostatic interactions of the protein with P. Arginines L135 and M164 are homologous residues of the L and M subunits, and are almost symmetrically positioned on either side of P. The C_ζ atom of R(L135) is 12.2 Å from the Mg of P_L and 19.5 Å from the Mg of P_M, while C_ζ of R(M164) is 13.8 Å from the Mg of P_M and 21.0 Å from that of P_M. Although the arginines are located near the periplasmic surface of the RC, their side chains are almost completely buried. The sum of the solvent-accessible surface areas (*194*) for the guanidinium NH1 and NH2 nitrogens of R(L135) is 5.3 $Å^2$, and that for R(M164) is only 0.1 $Å^2$. In a fully exposed side chain, these atoms would have a total solvent-accessible surface of approximately 75 $Å^2$. R(L135) and R(M164) are located one turn from the carboxyl end of a transmembrane α-helix, which could stabilize a positive charge on the side chains. The charge on R(L135) also could be stabilized by hydrogen bonds to Y(L164) and a crystallographic water, while R(M164) could form a salt bridge with E(M173). In addition, there are small pockets on the protein surface that could allow a counterion to sit close to the guanidinium group of each arginine. The guanidinium groups also are close to, but not within hydrogen-bonding distance of the keto oxygen atom of either P_L or P_M: these distances are 7.3 Å for R(L135) and P_L and 9.2 Å for R(M164) and P_M.

The carboxyl group of Asp (L155) is located approximately 14 Å from the Mg atoms of P_L and P_M. This residue is well exposed to the solvent, giving the γ carboxyl group 45 $Å^2$ of accessible surface. The sulfur of Cys (L247) is 6.5 Å from the Mg of P_L and is completely inaccessible to the solvent.

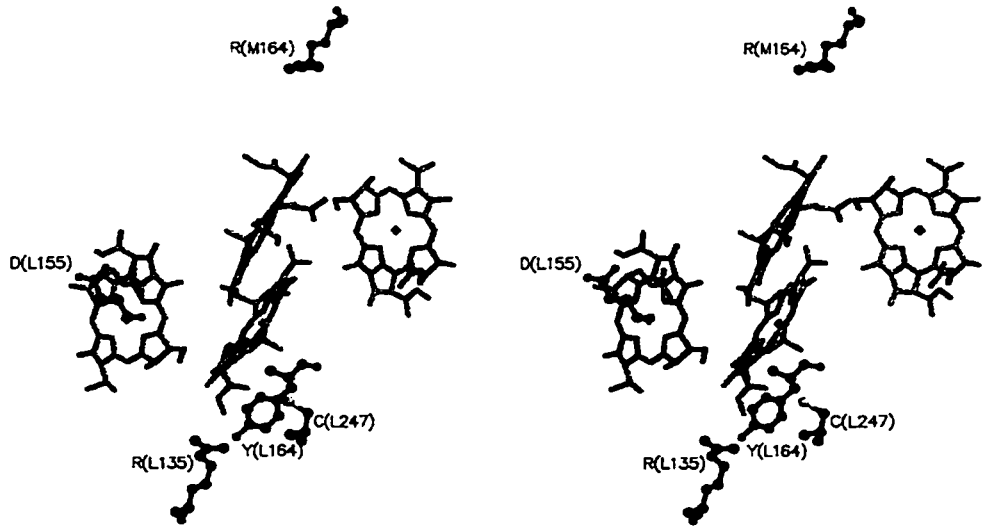

Figure 29. Stereo view of the bacteriochlorophylls and the mutation sites in the photosynthetic reaction center of *Rb. sphaeroides* (*43*). The phytol side chains of the bacteriochlorophylls are removed for clarity. The view is approximately along the C_2 pseudosymmetry axis. The figure was prepared with Molscript (*76*) and Raster3D (*77*).

Table 7. Measured Shifts in the E_m of P/P$^+$ in Mutant RCs and the Shifts Calculated by PDLD and DELPHI with the Linear Response Approximation [a]

Strain	ΔE_m^{expt}	ΔE_m^{calc} (PDLD) [b]	ΔE_m^{calc} (DELPHI) [c]
R(L135)K	- 3	-6	+10
R(L135)L	-20	-98	-101
R(L135)Q	-24	-128	-121
R(L135)E	-37	-194	-238
D(L155)N	+12	+100	+81
Y(L164)F	+2	-58	-41
R(M164)L	-16	-56	-114
R(M164)E	-32	-147	-261
C(L247)K	+51	+332	+341
C(L247)D	-40	-346	-315
R(L135)E/C(L247)K	+8	+291	+211

[a] ΔE_m^{expt} and ΔE_m^{calc} are the measured and calculated shifts of the E_m in mV, relative to wild-type RCs. Each ΔE_m^{expt} is an average of 3 to 5 measurements and has a standard error of the mean (SEM) of approximately ±5 mV. R, K, E or D at the mutation site is assumed to be charged while all other ionizable groups are neutral. All the models include a membrane with a 25 Å hydrophobic region.

[b] The PDLD calculation of ΔV_{sol} for each structure includes an average over 10 randomly chosen origins for the solvent/membrane grid. The total standard error of the mean (SEM) of ΔE_m^{calc} for each mutant was approximately ±8 mV, including the error associated with choosing the grid origin.

[c] The DELPHI calculation of ΔV_{sol} is for 0 M ionic strength, $\varepsilon_{in} = 4$, and $\varepsilon_{out} = 80$. The SEM of ΔE_m^{calc} for each mutant was approximately ±10 mV.

E_m Values. Figure 30 shows representative redox titrations of P in the mutants of R(L135), and Table 7 gives the measured shifts of the E_m (ΔE_m^{expt}) for all the mutants relative to wild-type RCs. The conservative mutations R(L135)K and Y(L164)F have only marginal effects, shifting the E_m by –3 and +2 mV respectively. The balance of the mutations of Arg (L135) replace a side chain that likely is positively charged by a neutral or negatively charged side chain. These substitutions all lower the E_m: leucine shifts the E_m by –20 mV; glutamine, by –23 mV; and glutamic acid, by –36 mV. The similar effects of leucine and glutamine, which are both neutral but differ in polarity, suggest that the shift results mainly from the loss of the positive charge of the Arg. The slightly larger effect of glutamine, though not statistically significant, could possibly reflect a weak stabilization of P^+ by the dipole of the δ amide group. Glutamic acid shifts the E_m by nearly twice as much as leucine, as would be expected if its δ carboxylic acid group is negatively charged.

Mutations of Arg (M164) to neutral or negatively charged residues also decrease the E_m; however, the shifts are consistently about 4 mV smaller than those caused by homologous mutations of (L135). The Leu and Glu mutations shift the E_m by -16 and -32 mV. This is consistent with the slightly longer distance between Arg (M164) and P (see above), and with earlier evidence that the positive charge of P^+ is distributed unequally between P_L and P_M, with the larger share going to P_L (*173*).

The D(L155)N mutation raises the E_m by 12 mV, consistent with a destabilization of P^+ by removal of a negative charge. Cysteine (L247) also was mutated to lysine and aspartic acid to explore the effects of replacing a neutral residue by a positively or negatively charged amino acid; the C(L247)K mutation increases the E_m by 51 mV and the C(L247)D mutation decreases it by 40 mV. The double mutation R(L135)E/C(L247)K changes the E_m by +8 mV, which is a nearly additive combination of the individual effects.

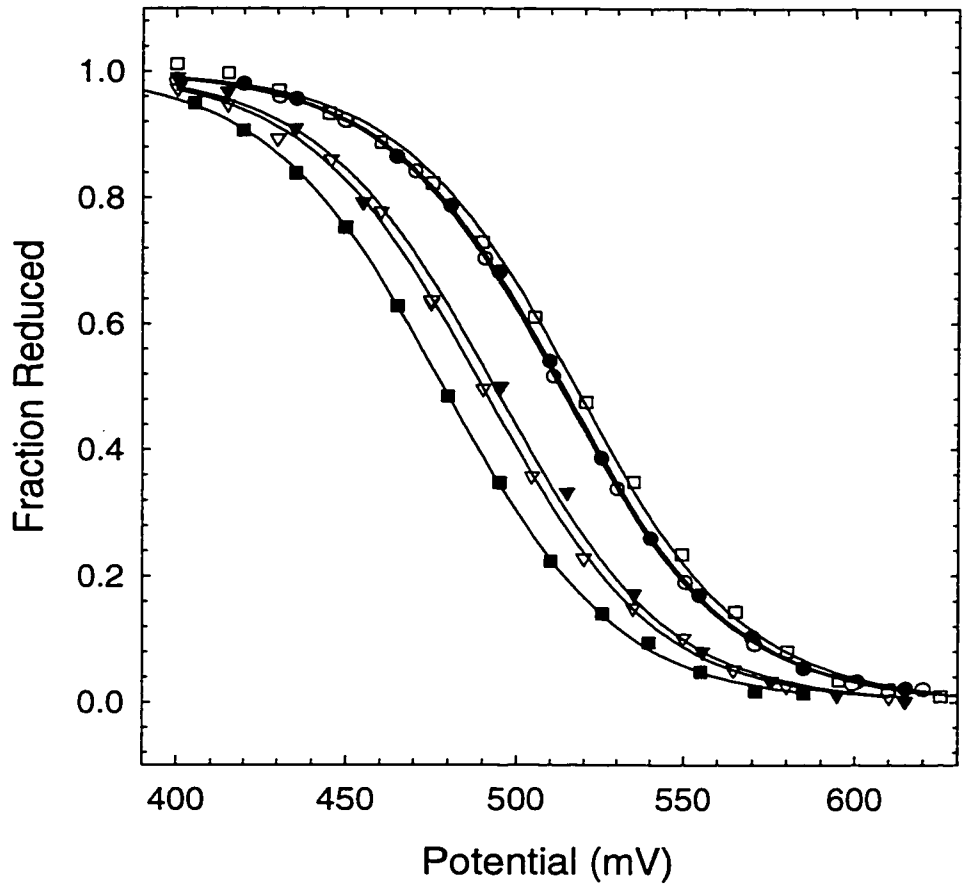

Figure 30. Representative redox titrations of P/P^+ in purified Y(L164)F (□), wild-type (●), R(L135)K (○), R(L135)L (▼), R(L135)Q (▽) and R(L135)E (■) RCs. The lines are best fits to the one-electron Nernst equation. The mean value of ΔE_m for each mutation is given in Table 7.

Calculations. Consider, first, the expected effects of the R(L135) mutations in the absence of dielectric screening. For the mutations R(L135)L and R(L135)E, the changes in the unscreened electrostatic energy difference between P^+ and P ($\Delta\Delta V_{Q\mu}$) are calculated to be -21.6 and -43.7 kcal/mol, respectively, whereas the observed changes in the E_m correspond to only -0.5 and -1.0 kcal/mol. Although P is buried in the intramembrane region of the protein and arginine L135 also is largely inaccessible to the solvent, the protein, solvent and electrolytes effectively screen the charge-charge interactions by an average factor of about 40. To explore possible explanations for this strong screening, we calculated the expected effects of the mutations using computational approaches that emphasize several different effects. Because the RC is an integral membrane protein and is purified with a belt of detergents (*195*), most of the models we considered included a 25 Å region with low polarizability sandwiched between two aqueous regions. Relaxations of the polar hydrogen atoms of the protein and crystallographic water atoms were treated by averaging over multiple configurations in the linear-response approximation (equation 3).

PDLD calculations include an explicit treatment of induced dipoles in the protein and its surroundings. For models with a 25-Å thick membrane, the predicted shifts in the E_m (ΔE_m^{calc}) agree qualitatively with experiment, but overestimate the effects of the mutations by factors of 2-8 (see Table 7 and Fig. 31*A*). Table 8 shows how the calculated ΔE_m for the R(L135)L and R(L135)E mutations depends on the width of the membrane. If the membrane is increased to 40 Å, the protein charges and P^+ are solvated less well, and the predicted shifts of the E_m depart further from the experimental results. A model with no membrane provides the largest screening, as expected, but still overestimates the shift significantly. As explained in Methods, these and the other electrostatics calculations described below considered separate ensembles of rotamers of the polar hydrogens for each mutant and for each oxidation state of P. They thus included a major component of the reorganization of the protein, although all

Table 8. Shifts in the E_m of P/P$^+$ in Mutant RCs Calculated by PDLD for Various Models of a Membrane and by PDLD/S for Various Values of ε_{in} [a]

Strain	ΔE_m^{expt}	ΔE_m^{calc} (PDLD)			ΔE_m^{calc} (PDLD/S)			
Membrane [b]		0	25	40	25	25	25	25
ε_{in}		-	-	-	2	4	8	20
R(L135)L	-16	-73	-98	-111	-106	-58	-33	-19
R(L135)E	-37	-134	-194	-241	-212	-115	-67	-38

[a] ΔE_m^{calc} is the calculated change of E_m in mV, relative to wild-type RCs. Each entry is an average of results for 5 structures with P in the reduced state and 5 in the oxidized state. 10 randomly chosen origins for the solvent/membrane grid were used for each structure. R, K, E or D at the mutation site is assumed to be charged while all other ionizable groups are neutral. The SEM was approximately ±8 mV in the PDLD calculations and ±10 mV in the PDLD/S calculations.

[b] With of the hydrophobic layer (Å).

the non-hydrogen atoms were fixed at their crystallographic positions. These models did not include counterions for the ionizable groups.

PDLD/S treats solvent induced dipoles explicitly in the same manner as the regular PDLD model, but uses an effective screening factor (ε_{in}) for direct charge-charge interactions rather than evaluating induced dipoles in the protein. Table 8 includes results for PDLD/S models with a 25 Å membrane and several values of ε_{in}. The best agreement with experiment requires an effective internal dielectric constant of about 20.

The Poisson-Boltzmann (DELPHI) treatment resembles PDLD/S in using a macroscopic ε_{in} for charge-charge interactions within the protein. Poisson-Boltzmann calculations with a 25 Å membrane and $\varepsilon_{in} = 4$ (a common choice) gave results similar to the PDLD/S treatment with $\varepsilon_{in} = 2$, overestimating the effects of the mutations by a factor of 3-6 (Table 7 and Fig. 31*A*).

Table 9 and Figures 31*A* and *B* show the shifts in the E_m calculated by using a distance-dependent screening factor for charge-charge interactions. A simple linear function ($f_{ij} = r_{ij}$), which is sometimes used in MD simulations because it avoids the calculation of $\sqrt{r_{ij}}$, greatly underestimates the screening for all the mutations considered here. However, the exponential function with $\eta = 0.10$ or 0.18 (equation 8) and the sigmoidal function (equation 9) both give good agreement with experiment. These simple, empirical expressions predict the experimental results within several mV for almost all the mutation sites, including both the surface and buried residues. (As in the PDLD, PDLD/S and DELPHI calculations, relaxations of polar hydrogen atoms around P and P^+ were treated separately in the linear-response approximation by averaging over 10 structures. However, the ΔE_m values calculated with the exponential or sigmoidal screening function varied little among these structures, giving standard errors of the mean of only ±4 and ±6 mV, respectively.)

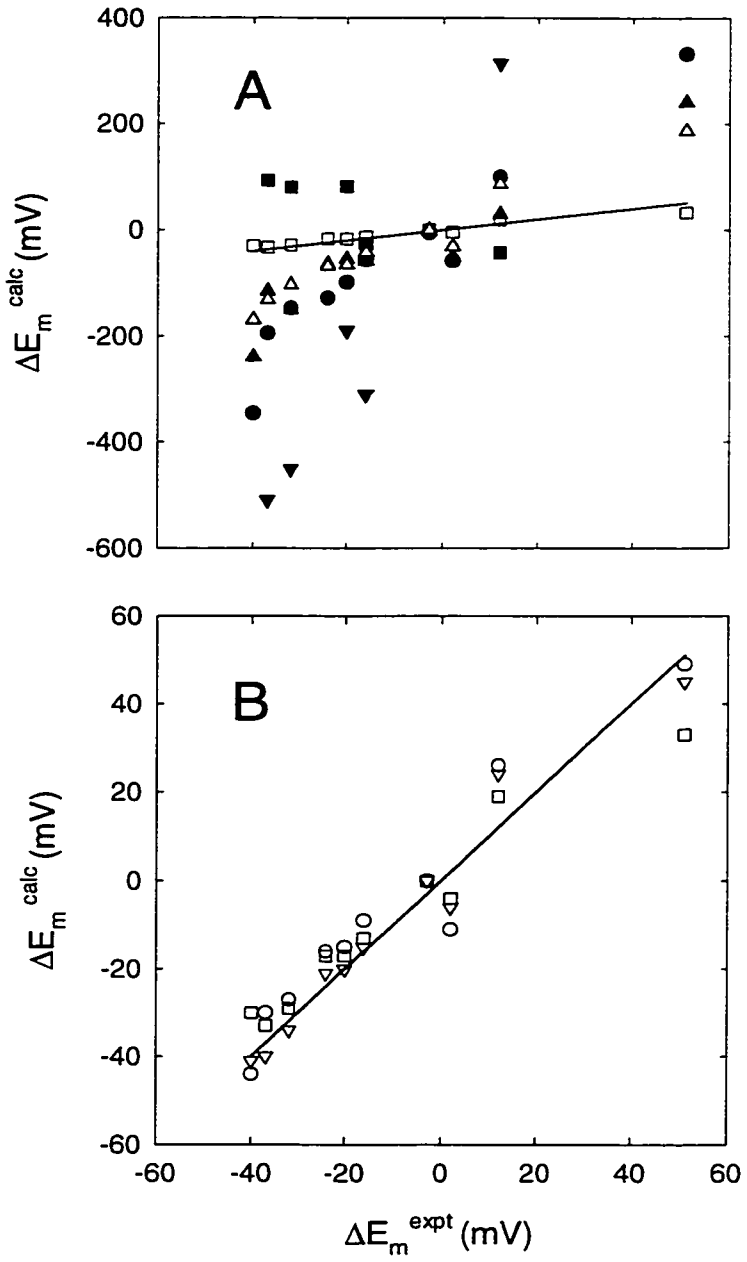

Figure 31. Correlation plots of calculated changes of the redox potential (ΔE_m^{calc}) versus the experimental value (ΔE_m^{expt}). For a perfect correlation, the data would fall on the solid line with a slope of 1 and *y*-intercept of 0. (Note that the ordinate and abscissa scales are different.) The ΔE_m^{calc} are calculated for the charge of P^+ divided equally between P_L and P_M, and are given in mV. (A) The changes in solvation energy were calculated by PDLD (●), DELPHI ($\varepsilon_{in} = 4$) (▲), MD without a counterion (▼), MD with a counterion for the mutated residue (■), a linear distance-dependent screening factor ($f_{ij} = r_{ij}$) (Δ) and an exponential distance-dependent screening factor (equation 8 with $\eta = 0.18$) (□). (B) Expanded view of results for calculations using distance-dependent screening factors given by equation 8 with $\eta = 0.10$ (∇) or 0.18 (□), and by equation 9 (○).

Table 9. Shifts in the E_m of P/P$^+$ Calculated with Distance-dependent Screening Functions and the Linear Response Approximation [a]

Strain	ΔE_m^{expt}	ΔE_m^{calc}			
		linear [b]	exponential [c] ($\eta = 0.10$)	exponential [c] ($\eta = 0.18$)	sigmoidal [d]
R(L135)K	- 3	0	0	0	0
R(L135)L	-20	-65	-20	-17	-15
R(L135)Q	-24	-68	-21	-17	-16
R(L135)E	-37	-131	-40	-33	-30
D(L155)N	+12	+87	+24	+19	+26
Y(L164)F	+2	-31	-6	-4	-11
R(M164)L	-16	-42	-15	-13	-9
R(M164)E	-32	-103	-34	-29	-27
C(L247)K	+51	+187	+45	+33	+49
C(L247)D	-40	-169	-41	-30	-44
R(L135)E/C(L247)K	+8	-8	0	0	-10

[a] ΔE_m^{calc} is the calculated change of the E_m in mV, relative to wild-type RCs. Each entry is an average of results for 5 structures with P in the reduced state and 5 in the oxidized state. R, K, E or D at the mutation site is assumed to be charged while all other ionizable groups are neutral. The SEM was approximately ±8 mV in the PDLD calculations and ±10 mV in the PDLD/S calculations. The measured shift for each mutant (ΔE_m^{expt}) is repeated from Table 7 for convenience.

[b] $f_{ij} = r_{ij}$. The SEM for each entry is approximately ±15 mV.

[c] The exponential screening function given by equation 8. The SEM for each entry is approximately ±4 mV.

[d] The sigmoidal screening function given by equation 9. The SEM for each entry is approximately ±6 mV.

Table 10. ΔG_{sol} and λ for P $\rightarrow$ P$^+$ and the Shift of the E_m of P/P$^+$ Calculated by MD Simulations with and without a Counterion for the Mutated Residue [a]

Strain	Charge [b]	Without Counterion			With Counterion [c]		
		ΔG_{sol}	λ	ΔE_m^{calc}	ΔG_{sol}	λ	ΔE_m^{calc}
R(L135)R	+1	-24.4	2.4	(0)	-30.6	2.0	(0)
R(L135)L	0	-28.7	1.9	-189	-28.7	1.9	+82
R(L135)E	-1	-36.1	2.0	-510	-28.5	1.6	+93
D(L155)D	-1	-35.2	2.3	(0)	-26.9	2.6	(0)
D(L155)N	0	-27.9	1.7	314	-27.9	1.7	-43
R(M164)R	+1	-24.6	1.7	(0)	-31.2	1.6	(0)
R(M164)L	0	-31.8	1.6	-310	-31.8	1.6	-26
R(M164)E	-1	-35.0	1.2	-451	-29.3	1.6	+80

[a] ΔG_{sol} and λ, the change in solvation free energy and the reorganization energy for the process P $\rightarrow$ P$^+$, are given in kcal/mol; ΔE_m^{calc} is in mV and is relative to the wild-type model for the residue that was mutated (R(L135)R, D(L155)D or R(M164)R). The MD simulations include explicit waters and no membrane. Separate 100-ps trajectories were propagated for P and P$^+$. The root-mean-square fluctuations of ΔV_{sol} in the individual trajectories were approximately 2.8 kcal/mol.

[b] Assumed charge of protein without a counterion. Only the residue that was mutated was charged.

[c] The MD simulations with a counterion included either a Na^+ or a Cl^- ion in the solvent near the charged residue to make the net charge of the system zero when P was in its reduced state and +1 when P was oxidized.

The results of molecular-dynamics (MD) simulations are shown in Figure 31 and are included in Table 10. The calculated shifts of the E_m for models that do not include counterions are similar to those generated by the PDLD calculations. Thus, although they allow the protein and solvent to reorganize more extensively in response to both the mutation and the oxidation of P, the MD simulations without explicit counterions still overestimate the effects of the mutations by a substantial factor.

To examine the effects of counterions, we carried out MD simulations for the wild-type RC and the R(L135), R(M164) and D(L155) mutations with a single Na^+ or Cl^- ion in the water near the mutated or corresponding wild-type residue. The counterion compensates for the change in charge on the protein, bringing the predicted shift in the E_m closer to the measured value for all the mutations. In most cases, however, the result is an overcompensation, so that the sign of the calculated change is incorrect (see Table 10). This effect could arise from inappropriate positioning of the counterion closer to P than the ionizable amino acid, possibly because the simulations continued for only 100 ps and included only one ionizable residue in each model. As discussed below, a more accurate treatment probably would have to consider secondary effects involving other ionizable residues and a large cloud of electrolytes surrounding the protein. It is interesting nevertheless that the single counterions considered here mainly affected ΔG_{sol} and had relatively little effects on the reorganization energy associated with the oxidation of P (see Table 10). This indicates that the position of the counterion probably was determined mostly by the ionizable amino acid, and not by the charge on P.

In all the calculations described above, we assumed for simplicity that the positive charge of P^+ is distributed equally between P_L and P_M. Measurements of the ENDOR of P^+ have shown that the actual charge in wild-type RCs is greater on P_L than on P_M, and that mutations that alter the numbers of hydrogen bonds to the two bacteriochlorophylls can change the charge distribution (*173*). ENDOR measurements showed that similar

changes of the charge distribution occur in the R(L135)L, R(L135)E, R(M164)L and R(M164)E mutants described here (E. T. Johnson, W. W. Parson, F. Müh, W. Lubitz, J. C. Williams, J. P. Allen, J. Breton and E. Nabedryk, unpublished). The estimated ratio of P_L^+ to P_M^+ varied from 1.29 to 3.2 in the order R(M164)E < R(M164)L < wild-type < R(L135)L < R(L135)E. We therefore calculated the expected shifts in the E_m for these mutants using these charge distributions, while retaining the classical picture inherent in equation 2. (As discussed in Methods, a more refined treatment requires evaluating the electrostatic effects on diabatic $P_L^+P_M$ and $P_LP_M^+$ basis states separately and then rediagonalizing the interaction Hamiltonian. Such an analysis will be presented elsewhere.) As Table 11 shows, calculations using an exponential or sigmoidal distance-dependent screening factor (equation 8 or 9) still predict the shifts in the E_m well. With these sets of charges, using 0.18 for the exponential factor (η) in equation 8 gives somewhat better results than $\eta = 0.10$, in agreement with recent calculations of protein pK_as by Schutz and Warshel (*154*).

Table 11. Shifts in the Em of P/P$^+$ Calculated with Distance-Dependent Screening Functions and Experimentally Measured Charge Distributions [a]

Strain	ΔE_m^{expt}		ΔE_m^{calc}	
		exponential [b]	exponential [b]	sigmoidal [c]
	($\eta = 0.10$)	($\eta = 0.18$)		
R(L135)L	-20	-23	-19	-19
R(L135)E	-37	-48	-39	-40
R(M164)L	-16	-13	-12	-8
R(M164)E	-32	-26	-24	-14

[a] ΔE_m^{calc} is the calculated change of the E_m, in mV, relative to wild-type RCs. The calculations were the same as in Table 9 except for the distribution of charge between P_L and P_M. These calculations were done only for the subset of the mutations for which ENDOR data are available. The ENDOR experiments measure the hyperfine coupling constants of the unpaired electron to nuclear spins on P_L and P_M, which can be related to spin densities and therefore to charge densities on the two bacteriochlorophylls. The wild-type spin density ratio of P_L:P_M is 2.1 and the spin density ratios for the mutations R(L135)L, R(L135)E, R(M164)L and R(M164)E are, respectively, 3.2, 2.9, 1.6, and 1.3 (E. T. Johnson, W. W. Parson, F. Müh, W. Lubitz, J. C. Williams, J. P. Allen, J. Breton and E. Nabedryk, unpublished). The measured shifts (ΔE_m^{expt}) are repeated from Table 7 for comparison.

[b] The exponential screening function given by equation 8 with η = 0.10 or 0.18. The SEM for each entry is approximately ±4 mV.

[c] The sigmoidal screening function given by equation 9. The SEM for each entry is approximately ±4 mV.

Discussion

An underlying assumption in this study is that the ionizable residues at the mutation sites actually are ionized, so that shifts in the E_m of P can be correlated with changes in the charges of the ionized side chains. In agreement with this assumption, the shift of the E_m observed in each of the mutants is qualitatively consistent with the expected effect of changing the charge at that site: the direction of the shift depends consistently on the signs of the nominal charges of the native and mutant residue, and removing an ionizable group causes approximately half the effect of substituting an oppositely charged amino acid. The effect of the R(L135)E/C(L247)K double mutation is close to the sum of the effects of the R(L135)E and C(L247)K mutations. Additionally, mutations of R(L135) cause slightly larger effects than corresponding mutations of R(M164), in agreement with the small difference between the distances on the two sides of the RC and with previous evidence that the charge distribution in P is somewhat asymmetrical.

Arginine residues have been shown to stabilize the native conformations of some proteins, and replacing Arg by Lys can have a destabilizing effect (*196*). In the present case, replacing Arg L135 by Lys had almost no effect on the E_m of P, in agreement with the supposition that the shifts of the E_m caused by the nonconservative mutations at this site reflect mainly long-range electrostatic interactions rather than structural changes. Because the mutation sites are relatively far from the bacteriochlorophylls, one would not expect the mutations to have large effects on the structure or molecular orbitals of P.

The effects of all the mutations on the E_m of P are much smaller than one might have expected, considering the hydrophobic surroundings of P and the fact that most of the residues we mutated have little exposure to the solvent. In spite of these factors, electrostatic interactions of P with the ionizable residues we considered are strongly screened. As noted in the Introduction, electrostatic interactions can be screened by movements of O-H, C=O and N-H dipoles. However, the electrostatics calculations

described in the present work considered ensembles of rotamers of polar hydrogen atoms for each mutant and for each oxidation state of P, and the MD simulations allowed all the atoms to move. The finding that both of these treatments underestimate the screening badly if counterions are not included in the model argues that movements of protein dipoles are not the dominant source of screening in the present case. It is possible, however, that the MD trajectories were not long enough for complete dipolar reorientation. In particular, they might not reflect the slow reorganization associated with movements of water into or out of the protein. Such movements might occur in response to the mutation, the oxidation of P, or both.

What other processes could account for the strong screening? Perhaps the simplest explanation is that the ionized side chains are accompanied by counterions, which keep the net charge of the system zero. In accord with this view, MD simulations that included explicit counterions predicted smaller shifts of the E_m than simulations that omitted counterions (Table 10). The association of a counterion with the charged residue effectively reduces the charge-charge interactions with P^+ to dipolar interactions, which fall off more rapidly with distance. Several previous investigators have found that including counterions increases the stability of MD simulations of proteins (*197-199*), although Walser et al. (*200*) recently found no such effect. The divergence of opinion on this point could reflect the difficulty of treating long-range electrostatic interactions. Neutralizing the model probably is the easiest way to obtain a convergent treatment, whether or not counterions are present in the actual system.

A second possibility is that removing or changing the charge of one residue alters the pK_a of one or more other ionizable residues, which then release or bind protons so that the total charge of the protein remains essentially constant. In this case, however, we would expect the effect of a mutation to depend on the constellation of other ionizable residues near the mutation site. Such a dependence might be difficult to detect in water-soluble proteins that have many ionizable residues, but should be more apparent in the RC, where ionizable groups are relatively sparse. Although the effective

screening clearly depends on the distance between P and the mutation site, it has no obvious dependence on the proximity of the mutation to other ionizable groups. The guanidino group of Arg (M164), for example, is only 4 Å from the carboxyl group of Glu (M173), whereas the guanidino group of Arg (L135) has no other ionizable groups within 13.5 Å. The distances from Cys (L247) and Asp (L155) to the nearest ionizable group (Arg(L135) in both cases) are 9.3 and 16.0 Å, respectively.

Although microscopic treatments that exclude counterions fail to reproduce the effects of the mutations reliably, the effects can be modeled well by using a distance-dependent screening factor that increases from 1 at short interatomic distances to 40 or more at 10 Å. A linear dependence ($f_{ij} = r_{ij}$) proved inadequate in this regard, but the exponential expression used by Warshel et al. (*54*) worked well with either $\eta = 0.1$ or $\eta = 0.18$, as did the sigmoidal function suggested by Hingerty et al. (*188*). The exponential function with $\eta = 0.18$ predicted the effects of mutating the surface residue Asp (L155) more closely than the other functions, although it underestimated the effects of mutating the buried Cys (L247). Additionally, it gave somewhat better results than the same function with $\eta = 0.10$ in calculations that considered the asymmetrical distribution of charge between the two bacteriochlorophylls of P (Table 11); the difference, however, was marginal.

It is remarkable that these functions proved so successful at describing interactions between buried charges in the RC. Distance-dependent screening factors were developed originally from theoretical analyses of saturation effects in ionic solutions (*201*), and were used in proteins to model electrostatic effects on surface residues that were in contact with water and electrolytes (*54, 188, 202*). Warshel and coworkers have argued that a similar screening occurs in the interior of water-soluble proteins (*54*). However, one would not necessarily expect the same functions to work well for buried groups in an integral membrane protein. Perhaps the fact that these functions do work well is an indication that protein interiors can accommodate water (*151*) and, in some cases at least, also ions.

Whatever the mechanism of the screening, the results presented here support the view that ionized side chains make only small contributions to the electrostatic energies of ion-pair states such as $P^+B_L^-$ and $P^+H_L^-$ in the RC, and thus do not play major roles in establishing the specificity or speed of light-induced charge separation (*31, 33*). In calculations of such energies, it clearly would be much more accurate to consider all the ionizable residues to be uncharged, rather than to use their nominal charges with a small ε_{in}.

CHAPTER 5: ELECTRONIC AND VIBRONIC COUPLING OF THE SPECIAL PAIR OF BACTERIOCHLOROPHYLLS IN PHOTOSYNTHETIC REACTION CENTERS FROM WILD-TYPE AND MUTANT STRAINS OF *RHODOBACTER SPHAEROIDES*

The initial steps of charge separation in photosynthetic organisms occur in a pigment-protein complex called the reaction center (RC). Reaction centers from purple photosynthetic bacteria typically contain three protein subunits (L, M and H), four bacteriochlorophyll (Bchl) molecules, two bacteriopheophytins (Bphe) and two quinones (see (*7*) for a recent review). Two of the Bchls (P_L and P_M) form a tightly coupled dimer (P) that serves as the primary electron donor. Upon excitation with light, P transfers an electron to one of the Bphes (H_L) by way of one of the two "accessory" Bchls (B_L). The reduced Bphe then passes an electron to one of the quinones.

P_L and P_M sit on either side of a two-fold rotational axis of noncrystallographic symmetry (*16-19*). A 180° rotation around this axis approximately interchanges corresponding atoms of the Bchls, along with the positions of homologous residues in the L and M polypeptides. The two accessory Bchls, the pair of Bphes, and to a lesser extent the two quinones also are arranged in symmetrical branches on opposite sides of the rotation axis. The charge-separation reactions, however, are strongly asymmetrical, with electron transfer to B_L and H_L occuring much more rapidly than transfer to their counterparts B_M and H_M in the opposite branch (*203-206*). The high specificity of this process appears to depend in part on the energies of the ion pairs $P^+H_L^-$ and $P^+B_L^-$, which are controlled largely by electrostatic interactions with the protein. The factors that create the electrostatic asymmetry have been explored by site-directed mutagenesis (*30, 207-209*) and computational approaches (*31, 32*), but remain only partially understood.

The oxidized electron donor (P^+) can be viewed as an electronically coupled system of two Bchls with basis states $|P_L^+\rangle$ and $|P_M^+\rangle$, in which the positive charge and the unpaired electron spin are localized entirely on either P_L or P_M (*47, 210-212*). In this model, stationary ground and excited states of P^+ (Ψ_+ and Ψ_-) are constructed from linear combinations of $|P_L^+\rangle$ and $|P_M^+\rangle$ with coefficients that depend on an electronic coupling strength (β) and the difference between the energies of the basis states (δ). The ratio of the net spins on P_L and P_M in the ground state (ρ_L/ρ_M) has been measured experimentally from the ENDOR or TRIPLE spectrum of P^+ (*213*). In RCs from wild-type *Rhodobacter sphaeroides*, ρ_L/ρ_M was found to be 2.1. The ratio of the net positive charges on the two molecules is assumed to be essentially the same as ρ_L/ρ_M. A broad absorption band in the region of 2700 cm^{-1} has been assigned to transitions between Ψ_+ and Ψ_- and has been studied by FTIR spectroscopy (*47, 180, 183, 214, 215*) (*211*).

This model for P^+ has been investigated by making site-directed mutations that add or remove hydrogen bonds to P_L or P_M. Each such hydrogen bond increases the reduction potential (E_m) of P/P^+ by approximately 50 mV (*166*) and combinations of hydrogen bonds can shift ρ_L/ρ_M over the range 0.28-4.94 (*173*). These results have been explained by assuming that adding a hydrogen bond to P_L or P_M selectively destabilizes either $|P_L^+\rangle$ or $|P_M^+\rangle$, respectively, without changing either β or the energy of the other cation.

In an extension of this work, Artz *et al.* (*168*) described a set of mutations that replaced Leu M160, a residue within H-bonding distance to the oxygen of the keto group of P_M, by eight different amino acids. All the mutations made the charge distribution more asymmetric and increased the E_m, as expected if the hydrogen bond destabilizes $|P_M^+\rangle$. In general, residues with sidechains that could approach the keto oxygen more closely had larger effects. The L(M160)H mutation had the largest effect, increasing ρ_L/ρ_M to 5 and raising the E_m by 60 mV. The asymptotic value for the E_m

when $|P_M^+\rangle$ is destabilized so severely that all the charge resides on P_L was estimated to be 710 mV. This is comparable to the E_m of 640-660 mV measured in "heterodimer" mutants, in which either P_L or P_M is replaced by Bphe and the positive charge of P^+ localizes strongly on the remaining Bchl. Fitting the E_m values and the charge ratios to the orbital model gave a value of β in the range 170-240 meV (*168*), or about 180 meV after a correction to one of the equations (*182*). However, the analysis implies that a hydrogen bond at M160 destabilizes $|P_M^+\rangle$ by nearly 200 meV. This is difficult to reconcile with the observation that the hydrogen bond introduced by the mutation L(L131)H in H(M202)L heterodimer RCs increases the E_m by only 80 mV (*167*).

The effects of some of the other hydrogen-bonding mutants that have been described also have been difficult to interpret. The mutation H(L168)F removes a hydrogen bond from the acetyl oxygen of P_L, which would be expected to stabilize P_L^+ and thus lower the E_m, and increase both ρ_L/ρ_M and the energy of the 2700-cm^{-1} transition. This mutation does lower the E_m (*216*), but it decreases ρ_L/ρ_M to less than 1 (*173*) and shifts the FTIR transition to lower energies (Breton and Nabedryk, unpublished). The mutation F(M197)H introduces a hydrogen bond to P_M, which should destabilize $|P_M^+\rangle$ and thus increase the E_m, ρ_L/ρ_M, and the energy of the 2700-cm^{-1} band. This mutation raises the E_m (*23*), but again decreases ρ_L/ρ_M slightly and lowers the energy of the 2600 cm^{-1} band (Breton and Nabedryk, unpublished). Finally, the mutation L(L131)H introduces a hydrogen bond to the keto oxygen of P_L, would be expected to destabilize $|P_L^+\rangle$ and decrease ρ_L/ρ_M and the energy of the 2600-cm^{-1} transition. While ρ_L/ρ_M decreases from 2.1 to less than 1 and the E_m rises as expected, this mutation causes very little change in the 2700-cm^{-1} absorption band (*217*).

These puzzling observations suggest that some of the H-bond mutations affect parameters other than simply the energy difference between $|P_L^+\rangle$ and $|P_M^+\rangle$. They could, for example, perturb the molecular orbitals of one or both BChls by reorienting the

acetyl groups, which could change both the energies of the basis states and the electronic coupling strength. In the current work, we have attempted to avoid these problems by mutating residues that do not interact directly with the pigments. We focused on arginines L135 and M164, which are the closest ionizable residues to P in the *Rb. sphaeroides* RC but are too far away to form hydrogen bonds to either P_L or P_M. The guanidino Nη atom of each of these residues is about 7 Å from the keto oxygen of the Bchl attached to the same subunit, and about 14 from the acetyl oxygen of the other Bchl (see Figure 32). Replacing Arg L135 or M164 by a neutral or anionic residue thus should shift the energies of $|P_L^+\rangle$ and $|P_M^+\rangle$ through long-range electrostatic interactions, with relatively little effect on β. We have measured the effects of these mutations by the changes in the E_m and the ENDOR and FTIR difference spectra of P^+, and have attempted to account for the results in the framework of a model that includes both electronic and vibronic coupling.

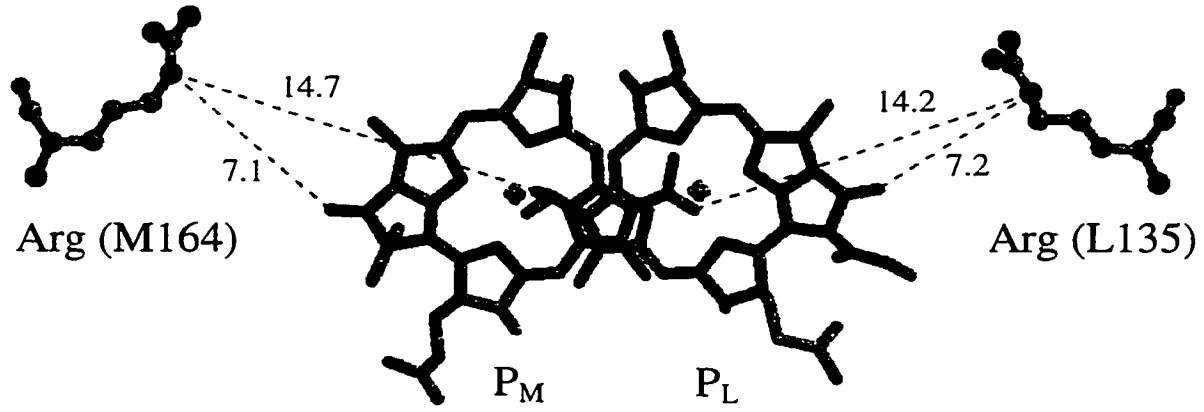

Figure 32. Locations of Arg L135 and Arg M164 relative to P_L and P_M in the crystal structure of *Rb. sphaeroides* RCs [Ermler, 1994 #1310]. The distances (Å) from the Arg Nη atoms to the keto oxygen of the closer Bchl and the acetyl oxygen of the more distant Bchl are indicated. The distances from Nη of Arg L135 to the Mg atoms of P_L and P_M are 12.5 Å and 19.7 Å, respectively; Nη of Arg M164 is 13.1 Å from the Mg of P_M and 20.1 Å from that of P_M.

Methods

Construction and Purification of mutant RCs. Oligonucleotide-mediated site-directed mutagenesis was accomplished with the Chameleon Kit (Stratagene) for the mutations of Leu and Glu at both R(L135) and R(M164). The mutagenesis was performed in puc18 or puc19 vectors containing portions of the L or M subunits, following methods developed by Williams *et al.* (*169*) (*166*) (*170*). After transformation into *Escherichia coli* strain DH5α cells and purification of the mutated plasmid DNA, the regions containing the mutations were subcloned into the *puc* operon. The R(M164) mutations were cloned into the pRKSCH vector (*170*). The R(L135) mutations were cloned into the pRKSCH/pHis vector, which contains a tail of seven histidine residues at the carboxyl terminal of the M-subunit (*171*). The plasmids were transformed into the *E. coli* strain S-17 and conjugated with ΔLM1.1, a *Rb. sphaeroides* strain that has the RC deleted (*169*). DNA from the mutant RC complemented ΔLM1.1 strains was purified and sequenced to ensure that the mutations had been introduced correctly.

Wild-type and mutant *Rb. sphaeroides* strains were grown semi-aerobically in rich media for 3-5 days in the dark (*169*). RCs from the R(M164) mutants were isolated by standard procedures (*172*) (*173*) with minor modifications. The solubilization of the RCs was achieved with 0.65% N,N-dimethyldodecylamine-N-oxide (LDAO, Fluka), which is slightly lower than the 1.2% used by Feher and Okamura (*172*), and after ultracentrifugation the supernatent was brought to 1% LDAO and 30% NH_4SO_4 (wt./vol) to precipitate the RCs. The Celite step was omitted and the solubilized floating pellet was dialyzed to remove salts and loaded onto a DEAE column. The RCs were eluted with a gradient of 0.03 M to 0.25 M NaCl. RCs from the R(L135) mutations were isolated using a protocol that exploited the histidine tag (*171*), and were purified further by chromatography on DEAE-sepharose (Bio-Rad). The purified RCs were dialyzed against 15 mM Tris pH 8, 0.025% LDAO, and 1 mM EDTA and concentrated to an OD_{800} of 40 in a 1 cm cuvette using an Amicon pressure cell or a Centricon-50

filter device. The purity of the sample was measured by the ratio OD_{800}/OD_{280} and typically was between 1.4 and 1.8. The RCs with R(L135) mutations were significantly less stable than those with mutations of R(M164).

RCs suspended in the detergent LDAO have been shown to have two stable conformations with different ρ_L/ρ_M ratios (*218*). To ensure that the RCs were in the conformation that absorbs at longer wavelengths, LDAO was replaced by the non-ionic detergent CHAPS. A concentrated solution of CHAPS was added directly to a dialysis bag containing the RCs to give 2 mM CHAPS, and the detergent exchange was completed by equilibrium dialysis overnight against 2 mM CHAPS, 15 mM Tris pH 8.0 and 1 mM EDTA. The RCs then were concentrated to an OD_{805} ~ 100 using centricon 50 filters (Amicon).

ENDOR and FTIR Spectroscopy. Special TRIPLE spectra were recorded at 288 K on a Bruker ESP 300E spectrometer with a home-built cavity and ENDOR/TRIPLE accessories as described (*219*). (A Special TRIPLE spectrum is similar to one wing of an ENDOR spectrum, and is obtained by monitoring the strength of EPR absorption while exciting nuclear magnetic resonances with an rf field at the free hydrogen Larmor frequency modulated with a swept second frequency.) P^+ was obtained by continuous illumination of the sample with saturating light from a 100-W tungsten halogen lamp filtered through 7 cm of water to reduce the light intensity for wavelengths greater than 1000 nm and glass filters to cut off light for wavelengths less than 600 nm (*220*). Because multiple ENDOR resonances overlap, deconvolution of the spectra is necessary to fit the individual bands (*221*).

Light-induced FTIR difference spectra of hydrated films were recorded with a Nicolet 60SX FTIR spectrometer equipped with a MCT-A detector, a KBr beamsplitter and a cryostat (*217*) (*222*). Between 100 and 1000 cycles of dark and light spectra were averaged to produce each final spectrum. Each FTIR measurement cycle required about 45 seconds, consisting of 12 s in the dark, 12 s in slightly subsaturating continuous

light, a second 12 s period in the dark, and about 9 s calculation time with the sample in darkness. The spectra were measured at room temperature for chromatophores and at 100 K for purified RCs. The RC films were cooled to 100 K either in the dark or during continuous illumination, allowing the protein to freeze in conformations that preferentially stabilized either P or P^+, respectively (*223*). Because the FTIR spectra above 3000 cm^{-1} are distorted by water absorption in hydrated films, we also prepared less hydrated ("dry") films of RCs. The difference spectra were normalized by setting the baseline equal to zero at 1770 cm^{-1} and scaling all the spectra so that the peak of the small, negative Q_A absorption band at 1604 cm^{-1} was constant (*224*).

Vibronic Model. Calculations of the eigenvectors and absorption spectra of the vibronic model of P^+ were done with the program PKS2 essentially as described (*225-227*). To determine the predicted spin distribution and E_m, we considered the ground state of P^+ to include a Boltzmann-weighted average of the three lowest eigenstates because, with the vibrational frequencies used (see Results) higher states would not be significantly populated at 288 K, the temperature used for the Special TRIPLE and E_m measurements. The calculated absorption spectrum of P^+ included transitions from a Boltzmann distribution of eigenstates to all possible excited states. Here we used the complete partition function for the ground state since this was already implemented in PKS2; including only the three lowest levels of the ground state would give essentially the same results. For presentation, each line in the stick absorption spectrum was dressed with a Gaussian with a homogeneous width of 130 cm^{-1}, independent of the frequency or character of the transition.

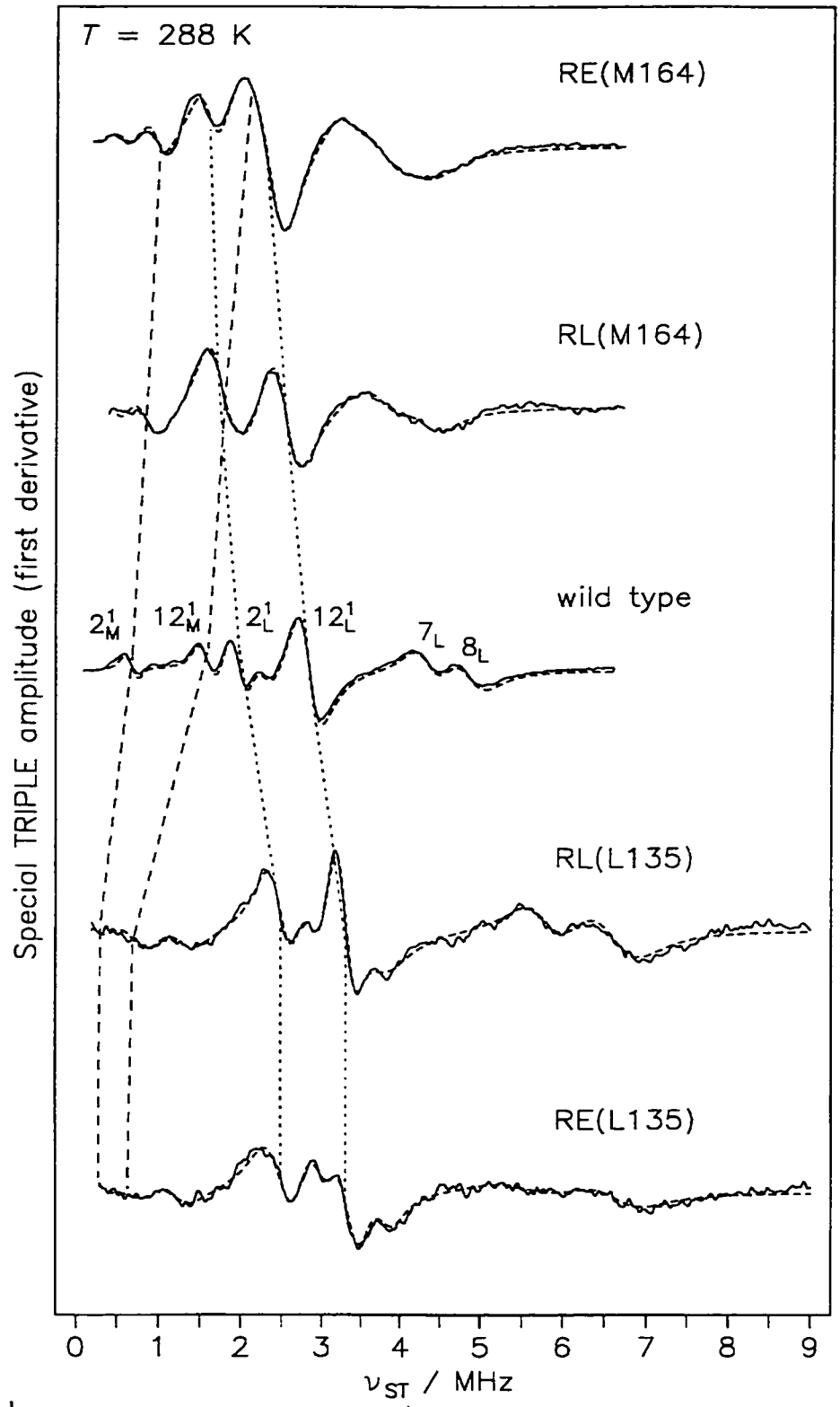

Figure 33. ^{1}H Special TRIPLE spectra of P^+ in wild-type *Rb. sphaeroides* RCs and the R(L135) and R(M164) mutants. The measured spectra are shown with solid lines; fitted spectra, with short-dashed lines.

Table 12. Hyperfine Coupling Constants for P^+ in Wild-Type and Mutant RCs [a]

	R(M164)E	R(M164)L	wild-type	R(L135)L	R(L135)E	
$A(12^1_L)$	4.8	5.1	5.70	6.6	6.6	
$A(2^1_L)$	3.2	3.4	3.96	5.0	5.0	
$A(12^1_M)$	4.3	3.8	3.20	2.6	2.4	
$A(2^1_M)$	1.9	1.7	1.37	1.4	1.3	
A(β)	8.4	8.6	9.70	13.2	13.2	7.5
	7.6	8.70	11.6	11.4		
	6.7		6.25	7.2	7.6	
	1.2		4.50	5.8	5.9	
				~0.6	~0.6	
R_L	1.5	1.5	1.44	1.3	1.3	
R_M	2.2	2.3	2.34	1.8	1.9	
Σ	14.2	14.1	14.23	15.6	15.2	
ρ_L/ρ_M	1.3	1.6	2.11	2.9	3.2	
ρ_L	0.6	0.6	0.68	0.75	0.76	

[a] $A(12^1)$ and $A(2^1)$ are the isotropic ^{1}H-hyperfine coupling constants (hfcs, in MHz) for the protons of methyl carbons 12^1 and 2^1; subscript L or P denotes P_L or P_M. The hfcs for the additional β protons (A(β)) used to calculate the simulated spectra in Figure 33 also are given. The estimated errors of the hfcs are ±0.03 MHz for wild-type and ±0.1 MHz for the mutants. R_L, R_M, Σ and ρ_L/ρ_M are defined in the text. ρ_L is the fraction of the spin localized on P_L.

Results

Effects of the Arg mutations on the spin distribution in P^+. To examine the effects of the mutations on the distribution of electron spin and charge in P^+, we measured the Special TRIPLE spectra of photochemically oxidized RCs at 288 K. Figure 33 shows the spectra obtained with wild-type, R(L135)L, R(L135)E, R(M164)L and R(M164)E RCs. The hydrogens of methyl groups 2^1 and 12^1 give prominent ENDOR signals that have been assigned by selective deuteration and comparisons to other known systems (*228-230*). (Methyl 2^1 is attached to Bchl ring I and 12^1 to ring III.) With the radical cation of monomeric Bchl in solution, the isotropic hyperfine coupling constants (hfcs) for these hydrogens are proportional to the densities of the unpaired electron spins on carbons 2 and 12 (*231*) (*232*). The situation in P^+ is more complicated because the spin is distributed between P_L and P_M. Previous work has shown that, in wild-type RCs, the hfcs for the methyl hydrogens of P_L ($A(2^1_L)$ and $A(12^1_L)$) are larger than the corresponding hfcs of P_M ($A(2^1_M)$ and $A(12^1_M)$), demonstrating that the spin is divided unequally in favor of P_L. Assuming that the π molecular orbitals of P_L and P_M are similar, the ratio of the spins of P_L and P_M can be evaluated as

$$\frac{\rho_L}{\rho_M} = \frac{A(2^1_L) + A(12^1_L)}{A(2^1_M) + A(12^1_M)}. \quad (1)$$

This same expression should give the ratio of the net positive charges on the two molecules.

Analyses of fits to the Special TRIPLE spectra are given in Table 12. The results for wild-type RCs are in agreement with previous measurements (*219*) (*173*). In the M164 mutants, the ENDOR features assigned to $|P^+_L\rangle$ shift to lower frequencies while those assigned to $|P^+_M\rangle$ shift upward. In the L135 mutants, the features assigned to $|P^+_L\rangle$ shift to higher frequencies while those of $|P^+_M\rangle$ are more difficult to resolve but evidently shift downward. The higher noise in the spectra of the L135 mutants could be due in

part to the greater instability of the RCs. However, simulated Special TRIPLE spectra calculated using the hfcs from Table 12 (dashed lines in Figure 33) agree well with the measured spectra. The changes in the ratios of the hfcs for P_L and P_M indicate that the mutations at M164 make the dimer more symmetric, presumably by stabilizing $|P_M^+\rangle$ relative to $|P_L^+\rangle$. The calculated charge ratio ρ_L/ρ_M decreases from 2.11 in wild-type RCs to 1.6 and 1.3 in the Leu and Glu mutants, respectively. The L135 mutations have the opposite effect, stabilizing $|P_L^+\rangle$ and making the charge distribution more asymmetric. Here ρ_L/ρ_M increases to 2.9 and 3.2 in the Leu and Glu mutations, respectively.

The ratios $R_{L,M} = A(12^1_{L,M})/A(2^1_{L,M})$ and sums $\Sigma = A(2^1_L) + A(12^1_L) + A(2^1_M) + A(12^1_M)$ provide probes of the intramolecular spin distributions, which could reveal effects of the mutations on the molecular orbitals of the individual Bchls (*173*). As shown in Table 12, R_L and R_M, are nearly unchanged in the M164 mutants. R_M may be somewhat smaller in the L135 mutants, but is less well determined here because the $A(2^1_M)$ resonances are not well resolved (see Figure 33). A comparable change in R_L occurs in the H(M202)L heterodimer mutant, and could just reflect localization of the charge on a single Bchl (*173*).

Effects of the mutations on the P*/P vibrational difference spectrum. Vibrational spectroscopy has been used extensively to explore the Bchls and the surrounding protein in the RC. Changes in the vibrational spectrum associated with the oxidation of P can be obtained by subtracting the FTIR spectrum of a sample in the dark (PQ_A) from the spectrum of the sample under continuous illumination ($P^+Q_A^-$). $P^+Q_A^-/PQ_A$ difference spectra obtained in this manner have positive and negative peaks that reflect, respectively, $P^+Q_A^-$ and PQ_A absorption. Oxidation of P causes changes in many vibrational modes, some of which have been assigned by comparison to the spectra of Bchl in solution and from the effects of isotopic substitutions and site-directed mutagenesis (*233, 234*) (*217, 235, 236*). The keto C=O stretching modes of $|P_L^+\rangle$ and P_L

in wild-type RCs have been assigned to bands at 1713/1693 cm^{-1} (1713 cm^{-1} for $|P_L^+\rangle$ and 1693 cm^{-1} for P_L) and those of $|P_M^+\rangle$ and P_M to 1703/1683 cm^{-1} (*217*). The ester carbonyl absorbs at 1753/1747 cm^{-1} but the contributions from the two Bchls here are not well resolved (*235*). The absorption bands of the acetyl groups of P_L and P_M are shifted relative to one another because of differences in hydrogen bonding. In wild-type *Rb. sphaeroides*, the acetyl of P_L is hydrogen bonded to His L168 and absorbs in the region of 1620 cm^{-1}, whereas the free acetyl of P_M absorbs near 1650 cm^{-1} (*237-239*). The acetyl bands are difficult to see in spectra of purified RCs, but are more apparent in spectra of chromatophores. Features attributable to Q_A^- or Q_A also can be identified in the $P^+Q_A^-/PQ_A$ difference spectra, but usually are less prominent than those associated with the Bchls.

Figure 34 shows $P^+Q_A^-/PQ_A$ difference FTIR spectra in the region 1800 to 1200 cm^{-1} for the wild-type and several mutant RCs at 100 K. Spectra of RCs that were cooled in the dark are in the upper panel, and spectra of RCs cooled under continuous illumination are in the lower. The clearest effects of the mutations are on the vibrations of the keto C=O vibrations in the region of 1700 to 1720 cm^{-1}. (Perhaps coincidentally, the keto groups are on the edges of the Bchls located closest to the mutation sites.) The R(L135)E mutation strengthens the higher-energy P^+ band relative to the band at lower energies, and moves the peaks apart to 1718 and 1700 cm^{-1} (Fig. 34, spectra *A*). In R(M164)E, by contrast, the P^+ absorption coalesces into a single band at 1709 cm^{-1} with a weak shoulder on the high-energy side (Fig. 34, spectra *C*). The two absorption bands of P in the region of 1685 to 1695 cm^{-1} also have more equal strengths in the R(M164)E mutant. The R(L135)L and R(M164)L mutations cause qualitatively similar changes (not shown).

Comparison of the $P^+Q_A^-/PQ_A$ FTIR spectra to similar spectra of the heterodimer mutants indicates that the positions and relative strengths of the keto stretching bands are correlated with the charge distribution between P_L and P_M. In the H(M202)L

heterodimer, where the charge is localized on P_L, the absorption by P^+ in the $P^+Q_A^-/PQ_A$ difference spectrum is split into two bands of nearly equal intensity at 1720-1722 cm^{-1} and 1712 cm^{-1} (*215*). As just described, these bands are similarly split in the L135 mutations. In the H(L173)L heterodimer of *Rb. capsulatus*, where the charge localizes on P_M, the P^+ bands merge into a single peak (*240*), and the same happens in the M164 mutants studied here. These features of the spectra are consistent with a shift of the charge distribution towards P_L in the L135 mutations and toward P_M in the M164 mutants.

The FTIR spectra of the R(L135)E, wild-type and R(M164)E RCs also differ in the intensities of bands in the regions of 1290, 1480 and 1560 cm^{-1} (see Figure 34). These bands have been attributed to "phase-phonon" vibrational modes that are formally forbidden by symmetry in monomeric Bchl, but become allowed by coupling to the electronic transition between ground and excited eigenstates of P^+ (*183, 211, 241*). The phase-phonon bands are enhanced in the R(M164)E mutant relative to wild-type RCs, and are weakened in the R(L135)E mutant. This is consistent with a strengthening of the electronic transition in the R(M164)E RCs, as discussed below.

The arginine mutations cause only minor changes in other carbonyl vibrations. The ester vibrations near 1750 cm^{-1} are nearly identical to those measured in the wild-type, displaying only a small shift of both the negative and the positive components to higher energy in R(M164)E compared to R(L135)E (see Fig. 34, spectra *D*). The changes in the acetyl C=O vibrations in the region 1620-1650 cm^{-1} are too small to interpret with confidence, as they are in the heterodimer mutants.

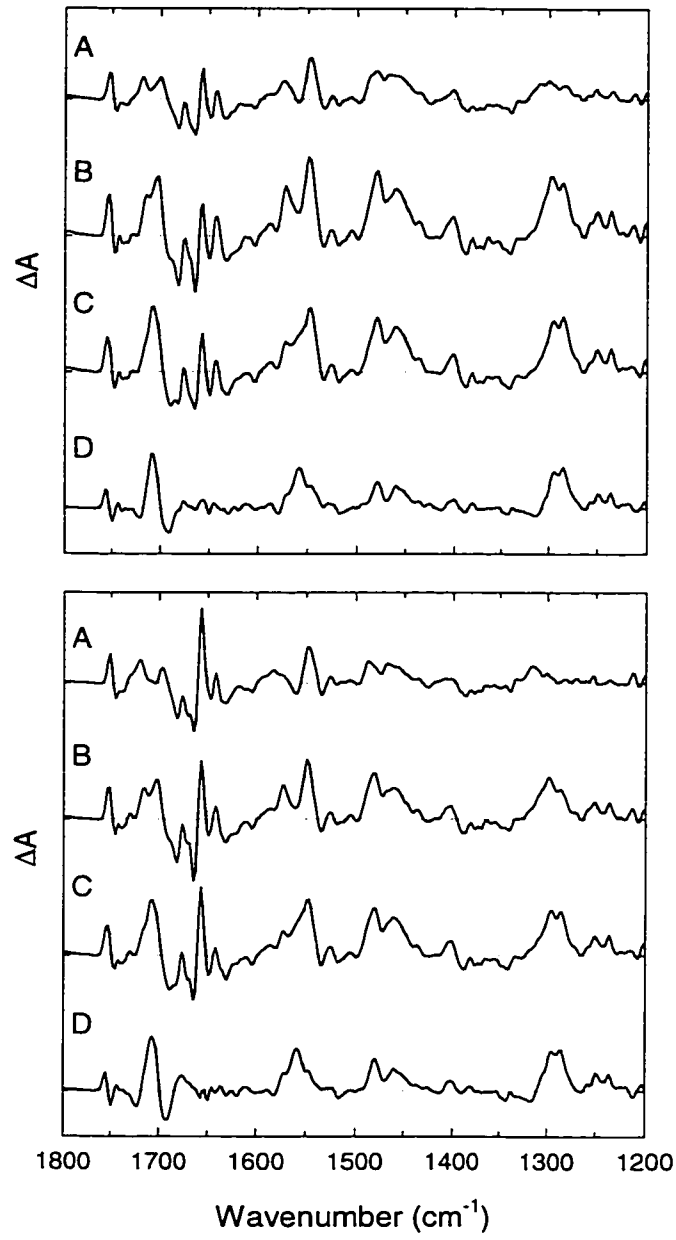

Figure 34. $P^+Q_A^-/PQ_A$ (light *minus* dark) FTIR difference spectra of RCs in hydrated films that were cooled to 100 K in the dark (*top panel*) or light (*bottom*). In each panel, spectra *A*, *B* and *C* are for R(L135)E, wild-type and R(M164)E RCs, respectively. Spectrum *D* is the double-difference spectrum, $\{P^+Q_A^-/PQ_A$, R(M164)E$\}$ *minus* $\{P^+Q_A^-/PQ_A$, R(L135)E$\}$. The spectra are normalized in the Q_A band at 1604 cm^{-1}. These spectra are expansions of the region between 1200 and 1800 cm^{-1} from the complete spectra shown in Fig. 5.

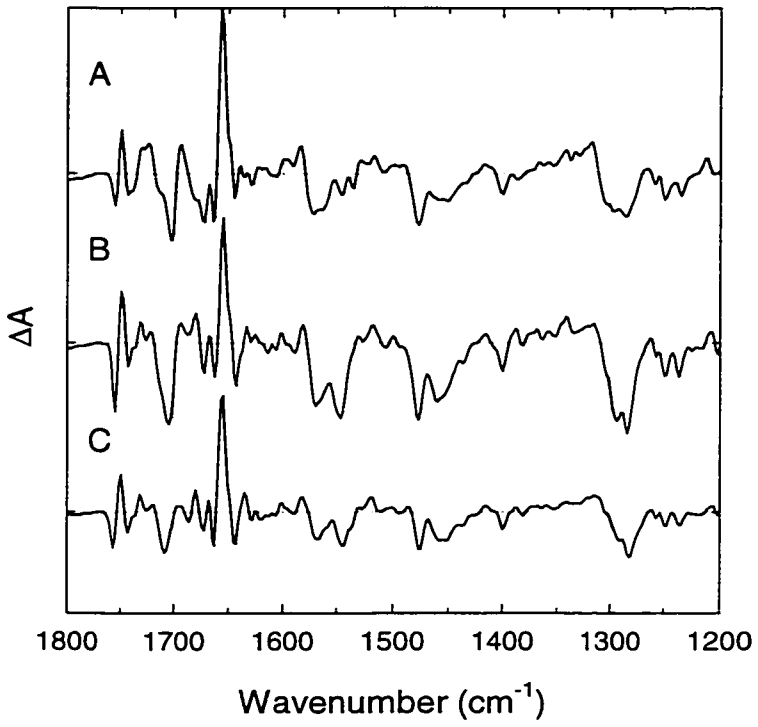

Figure 35. $P^+Q_A^-/PQ_A$ double-difference spectra between hydrated films of RCs cooled to 100 K in the light or dark. Positive peaks indicate larger absorbance increases (P^+ absorption) for RCs cooled in the light. Spectra *A*, *B* and *C* are for R(L135)E, wild-type and R(M164)E RCs, respectively. The single-difference spectra are shown in Figure 3.

Illuminating the RCs during cooling allows the protein to relax around the charge-separated state, $P^+Q_A^-$ (*223*). The effects of this relaxation on the FTIR difference spectra in the carbonyl region can be seen by comparing the upper and lower panels of Figure 34. Figure 35 shows double difference spectra obtained by subtracting the $P^+Q_A^-/PQ_A$ spectrum of RCs cooled in dark from the corresponding spectrum of RCs cooled in the light. For wild-type RCs, some of the effects of freezing in the light are qualitatively similar to the effects of the R(L135)E mutation: the P^* keto bands at 1703 and 1713 cm^{-1} move apart and become more equal in intensity, and the phase-phonon bands become weaker. In addition, the 10a-ester carbonyl stretching band near 1750 cm^{-1} shifts about 2 cm^{-1} to lower energies and a P^* band at 1655 cm^{-1} increases in intensity. The 1655-cm^{-1} band could reflect C=O stretching of a free acetyl group of $|P_L^+\rangle$ following rupture of the hydrogen bond to His L168. Rotation of the acetyl group or a perturbation of a protein carbonyl group also could possibly account for this band.

Freezing under illumination affects the FTIR spectra of the R(L135)E and R(M164)E RCs in much the same manner as it affects wild-type RCs. The prominent band at 1655 cm^{-1}, the attenuation of the phase-phonon bands, and the small red-shift of the 10a-ester band are seen in both strains. The splitting of the keto bands is particularly clear in the R(L135)E mutant. The difference between the frequencies of the keto bands, 18 cm^{-1} when R(L135)E RCs are cooled in the dark, increases to 22 cm^{-1} when they are cooled in the light. The attenuation of the phase-phonon bands, and a shift of the 1295-cm^{-1} band to higher energy also are more pronounced in this strain and in wild-type RCs than in the R(M164)E mutant. These effects are consistent with the picture that cooling under illumination results in further stabilization of the form of P^* that predominates at room temperature. The relaxation should shift the charge distribution further in the direction of $|P_L^+\rangle$ in wild-type and R(L135)E RCs, but stabilize a more even distribution of charge in the R(M164)E mutant.

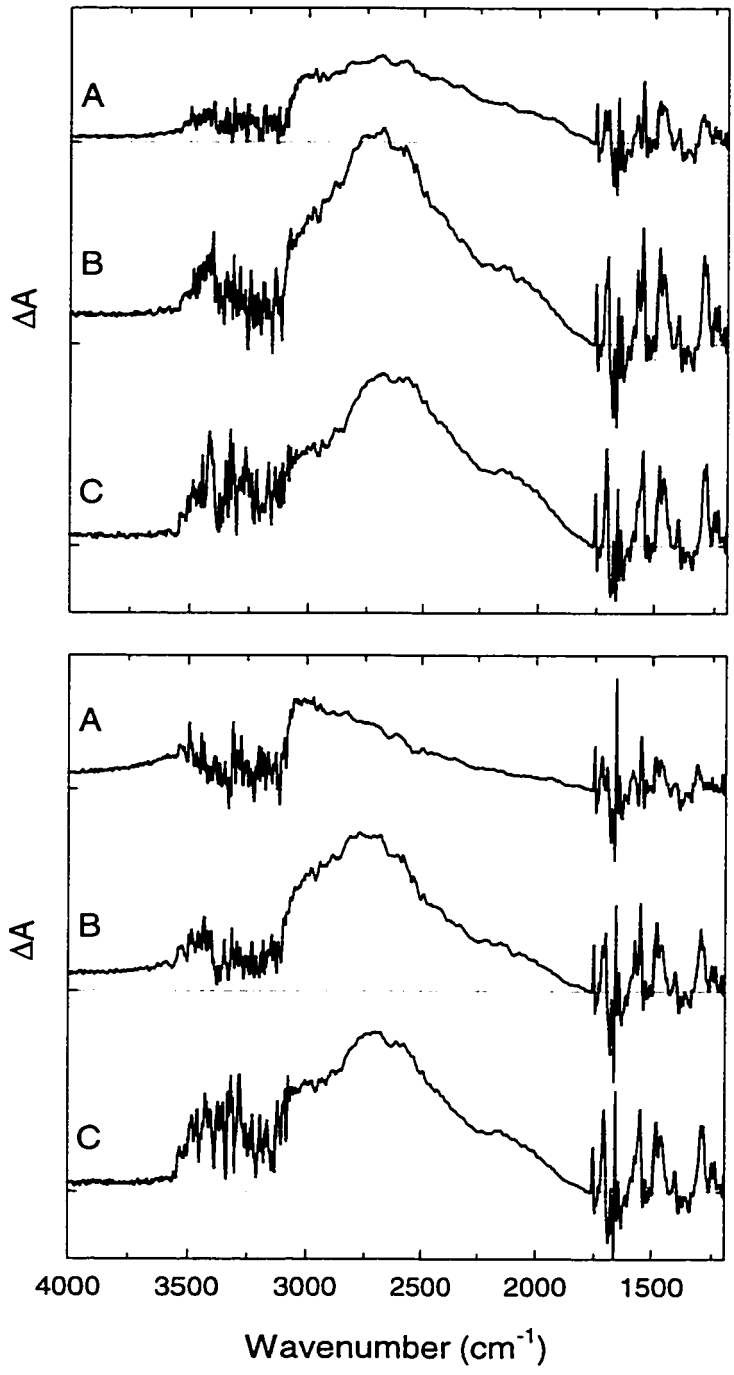

Figure 36. $P^+Q_A^-/PQ_A$ FTIR difference spectra of (*A*) R(L135)E, (*B*) wild-type and (*C*) R(M164)E RCs in hydrated films that were cooled to 100 K in the dark (*top panel*) or light (*bottom*).

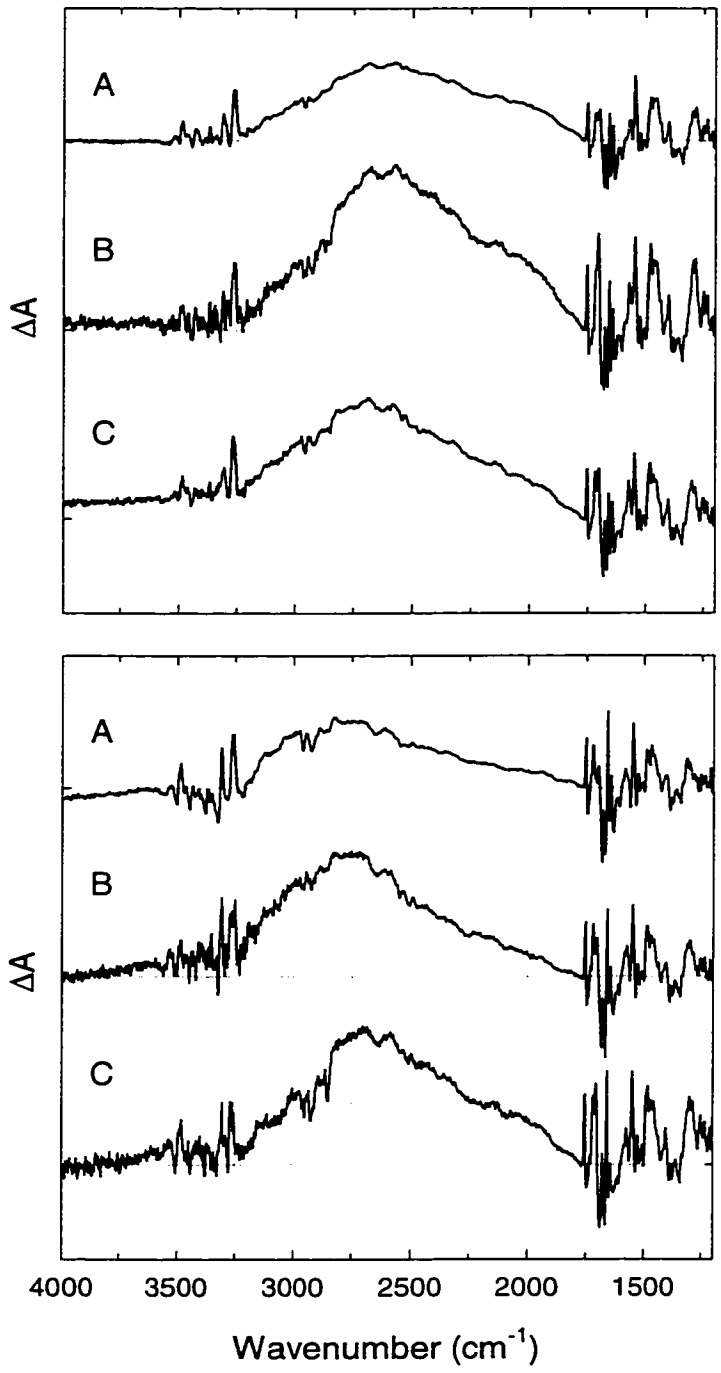

Figure 37. $P^+Q_A^-/PQ_A$ FTIR difference spectra of (*A*) R(L135)E, (*B*) wild-type and (*C*) R(M164)E RCs in "dry" films that were cooled to 100 K in the dark (*top panel*) or light (*bottom*).

Table 13. Reduction Potentials and FTIR Peak Energies in Wild-Type and Mutant RCs [a]

Strain	ΔE_m (mV)	ΔE_{FC} (cm^{-1})			
		hydr, dark[b]	hydr, light[c]	dry, dark[d]	dry, light[e]
R(M164)E	-32	2650	2700	2650	2700
R(M164)L	-16	ND	ND	ND	ND
Wt	(0)	2700	2750	2690	2750
R(L135)L	-20	2700	ND[f]	2650	2830
R(L135)E	-36	2700	>3000	2650	2840

[a] ΔE_m is the measured change in reduction potential relative to wild-type RCs (from (*242*)). The errors are ±5 mV. ΔE_{FC} is the measured absorption maximum of the electronic absorption band near 2700 cm^{-1}.
[b] Hydrated films cooled in the dark.
[c] Hydrated films cooled in the light.
[d] "Dry" films cooled in the dark.
[e] "Dry" films cooled in the light.
[f] Not determined.

Effects of the mutations on the 2700-cm^{-1} electronic absorption band of P$^+$. Figures 36 and 37 show light-induced FTIR difference spectra over a broader spectral range that includes the electronic absorption band of P$^+$ near 2700 cm^{-1}. The energy and dipole strength of this band are expected to depend on the energies of the basis states $|P_L^+\rangle$ and $|P_M^+\rangle$ and the coupling strength between these states (*47, 180, 183, 214, 215*) (*211, 241*). The phase-phonon bands in the regions of 1290, 1480 and 1560 cm^{-1}, which as mentioned above represent vibrational modes that become allowed by coupling to the electronic transition, also can be seen in Figures 36 and 37. The 2700-cm^{-1} band and the phase-phonon bands are seen in RCs in which P is oxidized either photochemically or electrochemically, but are not seen for monomeric Bchl in solution (*47, 215*). They are lost in the heterodimer RCs, where the charge of P$^+$ probably locates exclusively on the remaining Bchl (*47, 215*). The shape of the electronic band and the significance of the shoulder at 2200 cm^{-1} are not well understood, although several groups have attempted to describe the coupling of the electronic and vibrational transitions (*183*) (*211*).

Hydrated films of RCs cooled in the dark show only modest differences between the wild-type and mutant RC spectra in the 2700-cm^{-1} region (Figure 36, *upper panel*). The R(L135)E spectrum is broadened and has a smaller dipole strength, but the peak position is not changed significantly. The peak shifts about 50 cm^{-1} to lower energies in the R(M164)E mutant (see Table 13). Larger differences in the 2700-cm^{-1} band are seen if the RCs are illuminated during cooling (Figure 36, *lower panel*). In wild-type RCs, the peak shifts to higher frequencies by 70 cm^{-1} compared to RCs that are cooled in the dark. Such a shift would be be expected if $|P_L^+\rangle$ is further stabilized relative to $|P_M^+\rangle$, increasing the energy difference between the ground and excited stationary states. The R(M164)E spectrum remains red-shifted by 55 cm^{-1} relative to the wild-type spectrum measured under the same conditions, but the R(L135)E spectrum now is shifted strongly to the blue. The absorption maximum of the R(L135)E spectrum cannot be determined accurately because the spectrum is distorted by water absorption in the region above 3000 cm^{-1}.

To minimize interference by water absorption, samples also were prepared as "dry" films containing reduced amounts of water (Figure 37). These spectra show the shift of the 2700-cm^{-1} band to higher energies in the L135 mutants more clearly. When the RCs are cooled in the light, the absorption band peaks at 2700 cm^{-1} in R(M164)E RCs, 2750 cm^{-1} in wild-type RCs, and 2840 cm^{-1} in R(L135)E (see Figure 37, *lower panel*, and Table 13). In the R(L135)L mutant, the peak is at 2830 cm^{-1} (not shown).

In the carbonyl region, the $P^+Q_A^-/PQ_A$ difference spectra of chromatophores from the strains containing the Leu or Glu mutation at L135 or M164 were similar to the spectra of purified RCs (not shown). However, the differences in the 2700 cm^{-1} band observed in the detergent-solubilized RCs were less apparent in the chromatophore spectra. The spectra of the purified RCs are emphasized above because they allow a more direct comparison to the Special TRIPLE measurements.

Discussion

The data presented above show that mutations of ionizable groups near P^+ can cause significant redistributions of the charge between P_L and P_M. Arginines L135 and M164 are removed from direct interaction with the Bchls and mutations of these residues appear not to alter the intramolecular spin distributions of the individual Bchls significantly (see the ratios R_L and R_M in Table 12), indicating that the molecular orbitals are largely unchanged. In the wild-type RC, $|P_L^+\rangle$ is stabilized relative to $|P_M^+\rangle$, and mutations that replace Arg(L135) by a neutral or negatively charged group should further stabilize $|P_L^+\rangle$ and both lower the E_m and increase the charge-distribution ratio ρ_L/ρ_M. Homologous mutations of Arg(M164) should stabilize $|P_M^+\rangle$, lower the E_m and decrease ρ_L/ρ_M. The measured charge distributions are qualitatively consistent with these expectations.

In comparing experimental results from ENDOR/TRIPLE and FTIR spectroscopy, it is important to bear in mind the differences between the conditions used for the two experiments. Although purified RCs in CHAPS detergent were used throughout, the FTIR measurements required partially dehydrated films, while the TRIPLE spectra were recorded in solution. However, the RCs probably remain well solvated in the films because, as shown in Figures 36 and 37, films containing different amounts of water give similar spectra. Resonance Raman spectra of RCs in solution also are in good accord with FTIR spectra of films (*239*). The E_m values used in the analysis were measured in solutions containing LDAO, but were found not to depend significantly on the choice of detergent (*242*).

A second difference is that the TRIPLE spectra were measured at 288 K, while the FTIR spectra were measured at 100 K. However, ENDOR/TRIPLE spectra of wild-type RCs have been measured previously over a wide range of temperatures and the charge distribution ratio was found to be relatively insensitive to the temperature (*219*). Temperature also has relatively little effect on the FTIR spectra of wild-type RCs (*47*), and we found that $P^+Q_A^-/PQ_A$ difference spectra of wild-type and mutant chromatophores at room temperature (not shown) were similar to those of purified RCs at 100 K.

Finally, and perhaps most importantly, somewhat different protocols were used to generate P^+ for the TRIPLE and FTIR spectra. In the TRIPLE measurements, the sample was illuminated by saturating, continuous light. These conditions allow the protein to relax around P^+, which could further stabilize $|P_L^+\rangle$ relative to $|P_M^+\rangle$ and make the charge distribution more asymmetric. In the FTIR measurements, the sample is alternately exposed to dark and subsaturating light in order to obtain a difference spectrum. The illumination period of 12 s could be too short for the protein to relax fully around P^+. For this reason, the conditions used for the TRIPLE spectra probably are more comparable to those in RC films that are frozen in the light than to those of films frozen in the dark. Slow structural changes during and after illumination have

been implicated previously in a complex dependence of the steady-state electron-transfer kinetics on light intensity (*243*). The FTIR spectra suggest that loosening or rupture of the hydrogen bond between H(L168) and the acetyl group of P_L could be a major component of this relaxation.

To discuss the effects of the mutations more quantitatively, it is helpful to start with the simple model shown in Figure 38 for the oxidized dimer P^+. The model at this level includes electronic, but not vibronic coupling. The Hamiltonian for this system is

$$\mathbf{H} = \begin{vmatrix} E_L & \beta \\ \beta & E_M \end{vmatrix}, \quad (2)$$

where E_L and E_M are the energies of the diabatic basis states $|P_L^+\rangle$ and $|P_M^+\rangle$, and β is the electronic coupling strength. Diagonalization yields two eigenstates, $|\Psi_+\rangle = 2^{-1/2}(1+s)^{1/2}|P_M^+\rangle + 2^{-1/2}(1-s)^{1/2}|P_L^+\rangle$ and $|\Psi_-\rangle = 2^{-1/2}(1-s)^{1/2}|P_M^+\rangle - 2^{-1/2}(1+s)^{1/2}|P_L^+\rangle$, where $s = \delta/(\delta^2 + 4\beta^2)^{1/2}$ and $\delta = E_M - E_L$. The energies of these states are given by

$$E_\pm = \frac{E_L + E_M}{2} \mp \frac{1}{2}\sqrt{\delta^2 + 4\beta^2}\,. \quad (3)$$

Semiempirical molecular orbital calculations indicate that β is negative, making E_+ the lower eigenvalue (*244*).

In the two-state model, the midpoint reduction potential of P/P^+ is

$$E_m = E_+/e + B, \quad (4)$$

where e is the electron charge and B is a constant. The ratio of the net charges on P_L and P_M, which is obtained experimentally from the TRIPLE spectra as described above

(equation 1), can be related to the ratio of the squares of the coefficients for $|P_L^+\rangle$ and $|P_M^+\rangle$ in the ground-state eigenfunction:

$$\frac{\rho_L}{\rho_M} = \frac{|\langle P_L^+ | \Psi_+ \rangle|^2}{|\langle P_M^+ | \Psi_+ \rangle|^2} = \left(\sqrt{x^2+1} + x\right)^2, \quad (5)$$

where $x = \delta/2\beta$. Rearranging this expression gives

$$\frac{\delta}{\beta} = 2x = \left(\frac{\rho_L}{\rho_M}\right)^{\frac{1}{2}} - \left(\frac{\rho_L}{\rho_M}\right)^{-\frac{1}{2}}, \quad (6)$$

The electronic model also provides the 0-0 energy difference between the two eigenstates:

$$\Delta E_{00} = E_- - E_+ = \sqrt{\delta^2 + 4\beta^2}. \quad (7)$$

The broad FTIR absorption band peaking near 2700 cm^{-1} has been assigned to this excitation (*47*).

In previous analyses of mutations that add or remove a hydrogen bond to P_L or P_M, it was reasonable to assume that each mutation affected only the Bchl closer to the amino acid residue that was modified (*168, 182*). This simplifying assumption probably would be unrealistic in the present study, where the distances from the two arginines to the nearest atom of P_L or P_M differ by less than a factor of 2 (see Figure 32). Not surprisingly, fitting the present data under this assumption required using very different values of β for the M164 and L135 mutants. We therefore estimated the effects of the mutations on the solvation energies of $|P_L^+\rangle$ and $|P_M^+\rangle$ by electrostatics calculations, using the expression

$$\Delta V_{sol} = \sum_{i}^{P} (Q_i^+ - Q_i^o) \sum_{j}^{protein} \frac{q_j}{f_{ij} r_{ij}} . \quad (8)$$

Here index i runs over the atoms of P_L and P_M, Q_i^+ and Q_i^o denote the charges of atom i in P^+ and P; q_j is the charge of protein atom j; r_{ij} is the distance between atoms i and j; and f_{ij} is a distance-dependent screening function. We used the screening function

$$f_{ij} = 1 + 60(1 - \exp(-0.1 r_{ij})), \quad (9)$$

which has been found to reproduce measured effects of ionizable groups on pK_a and E_m values in these mutants and other proteins (*54*) (*242*).

A disadvantage of using a phenomenological distance-dependent screening function is that the self-energies of the basis states cannot be calculated directly. The total energy difference between the basis states (δ) is, therefore, given by the calculated difference in solvation energies ($\delta_{calc} = \Delta V_{sol}^{P_M^+} - \Delta V_{sol}^{P_L^+}$) plus an unknown constant (δ_o). However, dividing the energy difference by the coupling strength gives

$$\left(\frac{\rho_L}{\rho_M}\right)^{1/2} - \left(\frac{\rho_L}{\rho_M}\right)^{-1/2} = \frac{\delta}{\beta} = \frac{\delta_{calc}}{\beta} + \frac{\delta_0}{\beta} . \quad (10)$$

Figure 39 shows a linear regression of the Special TRIPLE data to this expression, which yields $\beta = 40$ meV (320 cm^{-1}) and $\delta_o = -13$ meV.

The electrostatics calculations also provide the shifts in the energies of the basis states for each mutant relative to wild-type RCs, allowing the change in the E_m (ΔE_m) to be calculated by equations 3 and 4. The predicted shifts in the E_m are given in Table 14.

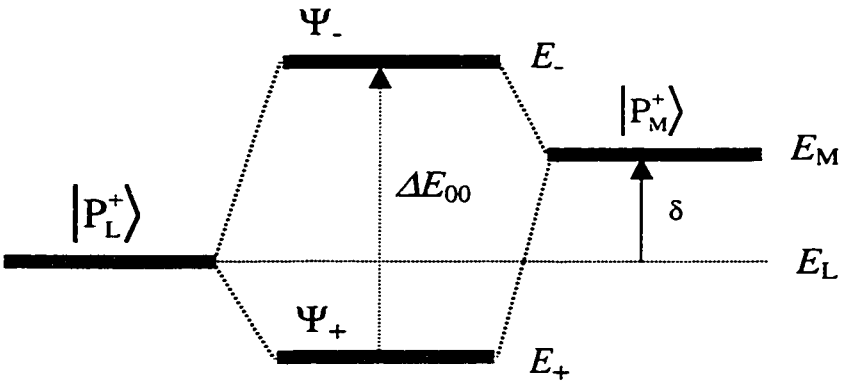

Figure 38. Two-state electronic model for P^+. E_L and E_M are the energies of the basis states $|P_L^+\rangle$ and $|P_M^+\rangle$. The difference between E_L and E_M (δ) and the electronic coupling of the basis states (β) determine the energies (E_+ and E_-) of the eigenstates (Ψ_+ and Ψ_-) ΔE_{00} is the 0-0 energy of the electronic transition between the eigenstates in the absence of vibronic coupling. The midpoint reduction potential (E_m) depends on the energy of the lower eigenstate.

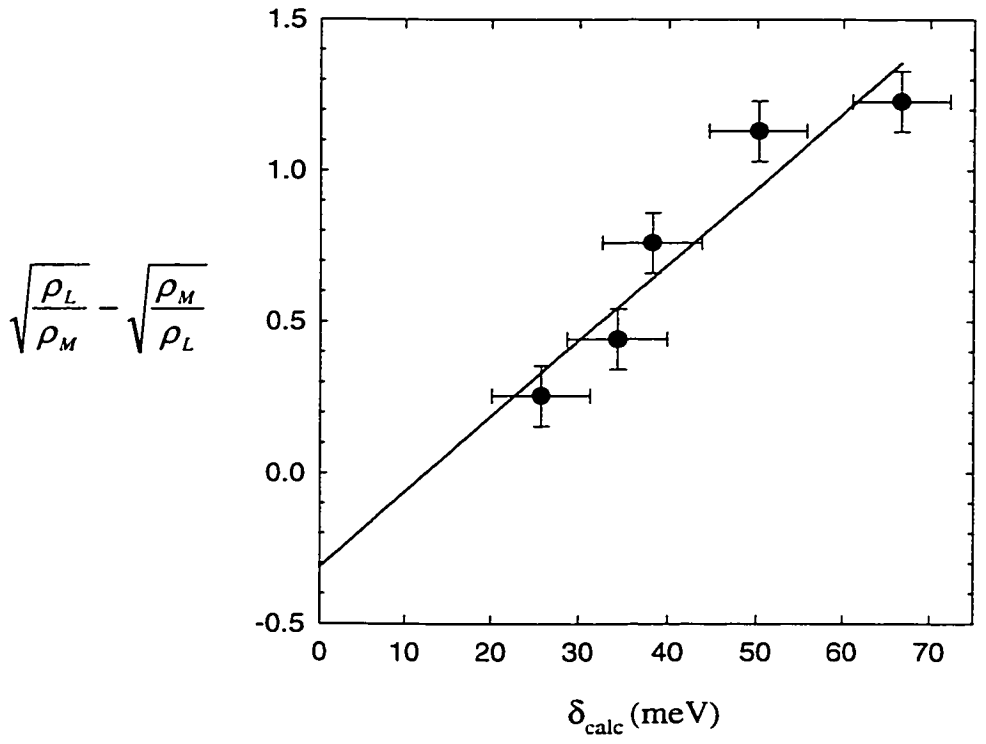

Figure 39. The calculated differences in solvation energy of $|P_L^+\rangle$ and $|P_M^+\rangle$ for wild-type, L135 and M164 mutant RCs calculated by equations 8 and 9, plotted against the ratio δ/β obtained from the Special TRIPLE spectra by equation 6. A least-squares fit of the data to equation 10 (*solid line*) gave $\beta = 40$ meV and $\delta_o = -12$ meV.

Table 14. Calculated Spin Distributions, Energies, Changes in Reduction Potential, and 0-0 Transition Energies in the Electronic Model [a]

Strain	δ_{calc} (meV)	ΔE_L (meV)	ΔE_M (meV)	δ (meV)	ρ_L/ρ_M	ΔE_m^{calc} (mV)	ΔE_{00}^{calc} (cm^{-1})
R(M164)E	26	-27	-39	13	1.4	-32	655
R(M164)L	35	-16	-19	22	1.7	-17	671
Wt	39	(0)	(0)	26	1.9	(0)	678
R(L135)L	51	-26	-14	38	2.5	-22	714
R(L135)E	67	-56	-28	54	3.5	-48	778

[a] The diabatic solvation energy difference (δ_{calc}) and changes in the basis state energies (ΔE_L and ΔE_M) were calculated with equations 8 and 9. δ_0 (-13 meV) and β (40 meV or 320 cm^{-1}) were obtained by fitting the measured ρ_L/ρ_M and δ_{calc} to equation 10. The total electronic energy δ was taken to be $\delta_{calc} + \delta_0$. The 0-0 transition energy (ΔE_{00}^{calc}) and the shift in the E_m relative to wild-type RCs (ΔE_m^{calc}) were calculated by equations 4 and 7. The model used here does not include vibronic coupling.

The calculated value agrees well with the measured ΔE_m in the R(L135)L, R(M164)L and R(M164)E mutants, but is somewhat too large in R(L135)E.

Table 14 also gives the calculated 0-0 transition energies (ΔE_{00}) for the electronic excitation of P. The predicted changes are comparable to the observed shifts in the 2700-cm^{-1} absorption band (cf. Table 13). The absolute values of ΔE_{00}, however, are on the order of 700 cm^{-1}, which is far below the observed Franck-Condon maximum of the absorption band. This difference is not unexpected, because the simple electronic model neglects vibronic coupling.

Vibronic coupling can have large effects on the absorption spectra of intervalence dimers with rotational symmetry and could also affect the apparent values of β and δ (*211, 225-227, 241*). To explore these points, we used the treatment developed by Piepho, Schatz and coworkers (*225-227*), which begins by defining symmetric and antisymmetric combinations of the highest occupied molecular orbitals (HOMOs) of P_M and P_L :

$$|a\rangle = \frac{1}{\sqrt{2}}(|P_M\rangle - |P_L\rangle) \tag{11a}$$

$$|b\rangle = \frac{1}{\sqrt{2}}(|P_M\rangle + |P_L\rangle). \tag{11b}$$

$|P_M\rangle$ and $|P_L\rangle$ here are equivalent to $|P_L^+\rangle$ and $|P_M^+\rangle$, respectively, in the model described above. With these definitions, the eigenstates of the electronic model (still omitting vibronic coupling) can be written

$$\Psi_+ = c_1|a\rangle + c_2|b\rangle \tag{12a}$$

$$\Psi_- = c_2|a\rangle - c_1|b\rangle. \tag{12b}$$

Here $$c_1 = \tfrac{1}{2}(1-s)^{1/2} - \tfrac{1}{2}(1+s)^{1/2}, \quad (13a)$$

$$c_2 = \tfrac{1}{2}(1-s)^{1/2} + \tfrac{1}{2}(1+s)^{1/2}, \quad (13b)$$

and as before, $s = \delta / (\delta^2 + 4\beta^2)^{1/2}$ and $\delta = E_M - E_L$. The vibronic basis then consists of products of the form $\chi_i \Psi_\pm$, where χ_i is the nuclear wavefunction for vibrational state *i*.

The diagonal and off-diagonal elements of the vibronic Hamiltonian were given by Piepho et al. (*225*) for a symmetric dimer ($\delta = 0$) and by Gasnya et al. (*226*) for an asymmetric dimer ($\delta \neq 0$). Both groups considered a single, symmetric vibrational mode with frequency ν_{sym} and coupling factor λ_{sym}, and a single antisymmetric mode with frequency ν_{anti} and coupling factor λ_{anti}, and we used the same model. For the reaction center, the symmetric mode could represent breathing motions that shift the centers of P_L and P_M towards or away from each other. Motions of this type would have relatively little effect on the orbital energy difference between $|P_M\rangle$ and $|P_L\rangle$ but could modulate the energy difference between the bonding and antibonding combinations, $|a\rangle$ and $|b\rangle$. The antisymmetric mode could represent an antisymmetric combination of monomer vibrations that are displaced along a local vibrational coordinate when the neutral Bchl is oxidized. This mode would modulate the energy difference between $|P_M\rangle$ and $|P_L\rangle$.

The eigenvectors of the vibronic Hamiltonian are

$$|\Psi_n\rangle = \sum_{i=1}^{N} \left\{ k_{i+}^n |\Psi_+\rangle + k_{i-}^n |\Psi_-\rangle \right\} |\chi_i\rangle. \quad (14)$$

Expanding equation 14 into the basis states and using the orthogonality conditions for electronic and nuclear states leads to the following expression for the spin-distribution ratio in eigenstate *n*:

$$\frac{\rho_L}{\rho_M} = \frac{\left|\langle P_L^+ | \Psi_n \rangle\right|^2}{\left|\langle P_M^+ | \Psi_n \rangle\right|^2} = \frac{\left|\langle P_M | \Psi_n \rangle\right|^2}{\left|\langle P_L | \Psi_n \rangle\right|^2} =$$

$$\frac{\sum_i^N \left\{ (k_{i+}^n)^2 (1 - 2c_1c_2) + (k_{i-}^n)^2 (1 + 2c_1c_2) - 2k_{i+}^n k_{i-}^n (c_1^2 - c_2^2) \right\}}{\sum_i^N \left\{ (k_{i+}^n)^2 (1 + 2c_1c_2) + (k_{i-}^n)^2 (1 - 2c_1c_2) + 2k_{i+}^n k_{i-}^n (c_1^2 - c_2^2) \right\}}. \quad (15)$$

This expression reduces to equation 4 of Gasyna et al. (*183*) if only one of the coefficients k_{i+}^n or k_{i-}^n is nonzero.

We constructed the vibronic Hamiltonian for various values of β, δ, and the two vibrational frequencies and coupling strengths, and obtained the eigenvalues and eigenvectors with the program PKS2 essentially as described (*225-227*). Figure 40 shows the dependence of the calculated spin-distribution ratio on the energy difference δ at various values of β and the vibronic couplings. The vibrational energies were ν_{sym} = 154 cm^{-1} and ν_{anti} = 1630 cm^{-1}, as suggested by Gasnya et al. (*183*). With no vibronic coupling ($\lambda_{sym} = \lambda_{anti} = 0$, panel *A*) the model reduces to the two-state electronic model discussed above (equation 5); ρ_L/ρ_M grows approximately quadratically with δ and the curvature decreases with increasing β. Strong electronic coupling thus tends to equalize the populations of P_M^+ and P_L^+ even at large δ, as expected. Panel *B* shows the effect of the coupling to the symmetric mode ($\lambda_{sym} > 0$) with $\lambda_{anti} = 0$ and β held at 600 cm^{-1}. For $0 < \lambda_{sym} < 1$, ρ_L/ρ_M retains the approximately quadratic dependence on δ up to at least 2000 cm^{-1}. With larger values of λ_{sym}, ρ_L/ρ_M goes through a maximum and then drops to an asymptotic value of 1 at large δ. Increasing λ_{sym} moves the peak to lower values of δ and decreases the peak height. Increasing β at constant λ_{sym} shifts the peak to higher values of δ (not shown). Strong coupling to a symmetric vibrational mode thus also can

equalize the populations of P_M^+ and P_L^+ even when δ is large, but this effect becomes less important if β is large.

Figure 40*C* shows the effect of coupling to the antisymmetric mode ($\lambda_{anti} > 0$) with $\lambda_{sym} = 0$ and β again fixed at 600 cm^{-1}. Increasing λ_{anti} makes ρ_L/ρ_M an increasingly strong function of δ.

The experimental spin-distribution ratios and a family of curves generated using the vibronic model are plotted as functions of δ in figure 41*A*. The values of δ for the experimental points were calculated using the distance-dependent screening function and no offset (equations 8-10 with $\delta_0 = 0$). The theoretical curves shown were calculated with ν_{sym} = 154 cm^{-1}, λ_{sym} = 2.6, ν_{anti} = 1630 cm^{-1}, λ_{anti} = 0.3, and values of β between 450 and 900 cm^{-1}. Qualitatively acceptable fits to the experimental ρ_L/ρ_M were possible using λ_{sym} between 2.25 and 2.75, and λ_{anti} between 0.1 and 0.3. Values of λ_{sym} greater than 3.0 made ρ_L/ρ_M increase too slowly with δ. Decreasing λ_{sym} below 2.5 led to significant disagreement between the calculated and experimental spectra (not shown). Adding or subtracting a small offset (δ_0) to δ_{calc} would shift the experimental values of ρ_L/ρ_M horizontally but would not greatly restrict the choice of β.

The calculated absorption spectrum of P^+ depends strongly on the vibronic and electronic coupling strengths. In general, the peak of the absorption shifts to higher energies as either λ_{sym} or λ_{anti} is increased. The dependence of the calculated spectrum on β is more complex and is illustrated in figure 41*B* for the same vibronic parameters as used in Figure 41*A*. In contrast to the simple electronic model, where increasing β always increases ΔE_{00}, the absorption spectrum for small β (β = 300 cm^{-1}) peaks above 2500 cm^{-1} and the spectrum shifts to the red as β is increased to 600 cm^{-1}. Further increases in β then shift the absorption to the blue. Values of β in the region of 750 to 900 cm^{-1} put the calculated peak near the observed energy for wild-type RCs.

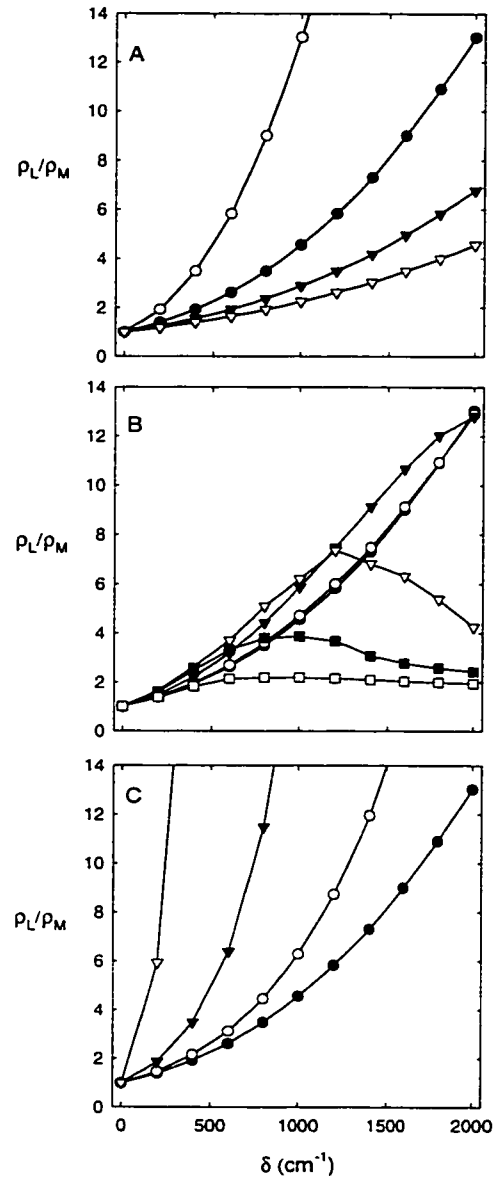

Figure 40. Spin-distribution ratio (ρ_L/ρ_M) calculated by equation 15, as a function of the basis state energy difference (δ) and the electronic coupling strength (β). (*A*) No vibronic coupling ($\lambda_{sym} = \lambda_{anti} = 0$); $\beta = 300$ cm^{-1} (○), 600 cm^{-1} (●), 900 cm^{-1} (▼) or 1200 cm^{-1} (▽). (*B*) Coupling to a symmetric mode only; $\beta = 600$ cm^{-1}; $\lambda_{anti} = 0$; $\lambda_{sym} = 0$ (●), 1.0 (○), 2.0 (▼), 2.3 (▽), 2.6 (■) or 3.0 (□). (C) Coupling to an antisymmetric mode only; $\beta =$ 600 cm^{-1}; $\lambda_{sym} = 0$; $\lambda_{anti} = 0$ (●), 0.3 (○), 0.6 (▼) or 1.0 (▽).

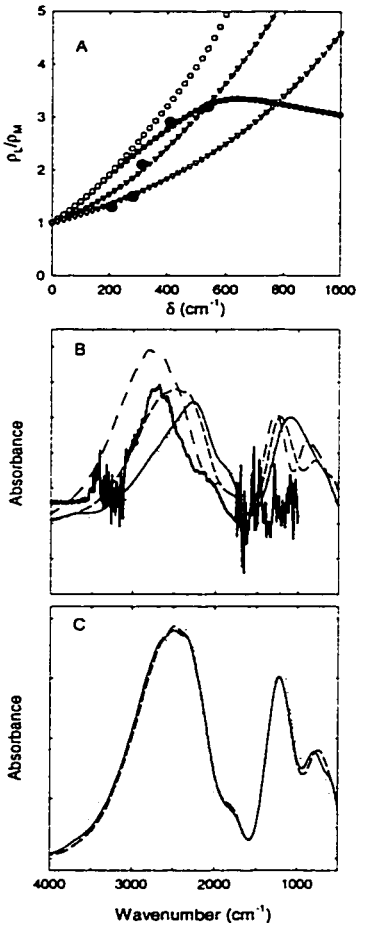

Figure 41. (*A*) Experimental spin-distribution ratios (ρ_L/ρ_M) for wild-type, L135 and M164 mutant RCs (+) as functions of δ_{calc} (the difference in solvation energy of $|P_L^+\rangle$ and $|P_M^+\rangle$ calculated by equations 8 and 9). The lines show the values of ρ_L/ρ_M calculated for the vibronic model by equation 15 with $\lambda_{sym} = 2.6$, $\nu_{sym} = 154$ cm^{-1}, $\lambda_{anti} = 0.3$, $\nu_{anti} = 1630$ cm^{-1} and $\beta = 450$ cm^{-1} (●), 600 cm^{-1} (○), 750 cm^{-1} (▼) or 900 cm^{-1} (∇). (*B*) Comparison of the experimental $P^+Q_A^-/PQ_A$ FTIR difference spectrum for a hydrated film of wild-type RCs (thick solid line) and calculated P^+ absorption spectra for the vibronic model with β = 450 cm^{-1} (thin solid line), 600 cm^{-1} (dotted line), 750 cm^{-1} (dashed line) and 900 cm^{-1} (dashed and dotted line). The other model parameters were as in (*A*). (*C*) Effects of the mutations on the P^+ absorption spectrum calculated with the vibronic parameters in (*A*) and $\beta = 750$ cm^{-1}. The basis state energies for the mutations in Table 3 were used to calculate the spectrum for wild-type (solid line), R(L135)E (dotted line) and R(M164)E (dashed line) RCs.

Table 15. Calculated Spin Distribution Ratios Changes in Reduction Potential, and Excitation Energies in the Vibronic Model [a]

Strain	δ (cm^{-1})	ρ_L/ρ_M	ΔE_m^{calc} (mV)	ΔE_{00}^{calc} (cm^{-1})	ΔE_{FC}^{calc} (cm^{-1})
R(M164)E	540	1.6	-31	1515	2484
R(M164)L	411	1.9	-16	1526	2488
Wt	314	2.0	(0)	1533	2488
R(L135)L	282	2.5	-22	1555	2504
R(L135)E	210	3.3	-48	1594	2700[b]

[a] The spin distribution ratio (ρ_L/ρ_M) and the shift in the E_m relative to wild-type RCs (ΔE_m^{calc}) were calculated using equations 11-15 and the vibronic parameters $\lambda_{sym} = 2.6$, $\nu_{sym} = 154\ cm^{-1}$, $\lambda_{anu} = 0.3$, $\nu_{anu} = 1630\ cm^{-1}$ and $\beta = 750\ cm^{-1}$. The diabatic electronic energy difference ($\delta = \delta_{calc}$) was calculated by equations 8 and 9 with no offset. ΔE_{00}^{calc} and ΔE_{FC}^{calc} are the calculated 0-0 and Franck-Condon (peak) transition energies.
[b] High-energy peak (see figure 41).

Figure 41*C* shows the calculated absorption spectra of P^* for the glutamate mutants, as calculated with β = 750 cm^{-1} and the vibronic parameters and values of δ given in Table 15. The R(M164)E mutation shifts the spectrum slightly to the red, while the R(L135)E mutation shifts the spectrum more strongly to the blue and reveals two absorption peaks in the 2700 cm^{-1} band. Table 15 gives the values of ΔE_m and ρ_L/ρ_M for the mutant and wild type strains calculated with β = 750 cm^{-1}. With these values of the parameters, the calculated spin-distribution ratio and ΔE_m agree largely with the experimental results, and the calculated spectral shifts in the mutants are in accord with the changes measured by FTIR spectroscopy. Although the calculated spectra reproduce the observed spectra only qualitatively, Figure 41*C* and Table 15 show that the P^* absorption can be shifted to energies considerably higher than calculated with the simple electronic model, while retaining a delocalized spin-distribution.

Semiempirical molecular orbital calculations using the atomic coordinates from early crystal structures from *Rb. sphaeroides* and a four-orbital model for the individual Bchls have given a value of about 500 cm^{-1} for β (*47, 180*), which is within the range of the values used here. The electronic coupling factor (β) that mixes $|P_L\rangle$ and $|P_M\rangle$ is similar to the coupling factor (β') that mixes charge-transfer transitions with exciton transitions in the absorption spectrum of P. However, the pertinent resonance integrals for P^* involve only the overlap of the HOMOs of P_L and P_M, while β' also includes contributions from overlap of the LUMOs of P_L and P_M (*27*). The relationship between the two resonance integrals is not simple, but for the structure of the dimer found in the RC, β' should be somewhat larger than β. A β' of 800 cm^{-1} was calculated from the atomic coordinates for *Rp. viridis* RCs and provided a reasonable account of the absorption spectrum (*27*). Our analysis of the present data seems consistent with this value of β'. More recently, Zhou *et al.* (*22*) fit the absorption spectrum of heterodimer and hydrogen-bonding double mutants of *Rb. sphaeroides* by including a distribution of

CT states energies. These authors obtained a smaller value of approximately 500 cm^{-1} for β'.

The electronic coupling of P^+ has been estimated from previous studies. Artz et al. (*168*) and Reimers et al. (*182*) fit the spin-distribution ratio and E_m from a series of hydrogen-bonding mutations to a model that includes only electronic coupling. These authors conclude that δ and |β| are, respectively, 1100 and 1400 cm^{-1} for wild-type RCs. A second work (Müh, submitted) extends this analysis to four series of hydrogen-bonding mutations and determine that δ is approximately 450 cm^{-1} and |β| is between 950 and 1300 cm^{-1} for the wild-type RC. These numbers are larger than the values obtained by our treatment and reflect, in part, the absence of vibronic coupling and, possibly, changes in β caused by the mutations.

Models that include explicit vibrational modes have also been used to describe the properties of P^+. Hush et al. (*211, 241*) have discussed the effects of a single antisymmetric mode in calculations of P^+ absorption and determine δ and |β|, respectively, to between 1600-2000 cm^{-1} and 500-800 cm^{-1}. Gasnya et al. (*183*) include both a symmetric and an antisymmetric mode in their model for P^+ and obtain qualitative fits to the P^+ absorption using δ and β equal to, respectively, 300 cm^{-1} and -480 cm^{-1}. However, the spin-distribution ratio for these values is 1.4 which is more symmetric than the observed value of 2.1. Gasnya et al. discuss the asymmetry of P^+ and choose δ and β based on Special TRIPLE spectra of wild-type RCs (*219*) , but their description of the spin-distribution ratio does not include mixing of the electronic states by the vibronic coupling.

Despite the success of the PKS2 model, the calculated P^+ absorption spectrum of Figure 41*C* has several deficiencies. The predicted peak is somewhat too low in energy when the spin-distribution ratio is fit, the high-energy tail of the calculated spectrum is broader than that of the experimental spectrum, and the theory does not account well for the shoulder observed at 2200 cm^{-1}. Further, the calculated spectrum has absorption

bands at 600 $cm^{-1}$and 1300 cm^{-1} that are considerably stronger than the observed phase-phonon bands. A model with more than two vibrational modes could possibly remedy these deficiencies, but would not seem justified in light of the limited number of experimental data points and the uncertainties in the calculated values of δ.

The keto C=O stretching regions of the FTIR difference spectra also have several puzzling features that remain to be explained. Although P^+ has bands at 1703 and 1713 cm^{-1} in wild-type RCs, we might expect RCs of the R(L135)E mutant described here and the H(M202)L heterodimer mutant to exhibit only one of these bands, since P^+ in both these strains appears to consist mainly of $|P_L^+\rangle$. Instead, as noted above, both these mutants have two bands with similar intensities near 1700 cm^{-1} and 1718 cm^{-1}. The two bands could possibly represent two vibrational modes of an individual P_L molecule, or RCs in two different conformations or ionization states. Alternatively, the presence of the second band may be a result of an electrochromic shift of the keto vibration of P_M induced by the presence of the charge on P_L. Vibrational Stark spectroscopy of the C=O vibration of CO bound to myoglobin has shown that the frequency of carbonyl vibrations can be sensitive to the local electric field (*245*). The observation of two negative bands for P near 1688 and 1696 cm^{-1} also is puzzling in the H(L173)L heterodimer mutant, where the oxidation probably involves mainly P_M. In addition, a comparison of the FTIR difference spectra for the R(L135)E and R(M164)E mutants (Figure 34) suggests that the lower-energy band in the region of 1685-1695 cm^{-1} could be due to P_L and the higher-energy band to P_M, which is opposite the assignment suggested previously (*217*). Complicating the interpretation, this region of the spectrum is congested and the keto vibration of B_L also has been assigned to 1689 cm^{-1} (*246*). Changes in the electric field introduced by R(L135)E and R(M164)E may affect B_L or B_M and contribute to the observed differences.

BIBLIOGRAPHY

1. Perutz, M. F. (1978) *Science 201*, 1187-1191.
2. Warshel, A., and Russell, S. T. (1984) *Quart. Rev. Biophys. 17*, 284-290.
3. Sharp, K. A., and Honig, B. (1990) *Ann. Rev. Biophys. Biophys. Chem. 19*, 301.
4. Warshel, A. (1991) *Computer Modeling of Chemical Reactions in Enzymes and Solutions*, John Wiley & Sons, New York.
5. Warshel, A., and Florián, J. (1998) *Proc. Natl. Acad. USA 95*, 5950-5955.
6. Woodbury, N. W., and Allen, J. P. (1995) in *Anoxygenic Photosynthetic Bacteria* (Blankenship, R. E., Madigan, M. T., and Bauer, C. E., Eds.) pp 527-557, Kluwer Academic Publishers, Dordrecht.
7. Hoff, A. J., and Deisenhofer, J. (1997) *Phys. Reports 287*, 1-247.
8. Williams, J. C., and Taguchi, A. K. (1995) in *Anoxygenic Photosynthetic Bacteria* (Blankenship, R. E., Madigan, M. T., and Bauer, C. E., Eds.) pp 1029-1065, Kluwer Academic Publishers, Dordrecht.
9. Deisenhofer, J., Epp, O., Miki, K., Huber, R., and Michel, H. (1985) *Nature 318*, 618-624.
10. Remsen, C. C. (1978) in *The Photosynthetic Bacteria* (Clayton, R. K., and Sistrom, W. R., Eds.) pp 31-60, Plenum Press, New York.
11. McDermott, G., Prince, S. M., Freer, S. M., Hawthornthwaite-Lawless, A. M., Papiz, M. Z., Cogdell, R. J., and Isaacs, N. W. (1995) *Nature 374*, 517-521.
12. Michel, H., and Deisenhofer, J. (1988) *Biochemistry 27*, 1-7.
13. Pfennig, N. (1978) in *The Photosynthetic Bacteria* (Clayton, R. K., and Sistrom, W. R., Eds.) pp 3-18, Plenum Press, New York.
14. Clayton, R. K. (1965) *Molecular Physics in Photosynthesis*, Blaisdell, New York.
15. Papiz, M. Z., Prince, S. M., Hawthornthwaite-Lawless, A. M., McDermott, G., Freer, A. A., Isaacs, N. W., and Cogdell, R. J. (1996) *Trends Plant Sci. 1*, 198-206.

16. Deisenhofer, J., Epp, O., Miki, K., Huber, R., and Michel, H. (1984) *J. Mol. Biol. 180*, 385-398.

17. Allen, J. P., Feher, G., Yeates, T. O., Komiya, H., and Rees, D. C. (1987) *Proc. Natl. Acad. Sci. USA 84*, 6162-6166.

18. El-Kabbani, O., Chang, C. H., Tiede, D., Norris, J., and Schiffer, M. (1991) *Biochemistry 30*, 5361-5369.

19. Ermler, U., Fritzsch, G., Buchanan, S. K., and Michel, H. (1994) *Structure 2*, 925-936.

20. Kirmaier, C., Holten, D., Bylina, E. J., and Youvan, D. C. (1988) *Proc Natl Acad Sci U S A 85*, 7562-6.

21. McDowell, L. M., Gaul, D., Kirmaier, C., Holten, D., and Schenck, C. C. (1991) *Biochemistry 30*, 8315-22.

22. Zhou, Z., and Boxer, S. G. (1997) *J. Phys. Chem. B 101*, 5759-5766.

23. Lin, X., Murchison, H. A., Nagarajan, V., Parson, W. W., Allen, J. P., and Williams, J. C. (1994) *Proc. Natl. Acad. Sci. USA 91*, 10265-10270.

24. Okamura, M. Y., and Feher, G. (1995) in *Anoxygenic Photosynthetic Bacteria* (Blankenship, R. E., Madigan, M. T., and Bauer, C. E., Eds.) pp 577-594, Kluwer Academic Publishers, Dordrecht.

25. Gouterman, M. (1961) *J. Mol. Spectrosc. 6*, 138-xxx.

26. Hoff, A. J., and Amesz, J. (1991) in *Chlorophylls* (Scheer, H., Ed.) pp 723-738, CRC Press, Boca Raton.

27. Warshel, A., and Parson, W. W. (1987) *J. Am. Chem. Soc. 109*, 6143-6152.

28. Parson, W. W., and Warshel, A. (1987) *J. Am. Chem. Soc. 109*, 6152.

29. Gromet-Elhanan, Z. (1995) in *Anoxygenic Photosynthetic Bacteria* (Blankenship, R. E., Madigan, M. T., and Bauer, C. E., Eds.) pp 807-830, Kluwer Academic Press, Dordrecht.

30. Heller, B. A., Holten, D., and Kirmaier, C. (1995) *Science 269*, 940-945.

31. Alden, R. G., Parson, W. W., Chu, Z. T., and Warshel, A. (1995) *J. Am. Chem. Soc. 117*, 12284-12298.

32. Gunner, M., Nichols, A., and Honig, B. (1996) *J. Phys. Chem. 100*, 4277-4291.

33. Parson, W. W., Chu, Z. T., and Warshel, A. (1990) *Biochim. Biophys. Acta 1017*, 251-272.

34. Nagarajan, V., Parson, W. W., Davis, D., and Schenck, C. C. (1993) *Biochemistry 32*, 12324-12336.

35. van Grondelle, R., Dekker, J. P., Gilbro, T., and Sundstrom, V. (1994) *Biochim. Biophys. Acta 1187*, 1-65.

36. Freer, A., Prince, S., Sauer, K., Papiz, M., Hawthornthwaite-Lawless, A., McDermott, G., Cogdell, R., and Isaacs, N. W. (1996) *Structure 4*, 449-62.

37. Koepke, J., Hu, X., Muenke, C., Schulten, K., and Michel, H. (1996) *Structure 4*, 581-97.

38. Wu, H. M., Reddy, N. R. S., and Small, G. J. (1997) *J. Phys. Chem. 1997*, 651-656.

39. Sauer, K., Cogdell, R., Prince, S. M., Freer, A. A., Isaacs, N. W., and Scheer, H. (1996) *Photochem Photobiol 64*, 564-576.

40. Breton, J., Vermeglio, A., Garrigos, M., and Paillotin, G. (1981) in *Photosynthesis III. Structure and Molecular Organization of the Photosynthetic Apparatus* (Akoyunoglu, G., Ed.) pp 445-459, Balaban International Science Services, Philadelphia.

41. Angerhofer, A., Bornhauser, F., Gall, A., and Cogdell, R. J. (1995) *J. Chem. Phys. 194.*

42. Shreve, A. P., Trautmann, J. K., Frank, H. A., Owens, T. G., and Albrecht, A. C. (1991) *Biochim. Biophys. Acta 1058*, 280-287.

43. Hess, S., Visscher, K. J., Pullerits, T., Sundstrom, V., Fowler, G. J., and Hunter, C. N. (1994) *Biochemistry 33*, 8300-5.

44. Jimenez, R., Dikshit, S. N., Bradforth, S. E., and Fleming, G. R. (1996) *J. Phys. Chem. 100*, 6825-6834.

45. Warshel, A. (1977) *Comp. Chem. 1*, 195-202.

46. Warshel, A., and Lappicirella, A. (1981) *J. Am. Chem. Soc. 103*, 4664-4673.

47. Breton, J., Nabedryk, E., and Parson, W. W. (1992) *Biochemistry 31*, 7503-7510.

48. Parson, W. W., Creighton, S., and Warshel, A. (1989) *J. Am. Chem. Soc. 111*, 4277.

49. Petke, J. D., Maggoira, G. M., Shipman, L. L., and Christofferson, R. E. (1980) *Photochem Photobiol 32*, 399-414.

50. Jentzen, W., Simpson, M. C., Hobbs, J. D., Song, X., Ema, T., Nelson, N. Y., Medforth, C. J., Smith, K. M., Veyrat, M., Mezzanti, M., Ramasseul, R., Marchon, J. L., Takenuchi, T., Goddard, W. A. I., and Shelnutt, J. A. (1995) *J. Am. Chem. Soc. 117*, 11085-11097.

51. Barkigia, K. M., Chantranupong, L., Smith, K. M., and Fajer, J. (1988) *J. Am. Chem. Soc. 110.*

52. Scherz, A., and Parson, W. W. (1984) *Biochim. Biophys. Acta 766*, 653-665.

53. Roothan, C. C. J. (1951) *Rev. Mod. Phys. 23*, 69.

54. Warshel, A., Russell, S. T., and Churg, A. K. (1984) *Proc. Natl. Acad. Sci. USA 81*, 4785-4789.

55. Murrell, J. N., and Tanaka, J. (1964) *J. Mol. Phys. 7*, 363-380.

56. Azumi, T., Armstrong, A. T., and McGlynn, S. P. (1964) *J. Chem. Phys. 41*, 3839.

57. Parson, W. W., Creighton, S., and Warshel, A. (1987) in *Primary Processes in Photobiology* (Kobayashi, T., Ed.) pp 43, Springer-Verlag.

58. Warshel, A., Creighton, S., and Parson, W. W. (1988) *J. Phys. Chem. 92*, 2696-2701.

59. Plato, M., Möbius, K., Michel-Beyerle, M. E., Bixon, M., and Jortner, J. (1988) *J. Am. Chem. Soc. 110*, 7279-7285.

60. Scherer, P. O. J., and Fischer, S. F. (1987) *Chem. Phys. Lett. 103*, 32-36.

61. Warshel, A., and Parson, W. W. (1991) *Ann. Rev. Phys. Chem. 42*, 279-309.

62. Moser, C. C., Keske, J. M., Warncke, K., Farid, R. S., and Dutton, P. L. (1992) *Nature 355*, 796-802.

63. Tinoco, I. (1962) *Adv. Chem. Phys. 4*, 113-159.

64. Hayes, J. M., Gillie, J. K., Tang, D., and Small, G. J. (1988) *Biochim. Biophys. Acta 932*, 287-305.

65. Reddy, N. R. S., Picorel, R., and Small, G. J. (1992) *J. Phys. Chem. 96*, 6458-6464.

66. Reddy, N. R. S., Cogdell, R. J., Zhao, L., and Small, G. J. (1993) *Photochem Photobiol 57.*

67. Manneback, C. (1951) *Physica 17*, 1001-1010.

68. Cogdell, R. J., Durant, I., Valentine, J., Lindsay, J. G., and Schmidt, K. (1983) *Biochim. Biophys. Acta 722*, 427-455.

69. Clayton, R. K. (1966) *Photochem Photobiol 5*, 669-677.

70. Cogdell, R. J., and Scheer, H. (1985) *Photochem. Photobiol. 42*, 669-689.

71. Angerhofer, A., Cogdell, R. J., and Hipkins, M. F. (1986) *Biochim. Biophys. Acta 848*, 333-341.

72. Sturgis, J. N., Hunter, C. N., and Niederman, R. A. (1988) *Photochem. Photobiol. 48*, 243-247.

73. Pullerits, T., Chachisvillis, M., and Sundstrom, V. (1996) *J. Phys. Chem. 100*, 10787-10792.

74. Novoderenzhkin, V. I., and Razjivin, A. P. (1993) *FEBS Lett. 330*, 5-7.

75. Novoderenzhkin, V. I., and Razjivin, A. P. (1995) *Biophys. J. 68*, 1089-1100.

76. Bradforth, S. E., Jimenez, R., Van Mourik, F., van Grondelle, R., and Fleming, G. R. (1995) *J. Phys. Chem. 99*, 16179-16191.

77. Nienhaus, G. U., Mourant, J. R., Chu, K., and Frauenfelder, H. (1994) *Biochemistry 33*, 13413-30.

78. Wu, H.-M., Savikhin, S., Reddy, N. R. S., Jankowiak, R., Cogdell, R. J., Struve, W. S., and Small, G. J. (1996) *J. Phys. Chem. 100*, 12022-12033.

79. Van Amerongen, H., Van Haeringen, B., Van Gurp, M., and Van Grondelle, R. (1991) *Biophys. J. 59*, 992-1001.

80. Kramer, H. J. M., van Grondelle, R., Hunter, C. N., Westerhuis, W. H. J., and Amesz, J. (1984) *Biochim. Biophys. Acta 765*, 156-165.

81. Nagarajan, V., Alden, R. G., Williams, J. C., and Parson, W. W. (1996) *Proc Natl Acad Sci U S A 93*, 13774-9.

82. Renge, I., Mauring, K., and Avarmaa, R. (1987) *J. Luminescence 37*, 207-214.

83. Lathrop, E. J. P., and Friesner, R. A. (1994) *J. Phys. Chem. 98*, 3050-3055.

84. Woodbury, N. W., and Parson, W. W. (1984) *Biochim. Biophys. Acta 767*, 345-361.

85. Simpson, W. T., and Peterson, D. L. (1957) *J. Chem. Phys. 26*, 588-593.

86. Forster, T. (1966) in *Modern Quantum Chemistry, Part III* (Sinanoglu, O., Ed.) pp 93-137, Academic Press, New York.

87. Connolly, J. S., Samuel, E. B., and Janzen, A. E. (1982) *Photochem. Photobiol. 36*, 565-574.

88. Fidder, H., Knoester, J., and Wiersma, D. A. (1991) *J. Chem. Phys. 95*, 7880-7890.

89. Gudowska-Nowak, E., Newton, M. D., and Fajer, J. (1990) *J. Phys. Chem. 94*, 5795-5801.

90. Sturgis, J. N., and Robert, B. (1996) *Photosynth. Res. 50*, 5-10.

91. Hess, S., Akesson, E., Cogdell, R. J., Pullerits, T., and Sundstrom, V. (1995) *Biophys J 69*, 2211-25.

92. Hess, S., Chachisvilis, M., Timpmann, K., Jones, M. R., Fowler, G. J., Hunter, C. N., and Sundstrom, V. (1995) *Proc Natl Acad Sci U S A 92*, 12333-7.

93. Monshouwer, R., and van Grondelle, R. (1996) *Biochim. Biophys. Acta 1275*, 70-75.

94. Savikhin, S., and Struve, W. S. (1996) *Chem. Phys. 210*, 91-100.

95. Kennis, J. T. M., Streltsov, A. M., Aartsma, T. J., Nozawa, T., and Amesz, J. (1996) *J. Phys. Chem. 100*, 2438-2442.

96. Xiao, W., Lin, S., Taguchi, A. K., and Woodbury, N. W. (1994) *Biochemistry 33*, 8313-8322.

97. Novoderenzhkin, V. I., and Razjivin, A. P. (1995) *FEBS Lett. 368*, 370-372.

98. Visser, H. M., Somsen, O. J. G., Van Mourik, F., Lin, S., Van Stokkum, H. M., and Van Grondelle, R. (1995) *Biophys. J. 69*, 1083-1099.

99. Leegwater, J. A. (1996) *J. Phys. Chem. 100*, 14403-14409.

100. Kumble, R., Palese, S., Visschers, R. W., Dutton, P. L., and Hochstrasser, R. M. (1996) *Chem. Phys. Lett. 261*, 396-404.

101. Feick, R., Van Grondelle, R., Rijgersberg, C. P., and Drews, G. (1980) *Biochim. Biophys. Acta 593*, 241-253.

102. Sebban, P., Robert, B., and Jolchine, G. (1985) *Photochem. Photobiol. 42*, 573-578.

103. Gottfried, D. S., Stocker, J. W., and Boxer, S. G. (1991) *Biochim. Biophys. Acta 1059*, 63-75.

104. Mulliken, R. S., Rieke, C. A., Orloff, D., and Orloff, H. (1949) *J. Chem. Phys. 17*, 1248-1267.

105. Kral, M. (1970) *Collect. Czech. Chem. Commun. 35*, 1939-1948.

106. Harada, N., and Nakanishi, K. (1983) *Circular Dichroic Spectroscopy: Exciton Couplings in Organic Stereochemistry*, University Science Books, Mill Valley.

107. Miller, J., Gerhauser, J. M., and Matsen, F. A. (1959) *Quantum Chemistry Integrals and Tables*, University of Texas Press, Austin.

108. Shipman, L. L. (1977) *Photochem. Photobiol. 26*, 287-292.

109. Bottcher, C. J. F. (1973) *Theory of Electronic Polarization*, 2nd ed., Elsevier, Amsterdam.

110. Becker, M., Nagarajan, V., Middendorf, D., Parson, W. W., Martin, J. E., and Blankenship, R. E. (1991) *Biochim. Biophys. Acta 1057*, 299-312.

111. Alden, R. G., Johnson, E., Nagarajan, V., and Parson, W. W. (1997) *J. Phys. Chem. B 101*, 4667-4680.

112. Koolhaas, M. H., van der Zwan, G., Frese, R. N., and van Grondelle, R. (1997) *J. Phys. Chem. B 101*, 7262-7270.

113. Koolhaas, M. H., Frese, R. N., Fowler, G. J., Bibby, T. S., Georgakopoulou, S., van der Zwan, G., Hunter, C. N., and van Grondelle, R. (1998) *Biochemistry 37*, 4693-8.

114. Fowler, G. J., Visschers, R. W., Grief, G. G., van Grondelle, R., and Hunter, C. N. (1992) *Nature 355*, 848-50.

115. Meier, T., Chernyak, V., and Mukamel, S. (1997) *J. Phys. Chem. B 101*, 7332-7342.

116. Kuhn, O., and Sundstrom, V. (1997) *J. Chem. Phys. 107*, 4154-4164.

117. Zhang, W. M., Meier, T., Chernyak, V., and Mukamel, S. (1998) *J. Chem. Phys. 108*, 7763-7774.

118. Wu, H.-M., Ratsep, M., Cogdell, R. J., and Small, G. J. (1997) *J. Phys. Chem. B 101*, 7654-7663.

119. Monshouwer, R., Abrahamsson, M., van Mourik, F., and van Grondelle, R. (1997) *J. Phys. Chem. B 101*, 7241-7248.

120. Nagarajan, V., and Parson, W. W. (1997) *Biochem. 36*, 2300-2306.

121. van Amerongen, H., and Struve, W. S. (1995) *Methods. Enzymol. 246*, 259-283.

122. Becker, M., Nagarajan, V., and Parson, W. W. (1991) *J. Am. Chem. Soc. 113*, 6840-6848.

123. Rahman, T. S., Knox, R. S., and Kenkre, V. M. (1979) *Chem. Phys. 44*, 197.

124. Chang, Y. J., Cong, A. P., and Simon, J. D. (1997) *J. Chem. Phys. 106*, 8639-8649.

125. Brito Cruz, C. H., Gordon, J. P., Becker, P. C., Fork, R. L., and Shank, C. V. (1988) *IEEE J. Quantum Electron. 24*, 261.

126. Vos, M. H., Breton, J., and Martin, J. L. (1997) *J. Phys. Chem. B 101*, 9820-9832.

127. Yariv, A. (1988) *Quantum Electronics*, 3 ed., John Wiley & Sons, Inc., New York.

128. Pollard, W. T., and Mathies, R. A. (1992) *Ann. Rev. Phys. Chem. 43*, 497-523.

129. Mukamel, S. (1994) *Principles of Nonlinear Optical Spectroscopy*, Oxford University Press, New York.

130. Knox, R. S., and Gulen, D. (1993) *Photochem. Photobiol. 57*, 40-43.

131. Wynne, K., and Hochstrasser, R. M. (1993) *J. Chem. Phys. 171*, 179-188.

132. Kumble, R., and Hochstrasser, R. M. (1998) *J. Chem. Phys. 109*, 855-865.

133. Chachisvilis, M., Kuhn, O., Pullerits, T., and Sundstrom, V. (1997) *J. Phys. Chem. B 101*, 7275-7283.

134. Leupold, D., Stiel, H., Teuchner, K., Nowak, F., Sander, W., Ucker, B., and Scheer, H. (1996) *Phys. Rev. Lett. 77*, 4675-4678.

135. Chachisvilis, M., and Sundstrom, V. (1996) *J. Chem. Phys. 104*, 5734-5744.

136. Krueger, B. P., Scholes, G. D., and Fleming, G. R. (1998) *J. Phys. Chem. B 102*, 5378-5386.

137. Gilson, M., and Honig, B. (1986) *Biopolymers 25*, 2097-2119.

138. Rees, D. C. (1980) *J. Mol. Biol. 141*, 323-326.

139. Zhou, Z., and Swenson, R. P. (1995) *Biochemistry 34*, 3183-3192.

140. Lockhart, D. J., and Kim, P. S. (1993) *Science 260*, 198-202.

141. Forsyth, W. R., and Robertson, A. D. (2000) *Biochemistry 39*, 8067-8072.

142. Forsyth, W. R., Gilson, M. K., Antosiewicz, J., Jaren, O. R., and Robertson, A. D. (1998) *Biochemistry 37*, 8643-8652.

143. Quiocho, F. A., Sack, J. S., and Vyas, N. K. (1987) *Nature 329*, 561-564.

144. Warshel, A. (1981) *Biochemistry 20*, 3167-3177.

145. Dobson, C. M., Refield, C., and Bartik, K. (1994) *Biophys. J. 66*, 1180-1184.

146. Demchuk, E., Genick, U. K., Woo, T. T., Getzoff, E. D., and Bashford, D. (2000) *Biochemistry 39*, 1100-1113.

147. Åqvist, J., Luecke, H., Quiocho, F. A., and Warshel, A. (1991) *Proc. Natl. Acad. Sci. 88*, 2026-2030.

148. Varadarajan, R., Lambright, D. G., and Boxer, S. G. (1989) *Biochemistry 28*, 3771-3781.

149. Varadarajan, R., Zewert, T. E., Gray, H. B., and Boxer, S. G. (1989) *Science 243*, 69-72.

150. Garcia-Moreno, B., Dwyer, J. J., Gittis, A. G., Lattman, E. E., Spencer, D. S., and Stites, W. E. (1997) *Biophys. Chem. 64*, 211-224.

151. Dwyer, J. J., Gittis, A. G., Karp, D. A., Lattman, E. E., Spencer, D. S., Stites, W. E., and Garcia-Moreno, E. B. (2000) *Biophys. J. 79*, 1610-1620.

152. Sham, Y. Y., Muegge, I., and Warshel, A. (1998) *Biophys. J. 74*, 1744-1753.

153. Warshel, A., Papazyan, A., and Muegge, I. (1997) *J. BIOL. INORG. CHEM. 2*, 143-152.

154. Schutz, C. N., and Warshel, A. (2001) *Proteins 44*, 400-417.

155. Alexov, E., and Gunner, M. R. (1997) *Biophys. J. 72*, 2075-2093.

156. Sham, Y. Y., Chu, Z. T., and Warshel, A. (1997) *J. Phys. Chem. B 101*, 4458-4472.

157. Muegge, I., Apostolakis, J., Ermler, U., Fritzsch, G., Lubitz, W., and Knapp, E. W. (1996) *Biochemistry 35*, 8359-8370.

158. Langen, R., Brayer, G. D., Berghuis, A. M., McLendon, G., Sherman, F., and Warshel, A. (1992) *J. Mol. Biol. 224*, 589-600.

159. Cutler, R. L., Davies, A. M., Creighton, S., Warshel, A., Moore, G. R., Smith, M., and Mauk, A. G. (1989) *Biochemistry 28*, 3188-3197.

160. Russell, A. J., Thomas, P. G., and Fersht, A. R. (1987) *J. Mol. Biol. 193*, 803-813.

161. Sternberg, M. J., Hayes, F. R., Russell, A. J., Thomas, P. G., and Fersht, A. R. (1987) *Nature 330*, 86-88.

162. Loewenthal, R., Sancho, J., Reinikainen, T., and Fersht, A. R. (1993) *J. Mol. Biol. 232*, 574-583.

163. Antosiewicz, J., McCammon, J. A., and Gilson, M. K. (1994) *J. Mol. Biol. 238*, 415-436.

164. Alexov, E. G., and Gunner, M. R. (1999) *Biochemistry 38*, 8253-8270.

165. Nielsen, J. E., Andersen, K. V., Honig, B., Hooft, R. W., Klebe, G., Vriend, G., and Wade, R. C. (1999) *Protein Eng. 12*, 657-662.

166. Williams, J. C., Alden, R. G., Murchison, H. A., Peloquin, J. M., Woodbury, N. W., and Allen, J. P. (1992) *Biochemistry 31*, 11029-11037.

167. Allen, J. P., Artz, K., Lin, X., Williams, J. C., Ivancich, A., Albouy, D., Mattioli, T. A., Fetsch, A., Kuhn, M., and Lubitz, W. (1996) *Biochemistry 35*, 6612-6619.

168. Artz, K., Williams, J. C., Allen, J. P., Lendzian, F., Rautter, J., and Lubitz, W. (1997) *Proc. Natl. Acad. Sci. USA 94*, 13582-13587.

169. Paddock, M. L., Rongey, S. H., Feher, G., and Okamura, M. Y. (1989) *Proc. Natl. Acad. Sci. USA 86*, 6602-6606.

170. Lin, X., Williams, J. C., Allen, J. P., and Mathis, P. (1994) *Biochemistry 33*, 13517-13523.

171. Goldsmith, J. O., and Boxer, S. G. (1996) *Biochim. Biophys. Acta*

1276, 171-175.

172. Feher, G., and Okamura, M. Y. (1978) in *The Photosynthetic Bacteria* (Clayton, R. K., and Sistrom, W. R., Eds.) pp 349-386, Plenum Press, New York.

173. Rautter, J., Lendzian, F., Schulz, C., Fetsch, A., Kuhn, M., Lin, X., Williams, J. C., Allen, J. P., and Lubitz, W. (1995) *Biochemistry 34*, 8130-8143.

174. Berman, H. M., Westbrook, J., Feng, Z., Gilliland, G., Bhat, T. N., Weissig, H., Shindyalov, I. N., and Bourne, P. E. (2000) *Nucleic Acids Res. 28*, 235-242.

175. Alden, R. G., Parson, W. W., Chu, Z. T., and Warshel, A. (1996) *J. Phys. Chem. 100*, 16761-16770.

176. Lee, F. S., Chu, Z. T., Bolger, M. B., and Warshel, A. (1992) *Protein Eng. 5*, 215-228.

177. Hummer, G., and Szabo, A. (1996) *J. Chem. Phys. 105*, 2004-2010.

178. Lee, F. S., Chu, Z. T., and Warshel, A. (1993) *J. Comp. Chem. 14*, 161-185.

179. Warshel, A. (1973) *Israel J. Chem. 11*, 709.

180. Parson, W. W., Nabedryk, E., and Breton, J. (1992) in *The Photosynthetic Bacterial Reaction Center II Structure Spectroscopy, and Dynamics* (Breton, J., and Vermeglio, A., Eds.) pp 79-88, Plenum Press, New York.

181. Parson, W. W., Nagarajan, V., Gaul, D., Schenck, C. C., Chu, Z. T., and Warshel, A. (1990) in *Reaction Centers of Photosynthetic Bacteria* (Michel-Beyerle, M.-E., Ed.) pp 239-249, Springer-Verlag, Berlin.

182. Reimers, J. R., Hughes, J. M., and Hush, N. S. (2000) *Biochemistry 39*, 16185-16189.

183. Gasyna, Z., and Schatz, P. N. (1996) *J. Phys. Chem. 100*, 1445-1448.

184. Klapper, I., Hagstrom, R., Fine, R., Sharp, K., and Honig, B. (1986) *Proteins 1*, 47-59.

185. Gilson, M., Sharp, K. A., and Honig, B. (1987) *J. Comp. Chem. 9*, 327-335.

186. Nicholls, A., and Honig, B. (1991) *J. Comp. Chem. 12*, 435-445.

187. Sitkoff, D., Sharp, K. A., and Honig, B. (1994) *J. Phys. Chem. 98*, 1978-1988.

188.Hingerty, B. E., Ritchie, R. H., Ferrell, T. L., and Turner, J. E. (1985) *Biopolymers 24*, 427-439.

189.Guenot, J., and Kollman, P. A. (1992) *Protein Sci. 1*, 1185-205.

190.Mehler, E. L., and Guarnieri, F. (1999) *Biophys. J. 77*, 3-22.

191.Parson, W. W., Chu, Z. T., and Warshel, A. (1998) *Biophys. J. 74*, 182-191.

192.Luzhkov, V., and Warshel, A. (1992) *J. Comp. Chem. 13*, 199-213.

193.Lee, F. S., and Warshel, A. (1992) *J. Chem. Phys. 97*, 3100-3107.

194.Lee, B., and Richards, F. M. (1971) *J. Mol. Biol. 55*, 379-400.

195.Roth, M., Arnoux, B., Ducruix, A., and Reiss-Husson, F. (1991) *Biochemistry 30*, 9403-9413.

196.Mrabet, N. T., Van den Broeck, A., Van den brande, I., Stanssens, P., Laroche, Y., Lambeir, A. M., Matthijssens, G., Jenkins, J., Chiadmi, M., van Tilbeurgh, H., Rey, F., Janin, I., Quax, W. J., Lasters, I., Demaeyer, M., and Wodak, S. J. (1992) *Biochemistry 31*, 2239-2253.

197.York, D. M., Darden, T. A., Pedersen, L. G., and Anderson, M. W. (1993) *Biochemistry 32*, 1443-1453.

198.Yelle, R. B., Park, N. S., and Ichiye, T. (1995) *Proteins 22*, 154-167.

199.Ibragimova, G. T., and Wade, R. C. (1998) *Biophys. J. 74*, 2906-2911.

200.Walser, R., Hunenberger, P. H., and van Gunsteren, W. F. (2001) *Proteins 43*, 509-519.

201.Debye, P. (1929) *Polar Molecules*, Dover, New York.

202.Mehler, E. L., and Eichele, G. (1984) *Biochemistry 23*, 3887-3891.

203.Kirmaier, C., Holten, D., and Parson, W. W. (1985) *Biochim. Biophys. Acta 810*, 33-48.

204.Kirmaier, C., Holten, D., and Parson, W. W. (1985) *Biochim. Biophys. Acta 810*, 49-61.

205.Breton, J., Martin, J.-L., Migus, A., Antonetti, A., and Orszag, A. (1986) *Proc. Natl. Acad. Sci. USA 83*, 5121-5175.

206. Lockhart, D. J., Kirmaier, C., Holten, D., and Boxer, S. G. (1990) *J. Phys. Chem. 94*, 6987-6995.

207. Kirmaier, C., He, C., and Holten, D. (2001) *Biochemistry 40*, 12132-9.

208. Robles, S. J., Breton, J., and Youvan, D. C. (1990) *Science 248*, 1402-1405.

209. Taguchi, A. K., Stocker, J. W., Alden, R. G., Causgrove, T. P., Peloquin, J. M., Boxer, S. G., and Woodbury, N. W. (1992) *Biochemistry 31*, 10345-10355.

210. Plato, M., Lendzian, F., Lubitz, W., and Möbius, K. (1992) in *The Photosynthetic Bacterial Reaction Center II Structure, Spectroscopy, and Dynamics* (Breton, J., and Vermeglio, A., Eds.), Plenum Press, New York.

211. Reimers, J. R., and Hush, N. S. (1995) *Chem. Phys. 197*, 323-332.

212. Reimers, J. R., and Hush, N. S. (1995) *J. Am. Chem. Soc. 117*, 1302-1308.

213. Lendzian, F., Huber, M., Isaacson, R. A., Enderward, B., Plato, M., Bonigk, B., Möbius, K., Lubitz, W., and Feher, G. (1993) *Biochim. Biophys. Acta 1183*, 139-160.

214. Breton, J., Nabedryk, E., and Clerici, A. (1999) *Vibrational Spectrosc. 19*, 71-75.

215. Nabedryk, E., Schulz, C., Müh, F., Lubitz, W., and Breton, J. (2000) *Photochem. Photobiol. 71*, 582-588.

216. Murchison, H. A., Alden, R. G., Allen, J. P., Peloquin, J. M., Taguchi, A. K., Woodbury, N. W., and Williams, J. C. (1993) *Biochemistry 32*, 3498-3505.

217. Nabedryk, E., Allen, J. P., Taguchi, A. K., Williams, J. C., Woodbury, N. W., and Breton, J. (1993) *Biochemistry 32*, 13879-13885.

218. Müh, F., Rautter, J., and Lubitz, W. (1997) *Biochemistry 36*, 4155-4162.

219. Rautter, J., Lendzian, F., Wang, S., Allen, J. P., and Lubitz, W. (1994) *Biochemistry 33*, 12077-12084.

220. Müh, F., Lendzian, F., Roy, M., Williams, J. C., Allen, J. P., and Lubitz, W. (2002) *J. Phys. Chem. B.*

221. Tränkle, E., and Lendzian, F. (1989) *J. Magn. Reson. 84*, 537-547.

222. Nabedryk, E., Breton, J., Williams, J. C., Allen, J. P., Kuhn, M., and Lubitz, W. (1998) *Spectrochim. Acta. A 54*, 1219-1230.

223. Stowell, M. H., McPhillips, T. M., Rees, D. C., Soltis, S. M., Abresch, E., and Feher, G. (1997) *Science 276*, 812-816.

224. Nabedryk, E., Bagley, K. A., Thibodeau, D. L., Bauscher, M., Mäntele, W., and Breton, J. (1990) *FEBS Lett 266*, 59-62.

225. Piepho, S. B. (1988) *J. Am. Chem. Soc. 110*, 6319-6326.

226. Gasyna, Z., Schatz, P. N., and Boyle, M. E. (1995) *J. Phys. Chem. 99*, 10159-10165.

227. Schatz, P. N. (1999) in *Inorganic Electronic Structure and Spectroscopy* (Solomon, E. I., and Lever, A. B. P., Eds.) pp 175-226, John Wiley & Sons, Inc., New York.

228. Norris, J. R., and Katz, J. J. (1978) in *The Photosynthetic Bacteria* (Clayton, R. K., and Sistrom, W. R., Eds.), Plenum Press, New York.

229. Feher, G., Hoff, A. J., Isaacson, R. A., and Ackerson, L. C. (1975) *Ann. N. Y. Acad. Sci. 244*, 239-259.

230. Norris, J. R., Scheer, H., and Katz, J. J. (1975) *Ann N Y Acad Sci 244*, 260-280.

231. McConnell, H. M. (1956) *J. Chem. Phys. 24*, 632.

232. Atherton, N. M. (1993) *Principles of Electron Spin Resonance*, Ellis Horwood PTR Prentice Hall, New York.

233. Mäntele, W., Wollenweber, A., Nabedryk, E., Breton, J., Rashwan, F., Heinze, J., and Kreutz, W. (1987) in *Progress in Photosynthesis Research* (Biggins, J., Ed.) pp 329-333, Martinus Nijhoff, Dordrecht.

234. Mäntele, W., Wollenweber, A., Nabedryk, E., and Breton, J. (1988) *Proc. Natl. Acad. Sci. USA 85*, 8468-8472.

235. Nabedryk, E., Breton, J., Wachtveitl, J., Gray, K. A., and Oesterhelt, D. (1992) in *The Photosynthetic Bacterial Reaction Center II Structure, Spectroscopy, and Dynamics* (Breton, J., and Vermeglio, A., Eds.), Plenum Press, New York.

236. Nabedryk, E. (1996) in *Infrared Spectroscopy of Biomolecules* (Mantsch, H. H., and Chapman, D., Eds.) pp 39-81, Wiley-Liss.

237. Nabedryk, E., Breton, J., Allen, J. P., Murchison, H. A., Taguchi, A. K., Williams, J. C., and Woodbury, N. W. (1992) in *The Photosynthetic Bacterial Reaction Center II Structure, Spectroscopy, and Dynamics* (Breton, J., and Vermeglio, A., Eds.).

238. Leonhard, M., and Mäntele, W. (1993) *Biochemistry 32*, 4532-4538.

239. Mattioli, T. A., Williams, J. C., Allen, J. P., and Robert, B. (1994) *Biochemistry 33*, 1636-1643.

240. Nabedryk, E., Robles, S. J., Goldman, E., Youvan, D. C., and Breton, J. (1992) *Biochemistry 31*, 10852-10858.

241. Reimers, J. R., and Hush, N. S. (1996) *Chem. Phys. 208*, 177-193.

242. Johnson, E. T., and Parson, W. W. ((submitted to Biochemistry)).

243. Goushcha, A. O., Holzwarth, A. R., and Kharkyanen, V. N. (1999) *Phys. Rev. E 59*, 3444-3452.

244. Atkins, P. W. (1983) *Molecular Quantum Mechanics*, 2nd ed., Oxford University Press, Oxford.

245. Park, E. S., Andrews, S. S., Hu, R. B., and Boxer, S. G. (1999) *J. PhYs. Chem. B 103*, 9813-9817.

246. Robert, B., and Lutz, M. (1988) *Biochemistry 27*, 5108-5114.

VITA

Ethan Johnson was born in Albuquerque, New Mexico. He earned a Bachelor of Arts in Physics from Cornell Univeristy in 1995. He received a Doctor of Philosophy at the University of Washington in Biochemistry in the spring of 2002.